Synthesis and characterisation of iron platinum nanoparticles

Howard, Luciano E. M.

Synthesis and Characterisation of Iron Platinum Nanoparticles

Luciano E. M. Howard M.Chem (Dunelm)
Trevelyan College
University of Durham

Supervisors: Dr John S. O. Evans and Dr Andrew K. Hughes

A thesis submitted in partial fulfilment of the requirements for the degree of Doctor of Philosophy.

Department of Chemistry
University of Durham
2007

Abstract

Synthesis and characterization of iron platinum nanoparticles PhD Thesis
Luciano Howard 2007

This thesis investigates the synthesis and characterization of FePt nanoparticles, a material which is a promising candidate for use as an ultra-high density magnetic storage medium; relevant literature is reviewed in **chapter one**.

Chapter two gives full details of the characterisation techniques and physical property measurements employed throughout the work described in the following chapters. This includes powder X-ray diffraction, SQUID magnetometry, transmission electron microscopy, extended X-ray fluorescence spectroscopy and Rutherford backscattering.

Chapter three describes the synthesis and characterisation of FePt nanoparticles prepared by a route presented in the literature as well as one developed during this study.

Chapter four describes a systematic investigation into the Rietveld refinement of powder X-ray diffraction data of iron platinum nanoparticles. From the study it is concluded which of the methodologies presented is most suitable for use in further work on iron platinum nanoparticle studies.

Chapter five describes a number of *in-situ* variable temperature X-ray diffraction studies designed to investigate the order-disorder transition in FePt nanoparticles. A comparison between this transition in samples made via both synthetic routes discussed in chapter three is made before analysing in-depth data in order to provide information about the phase transition and its relationship with precise synthetic conditions.

Chapter six describes work done on FePt nanoparticles to determine if EXAFS measurements can be obtained and modelled such that conclusions can be drawn as to the degree of order of samples prepared via different methods.

Chapter seven describes a variety of magnetic studies designed to investigate the structure and properties of FePt nanoparticles. The first part of the chapter focuses on typical experiments and what use they are whilst the second part discusses the methodology and equipment required to study the phase transition of iron platinum nanoparticles, i.e. variable temperature magnetic studies.

Acknowledgements

Firstly and most importantly my eternal gratitude must go out to John Evans. Thank-you for being one of the cleverest and most helpful people I know, always there at any time (3 AM in Daresbury?) to help with everything from the sublime to the ridiculous.

Thanks to Seagate Technologies who funded this work.

Andrew Hughes whose excellence and experience in organometallic synthesis led to the development of the Durham route to FePt nanoparticles.

Brian Tanner, Ian Terry and Arnaud Serres for all their help magnetically speaking. Special thanks to Sean Giblin who was my magnetism go to guy for the three years of magnetic work.

All of CG 31 who have helped in different ways over the years. Richard Gover for all things D8; Loc Nguyen, the synthetic powerhouse without whom the world of FePt would have been a lonely and empty place. Matt Hampson for being on a parallel path to me right until the end! Ivana for gossip and great food. Doctors Withers and Crossland for all their PhD knowledge and experience. Graham for the enjoyable exclamations now and again. Little Rich and Bex, Mr Hickey and Dave Lister, Martin, Laura and Hannah – project students who brought many things to my world and made it that much better.

Malcolm and Peter, without whose glassblowing skills extraordinaire I would have been up a creek without a paddle; Richard Thompson for RBS galore; Vivienne Thompson for her TEM knowledge.

Everyone at Trevs over the years. Special thanks must go to Carl, my fellow student, friend and housemate. Kathryn/Lorna/Barnes who were in the same situation as me somewhere in the country. Kiran/Coops/Blondie for chemistry related beer events. Mark, Mike, Mozza, Nick and Si, the rest of Trevs A (in spirit, at least).

To get here has taken 26 years, and a lot of help. Thanks to Elsa, Charlie, Gnipper and Bob for being my best friends. Auntie Pia and Uncle Peter for always encouraging me and making me feel special. Grandma for being the best. Nan and Bamps for keeping my feet on the ground. Mike, Dawn and Matt for being in my generation, and the next. Mum and Dad for, well, being Mum and Dad. I wouldn't be writing this were it not for you. Thanks to you I am who I am and can become what I hope to be.

Katie – thank-you. For everything. This thesis wouldn't exist without you. You've lifted me so much since I've known you that anything which makes me down is only relative, rather than absolute. To you I owe it all. Nobody does it better.

Declaration

The work described in this thesis is entirely my own work, except where I have acknowledged help from a named person or provided a reference to a published source or a thesis.

The research presented was performed in the Department of Chemistry, University of Durham between October 2002 and September 2005, the results of which have not been submitted for a degree in this or any other university.

This thesis conforms to the word limit set out in the Degree Regulations. It contains ~ 52, 000 words including appendices and footnotes but excluding references, or experimental data included on the CD located on the inside cover of the thesis.

Date: 14/5/07 Signature: 

Statement of Copyright

Glossary of Abbreviations

VT = Variable temperature

VTXRD = Variable temperature X-ray diffraction

XRD = X-ray diffraction

FC = Field cooled

ZFC = Zero-field cooled

MPMS = Magnetic properties measurement system

TEM = Transmission electron microscopy

RBS = Rutherford backscattering

SQUID = Superconducting quantum interference device

EXAFS = Extended X-ray absorption fluorescence spectroscopy

FCC = Face centred cubic

FCT = Face centred tetragonal

SRS = Synchrotron radiation source

Table of Contents

Table of Figures

Table of Tables

"What We Do In Life Echoes In Eternity"

[Maximus Decimus Meridius - Gladiator]

Chapter 1 - Introduction and Literature Review

1.1 Introduction to Nanotechnology

Nanotechnology is an all-encompassing term used to describe the chemistry and physics of nanostructured materials; these are defined as any material characterised by one or more dimension in the nanoscale regime (1-100 nm)[1]. The structural features of such materials are different to both molecular and bulk analogues, therefore nanostructured materials create a bridge between such systems[2]. As the structural features are different, so are the properties of nanomaterials. If the synthesis of nanomaterials can be sufficiently controlled, and the properties of these resultant materials understood and utilised intelligently, then exciting new products, devices and technologies can be developed.

There are two underlying themes of nanotechnology; the bottom-up approach and the top-down approach. The importance of the bottom-up approach was noted by Richard Feynman in his 1959 lecture entitled "There is plenty of room at the bottom"[3]. This is concerned with making nanomaterials smaller, i.e. miniaturising them. The top-down approach was remarked upon by Jean-Marie Lehn when he said "there is plenty of room at the top"[4], where each component is one part of a larger structure.

In the last 10-15 years there has been a large increase in the amount of research into nanostructured materials. There are many reasons for this. New methods of synthesising nanomaterials have been developed, extending from physical to chemical methods, or a combination of both. These in turn have led to the propagation of further techniques, each building upon the previous one in order to improve the quality of the resulting material. The better the resulting material, the easier to observe and understand the unique properties provided and work towards the exploitation of those properties. Potential applications of nanoparticles are wide and varied but include ultra-high density magnetic recording media[5], toxic chemical adsorbents[6], high-capacity batteries[6], gas storage[7], drug delivery[8] and 'nanocomputers'[9].

1.2 Nanostructured Materials

1.2.1 Introduction

A nanostructured material is one which, in at least one dimension, has a natural length scale between 1 and 100 nm[10, 11]. Materials in this size regime do not display properties characteristic of their bulk or molecular counterparts, and the properties they do exhibit are dependent on

their size[12]. The type of properties displayed by nanostructured materials includes electrical, structural, chemical, magnetic and catalytic[10, 11, 13-18] properties as well as, in the case of metals, their electronic and optical properties[19-21]. These interesting size dependent properties allow the nanostructured materials to be utilised in novel applications such as information storage[22], magnetic refrigeration[23] and as ferrofluids[24-27].

1.2.2 Chemical Reactivity

Typically, a material with a large surface will be more reactive than one with a comparatively small surface area. A nanostructured material has a greater surface to volume ratio, so more of its constituent particles are present in the surface layer. The fraction of atoms in the surface layer for a given particle can be approximated by **equation 1.1**.

$$\frac{N_{Surface}}{N_{Total}} = \frac{1.5}{D} \quad \textbf{(1.1)}$$

Where D is the diameter of the particle, $N_{Surface}$ is the total number of atoms on the surface of the particle and N_{Total} is the total number of atoms in the particle. This equates to ~ 100 % of the atoms being in the surface layer if the particle is 1 nm in diameter, ~ 15 % in a 10 nm particle and a small amount for a bulk material of infinite size. Therefore, a nanoparticle is typically more reactive than a bulk material; the smaller that nanoparticle, the more reactive. This effect has been described in systems throughout the literature. Bulk Ag particles have been shown to adsorb O^{2-} species at 80 K. Ag nanoparticles, in the same study, were shown to adsorb O^- ions also, having caused the dissociation of the O_2 species[28]. Copper, palladium and nickel particles have been observed interacting with CO species. In the case of copper[29] and palladium[30] particles, CO is absorbed by bulk or nano-sized particles. However, the retention of CO at higher temperatures (above 250 K) is greater the smaller the particles. Nickel nanoparticles, in addition to exhibiting similar properties to copper and palladium in this instance, are also capable of dissociating the CO yielding carbidic species which are then adsorbed onto the nickel nanoparticle surfaces[31].

1.2.3 Structural Parameters

It is a fact that a nanoscale material's structural properties are different to those of bulk materials. For example there is a lattice contraction as a function of decreasing particle size[32]. These structural differences compared to the bulk analogue of a material affect the properties, providing a physical basis for the unique properties of nanoscale materials.

1.2.4 Self-Assembly

Self-assembly is defined as the spontaneous formation of ordered aggregates, often called particle superlattices, by combination of separate or linked components[33]. This occurs in nature, for example opal formation[34], or the folding of polypeptide chains to form proteins[35] and as molecular self-assembly in the formation of monolayers[36] or phase separated polymers[37]. No human interaction is necessary. Self-assembly is interesting to scientists and technologists for four main reasons[33]:

1. Self-assembly is integral to life; a large number and variety of biological structures are formed in this way, from the previously mentioned proteins to nucleic acids and lipid membranes.
2. Synthetic routes to materials with regular structures such as liquid crystals or molecular crystals are aided by self-assembly.
3. As self-assembly is known to occur in larger systems than just molecules it has a potential benefit to materials and condensed matter science applications.
4. Nanocrystals self-assemble to form particle superlattices, or nanocrystal assemblies[12].

By creating such superlattices, again, the properties of the material can vary from that of macroscopic analogues. For example, the physical properties of a nanocrystal assembly of Co particles (5.8 nm) alter such that the magnetic blocking temperature increases[38, 39]. Also, fct phase FePt alloy nanocrystal assemblies exhibit ferromagnetic behaviour[22].

1.3 General Synthesis of Nanoparticles

It was shown in **section 1.2** that the size of a particle when that particle is in the nanoscale regime is of utmost importance to its properties, indeed, the size determines them. As that is the case, in order to utilise any advantageous properties which the size of the material may provide, the synthesis of any given nanostructured material is highly important. Ideally, monodisperse nanocrystals of controllable size and shape synthesised by a simple, effective and wholly reproducible route are desired. If these aims are achieved, the sample may be of sufficient use to correctly identify properties unique to the nanoparticles rather than bulk analogues. For the purposes of nanoparticle chemistry, monodisperse samples are defined such that the standard deviation in particle diameter is less than or equal to 5 % ($\sigma \leq 5$ %)[11] of the particle size. It should be noted that typically the term nanocrystal is reserved for crystalline material in the nanoscale regime, whereas nanoparticle is used to describe anything between 1 and 100 nm[11].
The chemistry of nanoparticles, in one form or another, has been ongoing since the 19th century. Colloidal chemistry, where a colloid is a one-phase mixture of multiple components, is a precursor to nanoparticle chemistry. One of the first colloidal dispersions to be systematically

studied is colloidal gold, studied by Michael Faraday in the 1850s. Faraday took an aqueous solution of gold chloride and reduced it with phosphorus yielding a ruby coloured liquid. Chemical testing showed the gold was no longer present in an ionic form, but reagents which were able to dissolve metallic gold in this situation removed the colour. Faraday concluded that the gold was present in the liquid in the form of very fine particles. Addition of small amounts of salts resulted in the ruby colour changing to blue and ultimately deposition of solid from the blue liquid. This process was irreversible[12]. The synthesis of colloids or variations thereof (ferrofluids, nanoparticles) has continued and advanced throughout the years.

In order to successfully prepare monodisperse colloids, or nanoparticles in solution from chemical precursors, three phases of particle synthesis are required. These are described below.

1.3.1 Nucleation[11]

A nucleation step occurs first. Upon integration of the reagents into the reaction vessel, the concentration of precursors is high. If this rises above the nucleation threshold, colloidal nanoparticles will form. Each of these particles will be of a similar size as the growth mechanism for each, and the time over which they are formed is the same. This stage must be fast for nanoparticle synthesis.

1.3.2 Growth[40]

Each of the nucleated particles will now grow from the solution and this is either diffusion or reaction limited. There are three important factors governing the growth: the rate at which mass can move across a particle's surface, the temperature of the solution and the saturation of the solution with either reagents or product. This stage must be slow for nanoparticle synthesis.

1.3.3 Ostwald Ripening[11, 40-42]

After the nucleation and growth stages, Ostwald ripening, or coarsening, occurs for the duration of the experiment. It is the process by which smaller particles disappear from the solution and larger particles continue growing. Essentially, the large surface energy prevalent in the small particles drives them to dissolution and the resultant material is consumed by the larger particles in order to grow further. It follows that as time proceeds in any given nanoparticle synthesis that the average particle size increases whilst the total number of colloidal particles decreases. This can be seen, in terms of the entire reaction process, in **figure 1.1**. This stage allows great flexibility in the nanoparticle synthesis; product can be removed at various times, yielding material of differing size and population. However, the particle size range will be large during this stage.

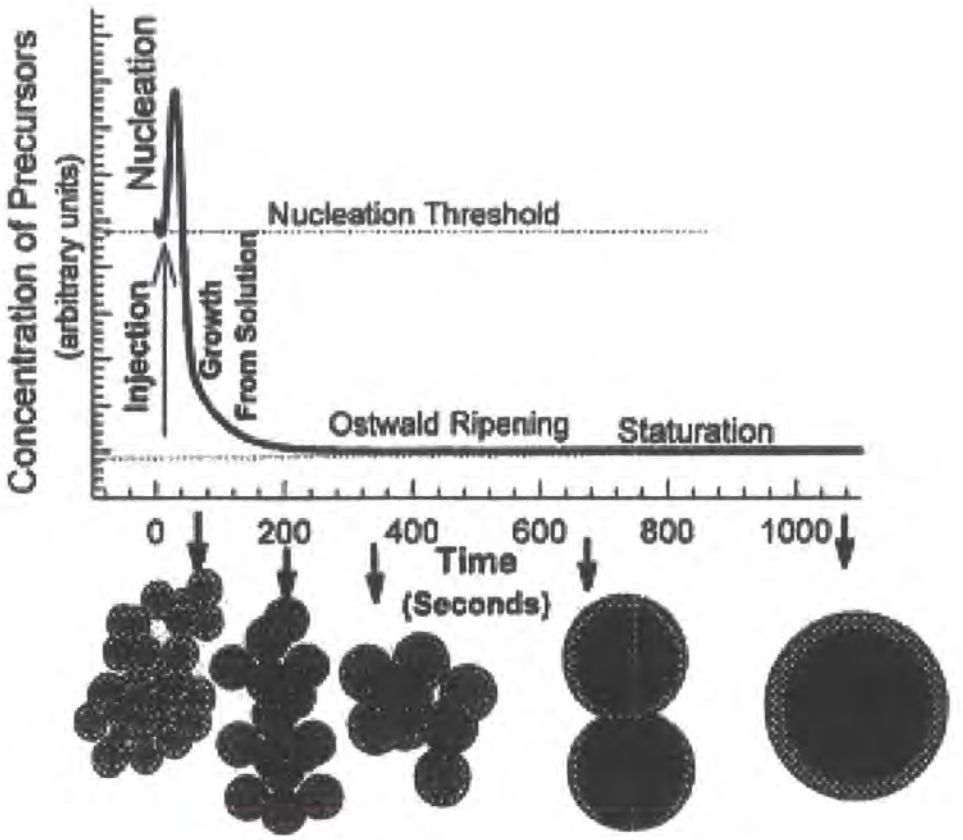

Figure 1.1 A schematic describing the process of colloidal nanoparticle synthesis, through the stages of nucleation, growth and Ostwald ripening[10].

1.3.4 Other Factors[40]

It has already been noted that particles in solution tend to a larger size due to energy effects. In order to avoid agglomeration of the particles, i.e. ensure all particles remain small in size and equal in size and shape, a stabiliser must be used. This is often a surfactant. Two methods of stabilisation are common, firstly, steric repulsion due to the coating of the particles by a surfactant molecule, for example, a long chain hydrocarbon[43], and secondly, by way of charged interactions between species adsorbed onto the colloidal particle's surface. In the case of steric repulsion, whereby surfactants (or other materials such as polymers) coat a particle, it has been shown experimentally that a monolayer of the surfactant, or 'capped ligand' generically is often present on the nanoparticle.

1.4 Synthesis of Nanoparticles

Although there are several factors common amongst the various synthetic methods used in nanoparticle production, there are still a number of differing specific techniques. Some of these, along with examples of their use will be described here. The scope of this review means that the

majority of techniques and processes described will be related to magnetic and/or metallic materials.

1.4.1 Sputtering

Sputtering is a physical method used for the deposition of thin-films of nanostructured materials. Typically, energetic ions bombard the target material resulting in the ejection of some atoms into the gas phase from within the target material. These gas phase atoms then get deposited on any nearby surface. A percentage of the atoms will be deposited on the chosen substrate. A schematic representing sputtering is shown in **figure 1.2**.

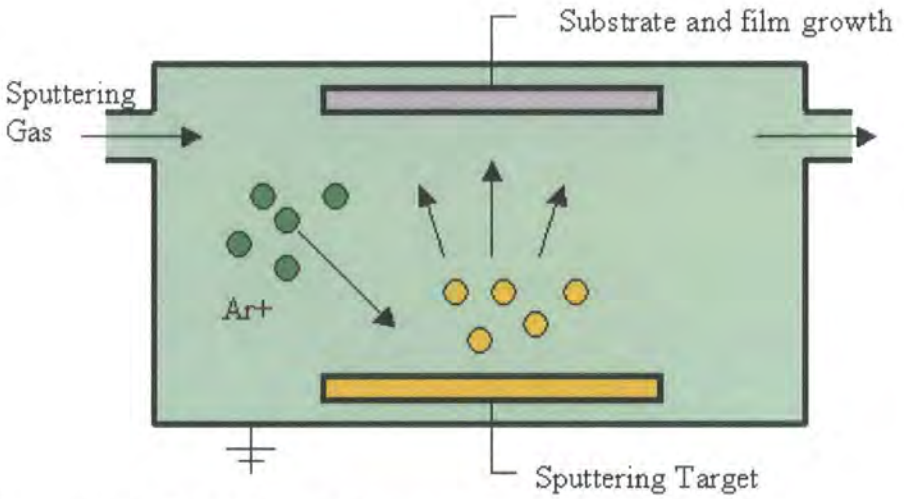

Figure 1.2 A schematic detailing the process of sputtering

The main advantage of using sputtering techniques to synthesise nanostructure material is the control of the layer-thickness afforded by it, i.e. nanoscale growth control in one direction is achieved. Typically, materials where small magnetic nanoparticles are embedded within a magnetic or non-magnetic matrix are synthesised using this technique[10]. FePt–$(C_4F_8)n$ films[44], FePt alloy thin films[45] of varying thickness and Fe_xPt_{1-x} cluster films[46] have all been synthesised using sputtering based techniques.

1.4.2 Sonochemical Decomposition[10, 47]

By applying high frequency sound (kHz – MHz) to any given solution, acoustic cavitation occurs – bubbles form and grow before collapsing via implosion. This results in localised areas of great temperatures – up to 5000 K. The pressures associated with these hotspots are large also, reaching many atmospheres. The large cooling rates of these hotspots (up to 1010 K/s[48, 49] have been used to aid production of iron nanoparticles[50]. Many other nanoparticles have been produced by the utilisation of sonochemical methods, including Fe/Co alloys[51, 52], Mo_2C semicarbide species that have catalytic properties[53] and metal/polymer nanoparticle composites

(nanoparticle in polymer matrix)[54]. An advantage of sonochemical synthesis of nanoparticles is that the reaction can be scaled up simply for industry[48, 55].

1.4.3 Mechanical Alloying[10]

A technique in existence before its application to the synthesis of nanoparticles, mechanical alloying, or ball milling, requires the grinding and mixing of requisite reagents, with or without a liquid present, by a grinding medium, which typically uses stainless steel balls. Effectively the powdered reagents, in solution or not, are reduced to a fine powder and alloys form from the constituent reagents. The technique is similar to that of the laboratory based pestle and mortar. The advantage of such a technique for the synthesis of nanoparticles is that the technique is already utilised in other areas, so is easy and cheap to convert to the synthesis of nanoparticles and large quantities of a given material can be produced. However, the monodispersity of the nanoparticles can not be controlled easily. Such a technique has been used to fabricate nanostructured materials of the type where metallic particles are contained within a matrix, where the matrix can be chemically dissimilar or the same material (but the nanoparticles are discrete structures within the random matrix)[56]. More specifically, Fe, Cu, Ni and CuNi[57] nanoparticles have all been synthesised using this technique, with sizes ranging from 17-26 nm[58]. Also TiN[59], Si[60] and Ge/Sn (a nominally immiscible binary system) dispersions[61] have all been produced using mechanical alloying methods.

1.4.4 Chemical Reduction[10]

For magnetic and metallic nanoparticles, chemical synthetic methods provide the best results, a case in point being that of FePt nanoparticles[22, 43, 62]. Nanoparticles can typically be collected as a powder from the reaction solution and redispersed in other solvents for storage or further reaction.

Five[63] important factors which have been touched upon previously are described in full below. These need to be remembered when developing any nanoparticle synthesis.

1. Monodisperse nanoparticles are required ($\sigma \leq 5$ %).
2. Particle size control.
3. Is it possible to obtain nanocrystals?
4. Particle shape control.
5. Particle deposition onto substrate for use in desired application.

A number of nanoparticles have been synthesised via chemical reduction, with the actual method used varying from system to system. One such method is based on the reduction of a metal salt by an alkali metal when both reagents are mixed into a hydrocarbon solvent with a boiling point

greater than the melting point of the alkali metal[64, 65]. Particle size can be controlled by variation of the temperature at which the reaction occurs.

Reduction of various metal salts in aqueous solution yields near monodisperse nanoparticles. Specifically, Au[66], platinum[67] and silver[68] have been produced by such methods.

Borohydride reduction of metal salts has also led to nanoparticle formation. For example, Brust *et al.*[69] were able to synthesis 1-3 nm sized gold nanoparticles by this method, whilst Fe[70], Co[71, 72], FeCo[73], Cu[74], Ni[75], CoB, NiB, FePt and FeB[76] have also been synthesised by this route. When using borohydride ions to reduce metal salts, resulting particles range in size from 2-100 nm and are typically ultra-fine particles with large inter-particle spacing, capped ligand coated ultra-fine particles or ultra-fine particles with a core-shell morphology (see **figure 1.3**). It is thought that FePt nanoparticles may have a core-shell morphology[77] in that the FePt core is coated by an Fe or Fe_2O_3 shell. It should be noted that whilst the shell may limit particle-particle interactions, thus helping avoid particle agglomeration, it may also lead to unwanted shell/core interactions. If both the shell and core are magnetic, for example, this would affect the magnetic properties of the nanoparticle[10].

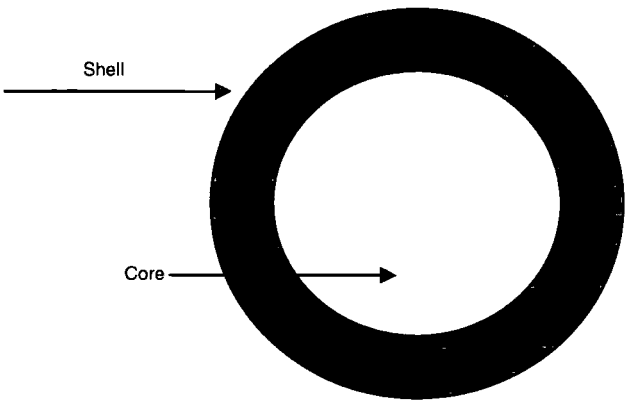

Figure 1.3 A schematic describing a core/shell nanoparticle. Each component is chemically distinct from the other.

1.4.5 UV Photolysis and Microwave Assisted Synthesis and γ Irradiation

UV light has been shown to provide the requisite energy for the synthesis of some nanoparticle systems. Specifically, AgPd alloys ranging in size from 3-11 nm have been produced[78]. Silver nanoparticles have since been produced by the utilisation of UV radiation as the energy source[79-81]. γ-irradiation has also been used to synthesis nanoparticles such as CdS[82].

Equally, microwaves have been used in place of heat or UV radiation as the chosen energy source for nanoparticle formation. FePt[83-85] and FePd[85], InGaP, InP, and CdSe[86], Au[87], Pt, Ir, Rh, Pd, Ru[88],

PtAg, PdAg[89] and Ag[90] have been produced using microwaves. The advantage of using microwave radiation as the energy source in such reactions is that much higher rates of heating can be achieved compared to conventional heating methods. The heating is also potentially more uniform across the entire reaction solution.

1.4.6 Electrochemical Methods

The use of electrochemical methods for the synthesis of nanoparticles has been achieved, for example in production of Pd and Ni clusters[91]. The benefit of such a method is the ability to control particle size by adjusting the current density passed through the system. Other nanoparticles which have been synthesised using electrochemical methods are Au[92, 93], Ag[94, 95], Cu[96], Pd[97] and Fe_2O_3[98].

1.4.7 Transition Metal Nanoparticles

The preparation of metallic and/or magnetic nanoscale materials has been a very active area of research for some time. In 1983 Hoon *et al.*[99] were able to prepare Ni ferrofluids, fine magnetic particles. Kilner *et al.*[100, 101] prepared both metallic iron ferrofluids and a novel technique for the preparation of metallic magnetic fine particles from metal atoms (decomposition of toluene-cobalt complex yielding a Co ferrofluid with excellent magnetic properties). Sun *et al.*[102]. were able to produce magnetic colloids of magnetic nanocrystals of cobalt using high temperature reduction of cobalt chloride in solution. These were found to self-assemble into nanocrystal assemblies. As-synthesised these nanoparticles exhibited a complex cubic structure, ε-Co. This form of Co is ferromagnetic and hexagonally close-packed. Annealing initiated a phase transition at ~ 300 °C whereby the nanoparticles converted from the ε-Co structure to hexagonally close packed Co, hcp-Co. Deposition of these hcp-Co nanoparticles when dispersed in a carrier solvent resulted in 2 and 3 dimensional nanocrystal assemblies. Many other workers have been able to produce Co[103-106] nanocrystals using various chemical methods.

Co[107] nanoparticles specifically, and a variety of nanoparticles[108] generally, have been synthesised using reverse micelles as a reactor for any chemical reaction occurring. A reverse`, or inverse micelle is a surfactant stabilised droplet of water in oil. Unfortunately this method has tended to yield poorly crystalline material and the particle size distribution is such that the particles are not monodisperse (σ = 9 %)[63].

Co nanoparticles with the hcp structure have been synthesised[109, 110] directly by way of the polyol process – see **section 1.5.5**. This is the term used to describe the reduction of a metal salt to a metal by a diol or polyalcohol[22].

Iron nanoparticles have been synthesised successfully by the thermal decomposition of iron pentacarbonyl in the presence of oleic acid at 100 °C[111]. This reaction yielded an iron-oleic acid complex which when heated at 300 °C resulted in 4-20 nm Fe particles.

1.5 FePt Nanoparticles

1.5.1 Introduction

Magnetic storage media are commonly used to record and store information throughout the world. Every personal computer will contain at least one magnetic hard disc drive and most people will be familiar with video and audio cassettes too. The first hard drive was sold by IBM in 1956[112]. Typically a number of bits (a collection of particle grains in current technologies equate to one bit) will be deposited onto a substrate. This substrate is the hard drive platter – more than one can be positioned in any given hard drive. Each of these grains, or bits, will be able to store information by way of its magnetic orientation (up or down equating to 1 or 0 in binary computer language). A recording head will be able to write to a bit and read from it. The conventional recording medium is a CoX[112] alloy (X = Pt, Cr, B, Ta). Particle grain sizes are less than 10 nm.

In order to increase the density of modern day magnetic storage media, scaling techniques are employed whereby the particle sizes are reduced. However, a problem associated with this is the superparamagnetic effect[113-115], which becomes a problem when particle grain size is reduced. Effectively, this is when the energy required to alter the direction of the associated magnetic moment is comparable to the ambient thermal energy. The individual grains are as such likely to randomly undergo change in the orientation of their associated magnetic moment. The magnetic storage media are not stable; information can become corrupted. There are a number of potential ways with which to postpone the superparamagnetic limit. One option would be to use a perpendicular recording technique but this thesis will focus on the synthesis of self-assembled nanocrystal superlattices as potential ultra-high density storage media.

FePt nanoparticles in the $L1_0$, or fct, phase are a strong candidate for ultra-high density magnetic storage applications when arranged in a self-assembled nanocrystal superlattice. The reason for this is twofold; firstly they have a large uniaxial magnetocrystalline anisotropy $K_U = 7 \times 10^6 J/m^3$ [116] and secondly they are chemically stable[117]. The magnetic stability of an individual particle varies according to the product of the grain volume and uniaxial magnetocrystalline anisotropy. FePt nanoparticles as small as 2.8 nm would be suitable for magnetic recording media applications due to the large K_U. The potential advances over current technologies would be significant.

1.5.2 Bulk FePt Alloys

Before FePt nanoparticles were synthesised and subsequently studied, bulk systems received a large amount of attention over time. It was in 1907[118] that the first significant FePt alloy study took place. Gradually more information about FePt systems was obtained. In 1950 three stable phases of FePt alloy were found; $FePt_3$, FePt and Fe_3Pt[119]. An order-disorder transition was shown to occur, similar to that seen in AuCu[120] alloys. This was confirmed by a variety of analytical methods including X-ray diffraction[119, 121], magnetic[122, 123], electrical[119, 124] and mechanical[125] property data. A phase diagram of FePt has been produced from the information documented in the references provided already, and that given by Hansen[126] and Bozorth[127]. **Figure 1.4** shows this phase diagram as presented by Watanabe *et al.* [128] and taken from Stahl *et al.* [129]:

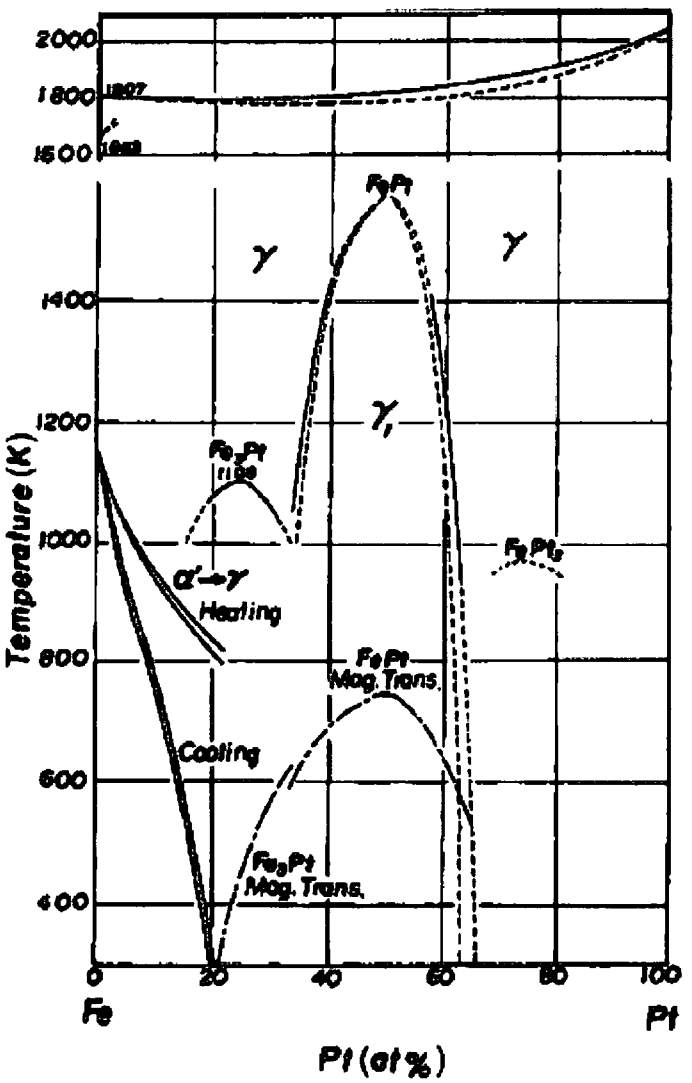

Figure 1.4 An FePt alloy phase diagram. The disordered (fcc) phase is represented by γ whilst the ordered fct phase is shown as γ1.

1.5.3 FePt Crystallography

It has already been stated that the order-disorder transition of FePt is similar to that of AuCu alloys. The crystallography of the ordered and disordered states is also similar. Chemically prepared as-synthesised FePt alloy typically exists in the chemically disordered γ, A1, or fcc phase. The structure of this material is shown in **figure 1.5**.

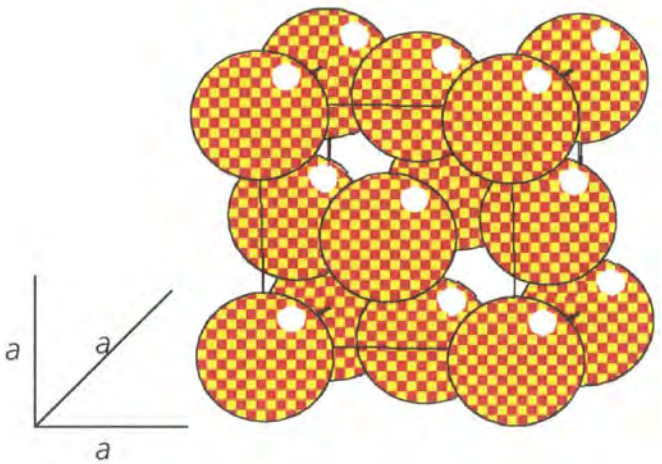

Figure 1.5 A diagram representing the disordered fcc phase of FePt alloy. The structure is cubic with the atoms arranged statistically on each atomic site. Each atom is represented as an 'average' iron/platinum atom.

Upon heating the as-synthesised material through the transition temperature (T_T), the unit cell changes from cubic to tetragonal with the atoms rearranging themselves into a thermodynamically more stable ordered configuration. The structure of the ordered, fct phase material is shown in **figure 1.6**.

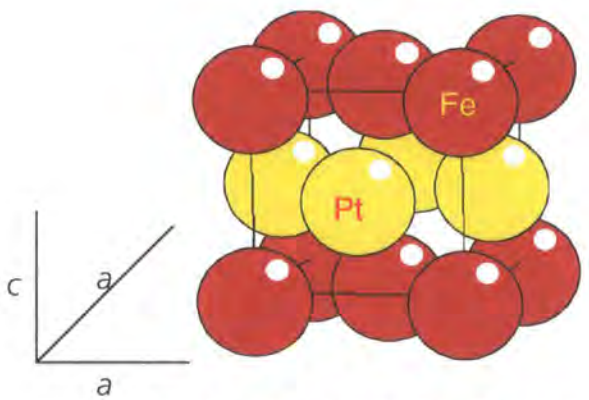

Figure 1.6 A diagram representing the ordered fct phase of FePt alloy. The structure is tetragonal with the atoms arranged in an ordered way such that iron atoms and platinum atoms occupy alternative planes.

The unit cell of fct, or $L1_0$, phase FePt bulk alloy has lattice parameter[123] a=3.838 Å and c=3.715 Å. This contraction in the c axis direction is due to the movement of the atoms into alternative iron/platinum planes. It has a tetragonal, or AuCu(I) type structure[120]. The space group of the

crystal system is P4/mmm. The material is stable in the fct phase at room temperature after cooling. **Figure 1.4** shows that if fct phase FePt is heated to very high temperatures it would convert to the disordered fcc phase, i.e. entropic gains overcome the enthalpic gains of ordering.

1.5.3.1 FePt Superlattice[120]

The X-ray diffraction pattern measured for the disordered fcc phase FePt will contain a number of peaks. The X-ray diffraction pattern for the ordered fct phase will also contain these same peaks, but at slightly different positions due to the change in the length of the c-axis. These are termed fundamental peaks. However, the diffraction pattern measured for the fct phase material will also exhibit peaks not corresponding to any in the fcc phase material's diffraction pattern. These are termed superlattice peaks.

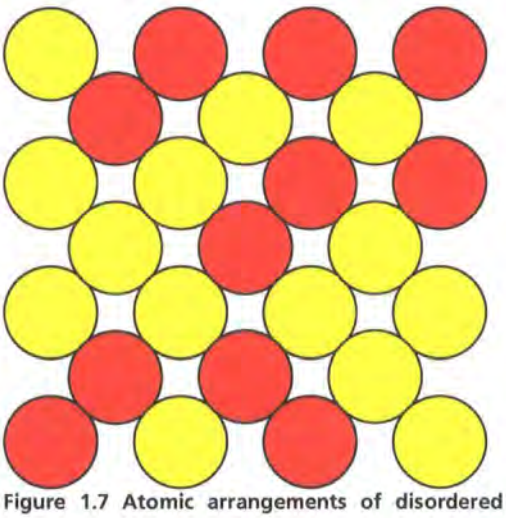

Figure 1.7 Atomic arrangements of disordered fcc phase FePt alloy on a [100] plane.

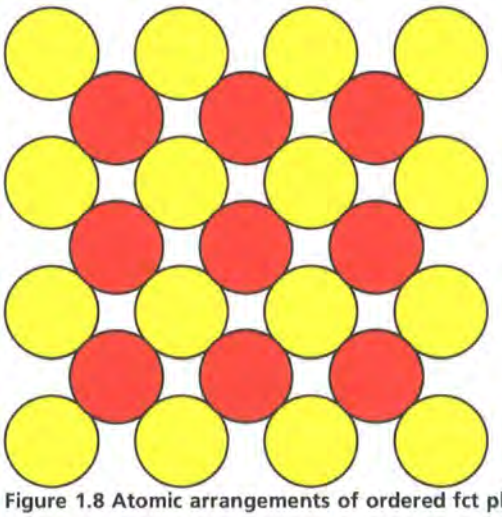

Figure 1.8 Atomic arrangements of ordered fct phase FePt alloy on a [100] plane.

For the disordered FePt, peaks are only present when the hkl indices are all odd or all even. In these cases the structure factor, F_{hkl}, is non-zero, thus indicating diffraction intensity. For ordered fct phase FePt, the structure factor is non-zero for both unmixed and mixed hkl indices. This means that superlattice peaks appear in the diffraction pattern of fct phase FePt and are direct evidence that ordering exists in that material.

1.5.4 Magnetic Properties of FePt Nanoparticles[10]

Changes in magnetisation of a material are governed, to some degree, by anisotropies present in the material. For nanoparticles, crystalline anisotropy is the most common anisotropy present. It is often uniaxial in nature.

Magnetocrystalline anisotropy, specific to a given material irrespective of its particle shape, arises due to spin-orbit coupling and tends to align along a specific crystal axis, termed the easy axis.

This is the thermodynamically favoured orientation. The larger the magnetocrystalline anisotropy, the larger the coercivity of the material. Materials which exhibit coercivity are ferromagnets. **Figure 1.9** describes coercivity and other relevant magnetic terms.

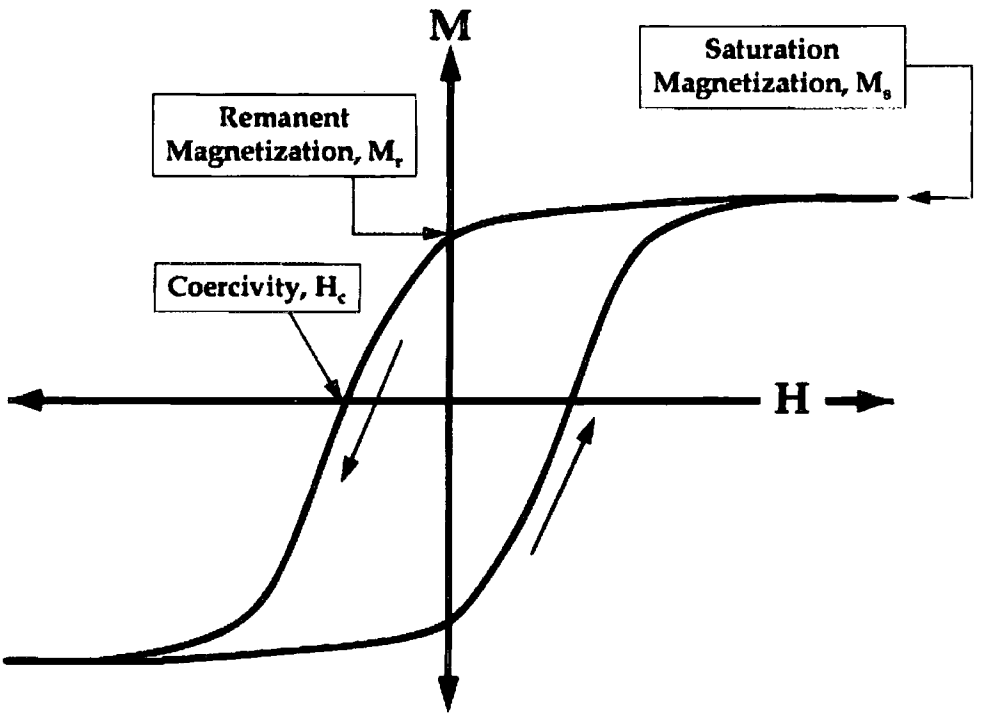

Figure 1.9 A schematic hysteresis loop describing certain magnetic definitions[10].

A hysteresis loop is the measurement of magnetisation (M) as a function of applied magnetic field (H). Typically the magnetisation will be measured from zero to high field, high field to low field and low field to high field, hence the term 'loop' used in the description of such an experiment. The coercivity (H_C) is the magnitude of applied field required to bring the sample magnetisation back to zero. To perform this the magnetisation must be in the opposite direction to the coercivity. The remnant magnetisation (M_r) is the magnetisation of a given sample in the absence of an applied magnetic field after exposure to one. The saturation magnetisation (M_S) is the maximum magnetisation of a given sample. If a material has a non-zero M_r, it is a ferromagnet as it can be permanently magnetised.

If the area of a hysteresis loop is large, the material is termed magnetically hard. Hard magnets are those used as permanent magnets in applications such as hard disc drives. Hard magnets will also have narrow domain walls, which lead to larger anisotropies[130]. FePt nanoparticles are hard ferromagnets.

A domain in a magnetic material is where a collection of spins are oriented in the same direction, therefore yielding a larger gross magnetic moment (than if they were all pointing in random directions). Each individual domain is separated by a domain wall. In large particles it is

energetically favourable to form domain walls. This is less favourable for smaller particles. This means that the larger the particle size, the more likely a multi-domain system will exists and the smaller, the more likely a single-domain system will exist[131, 132], i.e. there will be no domain walls and every spin pertaining to a given particle will be oriented in the same direction. In this situation the net magnetic moment will be larger than in a multi-domain material. This is described schematically in **figure 1.10**.

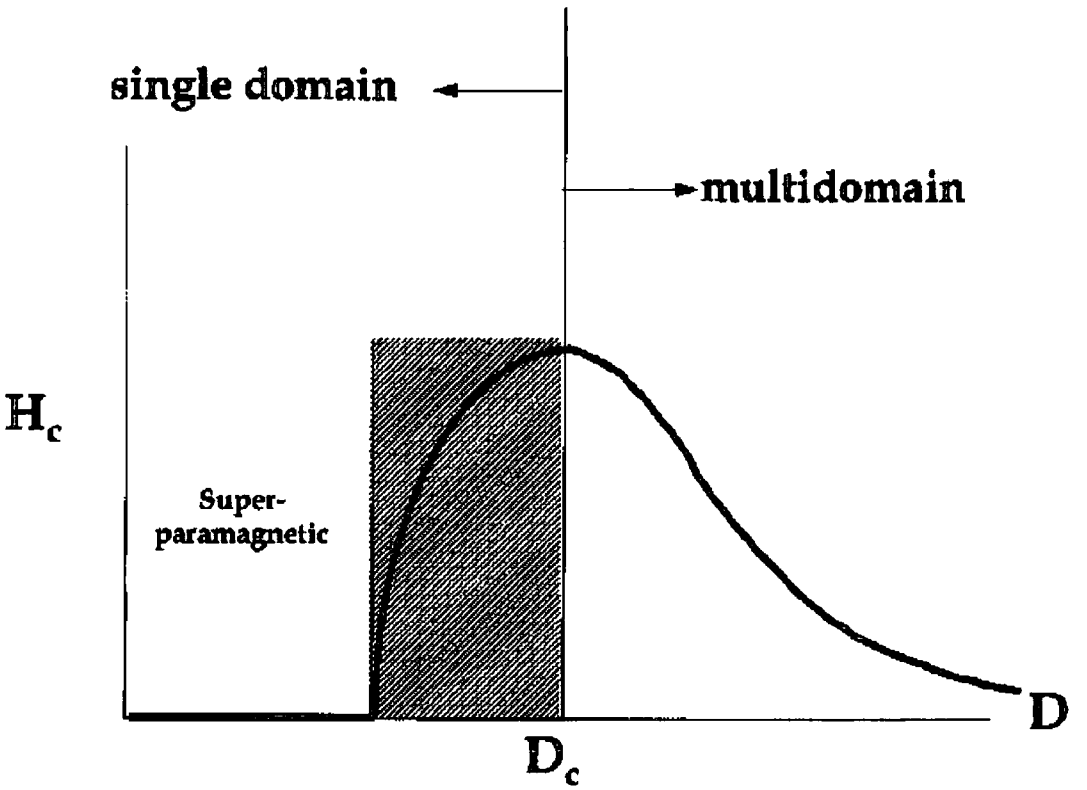

Figure 1.10 A schematic diagram describing the variation of coercivity as a function of particle diameter. At the critical particle diameter, DC, a given material becomes multi-domain or single-domain depending on the direction of size variation.

The movement of domain walls through a ferromagnet occurs when it is magnetised. Those domains closely aligned with the applied field grow and those not so well aligned shrink. Therefore in an applied field the magnetisation of a ferromagnet will increase due to domain wall-migration if it is a multi-domain material[130].

If the particles are small and the system is single domain changes in magnetisation cannot occur by way of domain wall migration. Therefore to retain large magnetisation and coercivities, the spins must interact coherently, i.e. all spins must be the same. Eventually, as the particle size continues to decrease, the material will become superparamagnetic[10].

The onset of superparamagnetism occurs when the product of the uniaxial magnetocrystalline anisotropy and particle volume is less than the ambient thermal energy. At this point the coercivity for a given ferromagnetic system approaches zero as the magnetisation is rendered

unstable due to thermal fluctuations[133]. The temperature at which the magnetisation of a single domain system begins to decrease is a direct result of the particle size decreasing and is termed the blocking temperature, T_B. It is the temperature at which the material becomes superparamagnetic rather than ferromagnetic. More formally it is defined as the point at which the relaxation time of the particle's magnetic moment is equal to the measurement time of the system being used[134]. The system exhibits paramagnetic properties in this state but each independent moment comprises multiple spins, rather than in a true paramagnetic material when each spin would equate to one independent moment[130].

Superparamagnetic behaviour can be confirmed by zero field cooled and field cooled experiments. In such experiments a sample's magnetisation is measured as a function of temperature. Firstly, it is cooled to a low temperature in the absence of an applied field, then on warming its magnetisation in the presence of an applied field is recorded (zero-field cooled measurement). The sample is then cooled again with the magnetic field still applied. The measurements are repeated (field-cooled). **Figure 1.11** provides an example of the ZFC and FC measurements recorded for monodispersed FePt nanoparticles.

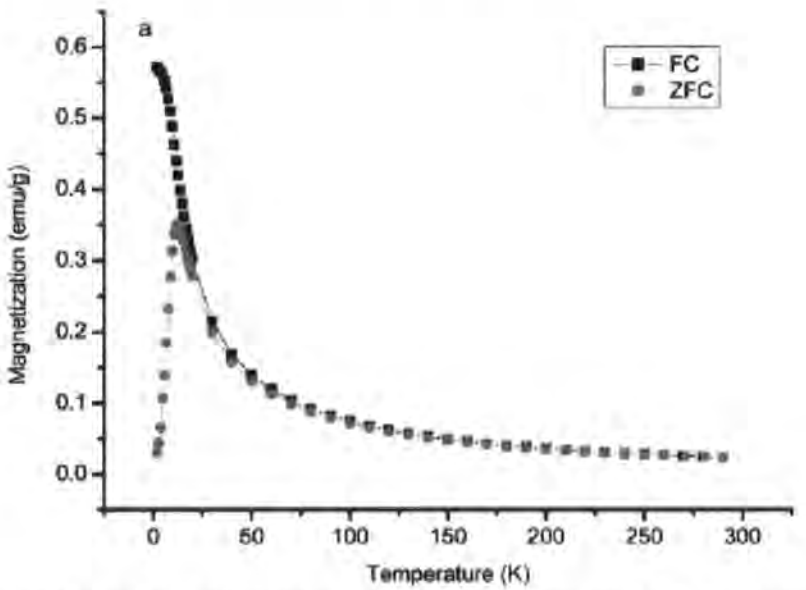

Figure 1.11 Zero-field cooled and field-cooled data obtained by measurement of FePt nanoparticles[85].

The zero-field cooled data show the existence of a blocking temperature, and the change from superparamagnetic to ferromagnetic behaviour in the FePt nanoparticles studied. This is ~ 20 K for the sample of **figure 1.11**.

1.5.5 Synthesis of FePt Nanoparticles

It was in 2000 that the first report on the synthesis of monodisperse FePt nanoparticles was published by Sun *et al.* [22]. It was stated that the size, composition and inter-particle spacing were

all tunable and controllable. The preparation method was based on the polyol process[135]. This is the term used to describe the reduction of metal salts to metal particles using a diol or polyalcohol to effect the reduction. To obtain the Fe metal required for the formation of FePt alloys, thermal decomposition of $Fe(CO)_5$ was employed. A typical execution of the experimental method described by Sun *et al.* is as follows. All reactions are conducted in airless conditions. $Pt(acac)_2$, 1,2-hexadecanediol were mixed into the chosen solvent, dioctylether. This is heated to 100 °C to allow reduction of the platinum salt. Oleic acid and oleylamine, functioning as surfactant molecules are then added to the reaction mixture at the same time as $Fe(CO)_5$ is injected into the system. The mixture is heated to reflux temperature (297 °C) and left for thirty minutes. After this allotted time, the mixture is left to cool, opened to ambient atmospheres and the resulting mixture worked-up to yield, a black powder. This black powder is determined to be FePt nanoparticles with an fcc type structure by X-ray diffraction analysis. The FePt nanoparticles can be redispersed in nonpolar solvents in a variety of concentrations. The particle size varies between 3 and 10 nm. This variation is achieved by synthesising 3 nm particles and then adding extra reagents to enlarge the particles used to seed such a reaction. The composition of the material is altered by using different molar ratios of iron pentacarbonyl to the platinum salt. $Fe_{48}Pt_{52}$ nanoparticles are obtained using a 3:2 molar ratio of iron pentacarbonyl to platinum salt; $Fe_{52}Pt_{48}$ nanoparticles are obtained using a 2:1 molar ratio of iron pentacarbonyl to platinum salt. As such it can be seen that stoichiometry control by this route is complex. Deposition of the FePt colloids onto a suitable substrate followed by evaporation of the solvent in which the particles were dispersed yields self-assembled nanocrystal arrays of FePt nanoparticles. **Figure 1.12** shows a TEM image of such an assembly.

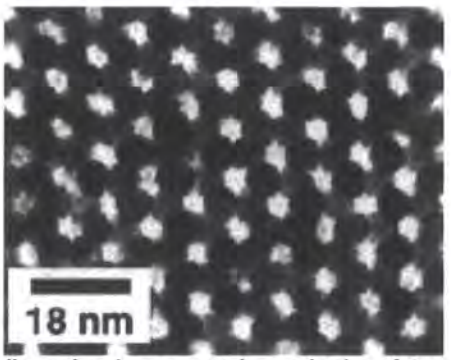

Figure 1.12 A TEM image of a 3-dimensional nanocrystal superlattice of 6 nm as-synthesised (fcc phase) FePt particles deposited onto an SiO coated copper grid from a dispersion of particles in a hexane/octane carrier solvent[22].

Magnetic studies of the as-synthesised particles showed that they were superparamagnetic (H_C = 0) at room temperature whilst on heat treatment (annealing) at 500 °C they had been converted to a ferromagnetic state. This was consistent with the findings via XRD that the material was in the ordered fct or $L1_0$ phase. This conversion can be seen by the growth of superlattice peaks in the X-ray diffraction patterns as a function of temperature in **figure 1.13**.

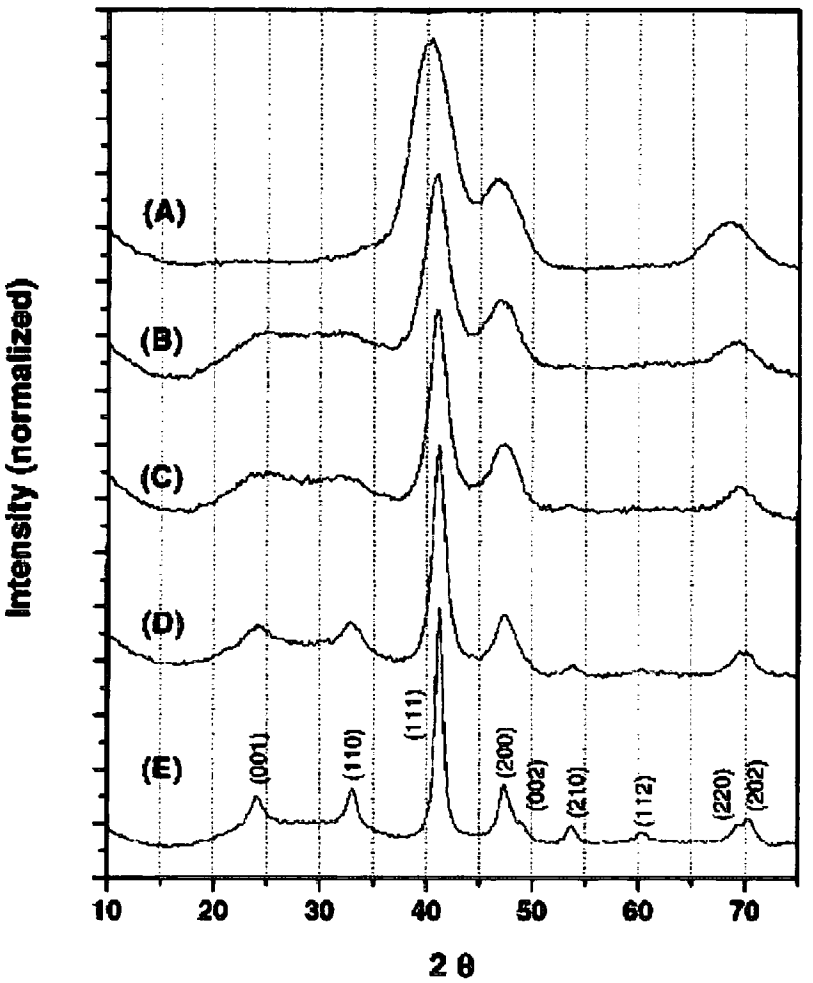

Figure 1.13 XRD patterns of FePt nanoparticle assemblies at different stages of heat treatment. (A) is as-synthesised 4 nm Fe52Pt48 nanoparticles. (B) are the same particles after heating to 450 °C under nitrogen for 30 minutes, (C) at 500 °C, (D) at 550 °C and (E) at 600 °C.

Peaks consistent with a face-centred cubic structure are seen at ~ 40, 47 and 67 °2θ. Superlattice peaks grow at ~ 24 and 33 °2θ. The coercivity of the material when in the ferromagnetic fct phase is reported as being tunable by control of the annealing time, annealing temperature, iron:platinum ratio and particle size.

Since this work was reported a large number of researchers around the world have used this synthetic method, or variations on it, to prepare FePt and other similar materials. The main aim of such work has been to prepare monodisperse fct phase FePt nanoparticles. In this particular case, after annealing the as-synthesised particles to obtain fct phase material, agglomeration of the particles can occur. This is also referred to as sintering[136]. This is where grain growth and coalescence occur, leading to particles with a large size distribution and differing shapes, i.e. not monodisperse, which results in a material not optimised for ultra-high density magnetic storage. **Figures 1.14** and **1.15** show a TEM image of a self-organised metallic array after high temperature annealing to the $L1_0$ phase and the loss of assembly inherent in annealed FePt nanoparticles respectively.

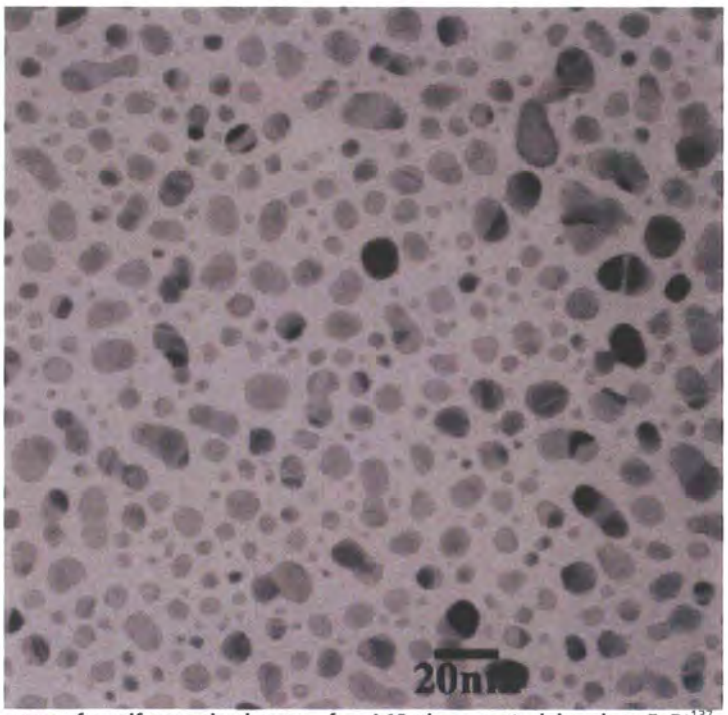

Figure 1.14 A TEM image of a self-organised array of an L10 phase material such as FePt[137].

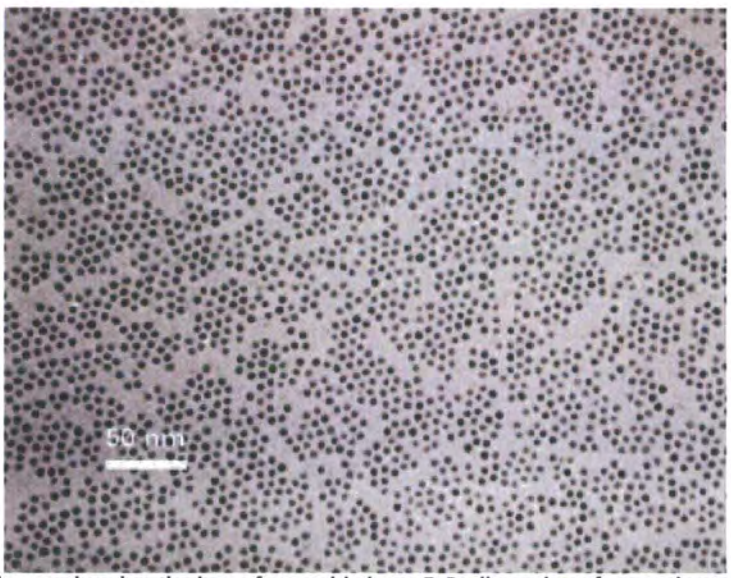

Figure 1.15 A TEM image showing the loss of assembly in an FePt dispersion after moderate annealing[137].

Sintering occurs in nanoparticles as a direct result of the large surface area. A surface can be described as a crystalline defect and if there is a great enough number of these then sintering is an energetically favourable reaction (reducing the number of surfaces or surface area will result in a lower energy state for the particles) [137].

Without fully understanding the annealing processes in FePt nanoparticles, and therefore being able to control them, the simplest way to obtain ordered FePt nanoparticle arrays is to synthesise material that will undergo the order-disorder transition at lower temperatures.

The transition temperature, or T_T, had previously been lowered to around 400 °C by the introduction of a third metal into sputtered thin-films of FePt. Examples of this are Cu[138-142], Ag[143-145], Zr[146], Au[138], B[147], Ir[147] and Al[148]. This approach was used to try and lower T_T of FePt nanoparticles. Specifically Au[149], Ag[144, 149, 150], Pd[149], Co[151], Cr[149], and Cu[149] have all been added to FePt nanoparticles with the result that the annealing temperature has been lowered. Despite this, however, the problems of sintering have been retained.

Variations of the synthetic method presented by Sun *et al.* have also been used to synthesise FePt nanoparticles with a low T_T. Jeyadevan *et al.*[140]. were able to produce FePt nanoparticles of size 3-4 nm with a T_T as between 593 and 893 K, dependent on the exact reaction conditions. This was achieved by the reduction of platinum and iron acetylacetonates in tetraethylene glycol at 300 °C. Since this was reported, other groups have performed similar syntheses using iron and platinum acetylacetonates with varying results regarding the T_T. Elkins *et al.*[152]. were able to produce monodisperse FePt particles 2 nm in size but with a T_T around 500 °C. Liu *et al.*[153]. also obtained monodisperse FePt in the fcc phase that converted to the fct phase only on annealing to 650 °C.

Kang *et al.*[154]. were able to synthesise directly partially ordered $Fe_{53}Pt_{47}$ nanoparticles by the simultaneous decomposition of iron pentacarbonyl and platinum acetylacetonate. The high boiling point chemical, hexadecylartine, was used as a solvent, and l-adamantanecarboxylic acid was used as a stabiliser. Unfortunately these particles, around 8 nm in size, display only small room temperature coercivity consistent with the belief via XRD that the particles are only partially ordered (the superlattice peaks are weak).

This thesis will report our work aimed at providing a new route to FePt nanoparticles in which stoichiometry, crystal structure and particle size can all be controlled.

1.6 References

1. J. Jortner and C. N. R. Rao, *Pure and Applied Chemistry*, 2002, **74**, 1491-1506.
2. C. N. R. Rao and A. K. Cheetham, *Journal of Materials Chemistry*, 2001, **11**, 2887-2894.
3. R. P. Feynman, *Miniaturization*, Reinhold, New York, 1961.
4. J. M. Lehn, *Supramolecular Chemistry*, VCH, Weinheim, 1995.
5. M. L. Plumer, J. v Ek and D. Weller, *The Physics of Ultra-High-Density Magnetic Recording*, Springer, Berlin, 2001.
6. O. Koper, I. Lagadic and K. J. Klabunde, *Chemistry of Materials*, 1997, **9**, 838-848.
7. C. Zandonella, *Nature*, 2001, **410**, 734-735.
8. J. T. Santini, M. J. Cima and R. Langer, *Nature*, 1999, **397**, 335-338.

9. C. N. R. Rao, B. C. Satishkumar, A. Govindaraj and M. Nath, *Chemphyschem*, 2001, **2**, 78-105.
10. D. L. LesliePelecky and R. D. Rieke, *Chemistry of Materials*, 1996, **8**, 1770-1783.
11. C. B. Murray, C. R. Kagan and M. G. Bawendi, *Annual Review of Materials Science*, 2000, **30**, 545-610.
12. C. N. R. Rao, G. U. Kulkarni, P. J. Thomas and P. P. Edwards, *Chemistry-a European Journal*, 2002, **8**, 29-35.
13. J. Eastman and R. W. Siegel, *Research & Development*, 1989, **31**, 56-60.
14. R. W. Siegel, *Nanostructured Materials*, 1993, **3**, 1-18.
15. V. G. Gryaznov and L. I. Trusov, *Progress in Materials Science*, 1993, **37**, 289-401.
16. H. Gleiter, *Progress in Materials Science*, 1989, **33**, 223-315.
17. A. P. Alivisatos, *Science*, 1996, **271**, 933-937.
18. J. Shi, S. Gider, K. Babcock and D. D. Awschalom, *Science*, 1996, **271**, 937-941.
19. R. Kubo, A. Kawabata and S. Kobayashi, *Annual Review of Materials Science*, 1984, **14**, 49-66.
20. E. L. Nagaev, *Physics Reports-Review Section of Physics Letters*, 1992, **222**, 199-307.
21. J. Perenboom, P. Wyder and F. Meier, *Physics Reports-Review Section of Physics Letters*, 1981, **78**, 173-292.
22. S. H. Sun, C. B. Murray, D. Weller, L. Folks and A. Moser, *Science*, 2000, **287**, 1989-1992.
23. R. D. Shull, *Ieee Transactions on Magnetics*, 1993, **29**, 2614-2615.
24. R. F. Ziolo, E. P. Giannelis, B. A. Weinstein, M. P. Ohoro, B. N. Ganguly, V. Mehrotra, M. W. Russell and D. R. Huffman, *Science*, 1992, **257**, 219-223.
25. I. Anton, I. Desabata and L. Vekas, *Journal of Magnetism and Magnetic Materials*, 1990, **85**, 219-226.
26. S. Odenbach, *Advances in Colloid and Interface Science*, 1993, **46**, 263-282.
27. K. Raj, B. Moskowitz and R. Casciari, *Journal of Magnetism and Magnetic Materials*, 1995, **149**, 174-180.
28. C. N. R. Rao, V. Vijayakrishnan, A. K. Santra and M. W. J. Prins, *Angewandte Chemie-International Edition in English*, 1992, **31**, 1062-1064.
29. A. K. Santra, S. Ghosh and C. N. R. Rao, *Langmuir*, 1994, **10**, 3937-3939.
30. E. Gillet, S. Channakhone and V. Matolin, *Journal of Catalysis*, 1986, **97**, 437-447.
31. D. L. Doering, J. T. Dickinson and H. Poppa, *Journal of Catalysis*, 1982, **73**, 91-103.
32. W. H. Qi, M. P. Wang and Y. C. Su, *Journal of Materials Science Letters*, 2002, **21**, 877-878.
33. G. M. Whitesides and M. Boncheva, *Proceedings of the National Academy of Sciences of the United States of America*, 2002, **99**, 4769-4774.
34. J. V. Sanders, *Acta Crystallographica Section a-Crystal Physics Diffraction Theoretical and General Crystallography*, 1968, **A 24**, 427-&.

35. V. Grantcharova, E. J. Alm, D. Baker and A. L. Horwich, *Current Opinion in Structural Biology*, 2001, **11**, 70-82.
36. A. Kumar, N. L. Abbott, E. Kim, H. A. Biebuyck and G. M. Whitesides, *Accounts of Chemical Research*, 1995, **28**, 219-226.
37. E. L. Thomas, *Science*, 1999, **286**, 1307-1307.
38. V. Russier, C. Petit, J. Legrand and M. P. Pileni, *Physical Review B*, 2000, **62**, 3910-3916.
39. C. Petit and M. P. Pileni, *Applied Surface Science*, 2000, **162**, 519-528.
40. B. L. Cushing, V. L. Kolesnichenko and C. J. O'Connor, *Chemical Reviews*, 2004, **104**, 3893-3946.
41. Y. De Smet, L. Deriemaeker and R. Finsy, *Langmuir*, 1997, **13**, 6884-6888.
42. H. Gratz, *Scripta Materialia*, 1997, **37**, 9-16.
43. L. E. M. Howard, H. L. Nguyen, S. R. Giblin, B. K. Tanner, I. Terry, A. K. Hughes and J. S. O. Evans, *Journal of the American Chemical Society*, 2005, **127**, 10140-10141.
44. K. Kakizaki, Y. Yamada, Y. Kuboki, H. Suda, K. Shibata and N. Hiratsuka, *Journal of Magnetism and Magnetic Materials*, 2004, **272-76**, 2200-2201.
45. P. T. L. Minh, N. P. Thuy and N. T. N. Chan, *Journal of Magnetism and Magnetic Materials*, 2004, **277**, 187-191.
46. D. L. Peng, T. Hihara and K. Sumiyama, *Journal of Magnetism and Magnetic Materials*, 2004, **277**, 201-208.
47. K. S. Suslick, M. M. Fang and T. Hyeon, *Journal of the American Chemical Society*, 1996, **118**, 11960-11961.
48. K. S. Suslick, *Science*, 1990, **247**, 1439-1445.
49. E. B. Flint and K. S. Suslick, *Science*, 1991, **253**, 1397-1399.
50. M. W. Grinstaff, M. B. Salamon and K. S. Suslick, *Physical Review B*, 1993, **48**, 269-273.
51. K. S. Suslick, T. Hyeon, M. M. Fang and A. A. Cichowlas, *Materials Science and Engineering a-Structural Materials Properties Microstructure and Processing*, 1995, **204**, 186-192.
52. K. S. Suslick, T. W. Hyeon and M. M. Fang, *Chemistry of Materials*, 1996, **8**, 2172-2179.
53. K. S. Suslick, T. Hyeon, M. Fang, J. T. Ries and A. A. Cichowlas, *Metastable, Mechanically Alloyed and Nanocrystalline Materials, Pts 1 and 2*, 1996, **225**, 903-911.
54. K. S. Suslick, M. Fang, R. Hyeon and A. A. Cichowlas, *A. A. Mater. Res. Soc. Symp. Proc.*, 1994, **351**, 443.
55. K. S. Suslick, *Mrs Bulletin*, 1995, **20**, 29-34.
56. C. C. Koch, *Annual Review of Materials Science*, 1989, **19**, 121-143.
57. J. S. C. Jang and C. C. Koch, *Scripta Metallurgica Et Materialia*, 1990, **24**, 1599-1604.
58. T. D. Shen, C. C. Koch, T. Y. Tsui and G. M. Pharr, *Journal of Materials Research*, 1995, **10**, 2892-2896.
59. T. D. Shen and C. C. Koch, *Nanostructured Materials*, 1995, **5**, 615-629.

60. T. D. Shen, C. C. Koch, T. L. McCormick, R. J. Nemanich, J. Y. Huang and J. G. Huang, *Journal of Materials Research*, 1995, **10**, 139-148.
61. P. Boolchand and C. C. Koch, *Journal of Materials Research*, 1992, **7**, 2876-2883.
62. S. H. Sun, E. E. Fullerton, D. Weller and C. B. Murray, *Ieee Transactions on Magnetics*, 2001, **37**, 1239-1243.
63. T. Hyeon, *Chemical Communications*, 2003, 927-934.
64. R. D. Rieke, *Accounts of Chemical Research*, 1977, **10**, 301-306.
65. T. P. Burns and R. D. Rieke, *Journal of Organic Chemistry*, 1987, **52**, 3674-3680.
66. S. Stoeva, K. J. Klabunde, C. M. Sorensen and I. Dragieva, *Journal of the American Chemical Society*, 2002, **124**, 2305-2311.
67. T. S. Ahmadi, Z. L. Wang, T. C. Green, A. Henglein and M. A. ElSayed, *Science*, 1996, **272**, 1924-1926.
68. C. J. Murphy and N. R. Jana, *Advanced Materials*, 2002, **14**, 80-82.
69. M. Brust, M. Walker, D. Bethell, D. J. Schiffrin and R. Whyman, *Journal of the Chemical Society-Chemical Communications*, 1994, 801-802.
70. G. N. Glavee, K. J. Klabunde, C. M. Sorensen and G. C. Hadjipanayis, *Inorganic Chemistry*, 1995, **34**, 28-35.
71. G. N. Glavee, K. J. Klabunde, C. M. Sorensen and G. C. Hadjipanayis, *Inorganic Chemistry*, 1993, **32**, 474-477.
72. Y. Wang, H. L. Wu, Q. H. Zhang and Q. H. Tang, *Microporous and Mesoporous Materials*, 2005, **86**, 38-49.
73. N. C. Tansil, R. V. Ramanujan and H. F. Li, *Transactions of the Indian Institute of Metals*, 2003, **56**, 509-512.
74. A. M. L. Jackelen, M. Jungbauer and G. N. Glavee, *Langmuir*, 1999, **15**, 2322-2326.
75. Y. P. Sun, H. W. Rollins and R. Guduru, *Chemistry of Materials*, 1999, **11**, 7-+.
76. A. Corrias, G. Ennas, A. Musinu, G. Marongiu and G. Paschina, *Chemistry of Materials*, 1993, **5**, 1722-1726.
77. M. Chen, J. P. Liu and S. H. Sun, *Journal of the American Chemical Society*, 2004, **126**, 8394-8395.
78. K. Torigoe and K. Esumi, *Langmuir*, 1993, **9**, 1664-1667.
79. H. H. Huang, X. P. Ni, G. L. Loy, C. H. Chew, K. L. Tan, F. C. Loh, J. F. Deng and G. Q. Xu, *Langmuir*, 1996, **12**, 909-912.
80. K. Zou, X. H. Zhang, X. F. Duan, X. M. Meng and S. K. Wu, *Journal of Crystal Growth*, 2004, **273**, 285-291.
81. K. Zou, X. H. Zhang, S. K. Wu and X. F. Duan, *Acta Chimica Sinica*, 2004, **62**, 1771-1774.
82. A. Chatterjee, A. Priyam, S. K. Das and A. Saha, *Journal of Colloid and Interface Science*, 2006, **294**, 334-342.

83. R. Minami, Y. Kitamoto, T. Chikata and S. Kato, *Electrochimica Acta*, 2005, **51**, 864-866.

84. R. Harpeness and A. Gedanken, *Journal of Materials Chemistry*, 2005, **15**, 698-702.

85. H. L. Nguyen, L. E. M. Howard, S. R. Giblin, B. K. Tanner, I. Terry, A. K. Hughes, I. M. Ross, A. Serres, H. Burckstummer and J. S. O. Evans, *Journal of Materials Chemistry*, 2005, **15**, 5136-5143.

86. J. A. Gerbec, D. Magana, A. Washington and G. F. Strouse, *Journal of the American Chemical Society*, 2005, **127**, 15791-15800.

87. X. P. Sun and Y. L. Luo, *Materials Letters*, 2005, **59**, 4048-4050.

88. W. X. Tu and H. F. Liu, *Journal of Materials Chemistry*, 2000, **10**, 2207-2211.

89. K. Patel, S. Kapoor, D. P. Dave and T. Mukherjee, *Journal of Chemical Sciences*, 2005, **117**, 311-316.

90. F. K. Liu, P. W. Huang, Y. C. Chang, F. H. Ko and T. C. Chu, *Journal of Materials Research*, 2004, **19**, 469-473.

91. M. T. Reetz and W. Helbig, *Journal of the American Chemical Society*, 1994, **116**, 7401-7402.

92. L. M. Shen, J. L. Yao and R. A. Gu, *Spectroscopy and Spectral Analysis*, 2005, **25**, 1998-2001.

93. S. X. Huang, H. Y. Ma, X. K. Zhang, F. F. Yong, X. L. Feng, W. Pan, X. N. Wang, Y. Wang and S. H. Chen, *Journal of Physical Chemistry B*, 2005, **109**, 19823-19830.

94. M. L. Rodriguez-Sanchez, M. J. Rodriguez, M. C. Blanco, J. Rivas and M. A. Lopez-Quintela, *Journal of Physical Chemistry B*, 2005, **109**, 1183-1191.

95. H. Y. Ma, B. S. Yin, S. Y. Wang, Y. L. Jiao, W. Pan, S. X. Huang, S. H. Chen and F. J. Meng, *Chemphyschem*, 2004, **5**, 68-75.

96. X. G. Yang, S. H. Chen, S. Y. Zhao, D. G. Li and H. Y. Ma, *Journal of the Serbian Chemical Society*, 2003, **68**, 843-847.

97. P. Zhang and T. K. Sham, *Applied Physics Letters*, 2003, **82**, 1778-1780.

98. H. Liu, T. Hihara, K. Sumiyama and K. Suzuki, *Physica Status Solidi a-Applied Research*, 1998, **169**, 153-160.

99. S. R. Hoon, M. Kilner, G. J. Russell and B. K. Tanner, *Journal of Magnetism and Magnetic Materials*, 1983, **39**, 107-110.

100. M. Kilner, S. R. Hoon, D. B. Lambrick, J. A. Potton and B. K. Tanner, *Ieee Transactions on Magnetics*, 1984, **20**, 1735-1737.

101. M. Kilner, N. Mason, D. B. Lambrick, P. D. Hooker and P. L. Timms, *Journal of the Chemical Society-Chemical Communications*, 1987, 356-357.

102. S. H. Sun and C. B. Murray, *Journal of Applied Physics*, 1999, **85**, 4325-4330.

103. J. S. Yin and Z. L. Wang, *Nanostructured Materials*, 1999, **11**, 845-852.

104. D. P. Dinega and M. G. Bawendi, *Angewandte Chemie-International Edition*, 1999, **38**, 1788-1791.

105. V. F. Puntes, K. M. Krishnan and P. Alivisatos, *Applied Physics Letters*, 2001, **78**, 2187-2189.
106. V. F. Puntes, K. M. Krishnan and A. P. Alivisatos, *Science*, 2001, **291**, 2115-2117.
107. J. P. Chen, C. M. Sorensen, K. J. Klabunde and G. C. Hadjipanayis, *Journal of Applied Physics*, 1994, **76**, 6316-6318.
108. M. P. Pileni, *Langmuir*, 1997, **13**, 3266-3276.
109. C. B. Murray, S. H. Sun, H. Doyle and T. Betley, *Mrs Bulletin*, 2001, **26**, 985-991.
110. C. B. Murray, S. H. Sun, W. Gaschler, H. Doyle, T. A. Betley and C. R. Kagan, *Ibm Journal of Research and Development*, 2001, **45**, 47-56.
111. T. Hyeon, S. S. Lee, J. Park, Y. Chung and H. Bin Na, *Journal of the American Chemical Society*, 2001, **123**, 12798-12801.
112. B. D. Terris and T. Thomson, *Journal of Physics D-Applied Physics*, 2005, **38**, R199-R222.
113. A. Moser, K. Takano, D. T. Margulies, M. Albrecht, Y. Sonobe, Y. Ikeda, S. H. Sun and E. E. Fullerton, *Journal of Physics D-Applied Physics*, 2002, **35**, R157-R167.
114. D. Weller and A. Moser, *Ieee Transactions on Magnetics*, 1999, **35**, 4423-4439.
115. S. H. Charap, P. L. Lu and Y. J. He, *Ieee Transactions on Magnetics*, 1997, **33**, 978-983.
116. K. Inomata, T. Sawa and S. Hashimoto, *Journal of Applied Physics*, 1988, **64**, 2537-2540.
117. D. L. Peng, T. Hihara and K. Sumiyama, *Applied Physics Letters*, 2003, **83**, 350-352.
118. E. Isaac and G. Tammann, *Z. anorg. Chem.*, 1907, **55**, 63-71.
119. A. Kussman and G. v. Rittberg, *Z. Metallkunde*, 1950, **42**, 470-477.
120. B. D. Cullity, *Elements of X-ray diffraction*, 2nd edn., Addison-Wesley Publishing Company, Inc., 1978.
121. U. Dehlinger and L. Graf, *Z. Physik*, 1930, **64**, 359.
122. L. Graf and A. Kussman, *Z. Physik*, 1935, **36**, 544-551.
123. H. Lipson, D. Schoenburg and G. V. Stupart, *J. Inst. Metals*, 1941, **67**, 333-340.
124. A. Kussman, M. Auwarter and G. v. Rittberg, *Ann. Physik*, 1948, **4**, 147-182.
125. V. A. Nemilov, *Z. anorg. Chem.*, 1932, **204**, 49-59.
126. M. Hansen, *Constitution of Binary Alloys*, McGraw Hill Book Co., Inc., New York, 1958.
127. R. M. Bozorth, *Ferromagnetism*, New York: D. Van Nostrand Company Inc., 1951.
128. K. Watanabe and H. Masumoto, *Transactions of the Japan Institute of Metals*, 1983, **24**, 627-632.
129. B. Stahl, J. Ellrich, R. Theissmann, M. Ghafari, S. Bhattacharya, H. Hahn, N. S. Gajbhiye, D. Kramer, R. N. Viswanath, J. Weissmuller and H. Gleiter, *Physical Review B*, 2003, **67**.
130. S. Blundell, *Magnetism in condensed matter*, Oxford University Press, Oxford, 2001.
131. E. C. Stoner and E. P. Wohlfarth, *Philosophical Transactions of the Royal Society of London Series a-Mathematical and Physical Sciences*, 1948, **240**, 599-642.

132. L. Neel, *Comptes Rendus Hebdomadaires Des Seances De L Academie Des Sciences*, 1947, **224**, 1488-1490.

133. L. Neel, *Comptes Rendus Hebdomadaires Des Seances De L Academie Des Sciences*, 1949, **228**, 664-666.

134. Q. A. Pankhurst, J. Connolly, S. K. Jones and J. Dobson, *Journal of Physics D-Applied Physics*, 2003, **36**, R167-R181.

135. F. Fievet, J. P. Lagier, B. Blin, B. Beaudoin and M. Figlarz, *Solid State Ionics*, 1989, **32-3**, 198-205.

136. Z. R. Dai, S. H. Sun and Z. L. Wang, *Nano Letters*, 2001, **1**, 443-447.

137. T. J. Klemmer, C. Liu, N. Shukla, X. W. Wu, D. Weller, M. Tanase, D. E. Laughlin and W. A. Soffa, *Journal of Magnetism and Magnetic Materials*, 2003, **266**, 79-87.

138. C. L. Platt, K. W. Wierman, E. B. Svedberg, R. van de Veerdonk, J. K. Howard, A. G. Roy and D. E. Laughlin, *Journal of Applied Physics*, 2002, **92**, 6104-6109.

139. Y. K. Takahashi, M. Ohnuma and K. Hono, *Journal of Magnetism and Magnetic Materials*, 2002, **246**, 259-265.

140. B. Jeyadevan, A. Hobo, K. Urakawa, C. N. Chinnasamy, K. Shinoda and K. Tohji, *Journal of Applied Physics*, 2003, **93**, 7574-7576.

141. K. W. Wierman, C. L. Platt and J. K. Howard, *Journal of Magnetism and Magnetic Materials*, 2004, **278**, 214-217.

142. T. Maeda, A. Kikitsu, T. Kai, T. Nagase, H. Aikawa and J. Akiyama, *Ieee Transactions on Magnetics*, 2002, **38**, 2796-2798.

143. Z. L. Zhao, J. S. Chen, J. Ding, K. Inaba and J. P. Wang, *Journal of Magnetism and Magnetic Materials*, 2004, **282**, 105-108.

144. S. Wang, S. S. Kang, D. E. Nikles, J. W. Harrell and X. W. Wu, *Journal of Magnetism and Magnetic Materials*, 2003, **266**, 49-56.

145. K. Aimuta, K. Nishimura, H. Uchida and M. Inoue, *Physica Status Solidi B-Basic Research*, 2004, **241**, 1727-1730.

146. S. R. Lee, S. Yang, Y. K. Kim and J. G. Na, *Applied Physics Letters*, 2001, **78**, 4001-4003.

147. K. Nishimura, K. Takahashi, H. Uchida and M. Inoue, *Journal of Magnetism and Magnetic Materials*, 2004, **272-76**, 2189-2190.

148. S. K. Chen, F. T. Yuan, S. N. Hsiao, H. C. Chang, C. Y. Liou and W. C. Chang, *Journal of Magnetism and Magnetic Materials*, 2004, **282**, 198-201.

149. J. W. Harrell, D. E. Nikles, S. S. Kang, X. C. Sun, Z. Jia, S. Shi, J. Lawson, G. B. Thompson, C. Srivastava and N. V. Seetala, *Scripta Materialia*, 2005, **53**, 411-416.

150. K. Sato, M. Fujiyoshi, M. Ishimaru and Y. Hirotsu, *Scripta Materialia*, 2003, **48**, 921-927.

151. D. E. Nikles, M. Chen, J. W. Harrell, S. S. Kang, X. C. Sun and S. T. Wang, *Abstracts of Papers of the American Chemical Society*, 2002, **224**, U447-U447.

152. K. E. Elkins, T. S. Vedantam, J. P. Liu, H. Zeng, S. H. Sun, Y. Ding and Z. L. Wang, *Nano Letters*, 2003, **3**, 1647-1649.

153. C. Liu, X. W. Wu, T. Klemmer, N. Shukla, X. M. Yang, D. Weller, A. G. Roy, M. Tanase and D. Laughlin, *Journal of Physical Chemistry B*, 2004, **108**, 6121-6123.

154. S. S. Kang, Z. Y. Jia, S. F. Shi, D. E. Nikles and J. W. Harrell, *Applied Physics Letters*, 2005, **86**.

Chapter 2 – Experimental Details

2.1 Introduction

This chapter describes all experimental details relevant to the work presented in this thesis. The sections describe powder X-ray diffraction studies, SQUID magnetometry, transmission electron microscopy, X-ray absorption fine structure and Rutherford backscattering.

2.2 Powder X-ray Diffraction[2-4]

2.2.1 Powder X-Ray Diffraction Studies

X-ray diffraction is an extremely important method used in the characterisation of the structures of crystalline materials as it allows, in the first instance, the identification of phases present, the determination of a given material's unit cell dimensions as well as providing information allowing determination of the absolute fractional coordinates of the constituent atoms in a material. By performing further studies as a function of time, temperature, pressure or dynamic chemical environment it is possible to obtain information which will aid the understanding of the behaviour of a material. This information can be the crystallite size and strain; the sample texture; the thermal motion of constituent atoms and also kinetic information providing a basis for the determination of mechanistic pathways or activation energies.

Typically in a laboratory X-ray source, a beam of electrons is emitted from a heated tungsten filament in a vacuum tube, accelerated through 40 kV and then impacted on copper target with sufficient energy so as to cause the ejection of an electron from a copper 1s orbital. An electron in the copper 2p orbital drops to the lower 1s energy level, thus yielding a photon with a wavelength corresponding to 1.5406 Å (Cu $K\alpha_1$) or 1.5443 Å (Cu $K\alpha_2$) (dependent on the spin state of the 2p orbital). The wavelength is ideal for X-ray diffraction as for interference to occur the size of the wavelength must be comparable to the size of the periodic structure which it is hoped will diffract. In a typical X-ray tube, the X-rays pass through a Be window on their exit. During the production of X-rays of the desired wavelength, white radiation, known as 'bremmstrahlung', and $K\beta$, are also produced. Normally a monochromator is positioned so as to select only the $K\alpha$ radiation, or a Ni filter is used to remove $K\beta$ lines.

If a material is exposed to an incident beam of X-rays, the X-rays interact with the atoms present which act as secondary point sources and re-radiate the X-rays in all directions. If the atoms exist in a periodic array, the constructive and destructive interference phenomenon of diffraction occurs. This can be most simply described in terms of Bragg's law.

It was shown by W. L. Bragg that every diffracted beam of X-rays can be regarded as a reflection from sets of parallel planes of lattice points. The angles of incidence and reflection must be equal and co-planar with each other, whilst also being normal to the reflecting plane. To define a plane, three integers are required to detail its orientation with respect to the edges of a given unit cell. These are known as the *hkl* or Miller indices. The spacing between successive planes within a material is determined by the lattice geometry and thus d_{hkl} is a function of the unit cell parameters.

The path difference, 2l, between two reflected beams is equal to $2d\sin\theta$ (**figure 2.1**). If constructive interference is to occur this path difference must be equal to an integer number of wavelengths, nλ. This leads to the Bragg equation (**equation 2.1**)

$$2d\sin\theta = n\lambda \quad \textbf{(2.1)}$$

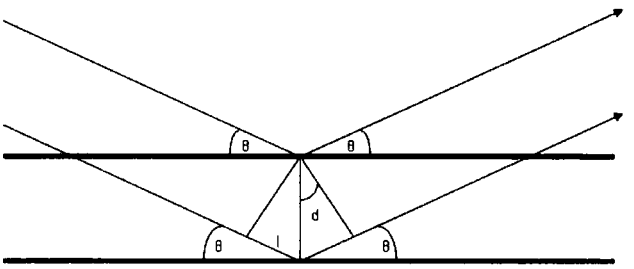

Figure 2.1 A diagram showing the path difference for two beams at angle □ reflected by different planes.

Typically, n=1 for all reflections when employing Bragg's law, with the d spacing between planes decreased (i.e. if n=2, when using Bragg's law n=1 and the d spacing is halved).

In a powder diffraction experiment, a large (and ideally infinite) number of crystallites are placed in the path of an incident X-ray beam. Each crystallite in the powder sample gives rise to a discrete diffracted beam of X-rays. However, as there are an infinite number of randomly oriented crystallites, each individual diffracted beam becomes a cone (**figure 2.2**) of diffraction, and the individual hkl spots 'smear out' into rings of intensity. For a crystalline sample each set of lattice planes in a given material will be in every possible orientation, meaning at least one of each set of planes will be at the Bragg angle to the incident beam, thus leading to diffraction for those planes. When recording a powder diffraction pattern, we are therefore left with a one dimensional diffraction pattern expressed (typically graphically) as the diffracted intensity versus the diffraction angle, 2-theta.

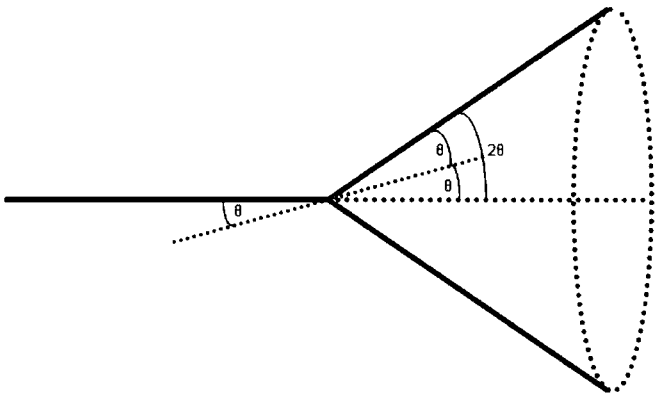

Figure 2.2 A diagram describing the formation of cones of diffraction when performing powder diffraction. X-rays travel from the source to the sample, at which point they are diffracted.

2.2.2 Rietveld Refinement[5, 6]

In order to quantify the changes in structure and microstructure of the material with temperature, Rietveld refinement can be performed on the data.

Rietveld refinement is a whole profile structure refinement method based on least-squares fitting. The powder diffraction pattern of the sample is obtained in digital form, and the Rietveld process treats these digital data as an intensity measurement (y_i) at each of several thousand increments (steps – i). A calculated profile of the structure is compared to the experimental profile, and then selected parameters are refined by a least-squares method in order to provide the best fit between the calculated and experimental profiles. Examples of instrument and sample based factors which must be taken into account when performing Rietveld refinements are given in **table 2.1**.

	Instrument/Experimental Factors	**Sample Based Factors**
Peak Positions	Wavelength Zero point error Sample height	Unit cell dimensions
Peak Shapes	Diffractometer geometry Slit sizes Type of detector X-ray source	Size of crystallites Strain Defects
Intensities	Amount of sample Lorentz-polarisation and other diffractometer factors	Atomic coordinates Temperature factors Absorption Site occupancies
Background	Air scatter Detector noise Sample holder	Fluorescence Disorder

Table 2.1 The parameters upon which the calculated a powder X-ray pattern is dependent. These parameters pertain to sample and instrument effects, and each must be considered during refinement in order to obtain the best agreement between the calculated and experimental models.

When a Rietveld refinement is performed, the fit of the calculated profile to the experimental profile is evaluated numerically, providing an indication of how good the fit is. This is usually done in terms of R values. However, this can also be shown graphically in terms of a difference profile plot. The weighted profile R value is termed R_{wp} (**equation 2.2**),

$$R_{wp} = \left\{ \frac{\sum_i w_i [y_i(obs) - y_i(calc)]^2}{\sum_i w_i [y_i(obs)]^2 \}^{1/2}} \right\} \qquad (2.2)$$

where y_i(obs) is the observed intensity at step i, y_i(calc) is the calculated intensity and w_i is the weighting. This indicator is of importance as it is the quantity actually minimised during a Rietveld refinement. It must be noted that a sample with a high background will automatically produce a lower R_{wp} value than a sample with a lower background purely because some of the intensity will be accounted for by the background function.

The better the fit, the lower the R_{wp}. This is true until the R_{wp} value tends towards the value of R_{exp} (**equation 2.3**), the statistically expected R value,

$$R_{\text{exp}} = \left[\frac{(N-P)}{\sum_i^N w_i y_i(obs)^2} \right]^{1/2} / \qquad (2.3)$$

where N is the number of observations and P is the number of parameters. R_{exp} reflects the quality of the statistics and the ratio of these two R values gives $\chi 2$ (**equation 2.4**), the goodness of fit.

$$\chi^2 = \frac{R_{wp}}{R_{\text{exp}}} \qquad (2.4)$$

This should approach unity; however, χ^2 is affected by the length of time over which data are collected. If data are collected rapidly, R_{exp} will be large making χ^2 artificially small (possibly less than one). If data are collected over a longer period of time, R_{exp} will be small making χ^2 very large. The value of χ^2 is therefore not always a good measurement of the reliability of a refinement.

Perhaps the most informative R factor for structural work is the Bragg R factor, R_{Bragg} (**equation 2.4**), where $I_{hkl} = mF_{hkl}^2$ (m = multiplicity). This is closely related to the quantities reported in single crystal work.

$$R_{Bragg} = \frac{\sum_{hkl} |I_{hkl}(obs) - I_{hkl}(calc)|}{\sum_{hkl} |I_{hkl}(obs)|} \qquad (2.5)$$

2.2.3 Rietveld Refinement Using *TOPAS Academic*[7]

TOPAS Academic (TOtal Pattern Analysis System) is a computer program which runs on the Windows operating system and allows Rietveld refinements to be performed on powder X-ray data. The program operates in one of two ways, via a graphical user interface (Interface mode) or via the Launch mode.

In Launch mode an input file is set up which contains information about the instrument pertaining to the calculated model peak positions, peak intensities and the background. Starting values for each parameter are provided and these are either fixed or varied during refinement. As appropriate in these studies, only Launch mode was used.

2.2.4 Multitopas[8] Methodology

Variable temperature X-ray diffraction data sets contain a large amount of data in the form of powder patterns recorded at different set temperatures. A FORTRAN 77 program called Multitopas facilitates the quick refinement of these measurements. When Multitopas is executed, a variety of information pertaining to any one data set is provided and a batch file is created. When executed, this batch file controls the sequential refinement of each measurement in the data set in *TOPAS Academic*. Initially, the first measurement is refined manually in *TOPAS Academic* using an input file as described in **section 2.1.3**; this is then used as a "seed" for the remaining measurements. Each refinement produces an output file which is used as the input file for the next refinement. This process is repeated until all measurements within one experiment have been refined; the relevant refined parameters for each measurement are written to a results file. These are the *a* and *c* lattice parameters, the *c/a* lattice parameter ratio, the temperature factors, the fractional occupancy of atomic sites, the order parameter, the R-factors and the crystallite size in the case of these studies.

2.2.5 FePt Nanoparticle Sample Effects Relevant to Rietveld Refinement

The FePt specific sample parameters which are taken into account when refining the data using the Rietveld method are the fractional occupancy, unit cell dimensions, crystallite size, temperature factors and the background.

In its fcc (**Figure 2.3a**) disordered form FePt nanoparticles have a face centred cubic cell with each of the a, b and c unit cell parameters ~ 3.85 Å. The Fe and Pt atoms are statistically disordered over all sites in the lattice (each site contains 50 % Fe atoms and 50 % platinum atoms). When the material is in its chemically ordered FCT (**Figure 2.3b**) phase, it has a tetragonal unit cell with an a cell parameter of ~ 3.90 Å and a c cell parameter of ~3.71 Å[9]. It is possible to use a smaller tetragonal cell. The cell chosen, however, allows direct comparison with the cubic material. The Fe and Pt atoms in this case occupy specific Fe and Pt sites only. The fractional occupancy defines the composition of each atomic site. FePt in the disordered fcc phase has a fractional occupancy of 0.5 for each site. For the fct phase the fractional occupancy is arbitrarily defined as 0. The order parameter is derived from the fractional occupancy, being 1-(2*Fractional occupancy).

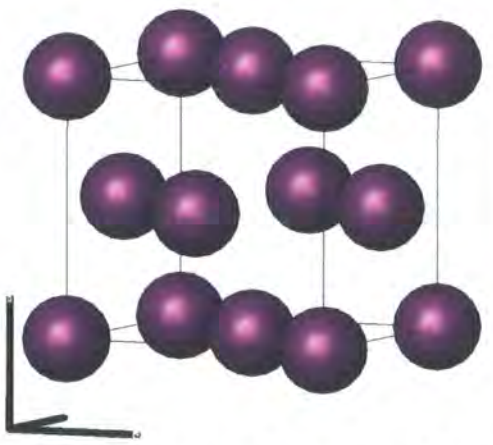

Figure 2.3a A diagram representing the face-centered cubic disordered structure of FePt nanoparticles. The purple atoms signify that each site may contain an Fe or Pt atom

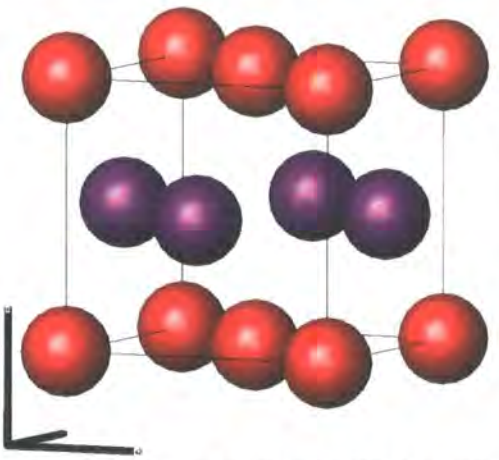

Figure 2.3b A diagram representing the face-centered tetragonal ordered structure of FePt nanoparticles. The red atoms are Fe and the blue atoms Pt

The *a* and *c* lattice parameters are allowed to differ at all times during Rietveld refinement. In reality, *a* may equal *c* (as in the fully disordered fcc phase). This is done to avoid having to perform a two-phase refinement.

Although crystallite size is not directly determinable from powder XRD data, once instrument effects have been excluded it is possible to obtain an approximate value as a function of the peak

width. In 1918, P. Scherrer[10] showed that if a monochromatic wavelength of X-ray radiation is focussed on a randomly oriented mass of crystals, the diffracted beam will be broadened increasingly as the particle size decreases (inversely proportional)[11]. Measurement of the broadening allows particle size estimation via the Scherrer equation (**2.6**)[12]

$$\beta = \frac{\lambda}{\varepsilon \cos\theta} \quad (2.6)$$

where β is the full width half maximum (FWHM) of the instrument corrected line profile, ε is the apparent particle size, λ is the wavelength and θ is the Bragg angle. The implementation of particle size is treated within TOPAS by convoluting a Lorentzian function with the full width half maximum of the peak (giving **equation 2.7**) with the instrumental peak shape.

$$Lorentzian\_FWHM = \frac{(0.1 \times r \times \lambda)}{(\varepsilon \times \cos\theta)} \quad (2.7)$$

where Lorentzian_FWHM indicates a Lorentzian function based on the full width half maximum of a peak, r is the diffractometer radius in mm and ε is the particle size. The 0.1 term is present for conversion to nanometres.

Temperature factors or the atomic displacement parameters are refined using the Rietveld method also and are a measure of the movement of the atoms in the given unit cell.

The background of a diffraction pattern is fitted using a Chebyshev polynomial function. The number of terms used is typically 18 in the case of an FePt nanoparticles sample. The number is chosen so as to fully fit the background of a given diffraction pattern whilst fitting none of the reflections due to the sample.

2.2.6 Bruker AXS D8 Advance Diffractometer

In Durham, the laboratory is equipped with a Bruker d8 Advance powder X-Ray diffractometer, which can be used for temperature-dependent studies. The range over which these can be carried out can be altered by the mounting of one of three variable temperature attachments described in **table 2.6**.

	Temperature range/K	Atmosphere
HTK1200 Furnace	298 – 1473	Air/Vacuum/Inert Gas/5 % H2/95 % Argon
TTK450 Cryofurnace	77 – 723	Vacuum (< 0 °C)/Air
PheniX Cryostat	15 - 300	Vacuum Only

Table 2.2 Technical information regarding each variable temperature attachment for use with the Bruker D8 advance diffractometer.

The work presented in this thesis obtained via the use of this diffractometer was wholly performed using the HTK1200 attachment with an atmosphere of 5 % H_2/95 % Argon.

From October 2002 until November 2004 (encompassing data sets d_01932 to d8_02697) the diffractometer was set-up as described below.

The X-ray generator was operated at 40 kV and 40 mA and the d8 uses Ge(111)-monochromated Cu Kα1 radiation (λ = 1.5405(9) Å). In the normal flat-plate reflection mode, or when any of the attachments described in **table 2.2** are present, the monochromatic X-rays pass through a 6 mm aperture slit and an anti-scatter tube to a fixed Soller slit and finally an automated divergence slit in either a fixed or variable slit mode before reaching the mounted sample. The Soller slit is designed to decrease the axial divergence in order to minimize the peak shifts and any asymmetric broadening of said peaks. A radial Soller precedes a Braun PSD-50M linear position sensitive detector (PSD) which detects the diffracted X-rays. A PC with Bruker DiffracPlus[13] software controls the diffractometer and HTK1200 furnace. From November 2004 until the end of this work the diffractometer was set-up slightly differently to that described above. The changes made were to the detector; instead of a Braun PSD-50M a VÅNTEC-1 linear position sensitive detector was used, and to the software, in that the Bruker XRD Commander software was used.

Sample materials were typically mounted on a 17 mm diameter amorphous silica disc. Silicone vacuum grease was used as an adhesive. The disc was then placed onto an alumina sample holder. This sample holder was then situated in the path of the X-ray beam, inside the HTK1200 furnace. The sample surface was imperfect and led to a larger background signal (due to the amorphous nature of the silica disc) in the diffraction pattern. This was unavoidable because the material available was not enough to fully cover the disc.

2.2.7 Reducing Fluorescence in Bruker D8 Advance Diffractometer

With the introduction of the VÅNTEC-1 detector a large background signal was observed when recording spectra of compounds containing iron. By reducing the fluorescence the signal:noise ratio could be improved. With the previous Braun detector this background was always there but it was not possible to do anything about it as with the VÅNTEC-1 detector.

2.2.7.1 Experimental

A sample of Fe_2O_3 was obtained. A spectrum was recorded over the range 10 – 90 °2θ in determine a suitable range over which to make multiple measurements, i.e. a range with the most intense peak centrally positioned. 31 – 38 °2θ was chosen.

The window width and lower limit of the X-ray detector were then changed. A series of measurements were made whereby the window width and lower limit varied from 0.5 V and 0.1 V to 0.15 V and 0.45 V in increments of 0.02 V. The sum of the window width and lower limit always totalled 0.6. The data obtained from these measurements were fitted in *Topas Academic* in order to obtain the integrated areas and background details. The intensity of the main peak for each measurement was measured in *DiffracPlusEVA*[14]

2.2.7.2 Results and conclusion

For each of the peaks at ~ 33 °2θ and ~ 35 °2θ the (height-background)/background)$^{1/2}$ is shown for each measurement in **figures 2.4** and **2.5**. The greater the value, the better the peak to background ratio and therefore the better the signal to noise ratio (fluorescence effect minimized).

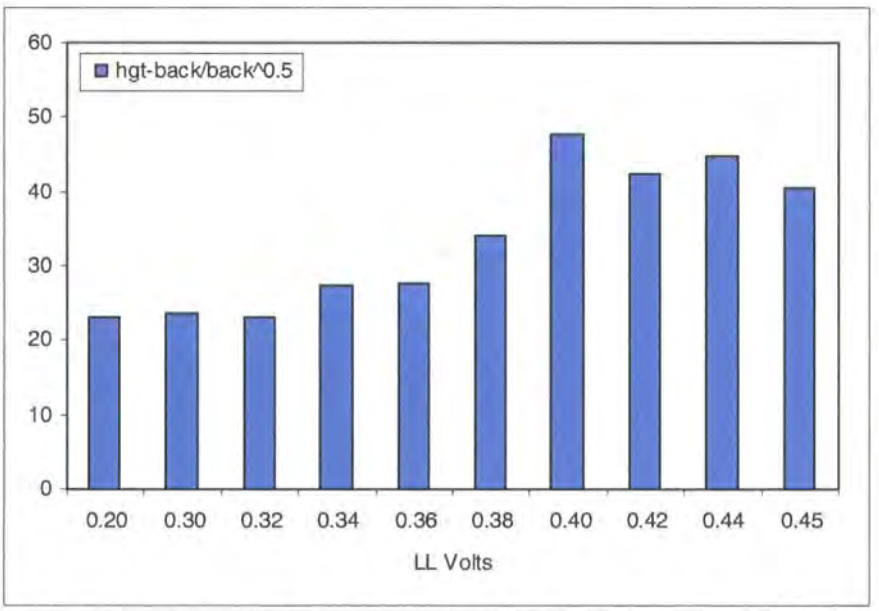

Figure 2.4. A graph showing the relative (height-background)/(back(1/2)) for the peak at ~ 33 °2θ.

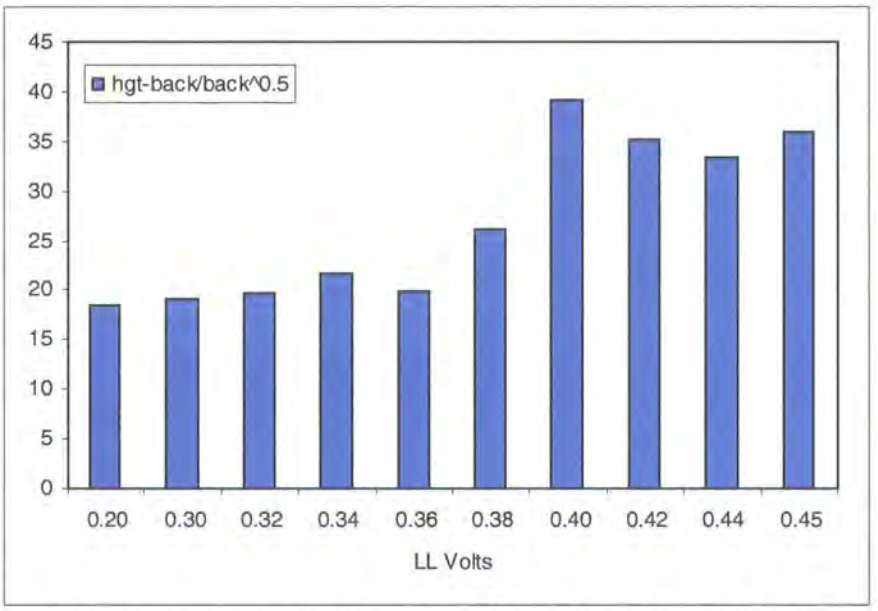

Figure 2.5. A graph showing the relative (height-background)/(back(1/2)) for the peak at ~ 35 °2θ.

The data show that the signal to noise ratio is best when the lower limit of the X-ray detector is set to 0.4 V and the window width at 0.2 V.

2.2.8 Siemens d5000 Powder Diffractometer

This machine was suitable for routine sample purity checks, as well as allowing the obtainment of Rietveld refinement quality data using longer scan times. The diffractometer was equipped with a Cu Kα radiation X-ray source (average λ = 1.54195 Å). The X-rays initially passed through a set of Soller slits and either a variable divergence slit (6 mm or 20 mm of sample illumination – V6 and V20) or a 1 degree fixed slit before reaching the sample mounted upon a silica disc within a plastic sample slide (or glass disc within the plastic sample slide) placed within the automatic sample changer. The X-rays that are then diffracted by the sample passed through a second set of Soller slits, a graphite (001) monochromator and a fixed 0.2 mm receiving slit before being detected by a scintillation counter. A PC with the Bruker DiffracPlus software suite installed controlled the diffractometer.

The use of variable slits means that a constant area of the sample is illuminated at any given time throughout the whole 2θ angle range. This leads to artificially higher intensities at high angle relative to fixed slit sizes. With very small fixed slits, the illuminated sample area at high angle is low.

Samples were mounted on a silica disc as for the D8 Advance diffractometer. The silica disc would be held within a plastic sample slide using blu-tack. If a glass slide sample holder was used, this was not necessary. The plastic sample slide could be placed in the d5000 sample

changer. An imperfect sample surface was obtained due to the lack of material available to cover the whole silica disc or glass slide. This meant a larger background signal was recorded in the diffraction patterns due to the amorphous nature of the silica or glass.

2.2.9 Bruker AXS d8 Advance Diffractometer With Sol-X Detector

Since 2004 the laboratory in Durham has been equipped with a second Bruker d8 Advance diffractometer equipped with a Sol-X point detector. This eliminated the need for a monochromator and provided an ~ 3 times increase in measured intensity. The machine was also equipped with a sample holder which could be loaded with up to 9 bulk powder samples at any time. Otherwise it was set up in the same way as the other d8 diffractometer, minus the variable temperature attachments. This instrument was utilised to obtain some X-ray data. Any data where this is the case are denoted by a D9_xxxx type code.

2.3 SQUID Magnetometry[15]

The equipment used to obtain magnetic measurements in Durham was a Quantum Design Magnetic Property Measurement System (MPMS). It contains four key components which allow it to make sensitive measurements: the detecting coil; the superconducting quantum interference device; the magnetic shield; and the magnetic coil.

The sample is attached to the end of a rod which is itself lowered into the centre of a 9 mm diameter sample chamber maintained at low pressure with helium gas evaporated from a liquid helium bath in the dewar surrounding the sample chamber. The detecting coil is a second order gradiometer and is positioned outside the sample chamber such that the magnetic field yielded from the sample is able to couple inductively to the coils as the sample is moved through them.

The detecting coil is connected to the SQUID via superconducting wires which allow the current from the coils to inductively couple to the SQUID sensor. The voltage output is proportional to the current flowing in the SQUID's input coil, thus making it a very sensitive current-to-voltage converter. By moving the sample through the coils the magnetic moment of the sample induces an electric current in the detection coils. The detection coils, wires and SQUID form a closed superconducting loop. Any alteration in the magnetic flux in the detection coils leads to a change in the persistent current in the detecting circuit. This is proportional to the change in flux. The output voltage of the SQUID, as a result, is proportional to the current of detecting coils which is itself proportional to the magnetic moment of the sample, meaning the output voltage of the SQUID is proportional to the magnetic moment of the sample.

To shield the SQUID sensor from both the magnetic flux which may be present in its surroundings, as well as the large magnetic fields which the superconducting magnet is capable

of producing, a superinsulator (superconducting shield) is utilised. This shielding provides a volume in which the SQUID is located which has a relatively low magnetic field - relative because the main requirement is not an absolute low field, but an extremely stable one. The sensitivity of the SQUID is such that it is able to detect the flux generated by a small sample (~ 1/1000 of a quantum – 2.07 x 10-7 Gm^{-2}) and as such must be protected from the magnetic field (a 1 cm^2 area of which yields a magnetic flux of around 2 million quanta).

The superconducting magnetic coil is a completely closed superconducting loop which it is possible to charge up to a specific current and then operate in persistent mode without an external current source or power supply. In order to charge the loop it must be opened by the heating of a small section of the loop to a temperature greater than the *Tc*, where *Tc* is the superconducting critical temperature. It is then possible to attach a power supply to either side of the gap and charge the magnet. The field can be made noisy as a result of fluctuations in the current from the power supply which means measurements are taken in persistent mode, and after the magnetic field has become stable.

The magnetic coil was operated in one of two ways – oscillation or hysteresis mode. Oscillation mode meant the magnetic field would continually overshoot, and then undershoot the set field; each cycle would be of decreasing amplitude. This method of measurement is slow but precise. Hysteresis mode on the other hand means the persistent current switch is left on at all times; the magnet is not run in persistent mode and the power supply is a continual part of the magnetic circuit. This method is most useful when a magnetisation (M) Vs. applied field (H) measurement is required rapidly. It does, however, require a sample with a large (>10-5) magnetisation.

Sample volumes were always small. As a result, a novel method of mounting the sample for SQUID measurements was developed. A measured amount of a given sample was placed in one half of a gelatin capsule (13.9mm long x 5.05mm wide), whilst the other half was turned upside down and pressed against the sample, inside of the first capsule half. This was then glued to the centre of a straw using a G-varnish/Solvent (10:1 Ethanol: Toluene) mixture, thus minimizing environment anisotropy – equal lengths of the straw were above and below the capsule. This meant that any signal above the capsule would be counter-balanced by that below.

Typical experiments involved either the measurement of the magnetisation as a function of applied field or the magnetisation as a function of temperature. Typically the sample would be cooled to 5 K in an M Vs. T experiment, before warming the sample to 290 K whilst measuring the magnetisation as a function of the temperature. In zero-field cooled experiments there was no applied field until after cooling. In field-cooled experiments, a field was present during cooling and warming (typically 100 Oe). The applied field varied from 0 to -5 T, to 5 T and then back to 0 T during a magnetisation versus applied field experiment. The number of steps in such a measurement was typically 43, but could have been any number dependent upon two choices –

the length of time the experiment was required to run (more steps, more time required) and the number of data points needed.

A number of magnetic measurements at high temperature are detailed in this thesis. In order to obtain these measurements modifications and additions to the SQUID magnetometer were required, as well as the development of a usable sample holder. These developments are detailed in this section.

Through use of an optional attachment, measurements at temperatures up to 800 K can be made. The oven is an insulated heater assembly which is placed directly in the magnetometer sample space. It is as long as the sample space so as to maximise its use of available space and leaves a sample space with a 3.2 mm diameter when installed. The oven employs a vacuum sleeve which is capable of isolating the temperatures within the oven from those surrounding it. This means the surrounding space's temperature is still controlled by the magnetometer rather than the oven.

2.4 Transmission Electron Microscopy (TEM)

2.4.1 Introduction to TEM[16]

TEM is a technique used for imaging whereby a beam of electrons is focused onto a given specimen which results in an enlarged version appearing on a fluorescent screen (or the image can be photographed and developed for printing onto photographic film).

Initially an electron beam is generated by the thermionic emission of a heated tungsten cathode (older instruments) or a field emission gun (modern instruments). This beam is then accelerated through an anode and focused onto the sample by a lens. The sample is typically mounted on a carbon film coated (200 micrometers) copper grid. The electron beam is either scattered by the sample or absorbed by it depending on the electron density where the electrons are focused and the remainder transmitted. Those electrons which are transmitted are collected onto an electromagnetic lens, magnified and projected towards a magnetic projector lens system where the image is magnified further. This image is projected onto a fluorescent screen where the image can be viewed by the user or either a digital or film image taken. The photography allows magnification of the image a further time. The exact magnification level is dependent on the instrument but can be anywhere between 100 – 1 million times the actual sample size. This allows an ultimate resolution greater than 0.2 nm. The newest machines are capable of resolving distances smaller than this.

Depending on the sample preparation, electron microscopy can cause certain problems, i.e. movement, evaporation or decomposition of the sample. This is generally minimized by ensuring the sample is dry and by using as weak an electron beam as possible.

2.4.2 Instrumentation

Philips CM100

A Philips CM100 (compustage) transmission electron microscope operated at 100 kV with a Magnification from x100 to x100000 was used for the characterisation of all samples prepared by Dr Loc H Nguyen (samples LHNXXX). For other samples (code LEMH XXX) a JEOL 100CX transmission electron microscope was used. Its highest accelerating voltage is 100 kV and it is capable of resolving of the order of about 0.2 nm, on suitable specimens. Practically the resolution is less.

JEOL 2010F

A JEOL 2010F field-emission gun (FEG) microscope was used to obtain images with greater resolution. Particles of sub-nanometre scale are resolved in detail such that lattice structure can be seen. The microscope operated at 200 kV and was used to characterise samples prepared by Dr Loc H Nguyen (LHNXXX).

2.5 EXAFS[17]

2.5.1 Synchrotron Radiation Source (SRS)

The Synchrotron Radiation Source (SRS) housed at Daresbury Laboratory, UK, is a second-generation synchrotron light source. It consists of a 12 MeV linear accelerator which injects a beam of electrons into an energy boosting ring (thus increasing the energy to 600 MeV), providing a high current (> 250 mA). Within this main ring the electrons are accelerated to energies reaching 2 GeV, and synchrotron light is emitted as the electrons pass through bending magnets and light-producing insertion devices. The emitted light is transported, tangentially to the ring, into experimental areas where it is utilized by experimentalists. The accelerator is a 96 m ring and the lifetime of the beam contained within can last more than twenty-four hours. Beam refills occurred once a day for the duration of experiments recorded in this thesis. In order to avoid fast decay of the electron beam a radio frequency device increases the energy of the electron beam each time it completes a circuit of the storage ring. To avoid beam loss due to inelastic collisions with other electrons and gas molecules an ultra-low vacuum of the order of 10^{-10} Torr is maintained.

The range of available radiation is large, from infra-red to X-rays and allows techniques such as X-ray diffraction, X-ray spectroscopy, EXAFS, small angle/wide angle scattering, soft X-ray spectroscopy, photoemission and imaging all to be used.

Stations 7.1 (Fe edge data) and 16.5 (Pt edge data) were used to collect EXAFS data for this thesis.

2.5.2 Introduction to EXAFS

Extended X-Ray Absorption Fine Structure (EXAFS) spectra show the absorption coefficient of a given material versus energy (typically a 500 – 1000 eV range beginning before an absorption edge of a given element). By analysing the oscillating spectrum post-absorption edge, it is possible to obtain information relating to the coordination environment of a centrally excited atom.

Typically, X-Ray absorption spectra are recorded over the range of 200 – 35000 eV. The major process occurring is that whereby a photon is totally absorbed and thus ejects a core photoelectron from the absorbing atom. This leaves a core hole. This atom with the core hole is now excited and as such is capable of producing further excitations. This is often ignored. The ejected photoelectron's energy will be equal to that of the absorbed X-ray, minus the binding energy, when in the atom core. This excited photoelectron is thus then able to interact with its surrounding, non-excited atoms.

If the ejected photoelectron is taken to have a wave-like nature and the surrounding atoms are described as point scatterers, it is possible to imagine the backscattered waves interfering with the forward waves and thus producing either peaks or troughs. This interference effect disrupts the measured absorption coefficient, thereby causing an oscillation in the EXAFS spectra obtained. **Figure 2.4** shows a typical EXAFS spectrum.

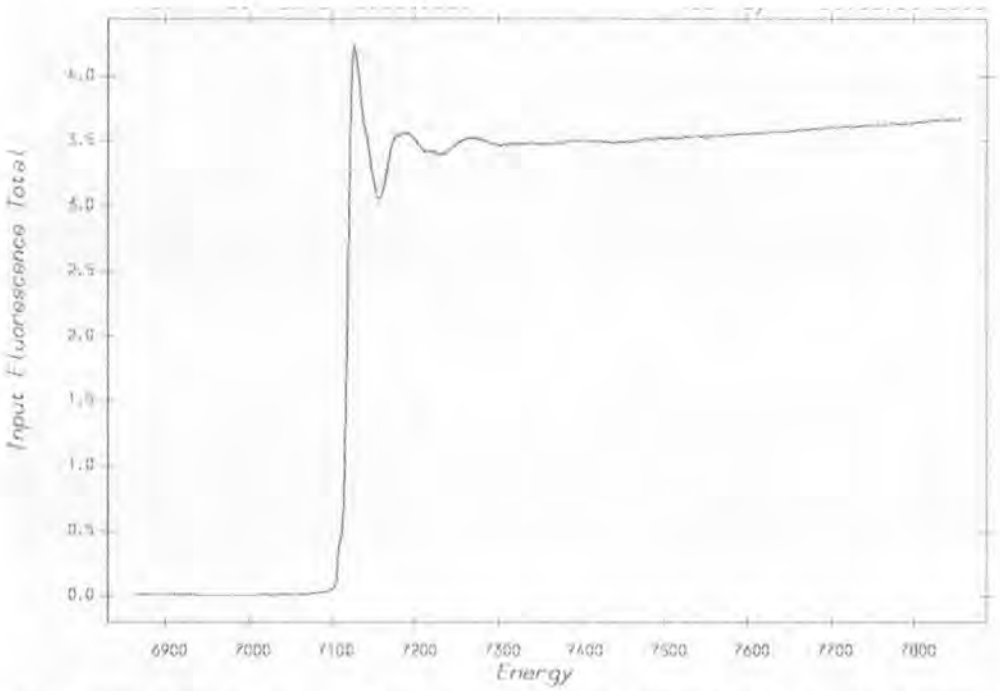

Figure 2.6 A typical EXAFS spectrum. Data shown are those obtained by performing EXAFS on FePt nanoparticles at the Fe edge.

The wavelength of the photoelectron is dependent on the energy and phase of the backscattered wave which exists at the central atom. This will change in relation to the energy of the incoming photon. As such the interference effect is oscillatory in nature, leading to an oscillating spectrum. The phase and amplitude of the backscattering wave are dependent on the type of atom doing the backscattering and the distance of said atom from the central atom, it is therefore possible to obtain information pertaining to the coordination environment of the original absorbing (centrally excited) atom by analyzing these EXAFS data.

2.5.3 EXAFS Data Collection

The EXAFS measurements of the FePt nanoparticles were performed at both the Fe K edge at 7112 eV at station 7.1 and the Pt L3 edge at 11555 eV at station 16.5 at Daresbury Laboratory, UK. At station 7.1 X-ray energy was selected with a double crystal Si(111) monochromator at ambient conditions. A nine element Ge detector with a maximum count rate of 150 kHz per channel was used. At station 16.5 X-ray energy was selected with a double crystal Si(220) monochromator, also at ambient conditions. A thirty element Ge detector with a maximum count rate of 300 kHz per channel was used. Data were collected in fluorescence mode with ion chambers filled with helium gas. Energy calibration was monitored using iron and platinum metal foil respectively at stations 7.1 and 16.5. The sample was mounted on top of conducting tape which was in turn mounted over a holey metal plate. The program EXCALIB was used to sum multiple data sets together, EXSPLINE was used for the removal of background and the program

EXCURV98 was used for the fitting and refinement of calculated models to the experimental data. These programs are described in greater detail in **sections 2.4.4 – 2.4.6**.

2.5.4 Excalib[18]

EXCALIB is a Unix based software program which allows multiple datasets collected on one sample to be combined.

The program must be provided with details of which station data were recorded on as well as what type of data (here fluorescence) will be processed. Then a dataset is read in to the program and the relevant monochromator type chosen. The fluorescence detectors must then be re-weighted whereby the detected spectrum from each individual detector channel is checked manually, and either rejected from the input data set or kept loaded. After re-weighting, the data are added to the summed area, and other data sets are read in and the process repeated. When all data sets obtained from one sample have been summed, a single output file is written.

2.5.5 Exspline[19]

The output file created by EXCALIB can be read into EXSPLINE in order to subtract the background from the data. On opening the program, a window into which the edge details (element, edge and energy) can be input appears. After this a summed dataset can be read in. A window divided into four sections – pre-edge, spline, EXAFS and Fourier Transform – is produced. By moving the polynomial curve superimposed on the data shown in the pre-edge and spline sections (effectively the raw data obtained), and increasing or decreasing the order of each polynomial curve, the background can be subtracted from the data. This can be judged, by eye, by looking at the EXAFS and Fourier Transform windows and how noisy the data is. When the background subtraction is satisfactory, an output file (3-column ascii) is written which can be directly imported into EXCURV98.

The background subtraction process is a matter of judgement. Various extreme approaches to the process were tried. The data were taken through the full analytical process and results were always consistent within experimental errors, giving confidence that background was being adequately modelled.

2.5.6 Excurv98[20]

EXCURV98 is a wave theory EXAFS analysis program housed at Daresbury Laboratory. The program simulates EXAFS spectra using rapid curved wave theory and Rehr Albers theory from the parameters of the radial shells of atoms surrounding the centrally excited atom. An

experimental spectrum is read in, and the potentials then phaseshifts of each element in the system are calculated. An initial parameter set for the first coordination sphere (shell) is input. This is the start of the calculated EXAFS model. These parameters are typically refined, then a second coordination sphere (more if necessary) is added and all parameters refined on addition of each sphere. The model is continually varied until the fit of the model to the experimental data is both scientifically sensible and statistically as good as possible. Typical refinements used on datasets presented in this thesis are described in further detail in **chapter 6**.

2.6 Rutherford Backscattering[21]

2.6.1 RBS Theory

Rutherford Backscattering, a technique based upon the outcome of collisions between atomic nuclei, is used in this thesis to obtain information about the elemental composition of any given sample. In order to obtain this information, the technique, and its theory must be understood.

When bombarding a sample with a beam of high energy particles (typically He^{2+} ions), the majority will penetrate so deep into the sample that they will be unable to escape. This can be understood by considering that the diameter of an atomic nucleus is of the order of 1×10^{-15} m, whilst the spacing between two given nuclei is 2×10^{-10} m. This means nuclei which bombard the material are able to pass through any two given sample nuclei. However, some will collide with surface level sample nuclei, and will therefore be backscattered. The energy of these backscattered nuclei is then measured. This measured energy is dependent on two processes.

A nucleus will lose energy both before and after a collision when passing through a sample. The amount of energy lost is dependent on the material's stopping power. A nucleus will lose energy as a direct consequence of any collision. The energy lost in this case depends on the mass of both the projectile nuclei and the sample nuclei. The ratio of energy from before and after a collision is termed the kinematic factor.

The kinematic factor is greater the lighter the target atom. Upon collision a significant amount of momentum is transferred from the incident particle to the target particle. The greater the target particle mass, the less the momentum transferred. On further target atom mass increase, the incident particle energy nears the backscattered particle energy. If a sample contains more than one element, RBS is more capable of distinguishing between these elements when the relative mass difference is large. It follows that RBS provides better mass resolution if lighter atoms are present rather than heavier ones.

The number of backscattering events which occur when projectile nuclei collide with nuclei of a given element also depends on two things:

1. The concentration of the element
2. The effective nucleus size

The probability a material will cause a collision is known as its scattering cross section. The scattering cross section is approximately proportional to the square of the atomic number of the target atom.

It can be seen from **figure 2.5** that the greater the mass of a target element, the better the backscattering yield.

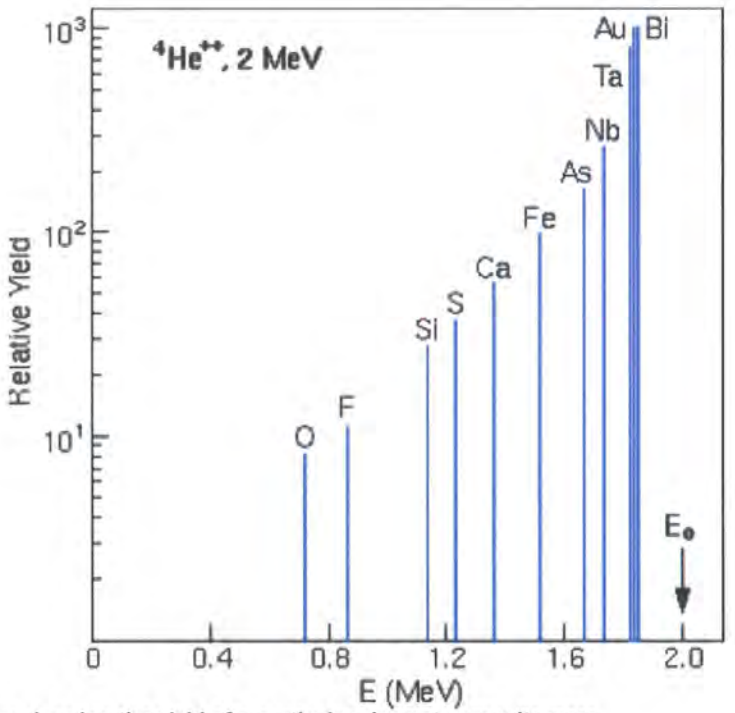

Figure 2.7 A diagram showing the yield of a particular element versus its mass

When an RBS spectrum is obtained, such as that shown in **figure 2.6** the elemental composition can be modelled. If the height of each peak is measured and normalized by use of the scattering cross section of each element, the ratio of the elements to each other can be found at any given sample depth. The peaks with the greatest backscattering energy will be due to the heavier elements present. Equally, the height of a backscattering peak for a given element is inversely proportional to the stopping cross section of that element.

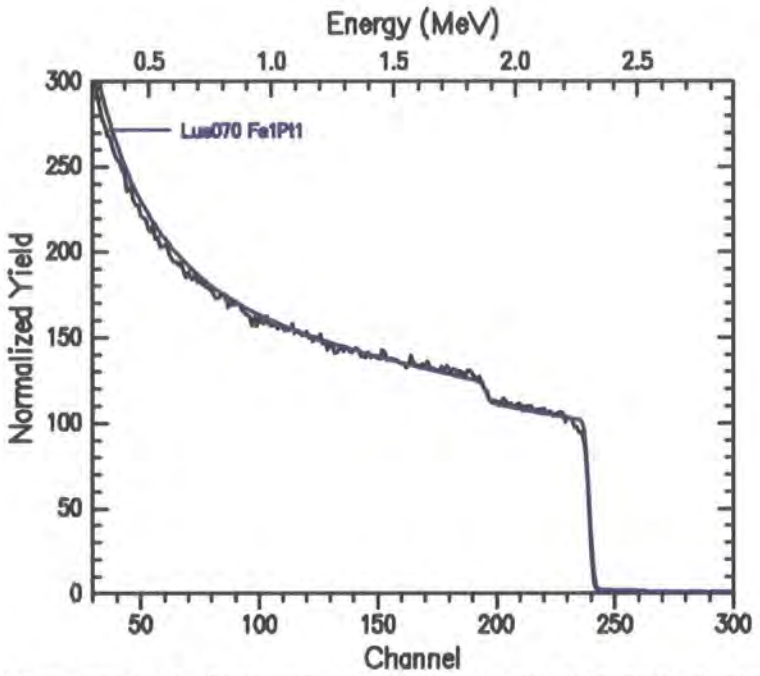

Figure 2.8 An RBS spectrum. The black curve is the experimental data obtained when analysing FePt nanoparticles; the blue curve is a calculated model with 1:1 Fe:Pt stoichiometry.

2.6.2 Equipment

In Durham we have an ion beam analysis service which is equipped with an NEC 5SDH Pelletron Accelerator[22] that allows RBS studies to be performed. All RBS data presented within this thesis have been obtained by Dr. Richard L. Thompson.

The accelerator is comprised of three main components – the ion source, Pelletron accelerator and the analytical endstation.

2.6.2.1 Ion Source

An ion source is needed for the production of negative or positive ions. Different sources can be used to obtain ions with varying mass and charge. Positive ion sources, such as those used to obtain He^{2+} ions, are placed inside the tank of a single-ended accelerator.

The ion source (radio frequency - RF - ion source for positive ions) typically yields a gas or gas mixture which is then allowed to migrate into a quartz bottle. An RF oscillator connected to this causes dissociation of the neutral gas, thus creating ions. By imparting a voltage gradient over the quartz bottle, the ions are forced out through the exit aperture causing a continuous beam of ions. These ions are then directed towards the Pelletron accelerator.

2.6.2.2 Pelletron

The ions produced by the ion source are accelerated by an electrostatic field which results in a true direct current beam. In a machine of this type, a single-ended machine, a high voltage terminal within which the ion source resides will be present at one end, whilst at the other end the ion beam emerges with energy approximately equivalent to the terminal voltage.

2.6.2.3 Analytical Endstation

This incorporates the computer controlled sample holder, capable of unlimited rotation about the ion beam, as well as the computer which controls the ion beam accelerator. The console allows sample positioning, data collection and sample imaging to be controlled. Analysis of the resulting data is conducted through the analytical endstation.

2.7 References

1. S. H. Sun, C. B. Murray, D. Weller, L. Folks and A. Moser, Science, 2000, 287, 1989-1992.
2. J. S. O. Evans and I. R. Evans, Chemical Society Reviews, 2004, 33, 539-547.
3. A. R. West, Basic Solid State Chemistry, 2nd edn., John Wiley and Sons, New York, 2001.
4. J. I. Langford and D. Louer, Reports on Progress in Physics, 1996, 59, 131-234.
5. H. M. Rietveld, Journal of Applied Crystallography, 1969, 2, 65-&.
6. L. B. McCusker, R. B. Von Dreele, D. E. Cox, D. Louer and P. Scardi, Journal of Applied Crystallography, 1999, 32, 36-50.
7. A. A. Coelho, TOPAS Academic, Bruker AXS, Karlsruhe, 2004.
8. J. S. O. Evans, Multitopas - Fortran 77 routine, University of Durham, 1999.
9. T. J. Klemmer, N. Shukla, C. Liu, X. W. Wu, E. B. Svedberg, O. Mryasov, R. W. Chantrell, D. Weller, M. Tanase and D. E. Laughlin, Applied Physics Letters, 2002, 81, 2220-2222.
10. P. Scherrer, Gottinger Nachrichten, 1918.
11. A. L. Patterson, Physical Review, 1939, 56, 978-982.
12. J. I. Langford and A. J. C. Wilson, J. Appl. Crystallogr., 1978, 11, 102-113.
13. Diffracplus, Bruker AXS, Karlsruhe, 1998
14. Diffracplus EVA, Bruker AXS, Karlsruhe, 1998
15. M. McElfresh, Fundamentals of Magnetism and Magnetic Measurements, Quantum Design, San Diego, 1994.
16. R. J. Hunter, Foundations of Colloid Science, 2nd edn., Oxford University Press, Oxford, 2001.
17. S. J. Gurman, Journal of Synchrotron Radiation, 1995, 2, 56-63.
18. A. J. Dent and J. F. W. Mosselmans, A Guide to EXCALIB, CLRC

Daresbury Laboratory, 1992. See also http://www.srs.dl.ac.uk.

19. EXSPLINE - a program for EXAFS background subtraction, Daresbury Laboratory, 2000. Based on an original program, SPLINE, P.Ellis (1995), PhD Thesis, University of Sydney.
20. Binsted N. (1998) EXCURV98: CCLRC Daresbury Laboratory computer program.
21. E. A. group, Rutherford Backscattering Spectrometry Theory Tutorial, 2005.
22. T. Davis, http://www.pelletron.com, 2006.

Chapter 3 – Synthetic Details

3.1 Introduction

This chapter describes all synthetic and experimental details relevant to the work presented in this thesis. The synthesis of FePt nanoparticle samples made via a well-known literature route[1] and the process involved in developing a novel synthetic route described as the "Durham Route" to FePt nanoparticles are detailed.

3.2 FePt Synthesis via Sun *et al.*'s Method

3.2.1 Synthetic Strategy

In a typical synthesis platinum acetylacetonate (98.5 mg, 0.25 mmol) and 1,2-hexadecanediol (195 mg, 0.75 mmol) were dissolved in dioctyl ether (10 cm^3) and heated to 100 °C. Oleic acid (0.08 cm^3, 0.25 mmol), oleylamine (0.085 cm^3, 0.25 mmol) and iron pentacarbonyl (0.065 cm^3, 0.05 mmol) were added to the reaction system via syringe, and the resulting mixture was heated to reflux temperature (297 °C) for thirty minutes before the heat source was removed and the reaction mixture allowed to cool to room temperature. The system was opened to the atmosphere and the black product precipitated by the addition of ethanol (~20 cm^3) before centrifugation. The yellow-orange supernatant was decanted off and the black product dispersed in hexane (~25 cm^3) in the presence of oleic acid (~0.05 cm^3) and oleylamine (~0.05 cm^3) and precipitated out by adding ethanol (~20 cm^3) and centrifuging. The yellow-orange supernatant was discarded and the black product collected.

This reaction must be done under an inert atmosphere (argon or nitrogen) otherwise iron oxides or other compounds may result instead of iron platinum. The work has been carried out using Schlenk-line techniques in preference to conducting the reactions in a glove box as described in the literature.

Table 3.1 provides specific information relating to individual syntheses performed.

Sample Name	Mass Pt(acac)2 (g)	Mass 1,2-hexadecanediol (g)	Volume Oleic acid (cm3)	Volume Oleyl Amine (cm3)	Volume Iron Pentacarbonyl (cm3)	XRD experiment code
LEMH 006	0.0985	0.195	0.08	0.085	0.065	d5_04135
LEMH 009	0.0985	0.195	0.08	0.085	0.065	d5_04177
LEMH 014	0.197	0.390	0.16	0.17	0.13	d5_04239
LEMH 021	0.197	0.390	0.16	0.17	0.13	d5_04327
LEMH 026	0.197	0.390	0.16	0.17	0.13	d5_04377
LEMH 028	0.197	0.390	0.16	0.17	0.13	d5_04390
LEMH 029	0.197	0.390	0.16	0.17	0.13	d5_04440
LEMH 031	0.197	0.390	0.16	0.17	0.13	N/A; too wet for XRD
LEMH 032	0.197	0.390	0.16	0.17	0.13	d5_04460
LEMH 033	0.394	0.780	0.32	0.34	0.26	
LEMH 035	0.197	0.390	0.16	0.17	0.13	d5_04544
LEMH 036	0.197	0.390	0.16	0.17	0.13	d5_04545

Table 3.1 A table detailing reagent masses and sample information for all syntheses performed using the method developed by Sun et al.1.

3.2.2 Results and Discussion

Characterisation of each sample was, in the first instance, by X-ray powder diffraction. This is discussed below. TEM images of one sample were also obtained. Some samples were annealed *in-situ* in the d8 diffractometer and the data obtained are presented in **section 3.2.5**. Certain samples also underwent *ex - situ* annealing and the results are shown in **section 3.2.6**.

3.2.3 X-Ray Diffraction

A powder diffraction pattern of each sample was obtained. These data allow determination of the crystalline phases present in the sample. Therefore XRD shows whether the sample is iron platinum, iron oxide, platinum or a mixture. The experimental data can be refined (Rietveld refinement) relative to a structural model. A Rietveld refinement was performed on the X-ray powder diffraction data collected on sample LEMH 009 (d5_04177). The peak shape used for all Rietveld refinements presented in this chapter is described using a pseudo-voight instrumental function (derived from a scan of highly crystalline Y_2O_3) convoluted with an expression to describe the size of the FePt nanoparticles (dependent on 1/cos theta). In total 17 parameters were refined. These were 12 background terms, a sample height correction, a scale factor for the phase, 1 lattice parameter (a), crystallite size and an atomic displacement parameter (temperature factor). **Figure 3.1** below shows the refined X-ray diffraction pattern of an early sample (LEMH 009):

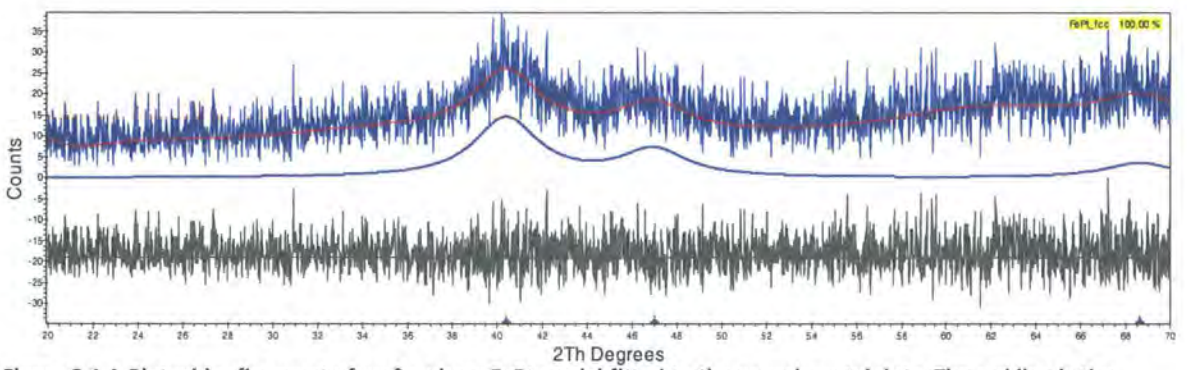

Figure 3.1 A Rietveld refinement of an fcc phase FePt model fitted to the experimental data. The red line is the fit of the model to the data, the smooth blue curve (the middle curve) is the model data and the grey is the difference between the model and experimental data.

The experimental data in **figure 3.1** have a poor signal to noise ratio but the fit of the calculated model to the data is reasonable. It confirms that FePt in the fcc phase has been synthesised.

However, a subsequent sample (LEMH 014) was shown to contain additional phases to iron platinum from the X-ray diffraction data after refining the parameters relative to an fcc phase FePt model. Again 17 parameters were refined. This can be seen in **figure 3.2**:

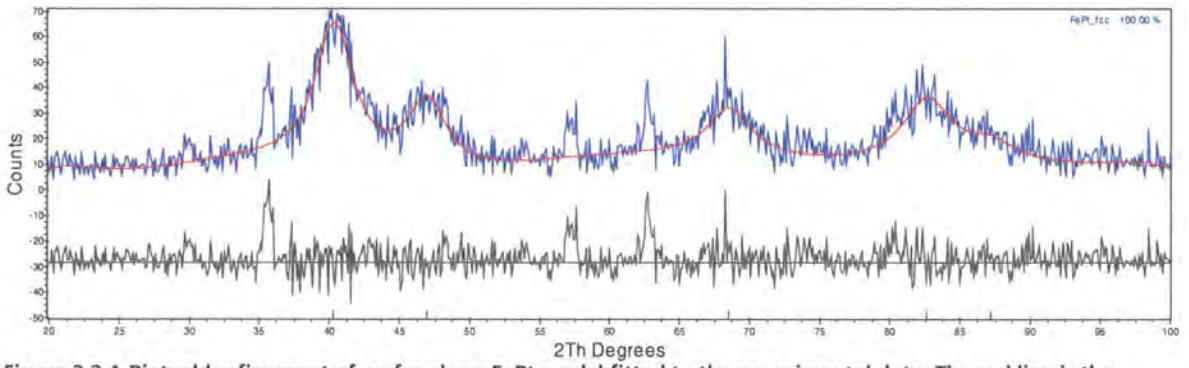

Figure 3.2 A Rietveld refinement of an fcc phase FePt model fitted to the experimental data. The red line is the fit of the model to the data and the grey is the difference between the model and experimental data.

Although the model fits very well to some peaks of the experimental data, there are other peaks, most notably those at ~ 35, 57 and 63 °2θ that are not fitted by this model. The unknown phase was found to be Fe_3O_4. Peaks which remained unaccounted for by fcc phase FePt were matched to Fe_3O_4 by comparing the experimental data to the powder diffraction database. A Rietveld refinement of a two-phase model incorporating both fcc phase FePt and Fe_3O_4 was then performed. In total 23 parameters were refined. The extra parameters refined relative to previous refinements were 1 lattice parameter (for Fe_3O_4), 1 scale factor, 3 atomic displacement parameters (3 for the Fe_3O_4) and the crystallite size of the Fe_3O_4. This can be seen in **figure 3.3**:

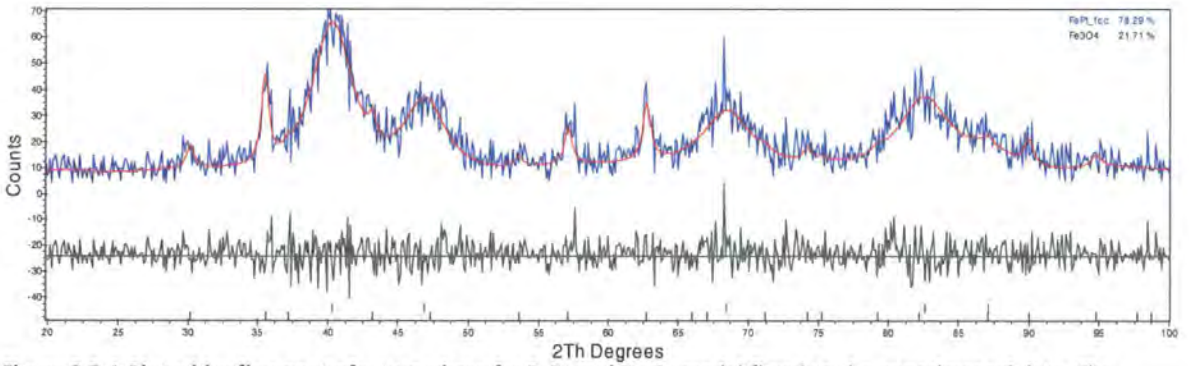

Figure 3.3 A Rietveld refinement of a two-phase fcc FePt and Fe_3O_4 model fitted to the experimental data. The red line is the fit of the model to the data and the grey is the difference between the model and experimental data.

The refined particle size of the iron oxide phase was 21.56(2) nm and was estimated to be 22 % of the sample.

By fitting models of fcc iron platinum and Fe_3O_4 all peaks are accounted for. This can be seen by the similarities between the experimental data and the superimposed red line of the fit.

A large number of samples were synthesised, each containing iron oxide as well as iron platinum phases. Many reasons for the iron oxide impurities were investigated and the major source of contamination was identified as oxygen in the solvents.

An example of the powder pattern of an FePt nanoparticle sample (LEMH 035) obtained after degassing of all solvents before use in any given synthesis (to ensure there is no oxygen in the system when performing any reaction, thus restricting Fe_3O_4 formation) is shown in **figure 3.4**:

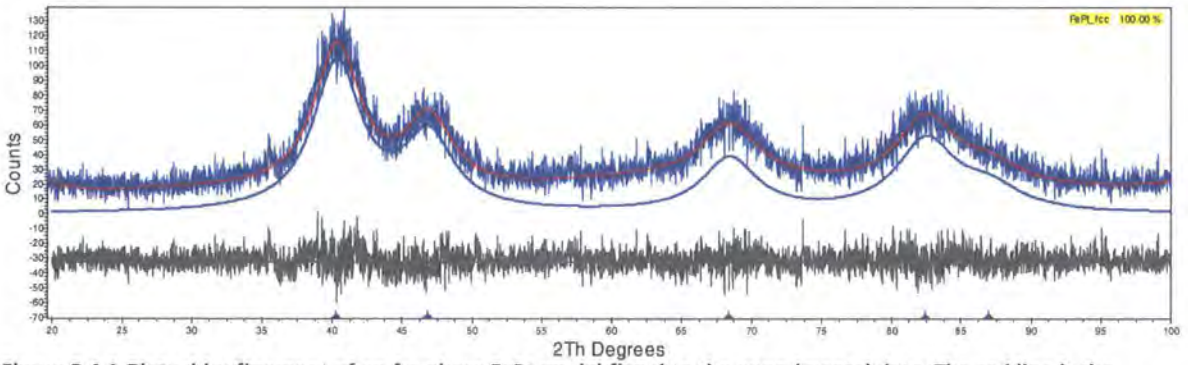

Figure 3.4 A Rietveld refinement of an fcc phase FePt model fitted to the experimental data. The red line is the fit of the model to the data, the smooth blue curve (the middle curve) is the model data and the grey is the difference between the model and experimental data.

The refinement data for **figure 3.4** can be seen in **table 3.2**:

Parameter	Value
Lattice Parameters	a = 3.87 (8)
Rwp (%)	17
Crystallite size	2.28 (4) nm
Height adjustment	-0.15 (7) mm

Table 3.2 A table showing the data obtained by conducting a Rietveld refinement of the X-Ray diffraction data obtained from LEMH 035.

3.2.4 Transmission Electron Microscope (TEM) Imaging

TEM imaging is used in order to obtain information relating to particle size and shape. By dispersing a sample of iron platinum (characterised previously by X-ray powder diffraction) in hexane and then dropping via a pipette onto a carbon grid on top of a copper mesh, a TEM image can be obtained. **Figure 3.5** shows the TEM image obtained for a sample (LEMH 014) made in Durham.

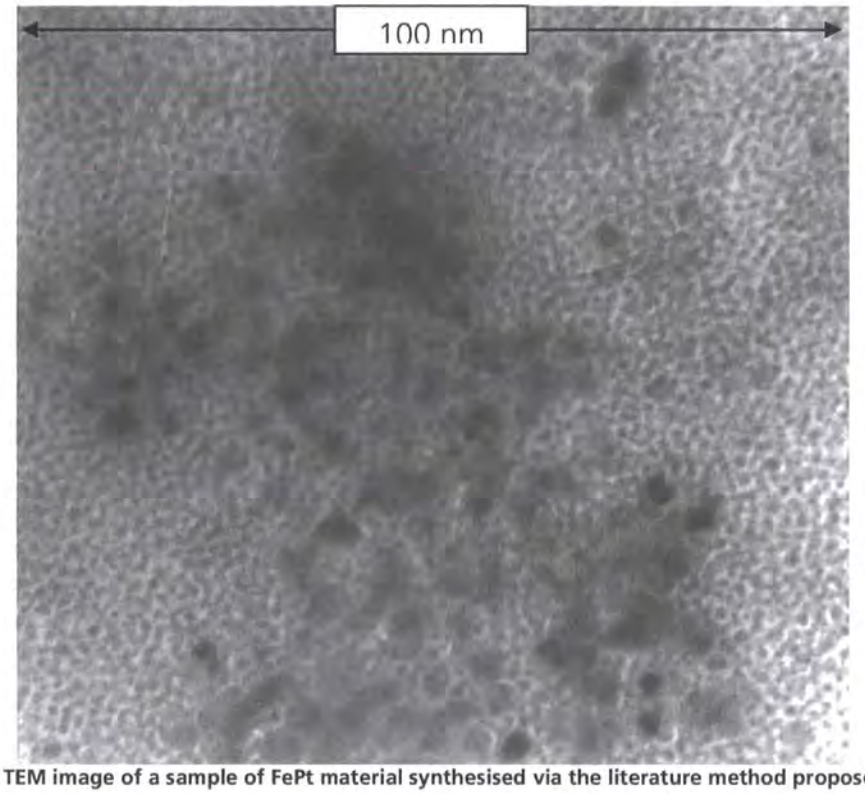

Figure 3.5 A TEM image of a sample of FePt material synthesised via the literature method proposed by Sun *et al.*[1]

Figure 3.5 shows a number of particles arranged primarily in clusters. The iron platinum particles are the circular black images. Based on the magnification used to record this image, the particles themselves are less than 10 nm in size.

The materials synthesised in Durham have been characterised by both X-ray powder diffraction and TEM imaging. From these methods it has been shown that the materials being synthesised are iron platinum and of the correct order of magnitude in size. This provides a useful benchmark for future work and samples for both *in-situ* annealing studies and further characterization by SQUID magnetometry.

3.2.5 *In-Situ* Variable Temperature X-Ray Diffraction Annealing Studies

As-synthesised iron platinum nanoparticles have an fcc structure. By annealing the particles they undergo a structural phase change to an fct structure. It is important to observe when this phase transition occurs (at the transition temperature, T_T). By conducting *in - situ* X-ray diffraction studies during the annealing of samples, it is possible to observe the phase changes. Proof of principle diffraction experiments have been conducted on five samples of iron platinum made via the literature method at Durham. **Figure 3.6** shows variable temperature diffraction data obtained from sample LEMH 014.

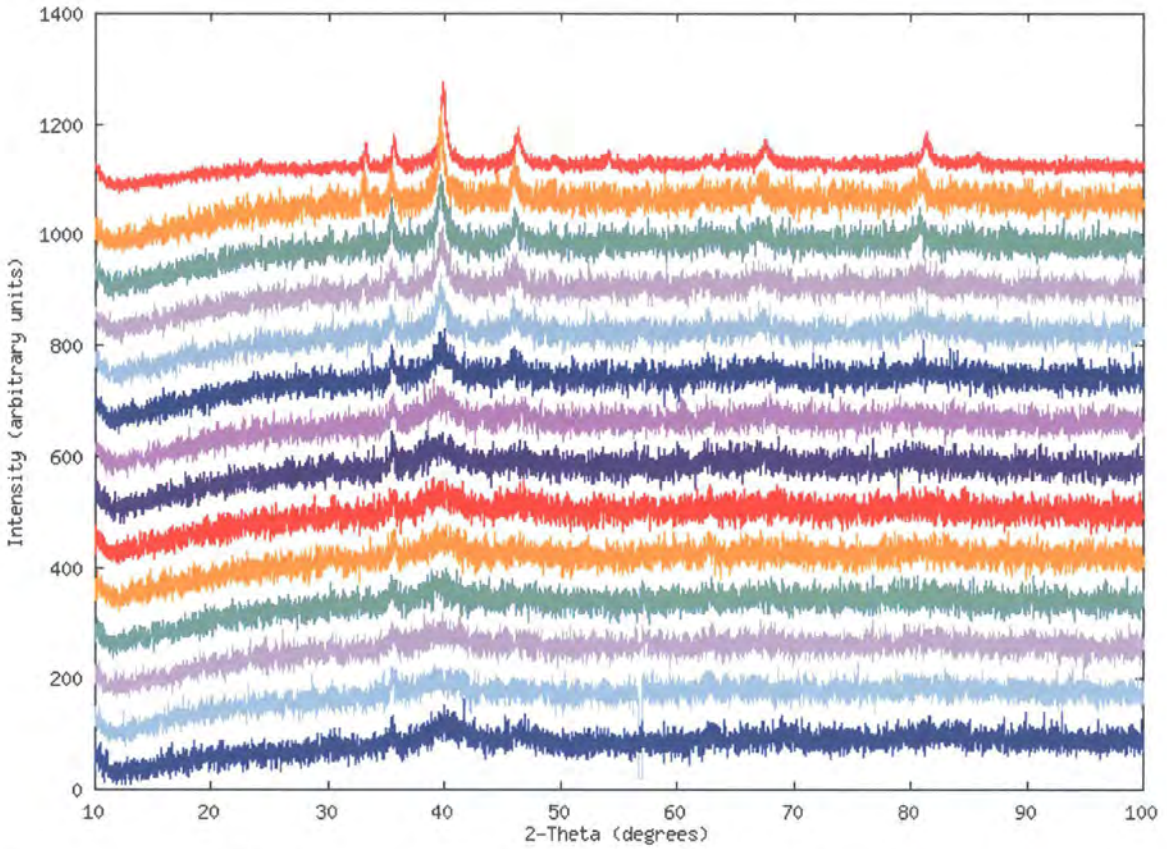

Figure 3.6 A set of variable temperature X-ray diffraction data obtained to follow the annealing process of sample LEMH 014. Each scan was for thirty minutes. A room temperature scan was obtained first, then four scans at each of the following temperatures: 693, 718, 743, 768, 793, 818, 843, 868, 893, 918, 943 and 968 K. Only one scan at each temperature is present.

The diffraction experiments in **figure 3.6** were performed under vacuum. The data do show, however, that using this methodology phase transitions of small samples of nanoparticles can be followed. In **figure 3.6** the broad diffraction peaks of as-synthesised FePt are clearly visible in the room temperature scan (the lowest data set which is blue). On heating to 968 K the appearance of sharper peaks can be readily observed. These peaks first emerge at ~793 K. In the final scan recorded after cooling the sample to room temperature the presence of crystalline iron oxide and platinum can be readily observed. Future experiments were performed under reducing conditions (Ar/H_2 5 %) in order to limit, or eliminate, the production of iron oxide.

3.2.6 *Ex-Situ* Annealing

It is also possible to observe the annealing process of iron platinum nanoparticles by annealing the sample for a set amount of time at a set temperature and then obtaining X-ray diffraction data before annealing again at a different temperature.

A sample (LEMH 035) was annealed ex - situ under an atmosphere of 5 % hydrogen/95 % nitrogen. A sample of LEMH 035 was mounted on a fused silica disk and placed in a glass boat before being placed in a tube furnace. The sample was annealed for thirty minutes at 450, 500, 550 and 600 °C. **Figure 3.7** shows the Rietveld refinement of the as-synthesised material whilst **figure 3.8** shows the Rietveld refinement of the material after being annealed at 600 °C.

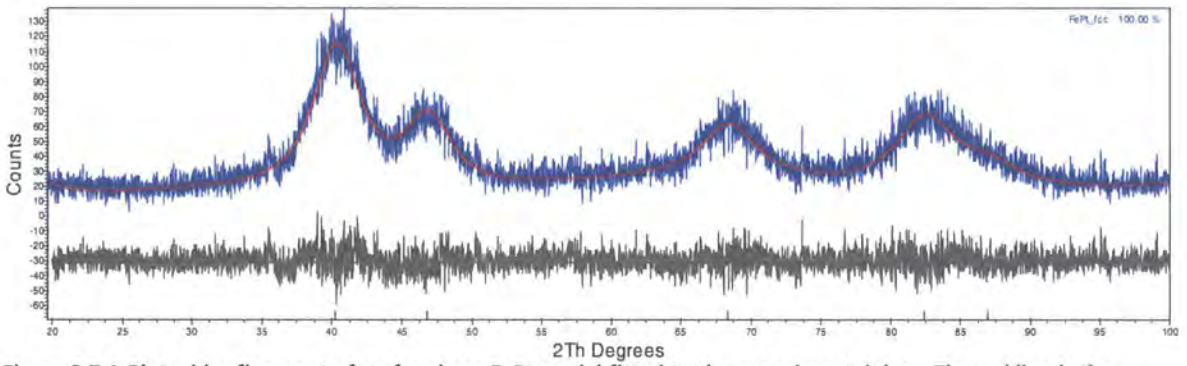

Figure 3.7 A Rietveld refinement of an fcc phase FePt model fitted to the experimental data. The red line is the fit of the model to the data and the grey is the difference between the model and experimental data.

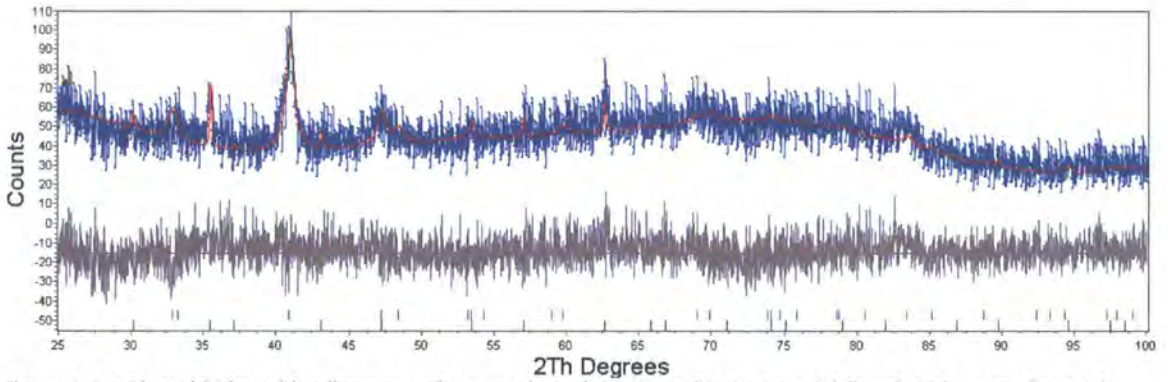

Figure 3.8 A Rietveld Rietveld refinement of a two-phase fcc FePt and Fe3O4 model fitted to the experimental data. The red line is the fit of the model to the data and the grey is the difference between the models and experimental data.

Details of the refinement presented in **Figure 3.8** are contained in **table 3.3**:

Parameter	Iron platinum (fct)	Iron oxide
Lattice Parameters (Å)	a = 3.84 (3); c = 3.76 (5)	8.39 (4)
Rwp (%)	17	17
Crystallite size (nm)	15.0 (0)	200.4 (1)
Height adjustment (mm)	-0.046 (4)	-0.046 (3)

Table 3.3 A table showing details of the Rietveld refinement presented in figure 3.8.

Figure 3.8 shows a Rietveld refinement with fct iron platinum and iron oxide as the structural models. The fit of the overall model to the experimental data is reasonable considering the poor signal to noise ratio of the data. Therefore the annealing process has happened as expected, with the iron platinum undergoing a phase transition from an fcc phase to the more chemically

ordered fct phase. However, there is some iron oxide present in the post-annealed sample. This is most probably also present in the as-synthesised sample.

3.3 FePt Synthesis via the Durham Route

3.3.1 Synthetic Strategy

It is potentially possible to effect a stoichiometrically controlled synthesis of FePt nanoparticles using Collman's reagent, $Na_2Fe(CO)_4$[2, 3]. This reagent is capable of directly reducing $Pt(acac)_2$ – formally the iron is in a 2- oxidation state, meaning it can reduce the Pt(II), negating the need for a third reagent – 1,2 – hexadecanediol in the case of the method developed by Sun *et al.*. The reaction can be formally written as in **equation 3.1**.

$$Fe^{2-} + Pt^{2+} = FePt \quad (3.1)$$

For this reason, near 1:1 stoichiometry should be achieved. This is important because the magnetically interesting fct FePt only forms over an $Fe_{1-x}Pt_x$ range where x~0.4 – 0.6. Equally important is the fact that in this reaction, the key reduction step that leads to FePt binary alloy nanoparticle formation requires the simultaneous presence of Fe^{2-} and Pt^{2+} ions; this should ultimately lead to the product alloy being intimately mixed on an atomic scale.

In a typical synthesis platinum acetylacetonate (71.6 g, 0.182 mmol) and oleylamine (0.06 cm^3, 0.182 mmol) were added to THF (10 cm^3). The reaction mixture was heated to reflux temperature yielding a yellow solution. $Na_2Fe(CO)_4$ (0.063 g, 0.182 mmol) was dissolved in THF (10 cm^3) yielding a brown-crimson solution with some solid present. The resulting mixture was transferred to the reaction mixture containing platinum acetylacetonate and THF. The resulting solution was then heated to reflux temperature for thirty minutes and the black-brown solution left to cool. Ethanol (40 cm^3) was added and the solution was centrifuged yielding a black solid. The brown-orange supernatant was decanted off then oleylamine (0.5 cm^3), hexane (25 cm^3) and ethanol (20 cm^3) were added to the black solid and the solution centrifuged. The clear orange supernatant was decanted off and the resulting black-brown precipitate was dried and collected.

In initial syntheses, the Collman's reagent was suspended in THF under argon whilst in a second vessel the platinum salt was dissolved in a solution of THF and oleylamine. This solution was heated to reflux temperature before transferring the Collman's reagent solution via cannula.

Sample	Mass of Collman's Reagent (g)	Mass of Pt(acac)2 (g)	Volume of Oleyl Amine (cm3)	XRD experiment code
LEMH 047	0.063	0.716	0.06	d5_04852
LEMH 050	0.140	0.159	0.14	d5_04865
LEMH 051	0.137	0.156	0.14	d5_04872
LEMH 052	0.570	0.648	0.54	d5_04888
LEMH 053	0.517	0.586	None	d5_04889
LEMH 054	0.416	0.473	None	N/A
LEMH 055	0.464	0.527	None	N/A
LEMH 056	0.798	0.907	0.08	N/A
LEMH 057	0.193	0.219	0.18	N/A
LEMH 067	0.1	0.114	0.1	d5_05119
LEMH 068	0.1	0.114	0.1	d5_05122
LEMH 069	0.1	0.114	0.1	d5_05123
LEMH 070	0.1	0.114	0.1	d5_05129

Table 3.4 A table detailing reagent masses and sample information for all syntheses performed using the Durham method.

3.3.2 Results and Discussion

An initial proof of principle reaction was performed in a qualitative manner which meant that the ratio of iron to platinum was not 1:1 initially; implying that the composition of FePt collected would not be 1:1. However, it meant that the suitability of this methodology for the synthesis of FePt nanoparticles could be rapidly obtained.

3.3.3 X-Ray Powder Diffraction

An X-ray powder pattern of the first sample made using this method (LEMH 047) was obtained. A Rietveld refinement of the experimental data was performed. In total 13 parameters were refined. These were 9 background terms, a scale factor, lattice parameter, crystallite size and temperature factor. The model was of an fcc FePt phase. This can be seen in **figure 3.9**. Data obtained from the refinement are tabulated in **table 3.5**.

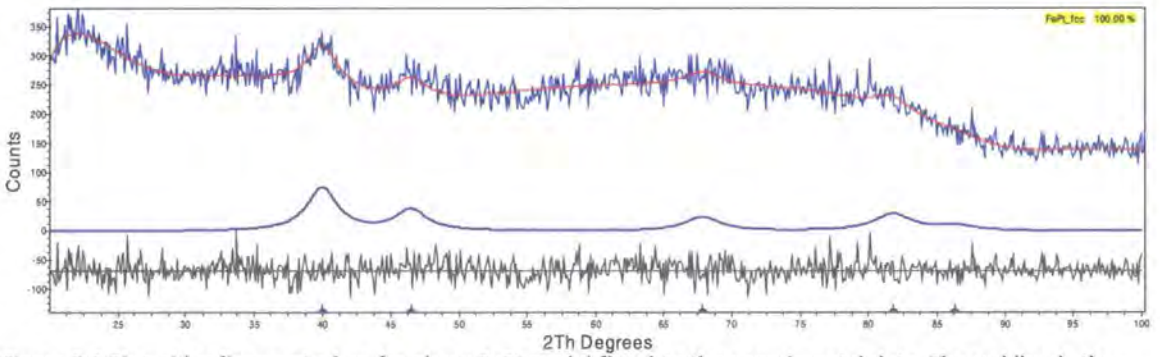

Figure 3.9 Rietveld refinement of an fcc phase FePt model fitted to the experimental data. The red line is the fit of the model to the data, the jagged blue curve is the experimental data, the smooth blue curve (the middle curve) is the model data and the grey is the difference between the model and experimental data.

Parameter	Value
Lattice Parameter	a = 3.90 (1) Å
Rwp *%)	7
Crystallite size	3.6 (6) nm
Height adjustment	0.0 (3) mm

Table 3.5 Data obtained by a Rietveld refinement of LEMH 047.

It can be seen from **figure 3.9** that the model data fits reasonably well with the experimental data obtained. Peaks in the powder pattern correspond to those expected for an fcc disordered Fe_xPt_y phase, suggesting the formation of metal nanoparticles. The experimental peak widths are consistent with nanosized particles.

The second to fifth samples made via this method all gave diffraction data that showed no FePt to be present. Further samples made had the same appearance as these – an orange/ brown powder with visually non-uniform particles – as opposed to the fine black powders of FePt. **Figure 3.10** and **figure 3.11** below show the diffraction patterns obtained for the second and third samples made via this method (LEMH 050 and LEMH 051). The diffraction patterns in **figure 3.10** and **figure 3.11** are very different to those presented previously. It is difficult to determine what the samples are composed of but FePt is not obviously present.

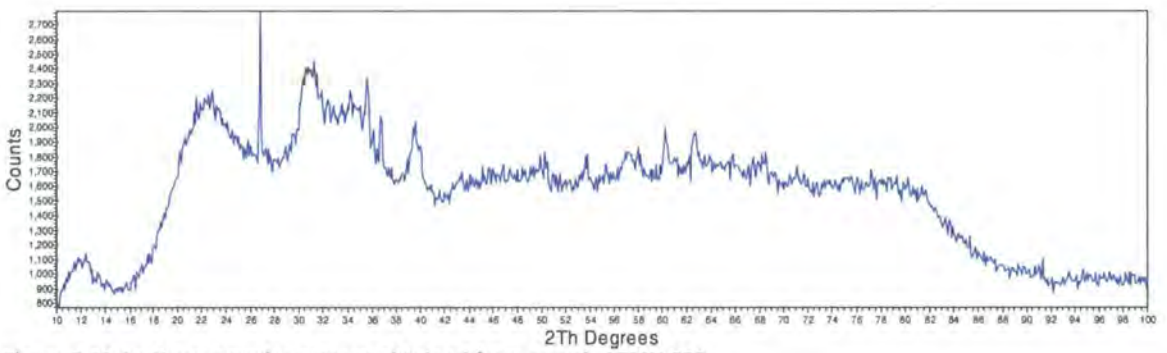

Figure 3.10 An X-ray powder pattern obtained from sample LEMH 050.

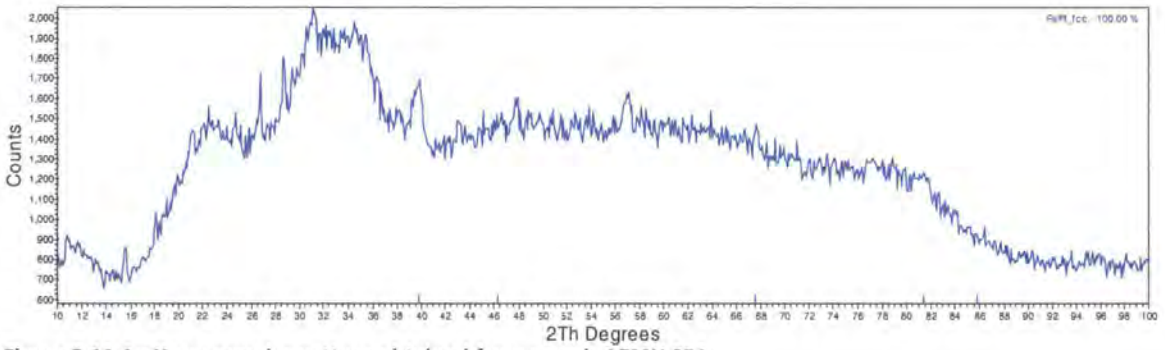

Figure 3.11 An X-ray powder pattern obtained from sample LEMH 051.

The synthetic method was then adjusted to try and produce FePt particles as achieved in the first test reaction (LEMH 047). The Collman's reagent and $Pt(acac)_2$ were pre-weighed in a glove box and mixed in a round bottom flask which was closed to the atmosphere. This was then integrated into the reaction system, whilst being kept under an inert atmosphere so as to avoid oxygen contamination. The reaction was then continued following the method previously stated. This procedure was intended to ensure a stoichiometric ratio of reducing agent to oxidising agent in the reaction mixture. Similar results to those obtained previously in attempts two to nine were obtained; i.e. no FePt was synthesised.

A further change to the experimental method was performed in which dioctyl ether was used as the solvent in place of THF. This allowed higher temperatures to be used. By conducting the synthesis at ~ 300 °C (reflux temperature of the dioctyl ether), a black powder was produced which could be suspended in hexane and flocculated in ethanol. X-ray diffraction data on four samples synthesised this way have been obtained and refined. The refinements are shown in **figure 3.12**. Data obtained from refinements of these data are tabulated in **table 3.6**. 17 parameters were refined in each refinement. These were 12 background terms, scale factor, lattice parameter, temperature factor, crystallite size and height correction. All models were based on an fcc FePt material.

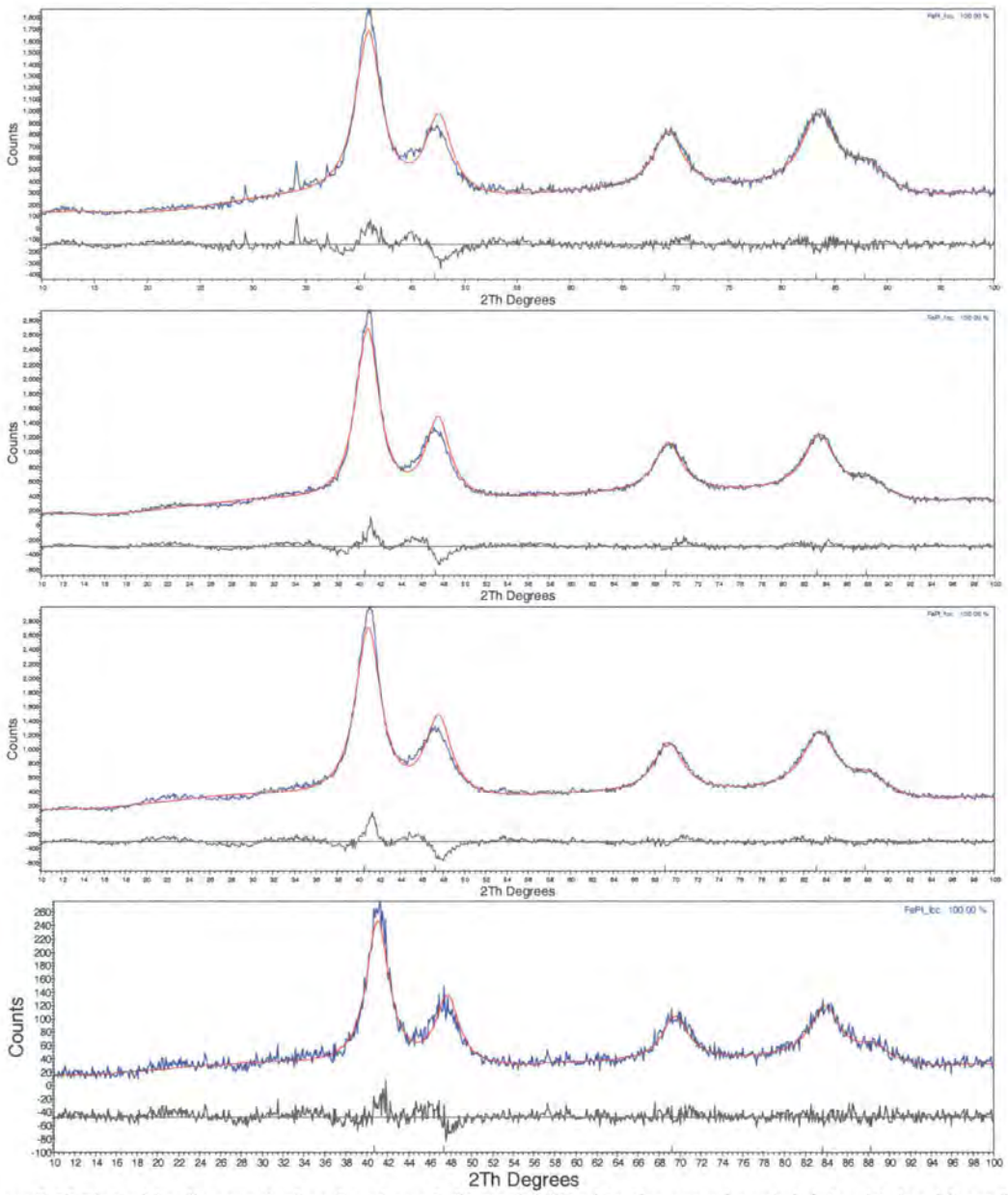

Figure 3.12 Rietveld refinement of an fcc phase FePt model fitted to the experimental data obtained from four separate FePt samples (LEMH 067, LEMH 068, LEMH 069 and LEMH 070). The red line is the fit of the model to the data, the blue curve is the experimental data and the grey is the difference between the model and experimental data.

Parameter	LEMH 067	LEMH 068	LEMH 069	LEMH 070
Lattice Parameters	a = 3.84 (7) Å	a = 3.84 (5) Å	a = 3.84 (7) Å	a = 3.83 (3) Å
Rwp (%)	8	7	8	15
Crystallite size (nm)	3.231 (5)	3.54 (6)	3.29 (9)	3.57 (5)
R Bragg (%)	2	1	1	1
Height correction (mm)	-0.53 (0)	-0.34 (5)	-0.51 (2)	-0.47 (7)

Table 3.6 Data obtained by Rietveld refinement of X-Ray diffraction data obtained from LEMH 067, LEMH 068, LEMH 069 and LEMH 070.

It is clear from **figure 3.12** and **table 3.6** that colloidal metal particles have been prepared with diffraction data consistent with samples produced via the polyol procedure[1]. These samples have been prepared via a straightforward route involving minimally volatile/liquid toxic metal reagents. This method of synthesis is reproducible.

3.3.4 Rutherford Backscattering (RBS)

Rutherford Backscattering is a technique which allows the composition of a sample to be analysed. A RBS experiment was conducted to analyse the composition of the first sample made via the Collman's reagent method (LEMH 047). The data obtained are shown in **figure 3.13** and **figure 3.14**, with the experimental data modelled with a 1:1 iron to platinum ratio and then a refined ratio of iron to platinum. All RBS data and model fits were performed by Dr Richard Thompson.

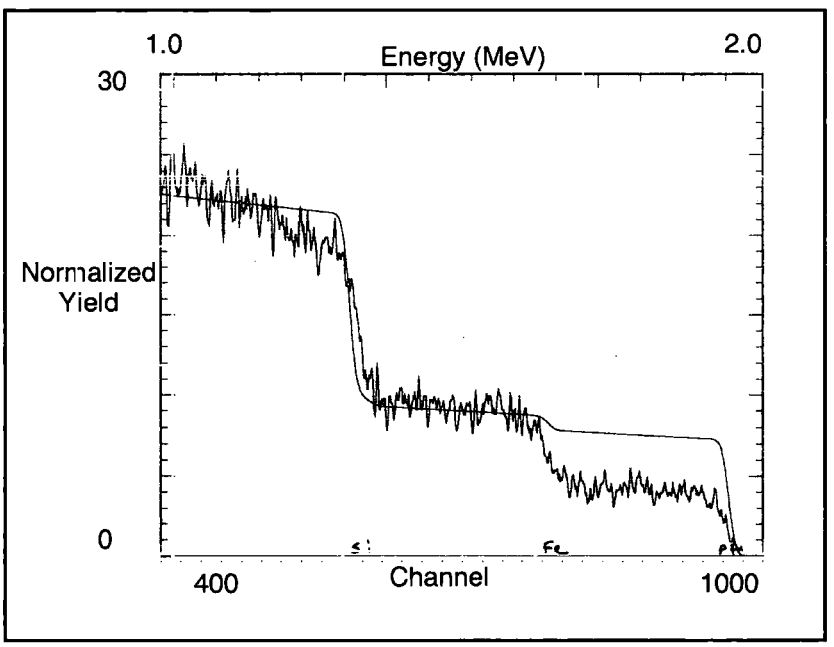

Figure 3.13 A graph showing the RBS data obtained and modelled as a 1:1 ratio of iron to platinum. The solid line is the fit of the model to the data.

Firstly a model of 1:1 iron to platinum was fitted to the data. The fit was very poor and it was concluded the sample did not have a ratio of 1:1 iron to platinum (**figure 3.13**). By varying the ratio and examining the fit to the data it was concluded that the ratio of iron to platinum was around 10:1 (**figure 3.14**). This was thought to be consistent with the small cell parameter of this sample compared to later samples.

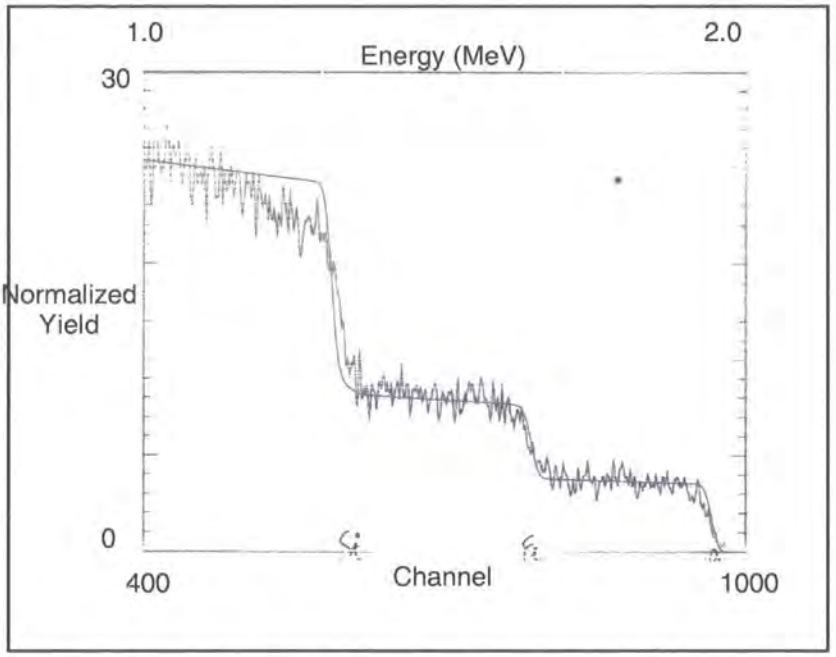

Figure 3.14 A graph showing the RBS data obtained with the ratio of iron to platinum found to be 10:1. The sharp line is the fit of this calculated model to the data.

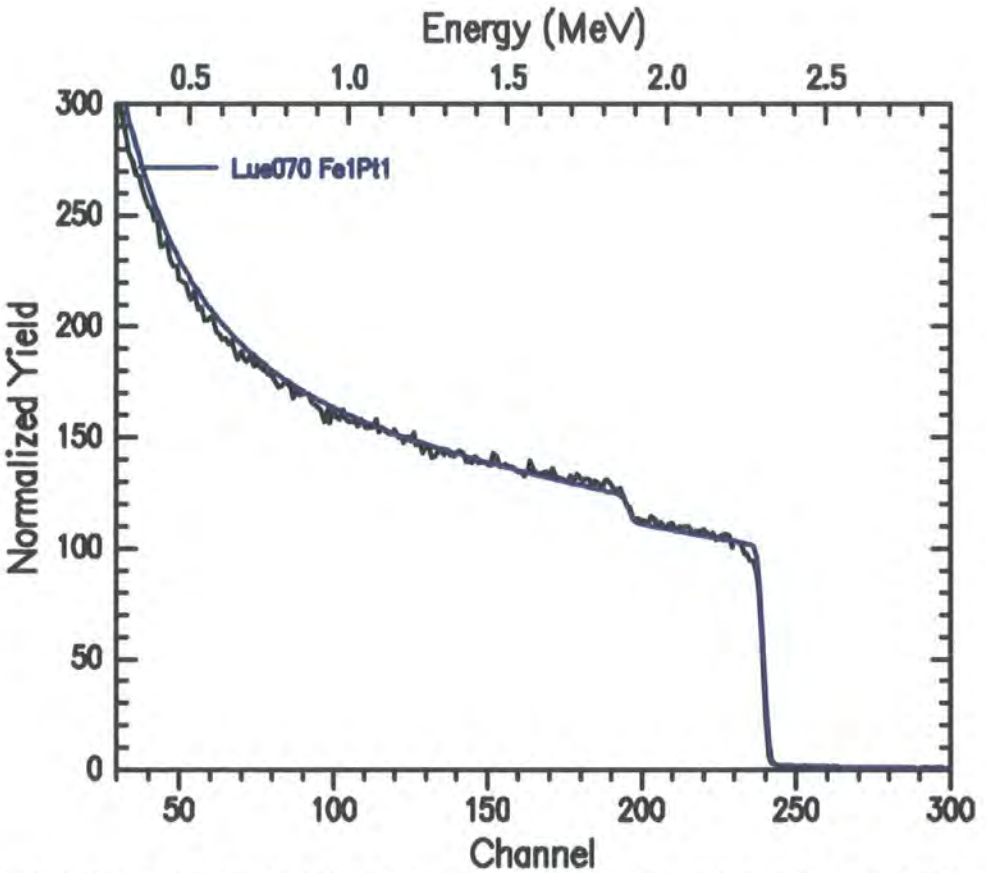

Figure 3.15 A graph showing the RBS data obtained from sample LEMH 070. An FePt 1:1 model (blue curve) is fitted to the data (black curve).

Obtaining RBS data on sample LEMH 070, which by XRD was FePt in the fcc phase, showed that the composition was 1:1 iron to platinum.

3.4 References

1. S. H. Sun, C. B. Murray, D. Weller, L. Folks and A. Moser, *Science*, 2000, **287**, 1989-1992.

2. J. P. Collman, *Accounts of Chemical Research*, 1975, **8**, 342-347.

3. J. P. Collman, R. G. Finke, J. N. Cawse and J. I. Brauman, *Journal of the American Chemical Society*, 1977, **99**, 2515-2526.

Chapter 4 – Methodology for the Rietveld Refinement of Variable Temperature X-ray Diffraction Parameters

4.1 Introduction

In this chapter a systematic investigation into the Rietveld refinement of variable temperature X-ray diffraction (VTXRD) data of iron platinum nanoparticles is described. **Section 4.1** describes a typical VTXRD study from conception to conclusion. Details of the experimental procedures and the Rietveld refinement processes are given. **Section 4.2** details an "ideal" iron platinum nanoparticle in-situ annealing experiment, and the information such an investigation can yield. **Section 4.3** applies the information learnt in **section 4.2** to an actual iron platinum nanoparticles experiment and **section 4.4** draws conclusions as to the optimal methodology for these studies.

4.2 A Typical *In-Situ* Variable Temperature X-Ray Diffraction Study of FePt

4.2.1 Experimental Details

FePt (sample LHN060) was prepared via the method detailed in **section 3.3**.

In-situ variable temperature X-ray diffraction data on FePt were collected using a Bruker d8 diffractometer equipped with a Cu X-ray tube, a Ge(111) incident beam monochromator (λ = 1.5406 Å), and an MBraun linear position sensitive detector. High temperature measurements were performed using an Anton Parr HTK1200 (**figure 4.1**) high temperature furnace (operating range 298 to 1473 K). The powdered sample was mounted on a circular silica disk with silicone vacuum grease smeared on top to act as an adhesive. A 1 ° divergence slit was used and VTXRD data were collected over the temperature range of 303 – 903 – 303 K. Measurements (50 in total) were recorded every 25 K (58 minutes each, with a 0.2 Ks-1 heating/cooling rate between temperatures, a 2θ range of 10 – 130 °, and a step size of 0.0359 ° 2θ) over 48 hours. The 50 diffraction patterns that comprise the measurement d8_02575 are shown in **figure 4.2**. A flow of 5 % Hydrogen and 95 % Argon gas was passed through the furnace and over the sample for the duration of the measurement.

Figure 4.1 A photograph of the Anton Parr htk1200 furnace mounted on the Bruker d8 diffractometer.

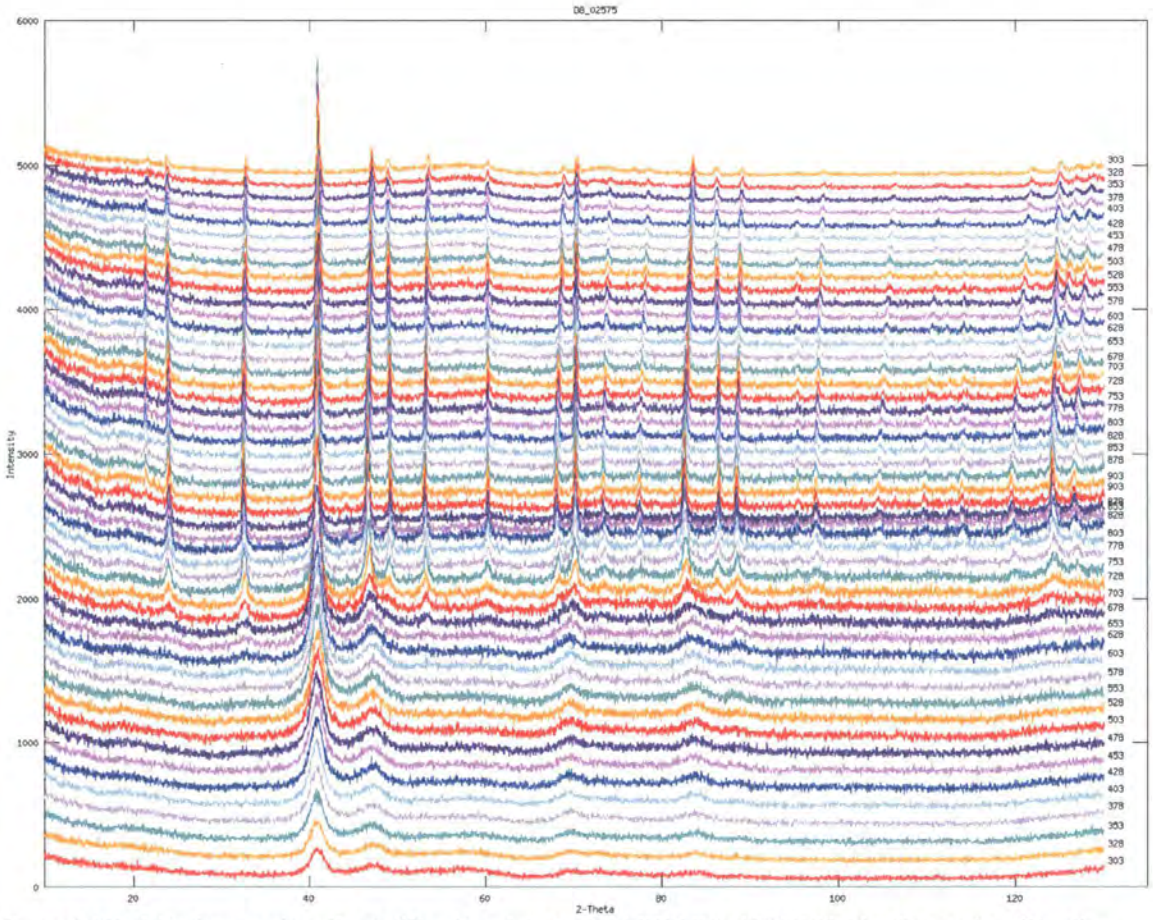

Figure 4.2 Variable temperature X-ray diffraction data for FePt (LHN060, d8_02575). The 50 powder diffraction patterns shown are from 303 K (base of figure) to 903 K (centre of figure) and to 303 K (top of figure) in 25 K steps. Patterns have been offset vertically for clarity and are on the same absolute scale.

As-synthesised nanoparticles of FePt typically exhibit the chemically disordered fcc structure (this can be seen at 303 K in **figure 4.2**). Controlled thermal annealing initiates an irreversible internal structural transition resulting in FePt nanoparticles in the fct phase with long-range chemical order. This is indicated by the formation of the characteristic (001) and (010) superlattice peaks at around 24 ° 2θ and 33 ° 2θ respectively. These peaks begin to appear at around 600 K but narrow and sharpen as the temperature is increased to 903 K. This is consistent with the fct

phase of FePt being thermodynamically stable with respect to the fcc phase. The as-synthesised fcc phase is kinetically stable with respect to the fct phase below ~ 600 K in the case of this sample. Peak sharpening shows particle size grows with increasing temperature.

4.2.2 A Typical Rietveld Refinement of FePt VTXRD Data

A Rietveld refinement was performed on VTXRD data collected on sample LHN060 (d8_02575). In total 25 parameters were refined. These were 18 background terms, a sample height correction, a scale factor for the phase, 2 lattice parameters (*a* and *c*), crystallite size, fractional occupancy and an atomic displacement parameter (temperature factor). The data were refined using Multitopas methodology as described in **chapter 2**. Graphs detailing the variation as a function of temperature of the important parameters are shown in **figures 4.3a – 4.3h** (in each the closed red squares show data collected on warming, and the closed blue triangles show the data on cooling).

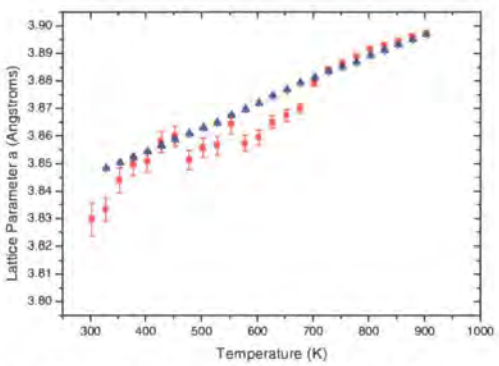

Figure 4.3a Refined lattice parameter a as a function of temperature.

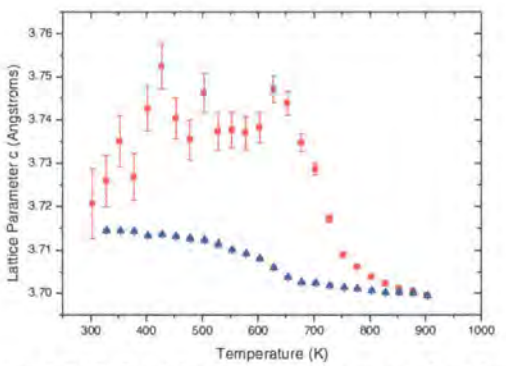

Figure 4.3b Refined lattice parameter c as a function of temperature.

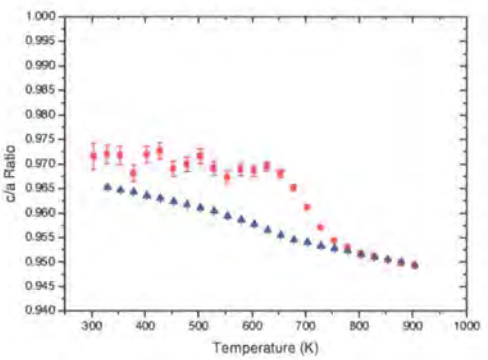

Figure 4.3c c/a lattice parameter ratio as a function of temperature.

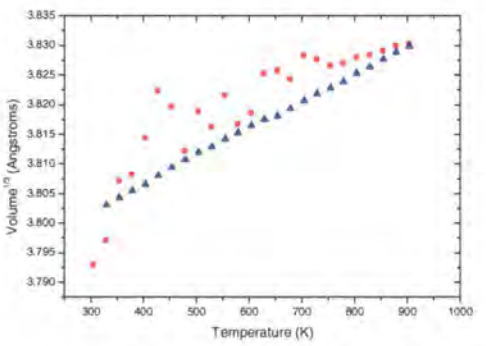

Figure 4.3d Volume of unit cell as a function of temperature.

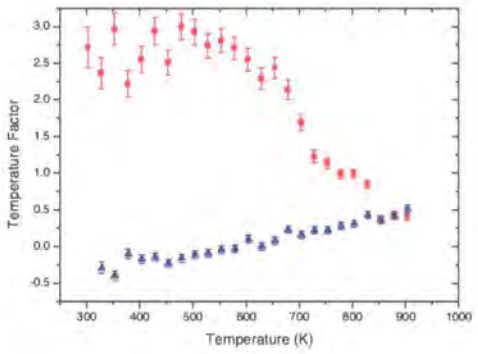

Figure 4.3e Refined temperature factor as a function of temperature.

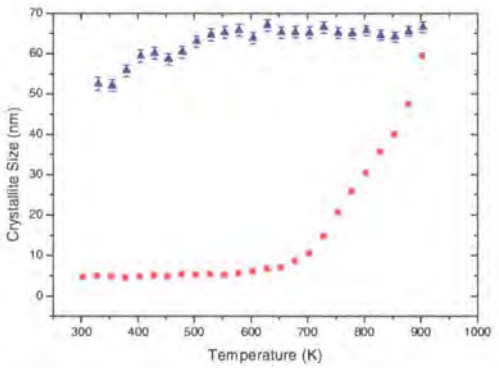

Figure 4.3f Refined crystallite size as a function of temperature.

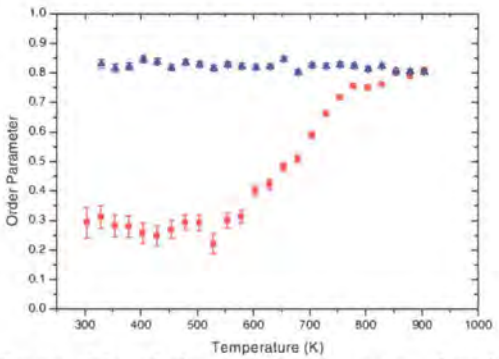

Figure 4.3g Order parameter as a function of temperature.

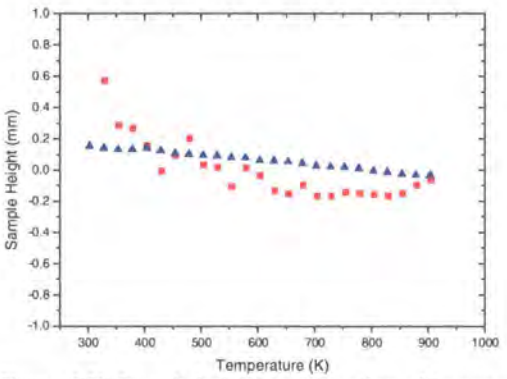

Figure 4.3h Sample height as a function of temperature.

On annealing, FePt nanoparticles undergo an irreversible structural transition whereby they convert from the chemically disordered fcc phase to the chemically ordered fct phase. During the annealing process three main things alter: one, the unit cell changes from cubic to tetragonal, two, atomic sites become chemically ordered; and finally the crystallite size changes.

Figures 4.3a to 4.3d yield information relating to the change of unit cell dimensions as a function of temperature. To interpret these data it is important to remember that below the fcc to fct phase transition the FePt material is cubic. The individual values of *a* and *c* have no real meaning. Given a highly crystalline material it would be expected that these would refine to similar values. However, for a material with peaks as broad as those seen in **figure 4.2** (where the fwhm is ~ 2 ° 2θ at 303 K) these values are highly correlated and therefore cannot be refined independently reliably. For this reason it is more useful to adopt the volume$^{(1/3)}$ (**figure 4.3d**) as an indicator of the thermal expansion of FePt. As the material undergoes the fcc to fct transition on warming, the individual values of a and c become better defined. The c parameter undergoes a sharp decrease paralleled by a decrease in the *c/a* ratio, and therefore the overall cell volume. This can be explained for an order-disorder transition of this type by thinking in terms of packing

efficiency. In a disordered material the packing of the Fe and Pt atoms is less efficient than can be achieved in an ordered material where the atoms alternate Fe:Pt:Fe:Pt (small:big:small:big). The size of the larger atom determines the inter-layer separation. In the ordered material you can have the layers offset for efficient packing. This would not be possible in a disordered material:

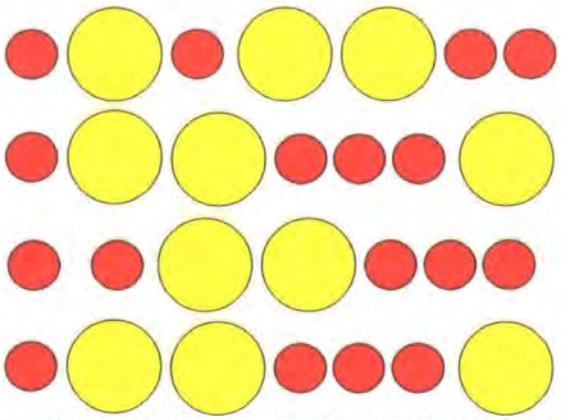

Figure 4.4 A schematic showing the packing in a disordered FePt material. Small circles represent Fe and large circles Pt

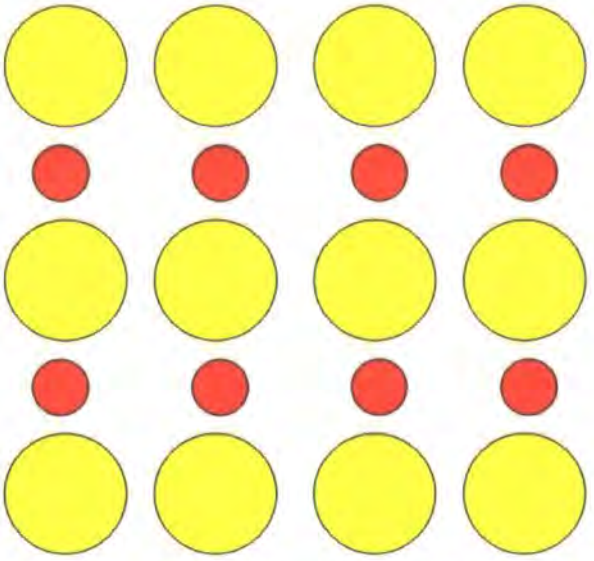

Figure 4.5 A schematic showing the packing in an ordered FePt material.

On cooling a clear change in cell parameters occurs at ~ 630 K. This is most probably related to a magnetocrystalline effect at the Curie temperature and has also been observed in bulk alloys (the Curie temperature of FePt is ~ 710 K[1]).

The final cell parameters of a = 3.84 (7) angstroms, c = 3.71 (4) angstroms and the c/a ratio of 0.96 compares to literature values of a = 3.85 (5) Å, c = 3.71 (1) Å and c/a = 0.96 (2)[2, 3].

The order parameter (**figure 4.3h**) also changes considerably during the phase transition. This parameter is determined by the presence or absence of superlattice reflections (e.g. those at ~ 24

and 33 ° 2θ) indicating ordering. At the beginning of the experiment these are absent leading to a poorly defined order parameter. Due to the low degree of ordering, the small particle size (leading to broad peaks) and the slowly undulating background it is hard to determine the intensity of the superlattice peaks. This is expressed by the large estimated standard deviations of the order parameter in the early stages of the experiment. Refined values of the order parameter of < 0.3 are not statistically significantly different from those when the order parameter is 0.0. From ~ 550 K to ~ 900 K the order parameter increases greatly from ~ 0.3 to ~ 0.8. Interestingly this ordering occurs before 650 K, the temperature at which the unit cell dimensions and crystallite size began to alter. On cooling the order parameter remains at ~ 0.8, indicating the ordering is permanent.

On annealing, sintering of the nanoparticles can occur, and as the temperature increases sintering actually increases. It can be seen in **figure 4.3f** that no significant size increase occurs until ~ 650 K at which point the sample rapidly increases in size from ~ 5nm to ~ 66 nm at 900 K. On cooling no size change occurs until ~ 510 K. The apparent size then decreases to ~ 53 nm at room temperature. This is an artifact of the sample height variation encountered during VTXRD experiments. Allen[3] showed that when performing VTXRD experiments on a Bruker D8 Advance diffractometer the sample height varies. This is due to thermal expansion effects of the furnace. Such effects are probably only significant on cooling of the sample. When particle size is small, and the peaks are broad, on warming the instrumental contribution to peak shape and its changes with temperature are less important. The size change is permanent. This indicates that $(53/4.6)^3 \approx 2110$ nanoparticles have fused upon annealing.

Typically, as thermal energy increases, the temperature factors for a material would increase gradually due to the increase in atomic vibrations. However, in **figure 4.3e**, on warming, it can be seen that the temperature factors are ~ 2.5-3 angstroms^2 and decrease sharply from ~ 650 K to ~ 900 K, where the value is ~ 0.4. Before the fcc to fct phase transition at ~ 650 K, the large temperature factors can be explained by the large amount of static disorder in the chemically disordered fcc phase and/or are a function of the small particle size which leads to a high proportion of surface atoms. After the transition, the temperature factors are much smaller as the degree of static disorder is much lower. This can also be seen by the steady decrease in the temperature factor value on cooling, as would be expected with a decrease in thermal energy. At room temperature after annealing the temperature factor is slightly negative. This is due to the surface roughness of the sample used which leads to artificially high intensities at high angles and is a well known phenomenon in Bragg-Brentano diffraction experiments.

4.2.3 Conclusion

In this section a typical VTXRD study into the structural changes of FePt upon annealing has been described from the data collection to the Rietveld refinement and analysis. It has been shown

that the fcc to fct phase transition can be observed by such methods. However, the study also provides a number of surprising results, e.g. the decrease of the temperature factors as a function of temperature and the refined crystallite size changing due to changes in sample height. These highlight the difficulty in determining certain parameters due to either unavoidable limits in the data, possible correlations between two or more variables or experimental and/or instrumental factors. Since a major portion of the work presented in this thesis is based upon these types of analyses, further test studies were performed on a simpler system. The simpler system chosen was a sample of fct phase FePt which had been heated to a sufficiently high temperature such that it was fully ordered in the fct phase and would therefore undergo no further changes in peak width due to sample sintering. The aim was that such a sample would yield valuable information about a variety of factors, for example the expected temperature dependence of temperature factors for FePt.

4.3 Bulk FePt VTXRD Experiment – Influence of Instrumental Factors

4.3.1 Introduction and Experimental Details

A sample of FePt already in the fct phase was measured to provide further insight into the limitations of VTXRD studies. This material was prepared initially by Dr. L. Nguyen and then annealed in a VTXRD experiment as described in **section 2.1.1**. Sixty-four measurements were made in total. Initially 12 measurements, each one hour long, were made at 903 K to ensure the sample had fully transformed to the fct phase. A further 4 measurements were then made at 303 K to ensure the sample reached equilibrium with its surroundings. The temperature was then increased to 903 K and then decreased to 303 K, with a diffraction pattern measured in 25 K intervals. The 64 diffraction patterns that comprise the measurement d8_02573 are shown in **figure 4.6**.

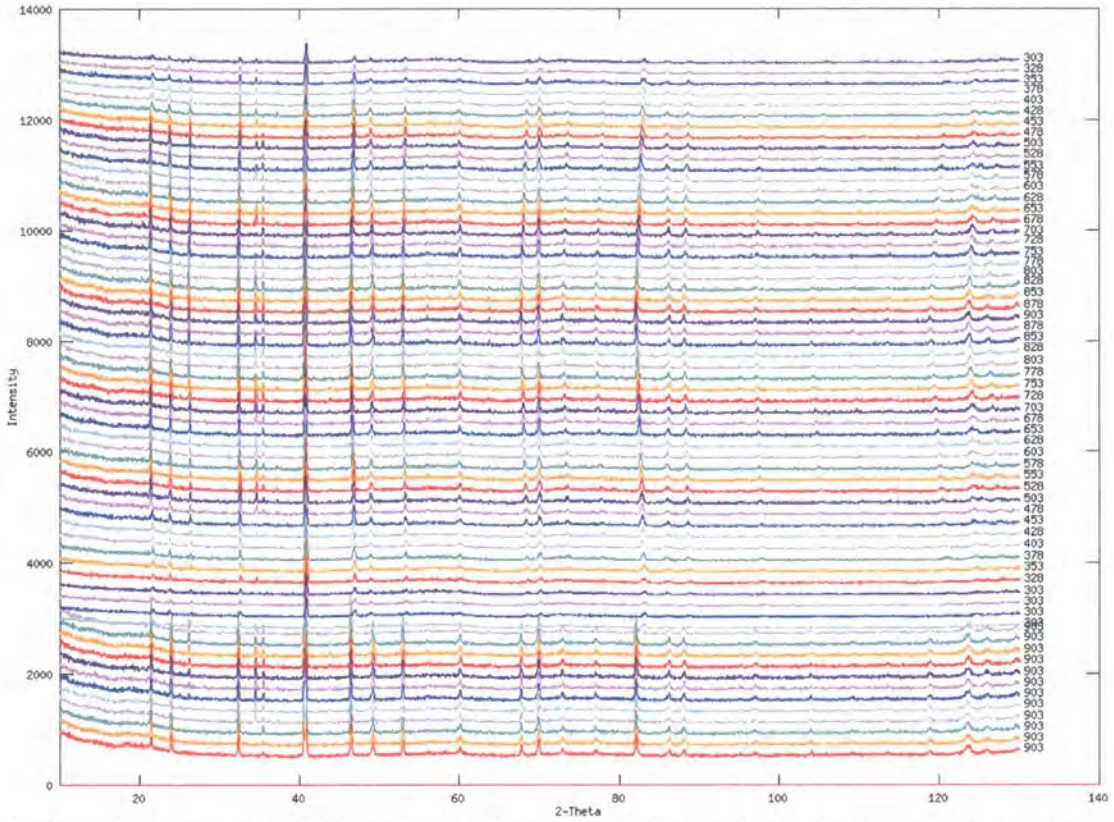

Figure 4.6 VTXRD data for FePt (d8_02573). 64 diffraction patterns are shown. The first 12 were recorded at 903 K, then the next 4 at 303 K. A measurement was then recorded in 25 K steps from 303 K to 903 K on warming and then 903 K to 303 K on cooling. Patterns have been offset vertically for clarity and are on the same scale.

As the data shown in **figure 4.6** were collected on a pre-annealed sample, very little change is observed in the diffraction patterns as the temperature varies. The (001) and (110) ordering peaks seen at approximately 24 ° and 32 ° 2θ are present in each measurement and neither the shape nor position of these peaks vary greatly with temperature. However, the intensity of the peaks does vary and is greater at higher temperature. This is a normal effect for the experimental set-up used and is related to the changes in sample height with temperature.

4.3.2 Parametric Methodology

Parametric methodology (or 'surface fitting') is an alternative way of performing Rietveld refinement that has been developed in the group. It is similar to multitopas methodology but it allows one to force parameters to vary in a prescribed fashion with temperature. This allows the investigation of the influence of parameter correlations on absolute values. For example, one of the most important pieces of information sought in an FePt VTXRD experiment is the temperature dependence of the order parameter (**4.3h**). However, parameters such as the temperature factor (**4.3e**) are also seen to vary considerably over similar temperature ranges to those in which the order parameter changes. As a result it is of great import to understand

whether the two parameters are correlated and influencing one another. If high quality VTXRD data could be obtained it should be possible to learn this directly from the correlation matrix. However, the data obtained from FePt experiments are often of an insufficient quality to rely on this approach.

The parametric methodology employed here allows each of the 50 diffraction patterns to be simultaneously fitted to a structural model in which certain parameters are constrained so as to follow a set temperature dependence. In this particular case the temperature factor has been constrained to depend on T according to **equation 4.1**.

$$U = U_0 + C/\{\exp(\theta/T) - 1\} \quad (4.1)$$

Where U is the temperature factor at a set temperature, U_0 is the temperature factor at 0 K, C is the refinable parameter and θ is Einstein temperature, here treated as a refinable parameter. All are refined from the data in this case.

In order to analyse the data the following processes were performed:

1. The VTXRD data presented in **section 4.4** were fitted using a standard Multitopas methodology of independent Rietveld refinements.
2. The VTXRD data were fitted parametrically to a model where the temperature factors were constrained according to **equation 4.1**.
3. The refinements obtained by way of parts one and two were compared for consistency.
4. The temperature dependence of the temperature factors in 2 was forced to behave in the way the experimental data in **section 4.1.3** do (i.e. forced to behave as would be expected for a bulk material which does not sinter). This was done in order to investigate the influence on important parameters of the temperature dependence of the temperature factors.

4.3.3 Data Analysis

Rietveld refinement of the VTXRD data was performed using both Multitopas methodology and parametric methodology. The relevant parameters obtained from these refinements are detailed in **figures 4.7a to 4.7g**. In all figures warming data refined by Multitopas methods are shown by closed red squares and parametric methods open red squares. For cooling, data refined by Multitopas methods are shown by closed blue squares and parametric methods open blue triangles.

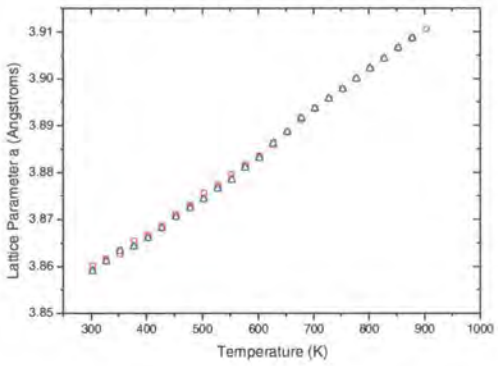

Figure 4.7a Lattice parameter a as a function of temperature.

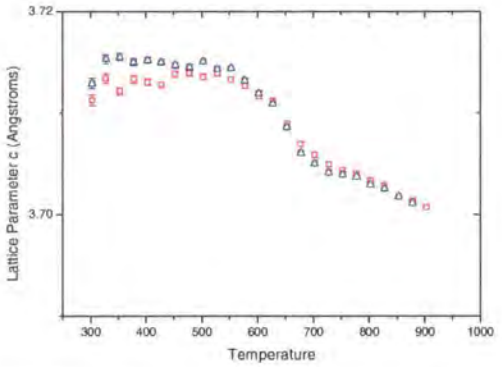

Figure 4.7b Lattice parameter c as a function of temperature.

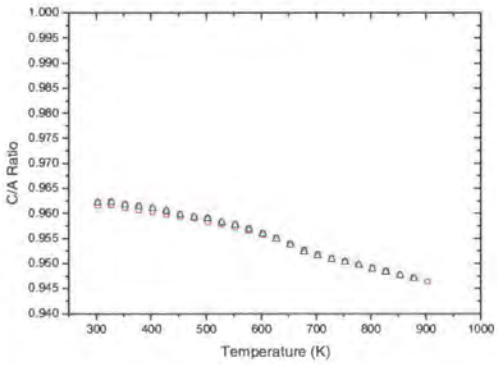

Figure 4.7c The c lattice parameter divided by the a lattice parameter ratio as a function of temperature.

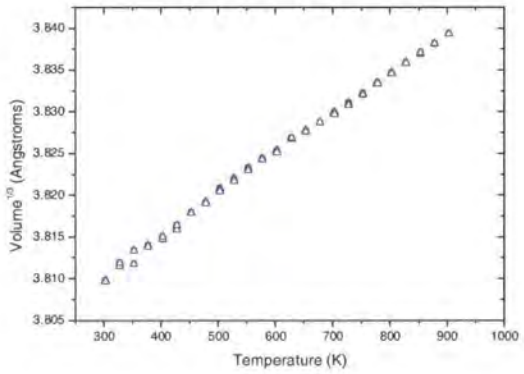

Figure 4.7d Volume1/3 as a function of temperature.

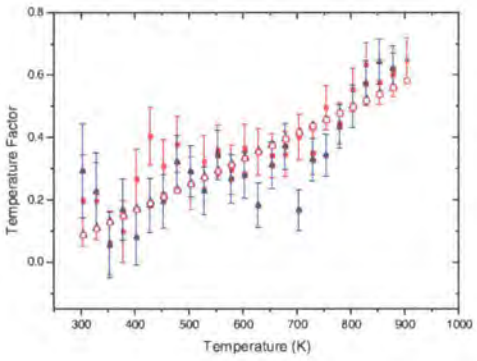

Figure 4.7e Rietveld refined temperature factors as a function of temperature.

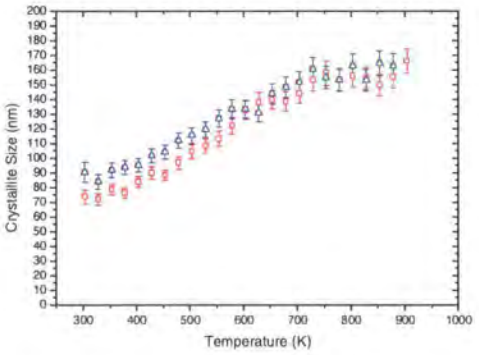

Figure 4.7f Rietveld refined crystallite size as a function of temperature.

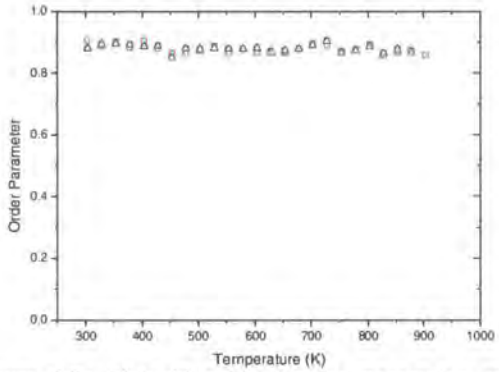

Figure 4.7g Rietveld refined order parameter as a function of temperature.

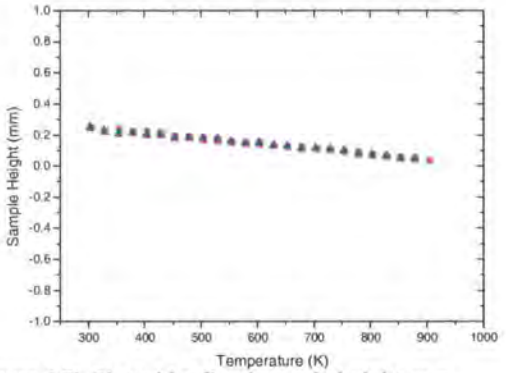

Figure 4.7h Rietveld refined sample height as a function of temperature.

It is clear from **figures 4.7a-4.7d** that no further structural changes occur after the sample has been annealed at 903 K for ~ 4 hours as the data before warming and after cooling match very closely. There is a marginal discrepancy in the refined warming/cooling c lattice parameter between 303 K and ~ 550 K. However, this is not apparent in the volume$^{1/3}$, or *c/a* ratio as shown in **figure 4.7d** and is probably within the true margin of error for these parameters.

All refined parameters obtained via Multitopas methodologies match those obtained via parametric methodologies; on both warming and cooling.

It should also be noted that the apparent crystallite size varies significantly during the experiment, with the size changing from ~ 70 nm to ~120 nm on warming and then back to ~70 nm on cooling. This can be explained by the changes in the sample height on warming and cooling. In the Rietveld refinement, the sizes of the crystallites are determined from the width of the X-ray peaks in the powder pattern. As the sample height changes on warming in the diffractometer, the sample moves from the ideal focus position. A small degree of sintering of the nanoparticles must have occurred though as the final crystallite size after the experiment is greater than before (~ 10 nm larger).

Figure 4.7e is of particular importance and will be used in **section 4.4**. It shows how one would expect the temperature factor of an 'ideal' FePt sample to vary with temperature. In particular its gradient (C = 0.194) will be imposed on refinements of data of **figure 4.2** to investigate possible correlations between temperature factors and order parameters.

4.4 Analysis of Nanoparticle VTXRD Using Parametric Methodologies

4.4.1 Introduction

In this section the same data collected in the experiment detailed in **section 4.1** (i.e. an fcc to fct transformation study) will be analysed, refined using three different methodologies. One, the Multitopas methodology as already described, two the parametric methodology with a fixed temperature factor gradient (the value used is that stated in **section 4.3.3**) and three, the parametric methodology with a temperature factor gradient which is free to refine but constrained to vary smoothly and have identical values on warming and cooling. By comparing the three sets of refined data, it will be possible to conclude whether the correlation between the temperature factors and order parameter observed in FePt VTXRD experiments, specifically that described in **section 4.1.4**, affects the other refined parameters or not.

4.4.2 Results and Discussion

The temperature factor refined using Multitopas methodology is clearly different to that obtained when using parametric methodology as can be seen in **figure 4.8**. However, whether the parametric methodology uses a fixed or freely refining temperature factor gradient, similar behaviour is observed. This is as the 'average' temperature factor at a given temperature happens to be close to the value of the bulk material in **figure 4.7e**. The temperature factors behave as expected in the parametrically refined data sets – a steady positive increase from low to high temperatures.

Figure 4.9 shows that regardless of the method used for refinement, the order parameter is approximately the same, when taking into account refinement errors. This gives confidence that the order parameter derived by this method is relatively robust.

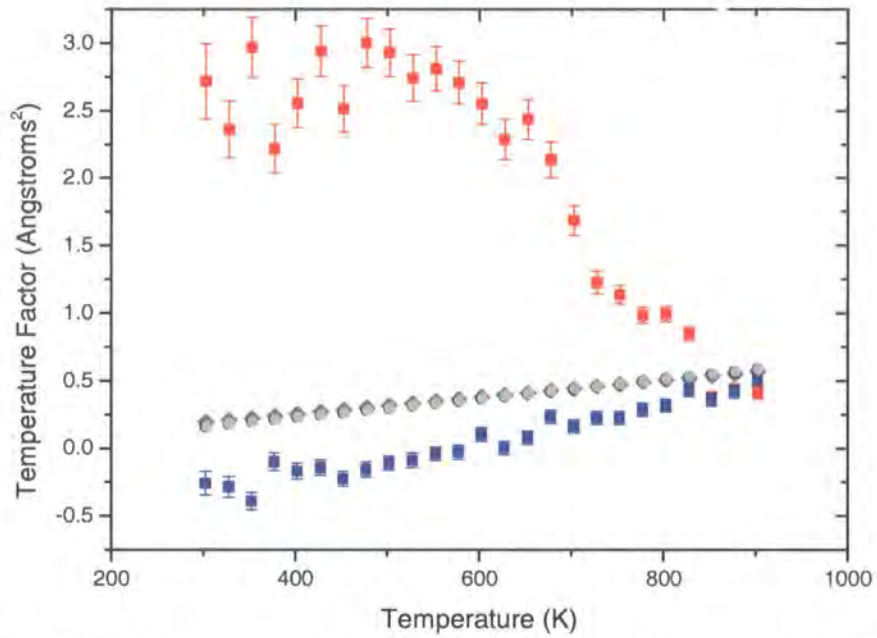

Figure 4.8 Rietveld refined temperature factors as a function of temperature. Warming data refined by multitopas methods (closed red squares), parametric methods with the temperature factor gradient fixed (closed black circles) and parametric methods with the temperature factor gradient free to refine (closed green diamonds). Cooling data refined by multitopas methods (closed blue squares), parametric methods with the temperature factor gradient fixed (closed grey circles) and parametric methods with the temperature factor gradient free to refine (closed pink diamonds).

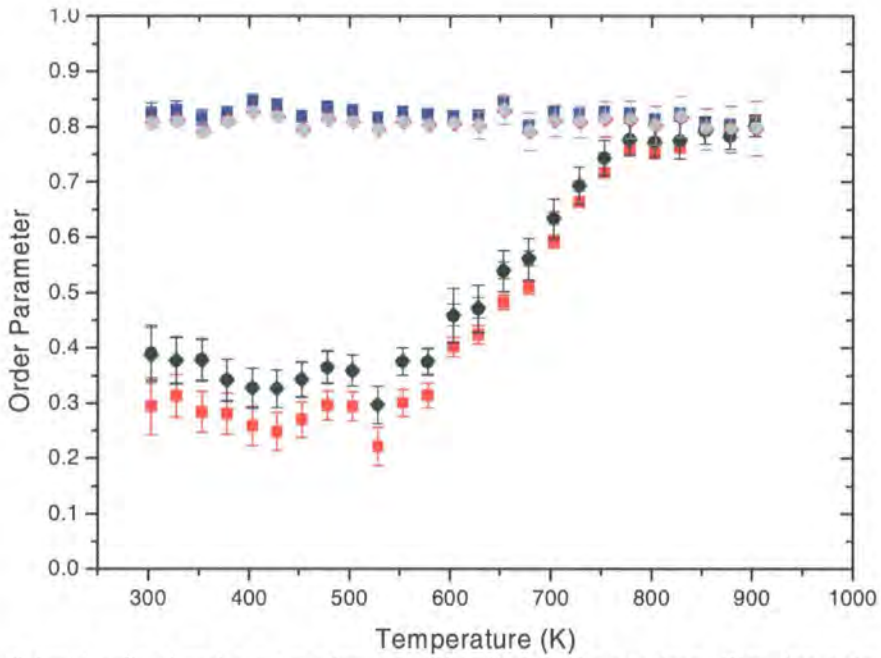

Figure 4.9 Rietveld refined order parameters as a function of temperature. Warming data refined by multitopas methods (closed red squares), parametric methods with the temperature factor gradient fixed (closed black circles) and parametric methods with the temperature factor gradient free to refine (closed green diamonds). Cooling data refined by multitopas methods (closed blue squares), parametric methods with the temperature factor gradient fixed (closed grey circles) and parametric methods with the temperature factor gradient free to refine (closed pink diamonds).

4.5 Conclusions

In this chapter it has been shown that by recording variable temperature X-ray diffraction data and performing Rietveld refinement on them, it is possible to obtain a large amount of useful information relating to the structure and properties of FePt nanoparticles. Most importantly this information includes the unit cell dimensions as a function of temperature, the order parameter and particle size. In addition the method allows the observation, as a function of temperature, of the fcc to fct phase transition which FePt nanoparticles undergo.

It has been shown that the refinement of VTXRD data can be performed using one of two methodologies: Multitopas, or Parametric refinement. The difference between the two is that Multitopas methodologies refine each measurement in a VTXRD study independently from all others, and refine all in succession. Parametric methodologies refine all measurements simultaneously. Parametric methodology was applied in order to determine whether the order parameter was influenced by its correlation with other parameters; this was shown not to be the case. Both methods result in refined order parameters of approximately the same magnitude. In effect, the analysis in this chapter confirms that results obtained by the refinement of VTXRD data using Multitopas methodologies can be trusted. This method will be used in **chapter 5** on a variety of samples.

4.6 References

1. S. Ostanin, S. S. A. Razee, J. B. Staunton, B. Ginatempo and E. Bruno, *Journal of Applied Physics*, 2003, **93**, 453-457.
2. T. J. Klemmer, N. Shukla, C. Liu, X. W. Wu, E. B. Svedberg, O. Mryasov, R. W. Chantrell, D. Weller, M. Tanase and D. E. Laughlin, Applied Physics Letters, 2002, 81, 2220-2222.
3. S. Saita and S. Maenosono, Chemistry of Materials, 2005, 17, 3705-3710.
4. S. Allen, University of Durham, 2003.

Chapter 5 - X-Ray Diffraction Studies of FePt Nanoparticles

5.1 Introduction

This chapter describes a number of in-situ variable temperature X-ray diffraction (VTXRD) studies designed to investigate the order-disorder transition in FePt nanoparticles. The first part of the chapter provides a comparison between the phase transitions of a FePt sample made by the method developed by Sun *et al.*[1]. and that developed in Durham (the Durham route) and discussed in **chapter 3**. The second part of this chapter analyses VTXRD data via Rietveld refinement methods in order to provide information about the phase transition and its relationship with the precise synthetic conditions for a variety of other samples.

5.2 A Comparison Between the Order-Disorder Transition of FePt Nanoparticles Made via Two Different Methods

5.2.1 Introduction

FePt nanoparticles made via the synthetic route developed by Sun *et al.*[1] have been shown to exhibit the fct internal structure after annealing to 540 °C. This high ordering temperature is required because of the composition of the nanoparticles prepared this way. Ideally any individual FePt nanoparticle will have a 1:1 FePt stoichiometry. This synthetic route has an excess of iron present, meaning the stoichiometry is potentially not 1:1. Also, there is a third party reducing reagent present. These factors mean that the Fe and Pt atoms in a given nanoparticle are not entirely randomly arranged. It's possible that, for example, a FePt nanoparticle may consist of a Pt core with a Fe shell. In order for such a material to order from the fcc to the fct phase a significant rearrangement of atoms would be required. Equally a given sample may have an overall stoichiometry of 1:1 whilst the individual component particles may have a range of stoichiometries[2].

The synthetic route developed in Durham utilises platinum acetylacetonate and Collman's reagent (disodium tetracarbonyl ferrate) which contain platinum in a 2+ oxidation state and iron in a 2- oxidation state, formally. This means the platinum will oxidise the iron and the iron will reduce the platinum. For this reduction to happen, the platinum and iron sources must be adjacent to each other therefore encouraging electron transfer. Also, the stoichiometry is such that one molecule of the iron source will react with one molecule of the platinum source, i.e. one Fe ion will react with one adjacent Pt ion to yield one "FePt" species. Less atomic rearrangement

will then be required for ordering than may otherwise have been necessary. This may lead to a lowering of the ordering temperature.

A lower ordering temperature is desirable because it will help avoid sintering – where particles fuse together due to the increased thermal energy. The surface area to volume ratio of nanoparticles is large, leading to a large surface energy. In order to reduce this, nanoparticles increase in volume. This can be achieved by ordering of individual particles. Ultimately small (~ 4 nm) fct nanoparticles of uniform size and shape are desired so that the potential areal recording density is high. If the ordering temperature is lowered, the degree of particle sintering can be decreased, or removed altogether.

By taking one sample made via Sun *et al.*'s route and a second made via the Durham route, a comparison between the two syntheses can be made in terms of the order-disorder phase transition and the temperature at which it occurs. Using Rietveld refinement methods it is possible to obtain quantitative information on the material's ordering process.

5.2.2 Investigating the Ordering Process of FCC Phase FePt Nanoparticles

It should be noted that the ordering process for FePt nanoparticles converting from the fcc to fct phase is complex. The ordering process of numerous fct, or $L1_0$, bulk alloys has been studied in detail, including CoPt, FePd and $FePt_3$. It was found to be similar to that of a 1:1 stoichiometric AuCu alloy. In the case of bulk AuCu, at a critical temperature of 410 °C (or below if the stoichiometry was either slightly less or more than 1:1) the cubic system would form a tetragonal unit cell. Simultaneously the atoms in the unit cell would change from being randomly oriented (in the cubic system) to being ordered. In this process a change in the unit cell volume would occur as a result of the crystal system changing from cubic to tetragonal and the individual atoms rearranging into an Fe:Pt:Fe:Pt (small:big:small:big) order. This packing is a more efficient use of space as in the disordered material the size and positions of the larger atoms determine the inter-layer separation.

In the case of nanoparticles there are a large number of crystalline defects (i.e. surfaces). This creates a second potential contributor to the overall change in cell size in addition to the chemical ordering, namely the growth of the crystallites.

There is a potential link between the degree of order of a given FePt nanoparticle and the change in volume$^{(1/3)}$. It may be possible to determine if this is the case by observing the diffraction pattern of a given material. However, for a disordered fcc phase nanoparticle this would be difficult. The reason for this is the lack of superlattice reflections. These grow into the diffraction pattern of FePt nanoparticles upon annealing and are a direct indication of ordering in the material. One possible reason for this link would be the existence of an anti-phase boundary.

In this case there are a number of ordered domains within a sample which mean it is not 100 % disordered, but these domains are small enough so that no long range order is present and no superlattice peaks are visible in the diffraction pattern obtained. This small degree of order can be detected during annealing. If the volume$^{(1/3)}$ change is smaller than expected, then the starting material has some degree of order. This is dependent on there being no particle growth contribution to the volume$^{(1/3)}$ change.

5.2.3 Experimental Details

Two FePt samples were used, one (LHN 162, d8_02987) synthesised via the Durham method and another (Seagate 001, d8_02953) made according to Sun *et al.*'s route. Both were used in an in-situ VTXRD experiment and the measurements were recorded using the method detailed below.

In-situ variable temperature X-ray diffraction data on FePt were collected using a Bruker d8 Advance diffractometer equipped with a Cu X-ray tube, a Ge(111) incident beam monochromator (λ = 1.5406 Å), and a Vantec linear PSD detector. High temperature measurements were performed using an Anton Parr HTK1200 furnace (operating range 298 to 1473 K). The powdered sample was mounted on a circular amorphous silica disc with silicone vacuum grease smeared on top to act as an adhesive. A 1 ° divergence slit was used and VTXRD data were collected over the programmed temperature range of 303 – 878 – 303 K. Measurements were recorded every 25 K, 58 minutes each, with a 0.2 Ks^{-1} heating/cooling rate between temperatures, a 2θ range of 10 – 90 °, and a step size of 0.017 ° 2θ over 48 hours.

5.2.4 Comparison of the Ordering Temperature of Two FePt Nanoparticle Samples Prepared via Different Methods

The 27 data sets comprising the measurement d8_02953 (Sea 001) during heating are shown in **figure 5.1** whilst those measured and recorded in d8_02987 (LHN 162) are shown in **figure 5.2**.

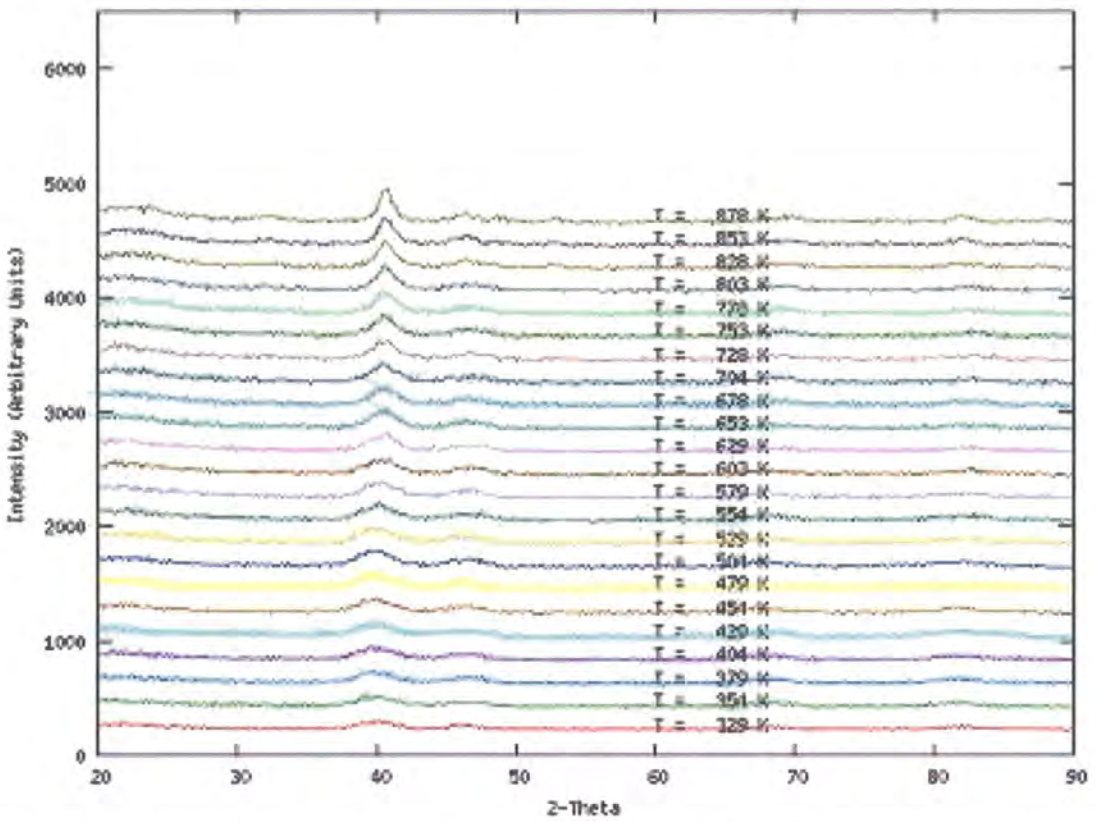

Figure 5.1 Variable temperature X-ray diffraction data for FePt (Seagate 001, d8_02953). The 23 powder diffraction patterns shown are from 329 K (base of figure) to 878 K (top of figure) in 25 K steps. Patterns have been offset vertically for clarity.

In **figure 5.1** it can be seen that between 329 K and 878 K the material synthesised via Sun *et al.*'s method converted from the fcc to fct phase. This can be seen by the growth of the superlattice peaks, primarily (and most easily observed) those at 2-theta values of ~ 24 ° and ~ 33 °. It must be noted that these peaks, as with all peaks present in both the fcc and fct material, sharpen and narrow as they are heated, making them more clearly seen by the naked eye. This is a direct result of the particle growth's contribution to the annealing process, not the internal crystallographic ordering. The superlattice peaks are a reliable indicator of fct structure presence when they are broad as much as when they are sharp. In this case the first appearance of a superlattice peak is probably in the diffraction pattern measured at 803 K, and this grows and sharpens as the heating is continued to 878 K. As the superlattice peak begins to grow at 803 K we can say this is the ordering onset temperature for this sample. This equates to ~ 530 °C which is comparable to the ordering temperature quoted in the literature. It is possible that if the sample had been held at this temperature the peaks would have continued to grow and sharpen in the same manner as they have shown upon heating to increased temperatures. The (*200*) peak also splits into two peaks (*200* and *002*) on annealing (~ 45 °2θ).

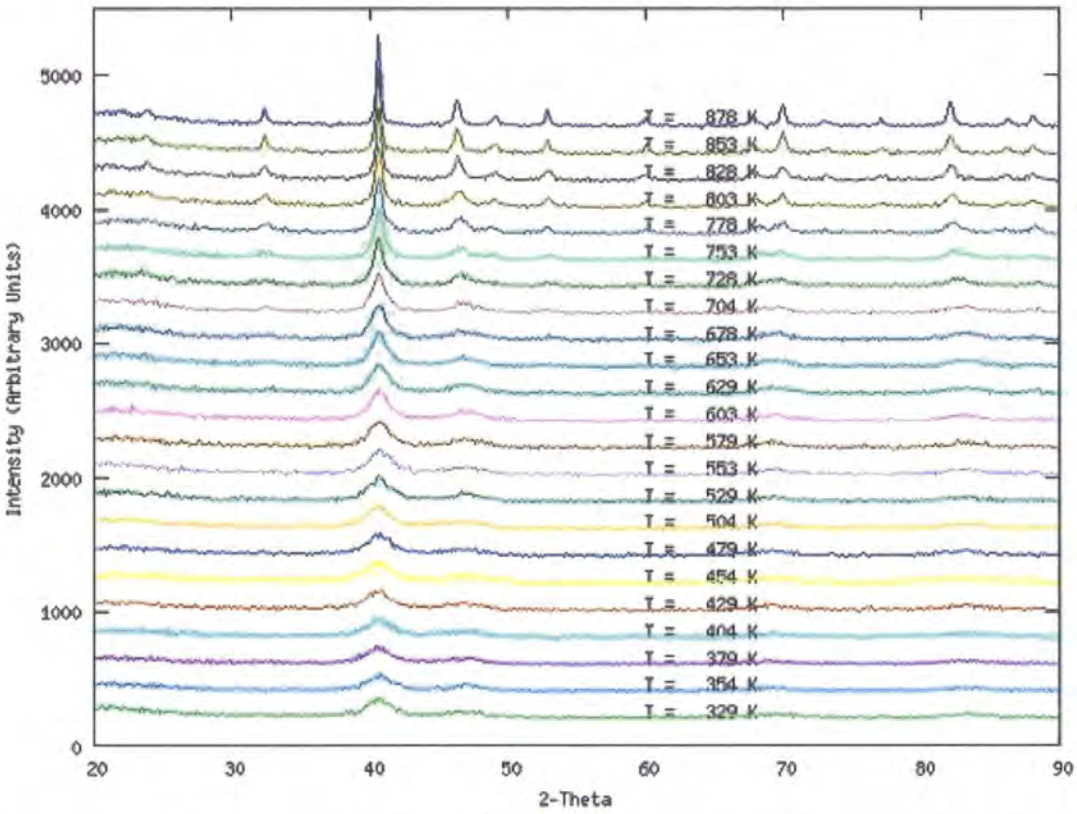

Figure 5.2 Variable temperature X-ray diffraction data for FePt (LHN 162, d8_02987). The 24 powder diffraction patterns shown are from 303 K (base of figure) to 878 K (top of figure) in 25 K steps. Patterns have been offset vertically for clarity.

Figure 5.2 shows equivalent diffraction patterns measured as a function of temperature for the sample synthesised via the Durham route, LHN 162. The conditions utilised for the synthesis were as similar to the other sample as possible. This means that although the reagents were different, the surfactants, solvent, heating method and temperature regime used were the same as in Sun *et al.*'s method. This was so as to provide the best comparison.

The growth of the relevant superlattice peaks in the diffraction pattern of LHN 162 first occurs at 704 K. As the temperature is increased further the peaks become sharper and are more easily seen. This sample's ordering onset temperature appears to be ~ 100 K lower than that of the other sample, indicating that the phase transition occurs, or begins, at a lower temperature when synthesising FePt nanoparticles using the Durham method.

5.2.5 Rietveld Comparison of the Ordering Temperature of Two FePt Nanoparticle Samples Prepared via Different Methods

Rietveld refinement was performed on each of the two datasets. Within each dataset, each diffraction pattern recorded in the experiment was refined using Multitopas[4] methodologies. In total 13 parameters were refined at each temperature. These were 6 background terms, a correction for the sample height, an FePt nanoparticle scale factor, lattice parameter *a* and lattice parameter *c*, the crystallite size, the material's fractional occupancy and the temperature factor. The structural model utilizes a TCHZ peak shape to define the instrumental peak shape.

Figures 5.3a – 5.3k show how the most important refined parameters varied with temperature during the VTXRD study of sample Sea 001. In all cases the closed red squares relate to the parameter value on heating; the closed blue triangles relate to the parameter value upon cooling. **Figures 5.4a – 5.4k** show the same refined parameters as a function of temperature for sample LHN 162.

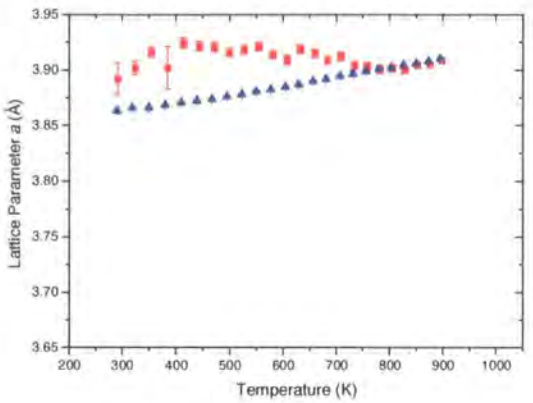

Figure 5.3a. Variation of the lattice parameter a as a function of temperature for sample Sea 001.

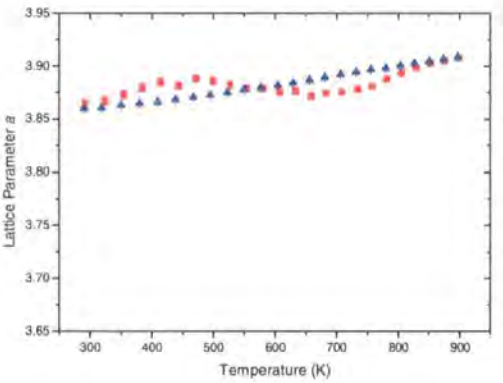

Figure 5.4a Variation of the lattice parameter a as a function of temperature for sample LHN 162.

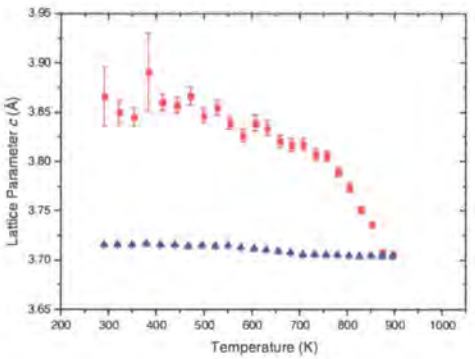

Figure 5.3b Variation of the lattice parameter c as a function of temperature for sample Sea 001.

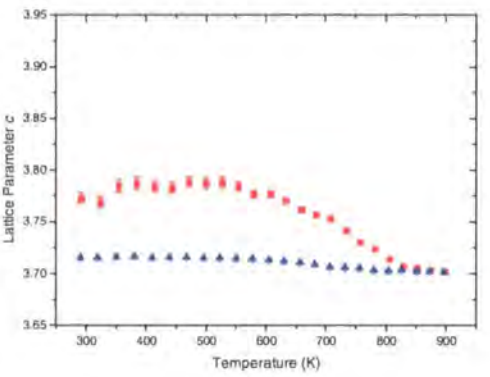

Figure 5.4b Variation of the lattice parameter c as a function of temperature for sample LHN 162.

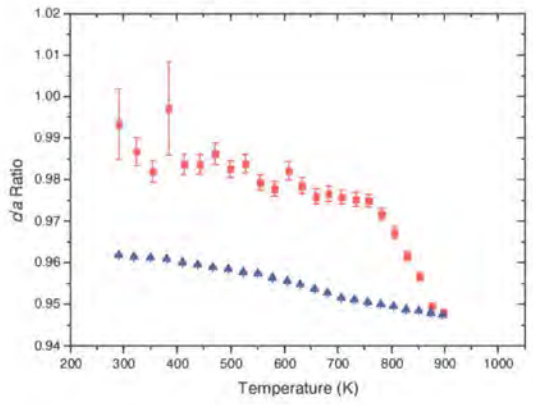

Figure 5.3c Variation c/a ratio as a function of temperature for sample Sea 001.

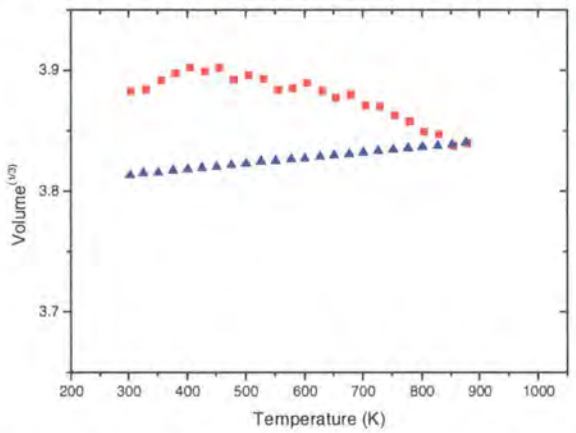

Figure 5.3d. Variation of volume$^{(1/3)}$ as a function of temperature for sample Sea 001.

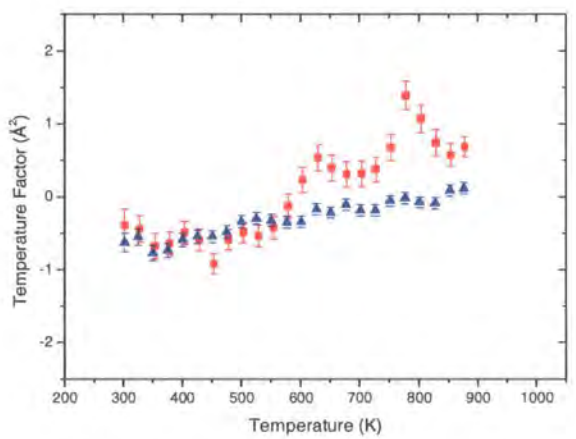

Figure 5.3e Variation of the refined temperature factor as a function of temperature for sample Sea 001.

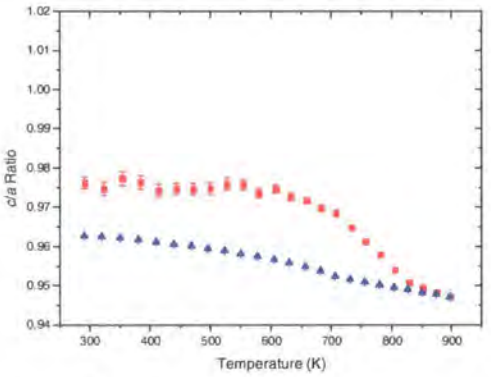

Figure 5.4c Variation c/a ratio as a function of temperature for sample LHN 162.

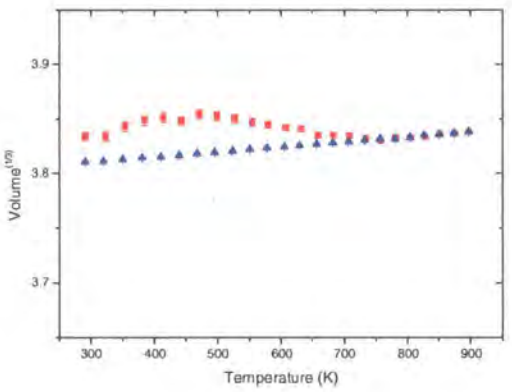

Figure 5.4d Variation of volume$^{(1/3)}$ as a function of temperature for sample LHN 162.

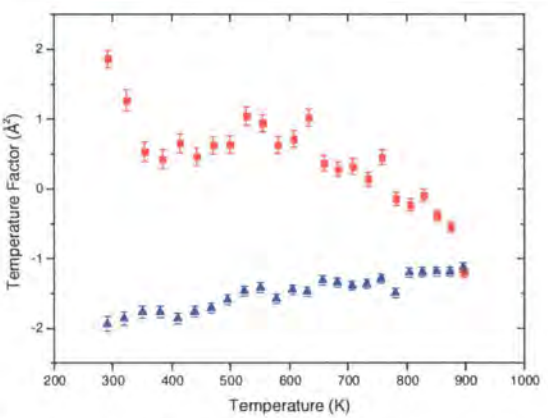

Figure 5.4e Variation of the refined temperature factor as a function of temperature for sample LHN 162.

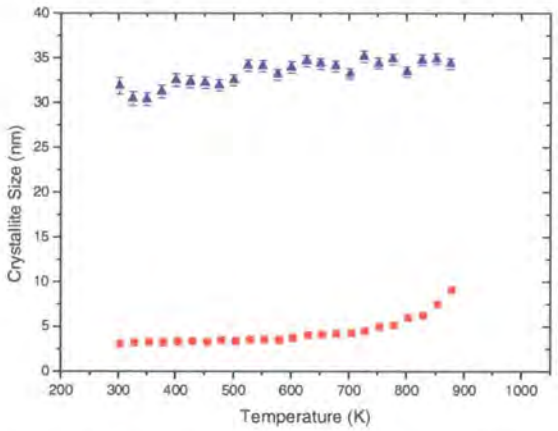

Figure 5.3f Variation in crystallite size as a function of temperature for sample Sea 001.

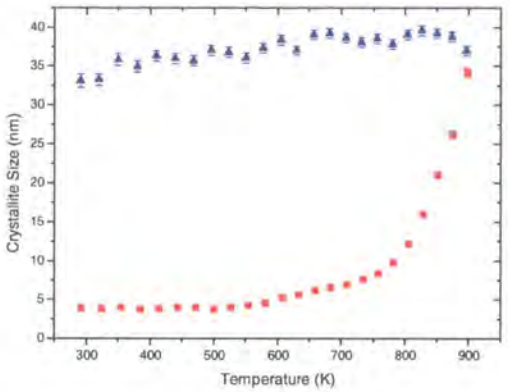

Figure 5.4f Variation in crystallite size as a function of temperature for sample LHN 162.

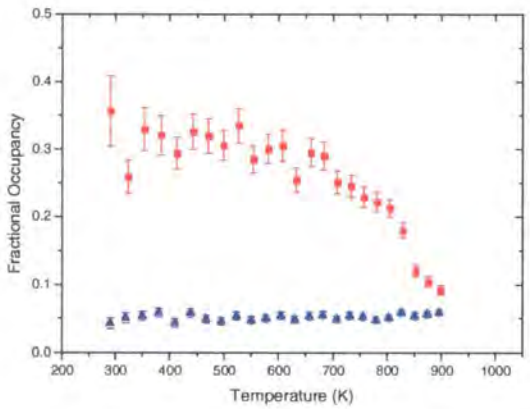

Figure 5.3g Variation of the fractional occupancy as a function of temperature for sample Sea 001.

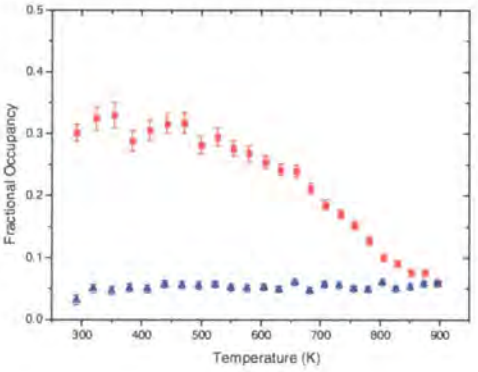

Figure 5.4g Variation of the fractional occupancy as a function of temperature for sample LHN 162.

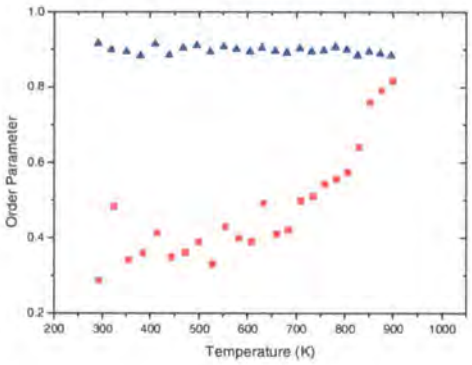

Figure 5.3h Variation of the order parameter as a function of temperature for sample Sea 001.

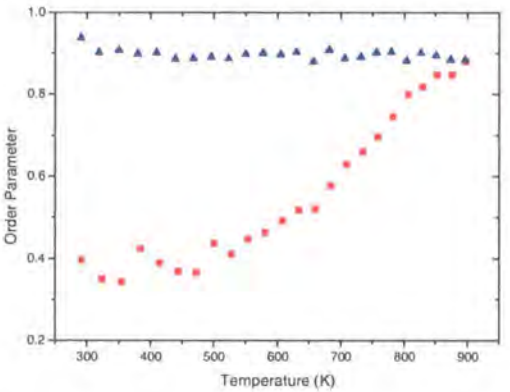

Figure 5.4h Variation of the order parameter as a function of temperature for sample LHN 162.

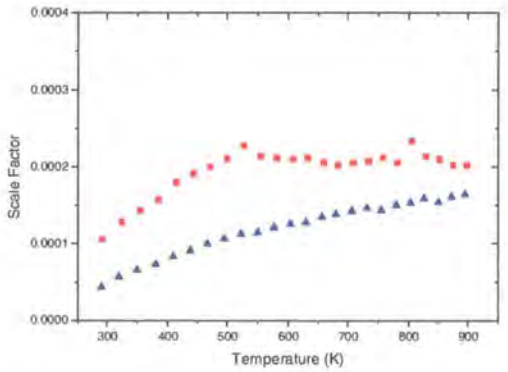

Figure 5.3i Variation of the scale factor as a function of temperature for sample Sea 001.

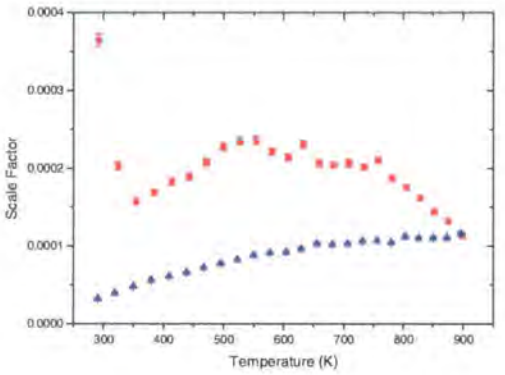

Figure 5.4i Variation of the scale factor as a function of temperature for sample LHN 162.

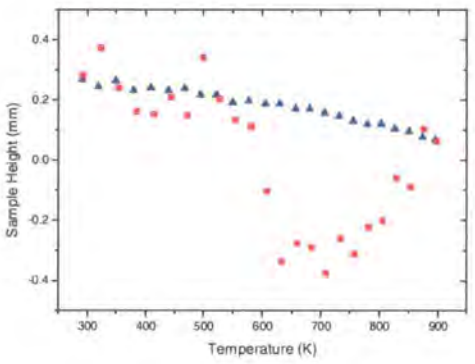

Figure 5.3j Variation of the sample height as a function of temperature for sample Sea 001.

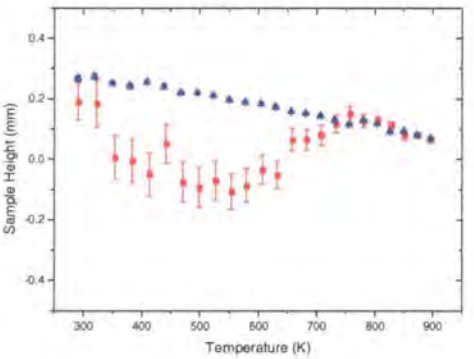

Figure 5.4j Variation of the sample height as a function of temperature for sample LHN 162.

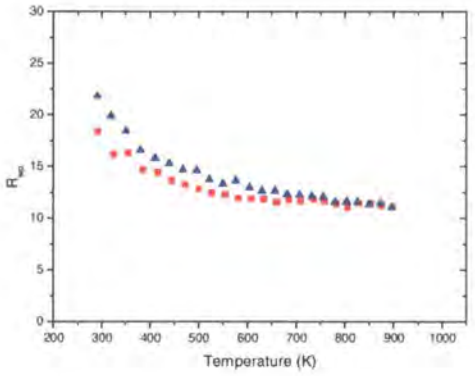

Figure 5.3k Variation of the Rwp of the refinement as a function of temperature for sample Sea 001.

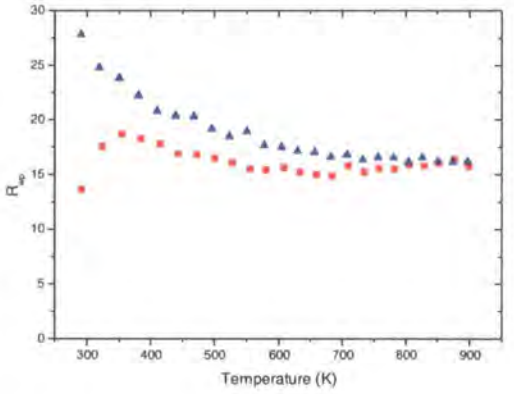

Figure 5.4k Variation of the Rwp of the refinement as a function of temperature for sample LHN 162.

The scale factor (**figure 5.3i**), Rwp (**figure 5.3k**), sample height (**figure 5.3j**) and temperature factor (**figure 5.3e**) are all presented in order to monitor the experiment. The sample height as a function of temperature should be close to zero (ideally ± 0.25 mm) and vary smoothly with temperature so as to ensure the sample was well positioned in the diffraction beam, and to allow

the collection of experimental data with as few systematic errors as possible. Three parameters allow the refinement itself to be monitored. These are the agreement of the fit of the calculated model to the experimental data (R_{wp}), the atomic displacement parameter (which should increase smoothly as the temperature increases) and the scale factor which allows different intensity data to be compared satisfactorily (by scaling each set of data to ensure each is on the same relative scale).

The other parameters plotted are chosen because they are directly related to the phase transition which the FePt nanoparticles undergo. The lattice parameter *a* (**figure 5.5c**) and *c* (**figure 5.5d**) change upon heating as the face-centred cubic FePt converts to a tetragonal structure. The *a* parameter stays approximately constant and the *c* parameter decreases. The volume$^{(1/3)}$ is a more useful quantity as it provides a single value which details how the effective cell length varies as a function of temperature. In reality the *a* and *c* lattice parameters are the same at low temperatures before annealing has taken place – the material is cubic. However, the refinement methodology is such that they are allowed to differ at both high and low temperatures (**figure 5.5**) – see **chapter 4**. As such, only the volume$^{(1/3)}$ has any physical meaning in the fcc phase.

Figure 5.5 shows that the value of (volume$^{1/3}$) is meaningful in the cubic phase (i.e. when lattice parameter *a* and *c* are allowed to differ in the cubic phase, correct volumes are obtained). Within the figure results of a separate set of refinements in which *a* and *c* were equated throughout are compared with the (volume$^{1/3}$). Both are identical within experimental uncertainty.

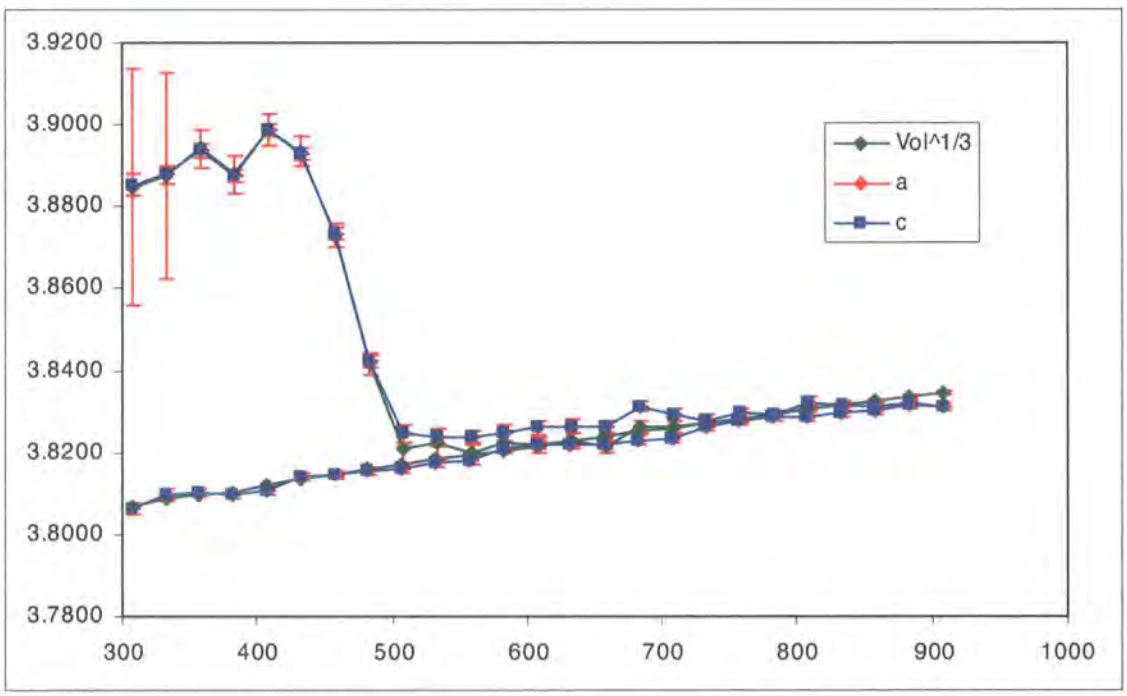

Figure 5.5 A comparison of unit cell parameters extracted using a cubic cell parameter with the volume$^{(1/3)}$ obtained when a and c are allowed to differ. Below the fcc to fct phase transition both methods give the same effective cell size (sample LHN 162 data used for illustration).

The fractional occupancy (**figure 5.3g**) and order parameter (**figure 5.3h**) provide an indication of the degree of ordering present in the material and allow qualitative statements to be made about whether the material is ordered, at what temperature it began to order and at what temperature further ordering ceases (i.e. fully ordered). The crystallite size (**figure 5.3f**) shows the growth of FePt crystallites as the temperature varies. This is important as ultimately ordered material with little or no sintering (thus ensuring monodisperse sizes and shapes if the synthesis provided such materials) is desired.

Looking at both **figure 5.3d** and **5.4d**, the change in unit cell dimensions for a sample prepared via the Durham route and one prepared via Sun *et al.*'s route can be observed. In the case of the sample made via the Durham route a significant and well defined decrease in cell volume occurs consistent with an order-disorder transition. A similar change occurs for the Sea 001 sample in **figure 5.3d** but is less well defined – the decrease in cell volume occurs over a larger temperature range and continues to higher temperatures. However, the absolute change is much greater for sample Sea 001.

After the transition has occurred the *a* and *c* parameters can be refined reliably as the material is at this point tetragonal. It can be seen in **figure 5.4b** at ~ 650 – 750 K a marked change in the cell parameter occurs which can not be explained by thermal expansion. This is most likely related to the Curie temperature (the Curie temperature, *Tc*, of a ferromagnetic material, is the temperature above which it loses its characteristic ferromagnetic ability: the ability to possess a net (spontaneous) magnetisation in the absence of an external magnetic field) of FePt which is approximately 710 K. **Figure 5.3b** shows a similar change at ~ 650 K, confirming that both samples undergo a magnetic transition. Magnetostriction is also observed in most ferromagnetic materials and is the spontaneous response of such a material to its own magnetisation – its physical dimensions alter (it changes shape)[5]. This effect may be expected to occur when FePt nanoparticles are subjected to an applied magnetic field.

For sample LHN 162, the final cell parameters of a = 3.859(3) Å, c = 3.715(4) Å and the final c/a ratio of 0.962(6) compare to literature values of a = 3.855 Å, c = 3.711 Å and c/a = 0.962(3)[6] or a = 3.85 Å, c = 3.71 Å and c/a = 0.963(6)[7]. For sample Sea 001 the final cell parameters are a = 3.862(9) Å, c = 3.715(6) Å and the final c/a ratio is 0.961(8). The numbers in parentheses are Rietveld derived standard uncertainties.

After annealing of each of sample Sea 001 and LHN 162, and cooling to room temperature, the (volume$^{1/3}$) is approximately the same, ~ 3.81 angstroms. However, before annealing this value was 3.88 angstroms for Sea 001 and 3.83 angstroms for LHN 162, i.e. the sample prepared via the synthetic route developed by Sun *et al.* starts off with a higher volume yet reduces to the same value after annealing. This could indicate two things, both of which suggest that samples made via Durham route yield more ordered material as-synthesised. Firstly there could be a

greater range of particle stoichiometries in sample Sea 001. Hence, on ordering, a larger percentage of the particles in the sample undergo atomic rearrangement, or the unit cell must change from cubic to tetragonal. Both effects would incur a volume$^{(1/3)}$ change. Secondly, sample Sea 001 could have a core-shell morphology, with a Pt core and an Fe_2O_3 shell[8]. If such morphology existed, the Pt core would have a larger unit cell than an FePt core. The shell may limit particle-particle interactions, thus helping avoid particle agglomeration; it may also lead to unwanted magnetic shell/core interactions

Figure 5.6 and **figure 5.7** combine, respectively, the variation as a function of temperature of the crystallite size and order parameter upon warming of both samples.

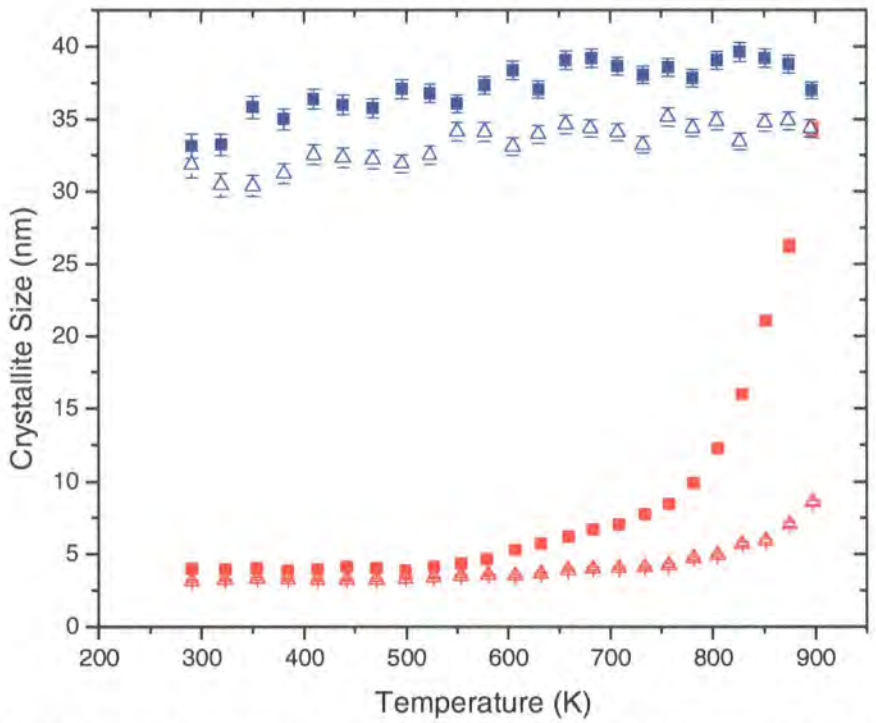

Figure 5.6 A graph showing the variation as a function of temperature of the crystallite size for a Durham route sample (LHN 162 – filled squares) and one made via Sun *et al*'s route (Sea 001 –open triangles) on warming and cooling.

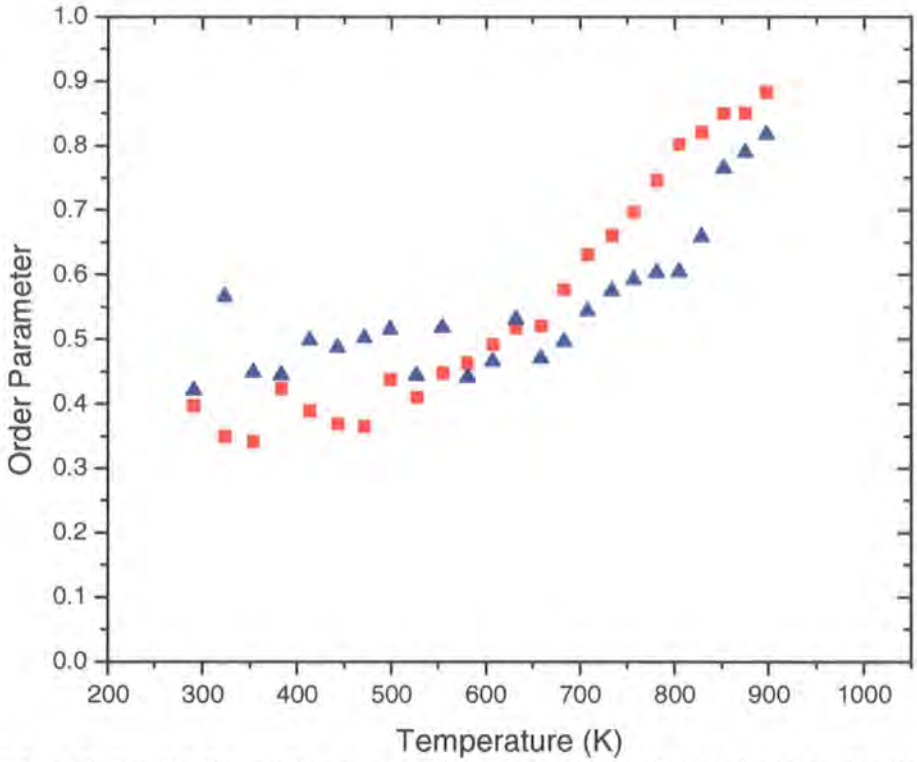

Figure 5.7 A graph showing the variation as a function of temperature of the order parameter for a Durham route sample (LHN 162 - red squares) and one made via Sun *et al*'s route (Sea 001 – blue triangles).

Interestingly, upon annealing, sample LHN 162 is more susceptible to particle growth, or sintering. The particle size is always larger than that of sample Sea 001 and also increases in size at both lower temperatures, and to a greater degree, as the temperature increases. This is corroborated by the breadth of the peaks at a given temperature in **figure 5.1** compared to **figure 5.2**. It can be seen from **figure 5.6** that the crystallite size is approximately the same after annealing as can be seen by the data collected at room temperature after cooling.

However, as regards the order parameter of each sample, the behaviour is quite the opposite, despite the two processes being linked (as the particles grow in size they are able to order further as their stoichiometry is closer to 1:1 due to there being more atoms in any given sample). The order parameter of sample Sea 001 does not change significantly until ~ 650 K. At this point the order parameter increases at a steady rate for the duration of the measurement. This temperature is lower than the temperature at which superlattice peaks are observed (**figure 5.1**). Sample LHN 162 exhibits a significant increase in the order parameter at ~ 450 K (again, this is lower than the temperature at which superlattice peaks are observed in **figure 5.2**). The stoichiometry of the material is 1:1, or at least closer to 1:1 than Sea 001 and so the material is capable of ordering more quickly, and at lower temperatures. The particles in Sea 001 need to grow in order to obtain the requisite number of atoms to allow the stoichiometry to become 1:1. At this point the particles are able to order on continued annealing. This is a significantly lower temperature than for the other sample, providing quantitative evidence (in addition to the

qualitative evidence presented in **figures 5.1** and **5.2**) that samples made via the Durham route order at a significantly lower temperature than samples prepared via Sun *et al.*'s method.

5.2.6 Conclusion

Firstly, it has been shown that the final cell dimensions of both sample LHN 162 and Sea 001 after annealing are similar to each other and compare favourably to literature values. This means that each synthetic method is suitable for the preparation of fcc phase $Fe_{1-X}Pt_X$ where 40 % < X < 60 % which are capable of undergoing an order transition leading to fct, or $L1_0$, phase FePt particles.

The absolute change in cell volume of sample Sea 001 was significantly larger than that of LHN 162. When fcc phase FePt orders to fct phase FePt the crystal system converts from cubic to tetragonal. Two factors lead to a volume change – chemical ordering and particle growth. It could be that the changes in (volume$^{1/3}$) are due to particle growth. Sample LHN 162 was, according to the refined data, 3.96(2) nm in size before annealing and 33.13(5) nm in size after annealing (and cooling to room temperature, therefore eliminating any thermal expansion effects). This is a particle growth of 29.19 nm. Sample Sea 001 was 3.13(9) nm in size before and 31.84(6) nm in size after annealing. This equates to a growth of 28.71 nm. The difference between the two samples in terms of growth is only 1.6 %. As the overall change for each particle is approximately the same, the discrepancy in the change in volume$^{(1/3)}$ is presumably related to a difference in the stoichiometry/degree of short range order in the two samples.
These factors give credence to the proposal that samples prepared via the Durham route are advantageous compared to samples made via Sun *et al.*'s route as they appear to order at a lower temperature and have the benefits provided by a simpler (one-pot) synthetic method. For these reasons, and the fact that sintering could be more comprehensively controlled as a result, the remainder of this chapter shall look only at samples prepared via the Durham route.

5.3 Influence of Synthetic Conditions on Particle Properties

5.3.1 Introduction

In **section 5.2** an investigation into the order-disorder transition of two FePt nanoparticle samples was described. The difference between each sample is the method by which they were prepared. Similarities and differences between the two samples have been discussed and conclusions drawn. It was concluded that FePt prepared via the Durham route is potentially advantageous to that prepared via the route developed by Sun *et al.* As a starting point for developing a suitable synthetic method that achieves the goals set out at the start – i.e. to lower the ordering temperature of the fcc to fct transition and therefore limit the problem of sintering

– that ultimately yields monodisperse nanoparticles of fcc phase FePt the studies in **section 5.2** provided useful information. However, after that initial step the synthetic method needs to be improved and streamlined in order to obtain particles as close to the desired specification as possible.

For this purpose it is sensible to prepare multiple samples via the same fundamental synthetic route whilst altering certain variables and determining the effects in terms of the particles obtained and their properties. The results obtained pertaining to any one or more property, for example the order parameter or unit cell dimensions of a given sample, can be compared to all others. This may provide information about correlations between certain properties, or trends relating to synthetic variables that can aid the evolution of the synthetic method. Any such trends, or correlations would then be used in the experimental design, allowing the preparation of material closer again to the ideal.

Firstly the samples under investigation in this section will be described in terms of their synthesis. These samples have all been studied via VTXRD methods. The data obtained from these experiments have been refined according to the Rietveld method. These refined data will then be used in order to establish what trends or correlations can be observed.

5.3.2 Samples Studied

Table 5.1 provides details about each of the samples used in the analyses in **section 5.3.3.** Each of these samples was prepared by Dr Loc H Nguyen of Durham University and have been attributed a sample code of the format LHNXXX.

Sample number	Sample code	D8 run	Heating Method	Solvent	Surfactant 1	Surfactant 2	Reflux Temperature (°C)	Reaction Time (hours)	T order onset (K)
1	LHN 073	D8_02588	Thermal	Nonadecane	Oleic Acid	N/A	335	5	628
2	LHN 078	D8_02642	Thermal	Octyl Ether	Oleylamine	N/A	297	1	603
3	LHN 128	D8_02780	Thermal	Nonadecane	Oleylamine	3-AR-P	250	1	555
4	LHN 009	D8_02808	Thermal	Octyl Ether	Oleylamine	Oleic Acid	297	1	583
5	LHN 131	D8_02813	Thermal	Nonadecane	C12 Acid	N/A	330	1	653
6	LHN 132	D8_02819	Thermal	Nonadecane	Stearic Acid	N/A	330	2	609
7	LHN 133	D8_02820	Thermal	Docosane	Oleylamine	3-AR-P	363	2	609
8	LHN 135	D8_02821	Thermal	Nonadecane and Tetrocosane	C12 Aniline	Oleic Acid	356	2	633
9	LHN 134	D8_02841	Thermal	Nonadecane and Tetrocosane	C12 Aniline	N/A	356	1	608
10	LHN 054	D8_02890	Thermal	Octyl Ether	Oleylamine	Oleic Acid	280	1	633
11	LHN 127	D8_02891	Microwave	Nonadecane	Oleylamine	3-AR-P	250	1	608
12	LHN 155	D8_02892	Microwave	Nonadecane	Oleylamine	Oleic Acid	130	1	533
13	LHN 155	D8_02930	Microwave	Nonadecane	Oleylamine	Oleic Acid	130	1	533
14	LHN 131	D8_02952	Thermal	Nonadecane	C12 Acid	N/A	330	1	609
15	LHN 144	D8_02973	Thermal	Octyl Ether	Oleylamine	Polyimine	297	1	689
16	LHN 162	D8_02987	Thermal	Octyl Ether	Oleylamine	N/A	297	1	629

Table 5.1 A table describing each of the samples studied in section 5.3.3.3 in terms of the synthetic conditions and experimental details.

Each of the sixteen samples described in table 5.1 was prepared via the Durham route; i.e. the redox reaction of $Na_2Fe(CO)_4$ and $Pt(acac)_2$. However, the conditions in which this reaction occurred were varied from sample to sample. For each reaction the following are required:

1. Collman's reagent ($Na_2Fe(CO)_4$)
2. $Pt(acac)_2$
3. A high temperature solvent
4. Heating method which is capable of reaching high temperatures
5. Surfactant(s)

In the initial development of this synthetic method (detailed in **chapter 3**) the high temperature solvent used was dioctyl ether, with a reflux temperature of 296 °C. The surfactants used were oleylamine and oleic acid. The heating of the reaction vessel was by sand bath and heating mantle. To extend studies a variety of different surfactants and solvents was used as detailed in **figures 5.8** and **5.9** and **table 5.1**. The heating method used was typically a sand bath within a heating mantle. However, microwave irradiation was used for some syntheses as it was believed this method of heating would selectively heat the metallic particles in the reaction vessel to very high temperatures at a far greater rate than conventional heating methods. This could potentially lead to faster nucleation rates and uniformity.

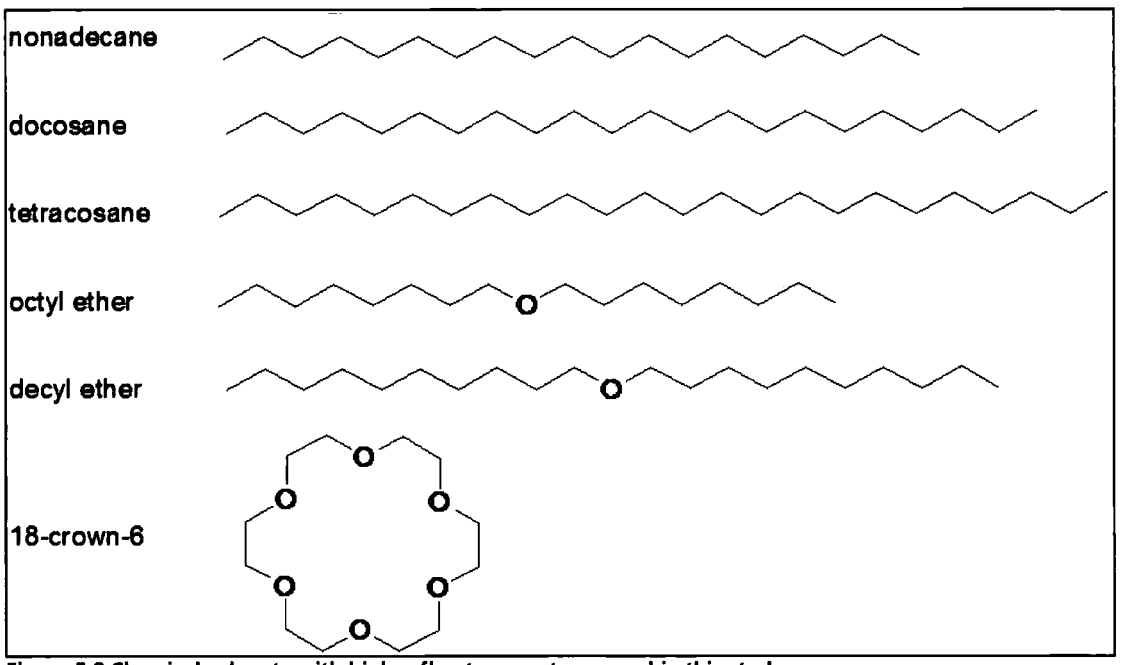

Figure 5.8 Chemical solvents with high reflux temperatures used in this study.

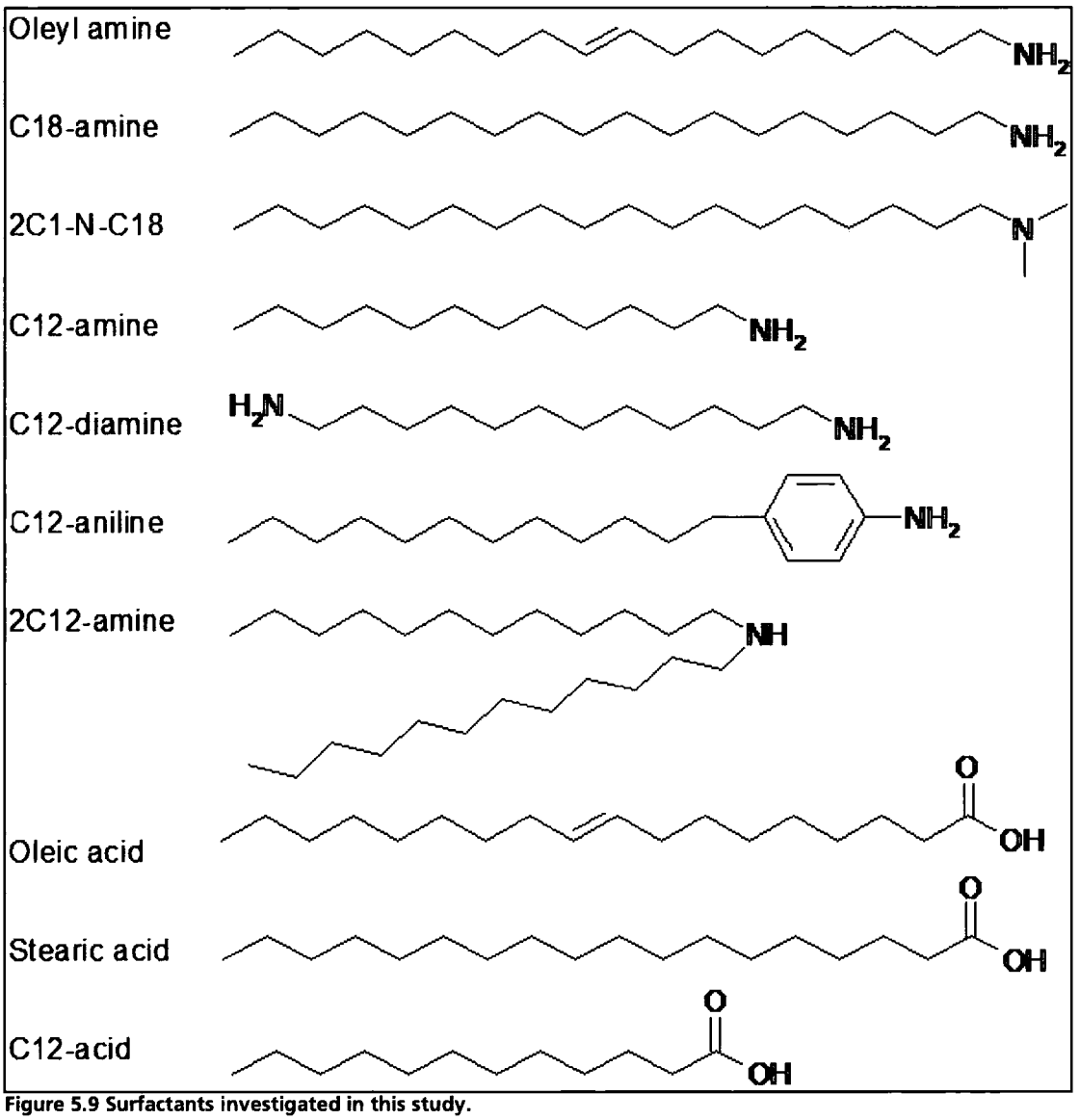

Figure 5.9 Surfactants investigated in this study.

5.3.3 Variable Temperature X-Ray Diffraction of FePt Samples

Each of the samples detailed in **table 5.1** were investigated via VTXRD studies. Each experiment was conducted in the same way, using the method described in **section 5.2.3**.

5.3.4 Rietveld Refinement of FePt VTXRD Data

For each sample one VTXRD data set comprising 48 diffraction patterns at different temperatures was recorded. Each range was refined using Multitopas methodologies. The refinement was performed in the same way as that of **section 5.3.2.2**. The refinement data can be found in the e-appendix. These appendices contain information equivalent to that in, for example, **figures 5.3a-k**. In the following section these results are collated and compared; each sub-section aims to answer one specific question.

5.3.5 Results and Discussion

5.3.5.1 Does the Initial (Volume$^{1/3}$) Depend on the Initial Crystallite Size?

By looking at a large number of FePt samples, all made via the Durham route (with variations of surfactant, solvent, heating method and temperature regime), it is possible to see if any trend exists between the effective cell parameter (volume$^{1/3}$) and crystallite size of as-synthesised particles.

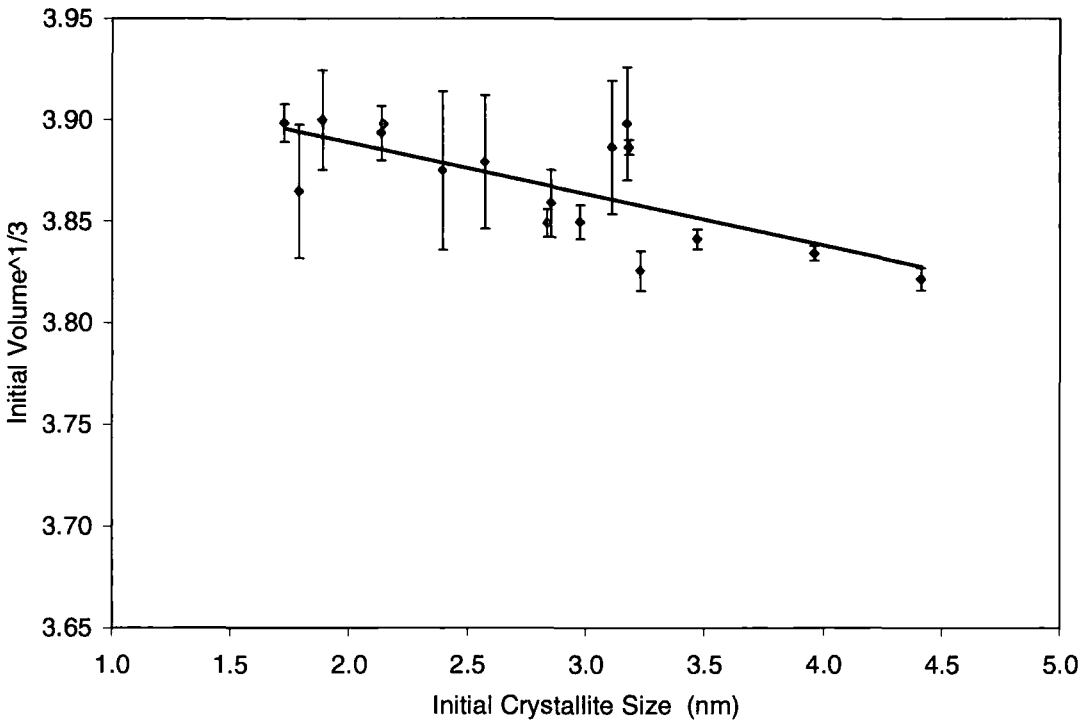

Figure 5.10 Variation of volume$^{(1/3)}$ as a function of crystallite size before annealing

Figure 5.10 shows that as the crystallite size of FePt increases, the effective cell parameter decreases. This phenomenon is a well known aspect of nanoscale compound particles[9]. The same effect has been documented for a number of specific systems, such as Fe_2O_3[9], MgO[10], MnF[29], ZrO_2[11], CeO_{2-x} suspended in toluene[12], whilst in the case of Ag[13], Cu[14], Pt[14] and Au[15], contrary results have been observed, namely lattice contraction on particle size decrease. Metallic nanoparticles of TiN[9] and Pd[16] exhibit lattice contraction on particle size increase. FePt according to **figures 5.10** and **5.13** undergoes a lattice contraction on particle size increase, like TiN and Pd nanoparticles.

A least-squares trendline - (volume)$^{1/3}$ = -0.0254(size) + 3.9397 Å - has been added to show the slope more clearly. The cell parameter of a bulk fcc phase FePt particle is 3.838 angstroms[17, 18]. As the initial crystallite size extends beyond 4 nm the initial volume$^{(1/3)}$ becomes more 'bulk-like'. The two data points lying at or around 4 nm have a volume$^{(1/3)}$ of 3.834 and 3.822 Å. Taking

into account the associated errors of these data the (volume$^{1/3}$) can be said to be the same as that of a bulk fcc FePt particle.

5.3.5.2 Does the Final (Volume$^{1/3}$) Depend on the Crystallite Size?

The cell dimensions of fct FePt after heating should be approximately the same from one sample to another. It is also true that the cell parameter will vary as a function of the Fe:Pt ratio. Vegard's law[19, 20] states that there is a linear relationship between the cell parameter and percentage composition of a number of ionic salt alloys, provided the temperature remains constant. This is not always true when extended to metallic alloys, but provides a basis upon which to compare actual cell parameter variation as a function of percentage composition[21]. If FePt followed Vegard's law, the result would be that shown in **figure 5.11**.

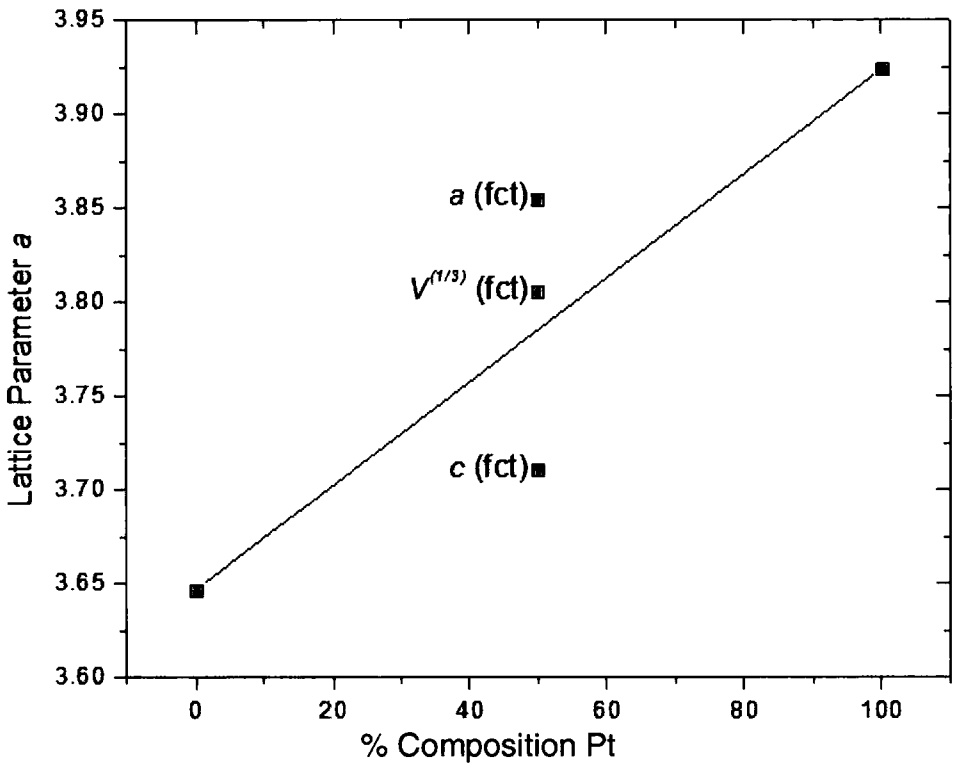

Figure 5.11 Describes the variation of cell parameter as a function of elemental composition in FePt, assuming it follows Vegard's law. FCC Fe has an a cell parameter of 3.6469 Å21 and FCC Pt has an *a* cell parameter of 3.9240 Å[21]. At 1:1 stoichiometry (50 % Fe composition) the cell parameter would be 3.7869 angstroms. The equation of the trendline is y=0.0028x + 3.6469. Marked on the graph are the literature values of the *a* and *c* cell parameters for fct phase FePt nanoparticles and the (volume$^{1/3}$) for a 1:1 stoichiometric FePt fct nanoparticle.

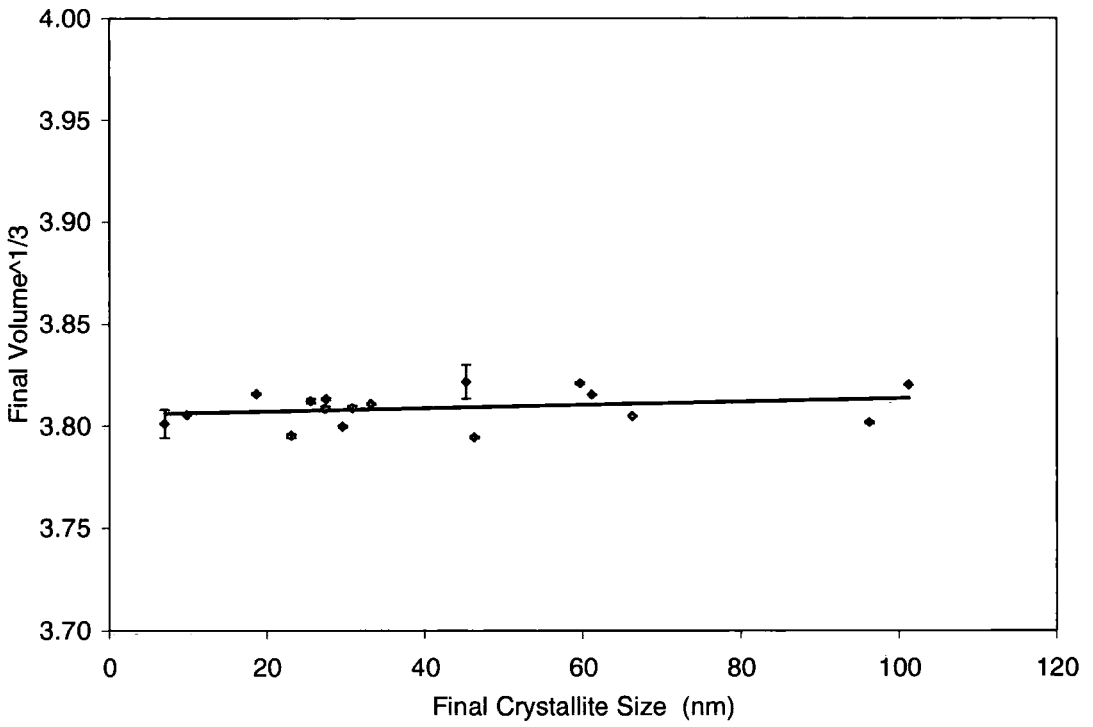

Figure 5.12 The volume$^{(1/3)}$ as a function of crystallite size after annealing.

Figure 5.12 makes it evident that all FePt samples after annealing have a similar cell parameter (volume$^{1/3}$). If it is assumed that FePt nanoparticles follow Vegard's law, the samples described in **Figure 5.12** will have the stoichiometry shown in **table 5.2** (column 3). This indicates two things. Firstly, each sample made via the Durham route is able to order to the fct phase; its stoichiometry corroborates this. **Figure 5.13** shows that the fct phase is stable if the iron composition is ~ 35 – 60 % (γ1 phase) at temperatures up to 1550 K. All the Durham samples have such a stoichiometry. Secondly, each of these samples will have a slightly varying stoichiometry as-synthesised. If the stoichiometry were exactly the same it would be expected that they would ultimately have the exact same cell parameter. We note that no dependency of the final (volume$^{1/3}$) on the final crystallite size is observed.

The literature values for the cell parameters of fct phase FePt nanoparticles indicate the volume$^{(1/3)}$ is greater than Vegard's law predicts. Taking this into account the experimental stoichiometries of the samples described in **figure 5.11** are closer to the ideal than expected. The experimental stoichiometries based on this ideal value are shown in the fourth and final column of **table 5.2**.

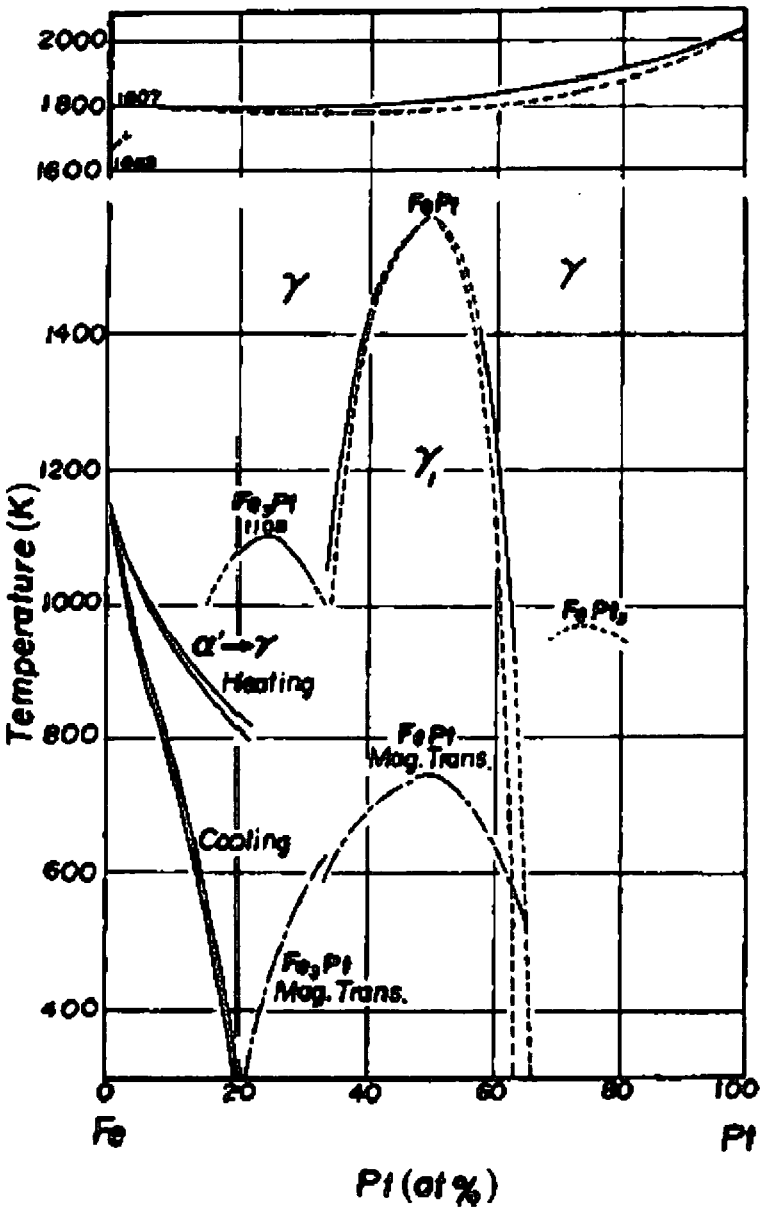

Figure 5.13 A FePt phase diagram[22].

Sample number	Final Crystallite Size (nm)	Final Volume$^{(1/3)}$	Stoichiometry if Vegard's law applied (% Pt composition)	Stoichiometry if Vegard's law not applied (% Pt composition)
1	**9.8 (3)**	3.8 (0)	56	49
2	**96.2 (4)**	3.8 (0)	55	48
3	**29.4 (6)**	3.7 (9)	55	47
4	**66.2 (9)**	3.8 (0)	56	49
5	**45.1 (6)**	3.8 (2)	62	55
6	**46.2 (3)**	3.7 (9)	52	45
7	**18.6 (8)**	3.8 (1)	60	53
8	**61.1 (6)**	3.8 (1)	60	53
9	**101.1 (7)**	3.8 (2)	61	55
10	**25.4 (6)**	3.8 (1)	58	52
11	**23.0 (7)**	3.7 (9)	52	46
12	**30.7 (3)**	3.8 (0)	57	50
13	**27.2 (9)**	3.8 (0)	57	50
14	**59.6 (4)**	3.8 (2)	62	55
15	**33.1 (3)**	3.8 (1)	58	51

Table 5.2 A table showing the percentage platinum composition of the FePt nanoparticles.

5.3.5.3 Does the Change in (Volume$^{1/3}$) Depend on the Crystallite Size?

The change in $V^{1/3}$, or $\Delta V^{1/3}$, on annealing occurs due to two processes in nanoparticles, as described previously in **section 5.3.1** - the atomic ordering and particle growth. The *a* cell parameter for bulk fcc FePt is 3.84 angstroms[17, 18]. The *a* cell parameter for bulk fct FePt is 3.838 Å, and the *c* parameter is 3.715 Å[23]. Therefore, the $V^{1/3}$ for bulk fcc FePt is 3.84 Å and the $V^{1/3}$ for bulk fct FePt is 3.81 Å. The $\Delta V^{1/3}$ is 0.043 Å for bulk FePt ordering, i.e. a 1.120 % contraction. In the case of bulk material with an effective infinite particle size this must be due only to atomic ordering.

It is possible that the crystallite size of as-synthesised FePt nanoparticles influences the change in $V^{1/3}$ as the material is annealed. In fact, it has been shown that the initial $V^{1/3}$ decreases with increasing crystallite size, and that after annealing the $V^{1/3}$ is similar irrespective of sample size. This means that the change in $V^{1/3}$ will also be dependent on crystallite size. The relationship should be similar to that of initial $V^{1/3}$ and crystallite size.

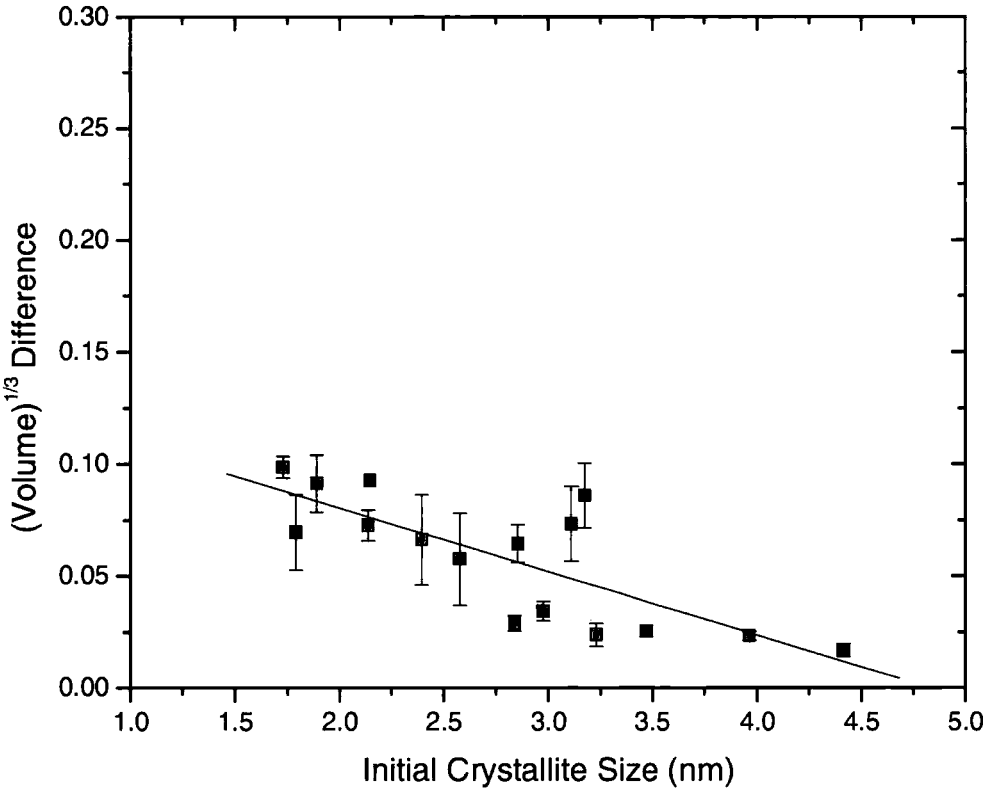

Figure 5.14 A graph describing the variation of the $V^{1/3}$ difference (difference before and after annealing) with crystallite size.

Figure 5.14 does show that the crystallite size of an as-synthesised FePt nanoparticle increases the change in the $V^{1/3}$ which takes place upon annealing becomes less. This is comparable to that seen in **figure 5.7** where the effective cell parameter decreases as a function of increasing particle size.

Table 5.3 shows the initial and final $V^{1/3}$ for each of the samples studied in this section as well as $\Delta V^{1/3}$ for each sample.

Sample Number	Initial volume$^{(1/3)}$ (Å)	Final volume$^{(1/3)}$ (Å)	□$V^{1/3}$ (Å)
1	3.90	3.81	0.09
2	3.79	3.80	-0.01
3	3.74	3.80	0.10
4	3.78	3.81	0.02
5	3.90	3.80	0.06
6	3.82	3.80	0.06
7	3.88	3.82	0.03
8	3.86	3.79	0.03
9	3.84	3.82	0.03
10	3.85	3.82	0.09
11	3.85	3.82	0.07
12	3.90	3.81	0.07
13	3.86	3.80	0.07
14	3.87	3.81	0.07
15	3.90	3.81	0.02
16	3.89	3.81	0.09

Table 5.3 A table detailing the initial and final $V^{1/3}$ of each sample studied in this section as well as the $\Delta V^{1/3}$

The $\Delta V^{1/3}$ for the fcc to fct phase transition of nanoparticles prepared via the Durham route is, on average, 0.05 angstroms. This is a larger change than for bulk FePt. This indicates that there is definitely a second contribution – crystallite growth – to the $V^{1/3}$ change.

5.3.5.4 Does $\Delta V^{1/3}$ Depend on the Initial $V^{1/3}$?

It has already been shown in **section 5.3.3.2** that each sample ultimately has the same $V^{1/3}$ after it has been ordered. Therefore the change in $V^{1/3}$ and initial $V^{1/3}$ must be directly related. This is shown in **figure 5.15**.

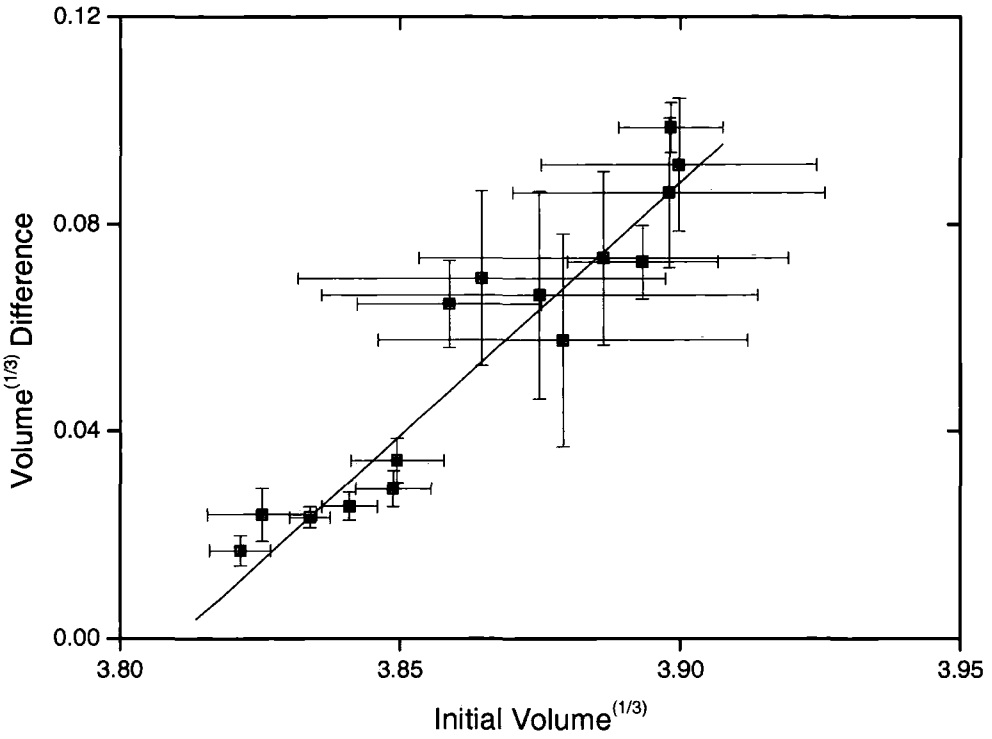

Figure 5.15 A graph showing the variation of $V^{1/3}$ difference as a function of the initial $V^{1/3}$.

A trendline has been added to **figure 5.15** to show the relationship between $V^{1/3}$ difference and initial $V^{1/3}$. The equation of the trendline is $\Delta V^{1/3} = 0.9716(V_0) - 3.6995$. The gradient of the line is approximately 1, suggesting that the change in volume does depend on the initial volume; in fact, the only reason the change in volume varies is because the initial volume has varied.

5.3.5.5 Is it Possible to Accurately Determine the Order Parameter of As-Synthesised FePt?

During any given Rietveld refinement the fractional occupancy is refined and from that the order parameter is determined. The fractional occupancy defines the composition of each atomic site. FePt in the disordered fcc phase is given a fractional occupancy of 0.5. For the fct phase the fractional occupancy of the site at *hkl*(0,0,0) is defined as 0.

Any Rietveld refinement relies on the calculated model being fitted to the experimental data. Certain experimental factors can make the results obtained from Rietveld refinement less useful. These are:

The more rapidly a diffraction pattern is recorded, the lower the signal:noise ratio; the data are of a lesser quality than had they been recorded over a greater time period. Signal:noise can also be affected by the amount of sample used experimentally.

The smaller the particles in a given sample, the broader the resultant diffraction peaks. This means they are spread over a significant 2θ range, and are difficult to define accurately in Rietveld analysis (e.g. two peaks are close together and fairly broad, so it is not possible to determine where one peak finishes and another begins).

Many factors can increase the background contribution. These include the sample holder (if the sample coverage is too small, the sample holder will be exposed to the X-ray beam), the furnace window which the X-ray beam must travel through before and after diffraction, air-scatter, fluorescence of the sample (especially for an Fe sample with a Cu X-ray tube), any non-crystalline component in the sample being measured and non-uniform sample surface. The background signal appears as undulations as a function of 2θ, i.e. broad areas of low intensity. It is possible that the fractional occupancy and background contribution can be correlated. This makes it more difficult to accurately determine the fractional occupancy when the data are of poor quality.

In the case of fcc FePt the diffraction pattern obtained is affected by many of the factors described above. **Figure 5.16** shows that the peaks of intensity are very broad, the data are relatively noisy and the background contribution (~ 20 2θ) can be as large as the actual sample peaks (~ 40, 45, 65, 83 2θ).

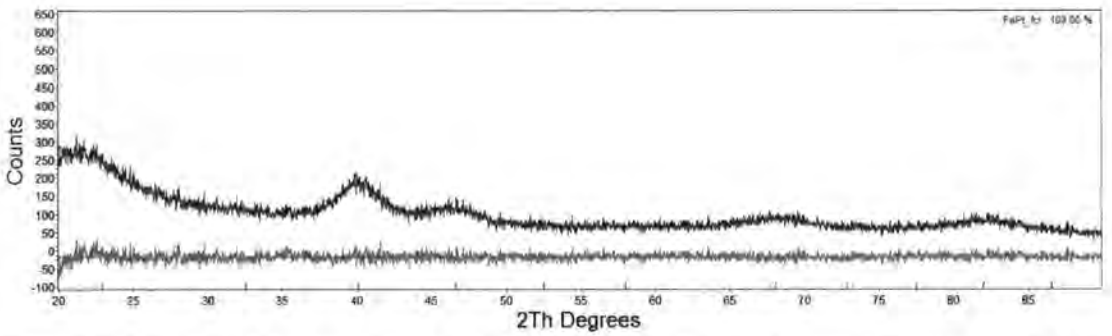

Figure 5.16 A Rietveld refinement of fcc phase FePt nanoparticles. The black curve is the experimental data, the red curve the fit of the model to the data and the grey curve is the difference.

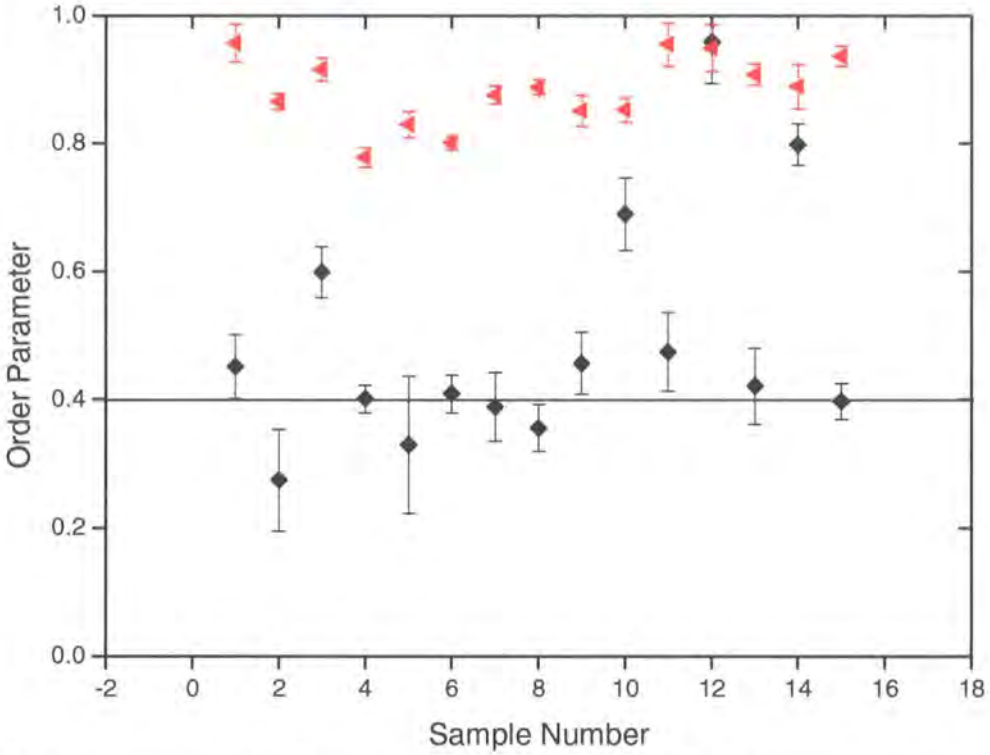

Figure 5.17 Order parameter before (Closed black diamonds) and after (closed red triangles) annealing against arbitrary sample number. A black line marks order parameter = 0.4.

Figure 5.17 shows refined initial order parameters for samples 1-16. Two things are apparent. One, the errors associated with the order parameter before annealing are large in comparison to those after annealing, and two, the scatter of the order parameter before annealing from sample to sample is greater than that of the order parameter after annealing. This is not unexpected. The difference between the diffraction patterns before (**figure 5.16**) and after (**figure 5.18**) annealing are such that the order parameter is more readily obtainable after annealing because the pattern is less noisy (better S:N ratio), there are more reflections in the data and the reflections are sharper.

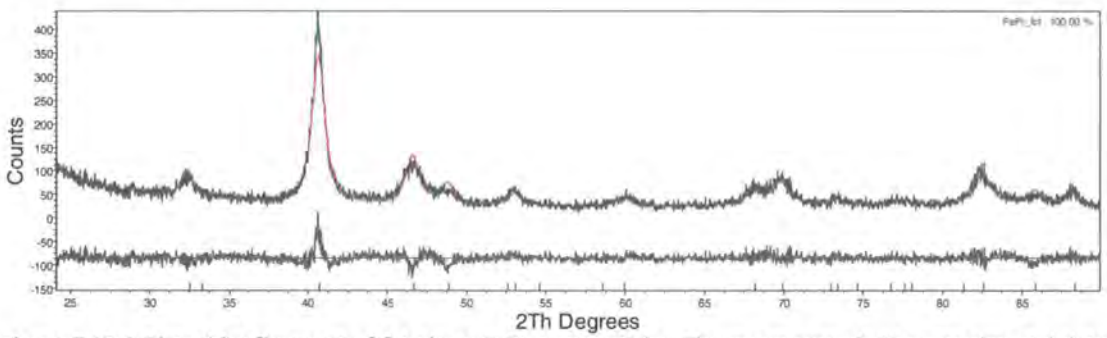

Figure 5.18 A Rietveld refinement of fct phase FePt nanoparticles. The green curve is the experimental data, the red curve is the fit of the model to the data and the grey curve is the difference curve.

The data indicate that extracting a reliable order parameter on as-synthesised particles is hard. The main reasons for this are the correlations between background parameters and the

intensities of the weak and broad ordering reflection intensities. As such it is best if the refined order parameter of an as-synthesised fcc FePt nanoparticle sample is not used, unless a lower limit is suggested. If, say, 0.4 were quoted as a minimum value for a sample's order parameter to reach before the errors become negligible compared to the actual value, it may be suitable to use when the order parameter >0.4. **Figure 5.17** shows this minimum marked on.

5.3.5.6 Conclusion

FePt nanoparticles prepared via the Durham route exhibit a trend indicating that the larger the crystallite size of the particles as-synthesised, the smaller the initial $V^{1/3}$, i.e. there is an apparent lattice contraction as a function of particle size. After annealing, when the particles have the fct structure, the $V^{1/3}$ is independent of the particle size.

These factors, and the fact that the change in $V^{1/3}$ decreases as a function of initial crystallite size, made it clear that crystallite growth and chemical ordering were both contributing to the $V^{1/3}$ change. The $V^{1/3}$ change that occurs as a result of crystallite growth in the case of the Durham route particles is 0.006 nm. This increases the entire $V^{1/3}$ change by 14 % compared to a $V^{1/3}$ change effected purely by chemical ordering, i.e. $\Delta V^{1/3}$ for the fcc to fct transition for a nanoparticle is 14 % greater than that for the transition in a bulk material. So the initial crystallite size is influential in determining the overall $V^{1/3}$ change.

It has also been shown that the order parameter of an fcc phase FePt nanoparticle is difficult to ascertain via laboratory X-ray methods. The reliability of such a refined parameter increases substantially as the material orders.

5.4 Is it Possible to Determine if As-Synthesised FePt Nanoparticles are Already Ordered to Some Degree?

In **section 5.2** it was shown that sample LHN 162 of FePt nanoparticles prepared via the Durham route had a lower onset ordering temperature and smaller $\Delta V^{1/3}$ on annealing than those prepared via Sun *et al.*'s route (Sea 001). These factors could suggest the material as-synthesised had a degree of ordering greater than zero. In **section 5.3** it was shown that a large percentage of $\Delta V^{1/3}$ for a given FePt nanoparticle prepared via the Durham route upon annealing is due to the chemical ordering. Equally the order parameter of a given sample is difficult to obtain unless the degree of order is > ~0.4.

This section is designed to determine if it is possible to quantify the degree of initial ordering of any given as-synthesised particle.

The $V^{1/3}$ for any given sample is known before and after annealing of the material from XRD methods. The same is true for the crystallite size also. It has been shown that for a small fcc phase FePt nanoparticle $\Delta V^{1/3}$ varies as a function of crystallite size. This is not the case for large particles whose size does not vary on annealing. Using data obtained in this study it is possible to plot the $\Delta V^{1/3}$ versus crystallite size for a number of samples. In the case of fcc particles before annealing, this relationship is denoted as $V^{1/3}{}_0$, i.e. the $V^{1/3}$ before annealing. For fct particles after annealing the same relationship is denoted $V^{1/3}{}_F$, i.e. the $V^{1/3}$ after annealing (final). By subtracting $V_F^{1/3}$ from $V_0^{1/3}$ a curve indicating the variation of $\Delta V^{1/3}$ as a function of crystallite size is produced. It is shown schematically in **figure 5.98**.

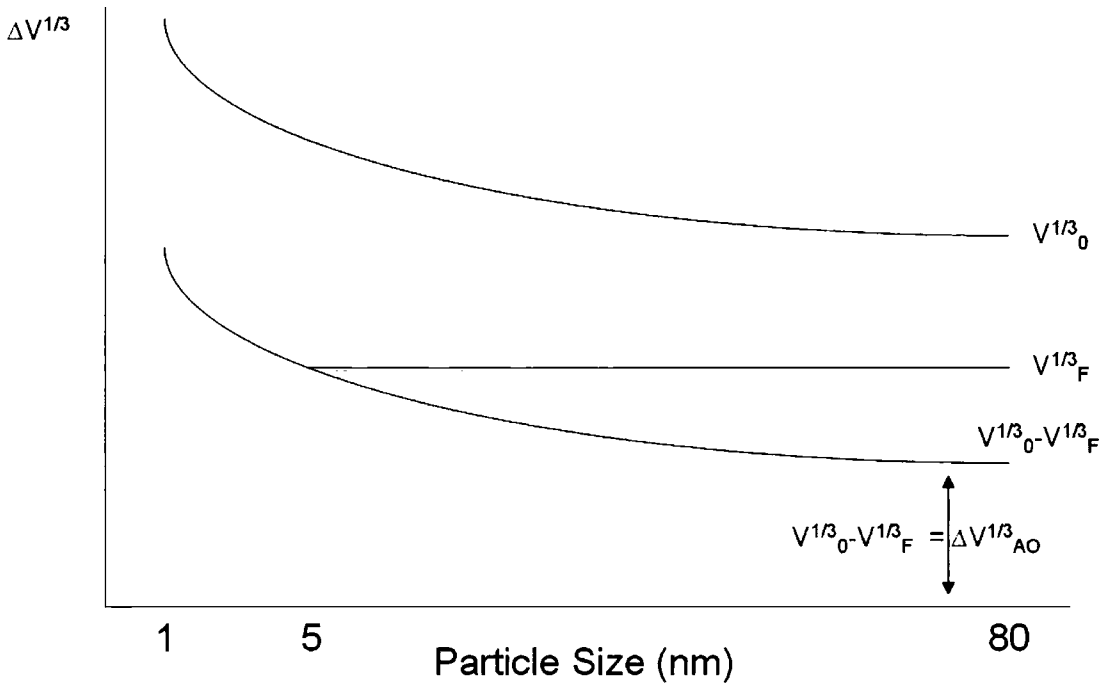

Figure 5.19 A schematic detailing three curves; one, labelled $V_0^{1/3}$ is the initial $\Delta V^{1/3}$ against crystallite size, two, labelled $V_F^{1/3}$, is the final $\Delta V^{1/3}$ against crystallite size and the third curve, $\Delta V^{1/3}{}_{AO}$, is the curve obtained from the subtraction of $V_F^{1/3}$ from $V_0^{1/3}$.

At large particle sizes $V^{1/3}{}_F$-$V^{1/3}{}_0$ does not vary. The value of $\Delta V^{1/3}$ at that point (~ 80 nm or greater in **figure 5.19**) can be termed $\Delta V^{1/3}{}_{AO}$ – the $\Delta V^{1/3}$ as a result of atomic ordering with no contribution from crystallite growth.

It has been shown in **section 5.4.2** that for an FePt particle of infinite size (i.e. bulk fcc material), the $\Delta V^{1/3}$ upon ordering from the fcc to fct phase is 0.043 Å. The $\Delta V^{1/3}$ for each FePt nanoparticle synthesised via the Durham route can be calculated also.

Table 5.4 shows the $\Delta V^{1/3}$ for each sample and the difference between it and the calculated value of $\Delta V^{1/3}$ for an infinite sized particle is also shown.

Sample Number	□V$^{1/3}$ (Å)	□V$^{1/3}$sample – □V$^{1/3}$infinite sized particle (Å)
1	0.09	0.05
2	-0.01	-0.06
3	-0.06	0.06
4	-0.03	-0.03
5	0.10	0.01
6	0.02	0.02
7	0.06	-0.02
8	0.06	-0.01
9	0.03	-0.01
10	0.03	0.04
11	0.03	0.03
12	0.09	0.02
13	0.07	0.05
14	0.07	0.03
15	0.09	-0.02
16	0.07	0.05

Table 5.4 A table showing the $\Delta V^{1/3}$ upon annealing for each given FePt nanoparticle sample as well as the $V^{1/3}$ difference between nanoparticle samples and an infinite sized material.

The difference between the $\Delta V^{1/3}$ of an infinitely sized (bulk) particle and actual nanoparticle samples ranges from -0.06 to +0.06. 10 of the nanoparticle samples exhibit a greater $\Delta V^{1/3}$ than bulk particles. However, as some also show a lesser $\Delta V^{1/3}$ than bulk particles it is not possible from these data to determine the contribution to $\Delta V^{1/3}$ from crystallite growth alone, separating the overall $\Delta V^{1/3}$ into two discrete contributions from crystallite growth and atomic ordering. For transparency, had all 16 nanoparticle samples exhibited a greater $\Delta V^{1/3}$ than bulk particles upon annealing it would have at least been possible to state a lower limit for the contribution of crystallite growth to $\Delta V^{1/3}$.

5.5 Do the change in $V^{1/3}$ increase in order parameter and increase in crystallite size all occur at the same temperature?

5.5.1 Introduction

Ultimately monodisperse fct FePt nanoparticles are desired. It has been shown that the ordering process can be monitored by following the order parameter as a function of temperature or the reduction in sample $V^{1/3}$; this is determined by both ordering and particle size growth. By observing and monitoring the order parameter, $V^{1/3}$ and crystallite size, it may be possible to determine which occurs first. It may also expose trends specific to certain synthetic conditions.

5.5.2 Defining $V^{1/3}_{TF}$, OP_{TF} and $Size_{TF}$

A schematic graphical representation is useful here. **Figure 5.20** and **figure 5.21** describe OP_{TF} and $Size_{TF}$ schematically where OP_{TF} (TF = final temperature) is the temperature at which the order parameter stops changing and $Size_{TF}$ is the final temperature at which the crystallite size varies. $V^{1/3}_{TF}$ is the point at which the $V^{1/3}$ on warming matches that on cooling. These effects can be seen in **figures 5.4f, h and k.** For example in the case of sample LHN 162, and as seen in **figures 5.4f,h** and **k**, the value of $V^{1/3}_{TF}$ is ~ 800 K, OP_{TF} is 877 K (the final temperature to which the sample was heated) and $Size_{TF}$ is also 877 K.

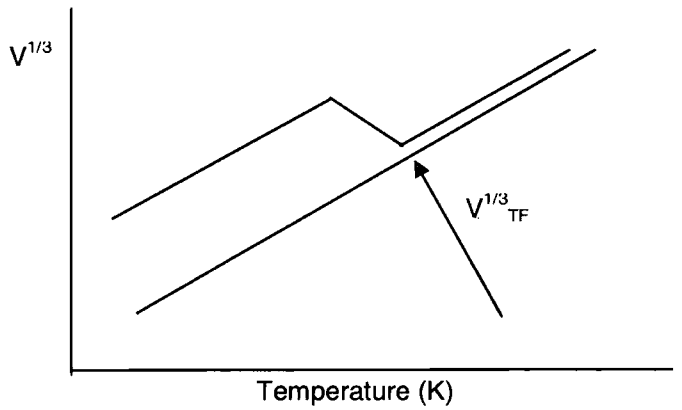

Figure 5.20 A schematic diagram defining $V^{1/3}$ as the point at which the order parameter stops increasing during any given measurement.

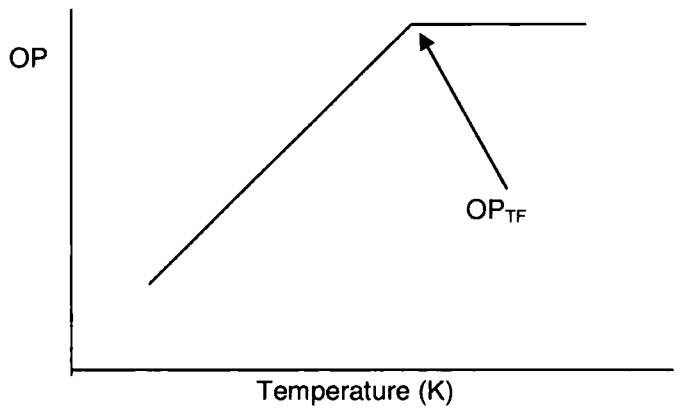

Figure 5.21 A schematic diagram defining OP_{TF} as the point at which the order parameter stops increasing during any given measurement.

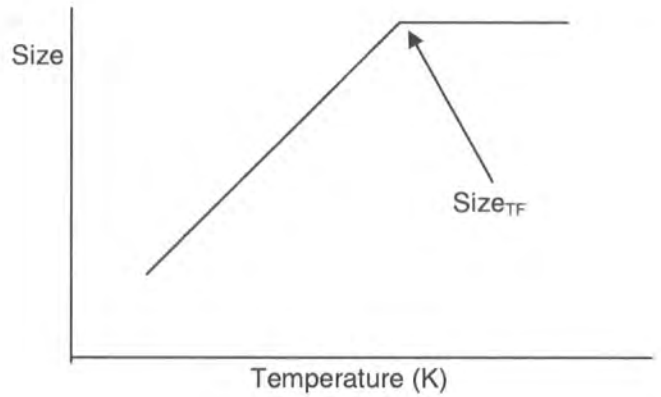

Figure 5.22 A schematic diagram defining $Size_{TF}$ as the point at which the crystallite size stops increasing during any given measurement.

5.5.3 Results and discussion

Figure 5.23 shows the values of $\Delta V^{1/3}{}_{TF}$, OP_{TF} and $Size_{TF}$ for each of the samples studied. The data are presented as a bar chart for ease of comparison.

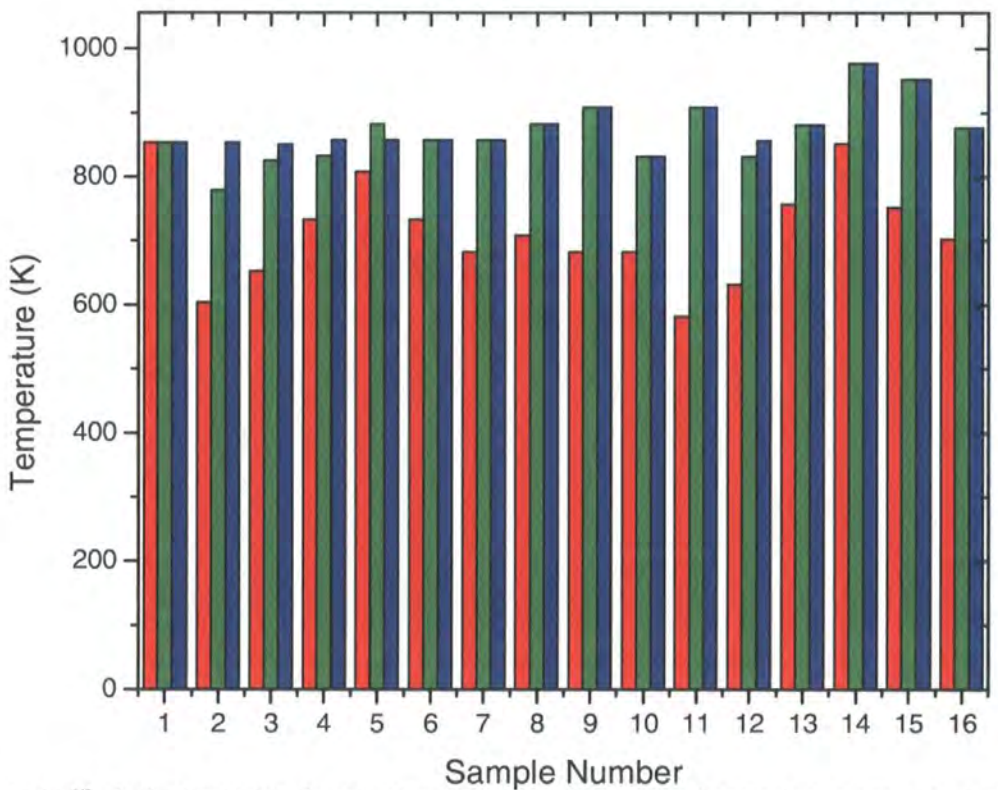

Figure 5.23 $V^{1/3}{}_{TF}$ (red column), OP_{TF} (green column) and $Size_{TF}$ (blue column) against sample number. Typically the final temperature was also the temperature at which the $Size_{TF}$ value was recorded.

The most striking aspect of the data shown in **figure 5.23** is that $V^{1/3}_{TF}$ is consistently lower than that of OP_{TF} or $Size_{TF}$. The latter two parameters are generally comparable to one another. The value of OP_{TF} varies from the value of $Size_{TF}$ by ±75 K (in 11 out of 16 samples $OP_{TF} = Size_{TF}$). In the large majority of cases $\Delta V^{1/3}_{TF}$ is significantly lower than either OP_{TF} or $Size_{TF}$. Since the major contribution to volume reduction is the fcc to fct phase transition on ordering this suggests that in these cases the particles have undergone the phase transition from a cubic system to a tetragonal one before reaching full order and also before they are fully sintered. This indirect observation of ordering without significant size growth suggests that the stoichiometry of individual particles is close to 1:1 allowing the phase transition to occur. It also suggests that small particles with a high magnetocrystalline anisotropy can be best obtained at lower temperatures than those at which full ordering is seen crystallographically. It may also be impossible to prepare particles that are crystallographically 'fully-ordered' below a certain critical size (at low sizes a significant fraction of atoms will be at the surface). Other work in the group[24] in which ferromagnetic fct particles have been prepared directly in solution with sizes of ~ 3-4 nm have had order parameters in the range of 0.4 – 0.6.

5.5.4 Does the surfactant used in a given synthesis affect the $V^{1/3}_{TF}$?

Having observed that the $V^{1/3}_{TF}$ of a given sample is lower than the OP_{TF} and $Size_{TF}$ values in the majority of cases investigated, and proposed a link between this and the true ordering of FePt nanoparticles in **section 5.3.5.2**, it is possible that the $V^{1/3}_{TF}$ for samples synthesised in the presence of a given surfactant is different to that when another surfactant is used.

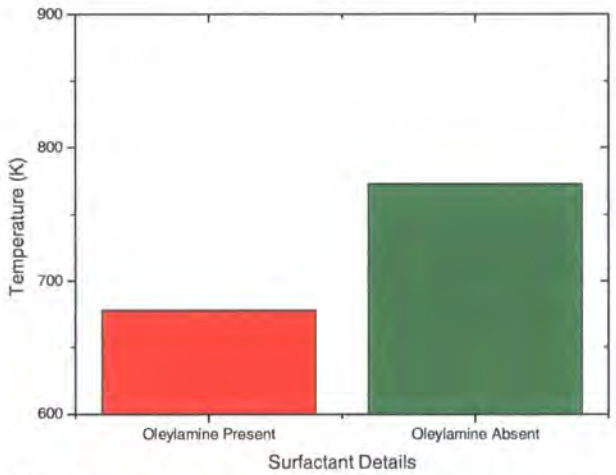

Figure 5.24 The average $V^{1/3}_{TF}$ of samples when oleylamine was present (10 samples) in the synthesis to when it wasn't (6 samples).

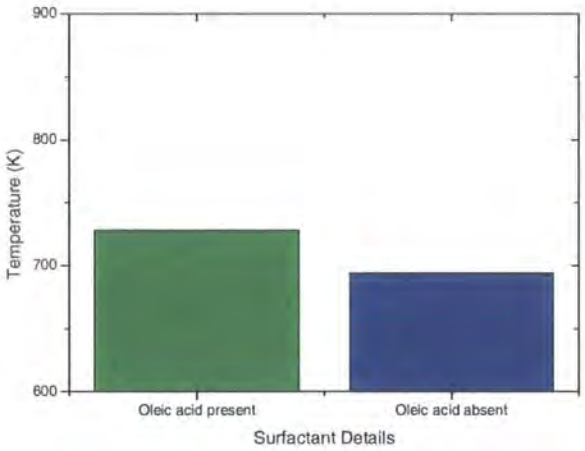

Figure 5.25 The average $V^{1/3}_{TF}$ of samples when oleic acid was present (6 samples) in the synthesis to when it wasn't (10 samples).

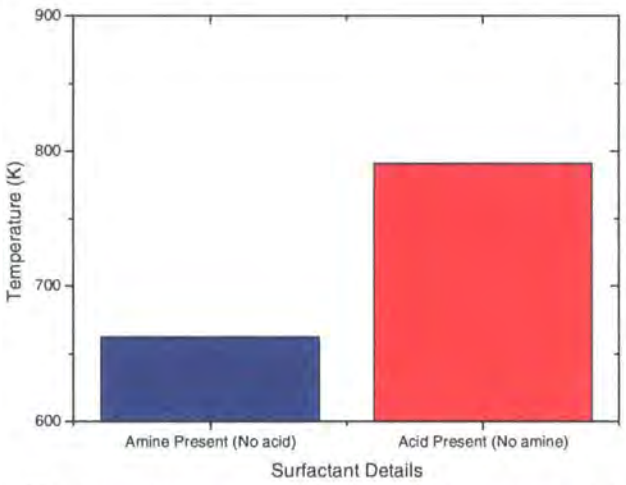

Figure 5.26 The average $V^{1/3}_{TF}$ of samples when amine was present in the synthesis but no acid (6 samples) to when acid was present but no amine (5 samples).

Figures 5.24 – 5.26 provide interesting information. There is a clear difference in the $V^{1/3}_{TF}$ values in each figure, especially **5.24** and **5.26**. Firstly, it has been shown in **figure 5.24** that when oleylamine is used as a surfactant, independent of any other surfactant that may or may not be present, the $V^{1/3}_{TF}$ is far lower (~ 100 K) than when it is absent from the synthesis.

Figure 5.25 extends this idea to oleic acid, and in that case the $(\Delta V(^{1/3}))_{TF}$ is greater when oleic acid is present, and lower when it's absent. This is the opposite effect to oleylamine, though of a lesser magnitude (~ 35 K).

Figure 5.26 takes a wider range of samples, looking at the $(\Delta V(^{1/3}))_{TF}$ when any amine surfactant is present, but no acids compared to there being any acid, but no amines, present. The difference in this case is large also (~ 130 K).

These data can be explained by one of two possibilities:

1. When amine is present in some form as a surfactant, it provides better control of particle stoichiometry, allowing particles to anneal without having to sinter. For this reason, the $\Delta V^{1/3}$ is able to finish sooner ($\Delta V^{1/3}{}_{TF}$ is lower).

2. The amine surfactant is more weakly bound to the surface of FePt nanoparticles and is therefore burned off more swiftly; this allows the resultant surfactant-free (or those with a lesser surfactant coating) particles to agglomerate and reach the ideal stoichiometry more quickly.

It is possible to check if option (2) is occurring by comparing the difference in size between nanoparticles at the start of the experiment and the point at which $\Delta V^{1/3}$ begins to vary for samples made with acid surfactants only to those made with amine surfactants only. The average difference for the six acid only surfactant samples is 2.8 (6) nm and for the five amine only surfactant samples it is 3.9 (2) nm. These data suggest that option two is occurring because the particles are greater in size when amine surfactants were used. This can be checked by comparing $V^{1/3}{}_{TF}$. If the size of samples when only amine surfactants were used is significantly greater than when acid/other surfactants were used, then agglomeration is occurring and option (2) is the mechanism in place. The average $V^{1/3}{}_{TF}$ for samples where only amine surfactants have been used is 662 K. When amine is not present it is 809 K. These values are significantly different, indicating agglomeration, and therefore option (2) is occurring.

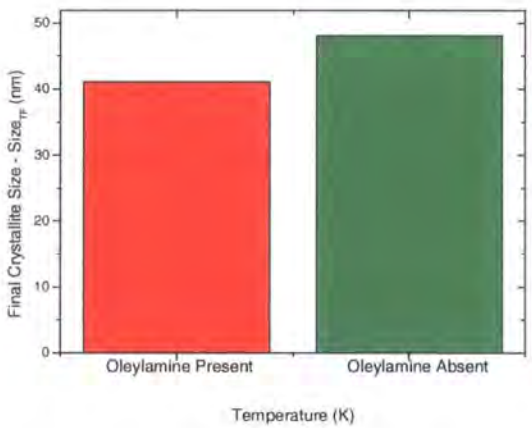

Figure 5.27 A graph comparing the Size$_{TF}$ of samples when oleylamine was present (10 samples) in the synthesis to when it wasn't (6 samples).

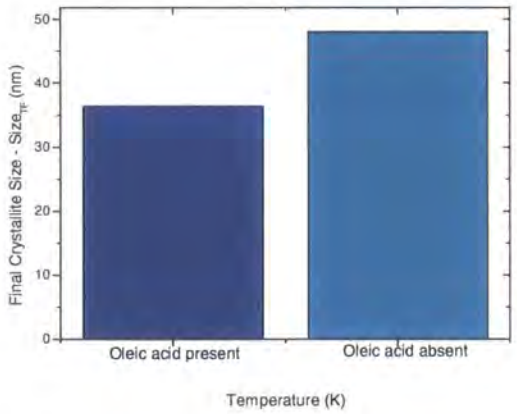

Figure 5.28 A graph comparing the Size$_{TF}$ of samples when oleic acid was present (10 samples) in the synthesis to when it wasn't (6 samples).

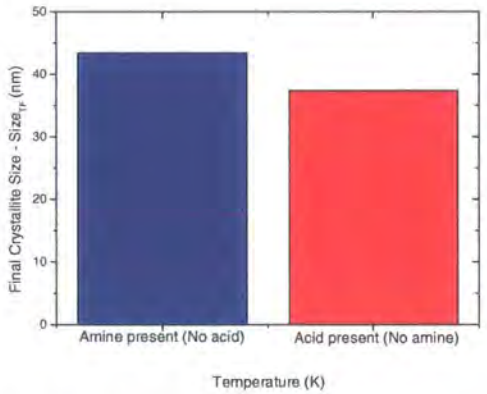

Figure 5.29 A graph comparing the Size$_{TF}$ of samples when amine was present but no acid(6 samples) in the synthesis to when acid was present but no amine (5 samples).

Figures 5.27-5.29 indicate that when amines are used as the surfactant, either in addition to acids, or more significantly as an alternative, the final crystallite size of the nanoparticles is greater (although the effect is small compared to that of the $V^{1/3}{}_{TF}$ change). These data suggest the opposite to those presented in **figures 5.24-5.26**, i.e. that the presence of amines does less than the presence of acid to hinder sintering. If the data are to be believed, the use of amine surfactants allows for a phase transition at a lower temperature but can also lead to greater sintering. It should be noted that according to **figure 5.23** the $V^{1/3}{}_{TF}$ is at a lower temperature than the Size$_{TF}$. This means that in the case of nanoparticles synthesised in the presence of amines, after the phase transition has occurred the $V^{1/3}{}_{TF}$ does not change further, whereas when acids are present this effect is not seen as the sintering is happening concurrently with the ordering process.

5.6 Conclusion

Initially a comparison between the ordering process of an FePt nanoparticle synthesised via the method developed by Sun *et al.* and FePt nanoparticles made via the Durham route was undertaken. This showed that when the two syntheses are performed under conditions as similar as possible to each other (excepting those which are integral to the given method) the temperature at which the nanoparticles undergo a phase transition from the fcc to fct phase is at least ~ 100 K lower for the Durham route. The transition also occurs over a narrower temperature range. This provides a strong argument for the use of the Durham synthetic method over that developed by Sun *et al.* The temperature is lower so if the production was scaled up the cost would be less when annealing the nanoparticles, as well as the fact that by providing less heat the sintering of nanoparticles should be reduced and this in turn will aid the control of the size and shape of the nanoparticles.

When investigating the ordering process the first conclusion is that by a combination of VTXRD studies and Rietveld refinement a large amount of information can be accrued and these data are useful when observing the ordering process – they provide a variety of important information. These details are for example the order parameter of a sample at a given temperature and how it varies as a function of temperature. Using these data the ordering temperature for a given sample can be determined. Other important parameters which provide information about the ordering process are primarily the (volume$^{1/3}$) and the crystallite size. These three parameters can all be observed as a function of temperature using the methods detailed herein and they are important in real terms as they allow the determination of which sample (and thus conditions) yield the lowest ordering temperature, the smallest crystallites after annealing (or least altered) and the sample which has ordered most fully.

It has been shown that using the $V^{1/3}$ to describe the effective cell length, as opposed to using the individual lattice parameters, is scientifically sound. It has also been shown that the reliability of the order parameter increases as the order parameter increases, but that it is unreliable at low values (< 0.4).

It has been shown that particles prepared via the Durham route have a smaller $\Delta V^{1/3}$ on ordering and a greater order parameter. This suggests that the as-synthesised material has a greater intrinsic order than samples prepared via Sun *et al.*'s method.

By examining a large selection of data certain trends have been noticed such as a larger crystallite size when synthesised indicates the $V^{1/3}$ is smaller and that a larger crystallite size means the $\Delta V^{1/3}$ on annealing is less. These trends provide information which will allow greater control of FePt nanoparticles synthesis.

It has been shown that it is not possible to determine if an as-synthesised nanoparticle is ordered to some degree.

The $\Delta V^{1/3}$ and Δ_{OP} are not parallel occurrences. This means that a material which is ordering is likely to become tetragonal, and undergo some atomic rearrangement before the order parameter has fully altered. Certain particles may not have a 1:1 stoichiometry and on continued particle growth they obtain a stoichiometry closer to the ideal 1:1. This allows them to order further as for full ordering an exact 1:1 stoichiometry is required. It may be impossible to get a fully ordered nanoparticle under a critical size for this reason.

Amine surfactants allow transformation from the fcc to fct phase at a lower temperature than acid surfactants. However, sintering occurs more readily when amine is used as a surfactant also. It appears that the amine is burnt off more swiftly than acid surfactants, allowing the FePt nanoparticles to agglomerate more quickly and reach ideal stoichiometries (and therefore order) more quickly; at a lower temperature.

5.7 References

1. S. H. Sun, C. B. Murray, D. Weller, L. Folks and A. Moser, Science, 2000, 287, 1989-1992.

2. B. J. Hwang, L. S. Sarma, J. M. Chen, C. H. Chen, S. C. Shih, G. R. Wang, D. G. Liu, J. F. Lee and M. T. Tang, Journal of the American Chemical Society, 2005, 127, 11140-11145.

3. T. J. Klemmer, C. Liu, N. Shukla, X. W. Wu, D. Weller, M. Tanase, D. E. Laughlin and W. A. Soffa, Journal of Magnetism and Magnetic Materials, 2003, 266, 79-87.

5. J. S. O. Evans, Fortran 77 routine, University of Durham, 1999.

5. A. E. Clarke, Ferromagnetic Materials: A Handbook on the Properties of Magnetically Ordered Substances Vol. 1, North–Holland, Amsterdam, 1980.

6. T. J. Klemmer, N. Shukla, C. Liu, X. W. Wu, E. B. Svedberg, O. Mryasov, R. W. Chantrell, D. Weller, M. Tanase and D. E. Laughlin, Applied Physics Letters, 2002, 81, 2220-2222.

7. S. Saita and S. Maenosono, Chemistry of Materials, 2005, 17, 3705-3710.

8. M. Chen, J. P. Liu and S. H. Sun, Journal of the American Chemical Society, 2004, 126, 8394-8395.

9. K. Barmak, J. Kim, D. C. Berry, W. N. Hanani, K. Wierman, E. B. Svedberg and J. K. Howard, Journal of Applied Physics, 2005, 97.

10. H. Kanazawa, G. Lauhoff and T. Suzuki, Journal of Applied Physics, 2000, 87, 6143-6145.

11. A. R. Denton and N. W. Ashcroft, Physical Review A, 1991, 43, 3161-3165.

12. L. Vegard, Z. Phys., 1921, 5, 17.

13. B. D. Cullity, Elements of X-ray diffraction, 2nd edn., Addison-Wesley Publishing Company, Inc., 1978.

15. B. Stahl, J. Ellrich, R. Theissmann, M. Ghafari, S. Bhattacharya, H. Hahn, N. S. Gajbhiye, D. Kramer, R. N. Viswanath, J. Weissmuller and H. Gleiter, Physical Review B, 2003, 67.

15. H. Lipson, D. Schoenburg and G. V. Stupart, Journal of the institute of metals, 1941, 67, 333-340.

16. M. Fukuhara, Physics Letters A, 2003, 313, 427-430.

17. A. Cimino, P. Porta and M. Valigi, Journal of the American Ceramic Society, 1966, 49, 152-&.

18. H. K. Schmid, Journal of the American Ceramic Society, 1987, 70, 367-376.

19. S. Tsunekawa, R. Sahara, Y. Kawazoe and K. Ishikawa, Applied Surface Science, 1999, 152, 53-56.

20. Wasserma.Hj and J. S. Vermaak, Surface Science, 1970, 22, 164-&.

21. Wasserma.Hj and J. S. Vermaak, Surface Science, 1972, 32, 168-&.

22. J. S. Vermaak and Kuhlmannw.D, Journal of Physical Chemistry, 1968, 72, 4150-&.

23. T. Kuji, Y. Matsumura, H. Uchida and T. Aizawa, Journal of Alloys and Compounds, 2002, 330, 718-722.

24. Nguyen, H.L., Howard, L.E.M., Stinton, G.W., Giblin, S.R., Tanner, B.K., Terry, I., Hughes, A.K., Ross, I.M., Serres, A., and Evans, J.S.O., *Chem. Mater.*, 2006, 18, 26, 6414 – 6424.

Chapter 6 - An Investigation into the Local Structure of FePt Nanoparticles via EXAFS

6.1 Introduction

Performing EXAFS experiments on FePt nanoparticles potentially provides information about the short-range order of the materials, which X-ray diffraction techniques are unable to obtain. Typically studies can yield data pertaining to the near-edge X-ray absorption spectroscopy region (XANES) as well as the extended X-ray absorption fine structure region (EXAFS). XANES data are collected within ~50 eV of the absorption edge and EXAFS further above the edge. These techniques have been applied successfully to studies of nanoparticles[1, 2]. XANES data provide insight into the oxidation state of the atoms in a nanoparticle which are absorbing the radiation and the electronic environment. EXAFS data provide evidence of the number of atoms absorbing the radiation, the type and the distance between the absorbing atom and its neighbours[3].

In the case of bimetallic nanoparticle alloys little work has been done to understand the distribution of atoms (alloying extent) in a given nanoparticle. This distribution will be influenced by factors such as the relative strengths of A-A, B-B and A-B interactions as well as the tendencies of individual atoms to locate at particle surfaces. Hwang *et al*[3]. developed a methodology to determine the alloying extent in such materials. In doing so they identified seven categories of atoms in a bimetallic nanoparticle alloy (although there is an infinite number of possible arrangements). **Figures 6.1a** to **6.1e**[3] show some of these possible arrangements.

Figure 6.1a The two components exist as separate clusters of atoms combining as one nanoparticle.

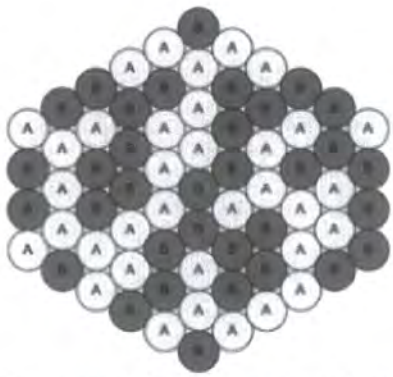

Figure 6.1b The alloying extent is at its greatest. The nanoparticle contains a perfectly random distribution of A and B atoms.

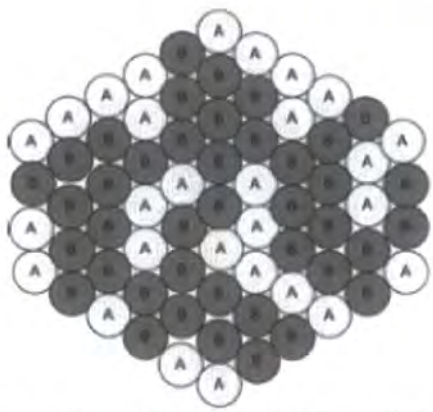

Figure 6.1c Atom type A coordinates preferentially with atom type A; atom type B coordinates preferentially with atom type B. B-B clustering dominates resulting in a greater dispersion of atom type A throughout the nanoparticle. The core is rich in atom type B; the shell in atom type A.

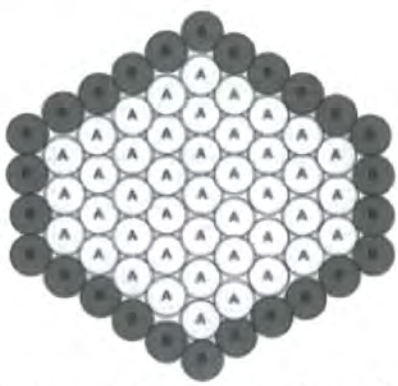

Figure 6.1d The nanoparticle exhibits a core-shell morphology. The coordination number of A will be greater than that of B.

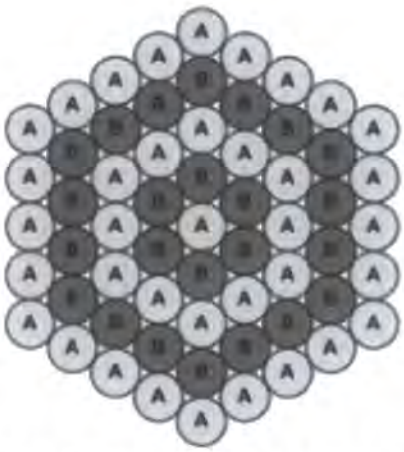

Figure 6.1e A layered morphology. A preferentially coordinates with B and vice-versa, leading to shells of A and B type atoms.

In terms of FePt nanoparticles a core-shell morphology has been suggested by Chen *et al.* [4] and discussed in **chapters 1 and 5** for nanoparticles prepared using the polyol method developed by Sun *et al.* [5]. **Figure 6.1d** shows a full core-shell morphology but **6.1c** also describes a structure within which the core is rich in one atom type and the shell in another. Either of these structures would be possible for FePt nanoparticles if a core-shell morphology is believed to be present.

For a material with some degree of ordering perfect alloying would be required. It may be possible to determine if the distribution in **figure 6.1a** exists as the XRD pattern may be different to that expected for an FePt nanoparticle, i.e. Fe and Pt metal peaks may be seen. In the case of **figure 6.1d** XRD spectra may only exhibit the type A atom core leading to a different cell parameter.

It would be expected that when observing the local structure of fcc phase FePt nanoparticles prepared via the literature route, there would be an abundance of Fe-Fe and Pt-Pt nearest neighbours. These materials only transform to the fct phase at high temperatures and the reason for this is believed to be that upon synthesis the material comprises large clusters of Fe or Pt atoms. In the case of fcc phase material prepared via the Durham route presented in **chapter 3**, it is thought that Fe-Pt nearest neighbours will be more abundant (**figure 6.1b** for example, as opposed to **6.1d** where Fe-Fe and Pt-Pt interactions would be much greater). This stems from the belief that upon preparation the material is composed of fewer clusters of Fe or Pt atoms; the atoms are more intimately mixed. Stoichiometry of FePt nanoparticles will affect the atomic distribution also.

This chapter details the experimental aims defined before collecting any EXAFS data, the collection of those data, the manipulation of those data and finally the modelling of those data in order to better understand the structures of the FePt nanoparticles.

6.2 Experimental

6.2.1 Experiment Aims

Essentially there were five aims for these experiments. These were:

1. Obtain EXAFS measurements via utilisation of synchrotron radiation on FePt samples prepared in Durham and model said data via least squares refinement.
2. Does iron edge EXAFS data provide any advantages over Pt edge data or vice-versa?
3. Do Durham nanoparticles show a different structural evolution upon annealing compared to those prepared via the literature route?
4. By looking at a series of samples from as-synthesised material to annealed material is it possible to observe structural changes?
5. Are as-synthesised fct phase nanoparticles different to those converted to fct phase via annealing?

6.2.2 Experimental

In order to fulfil the aims of these EXAFS experiments, three classes of sample were used:

1. Samples synthesised via the conventional thermolysis route described in the literature. These samples were as-synthesised fcc FePt nanoparticles. Additionally, some of these samples were annealed in order for conversion to the fct phase to occur.
2. Comparable samples prepared via the Durham route were synthesised. These were as-synthesised fcc phase materials; some samples were annealed in order to effect the transformation to the fct phase.
3. As-synthesised fct phase materials prepared via a modified Durham route synthesis described in **chapter 3**.

The experimental method is described in detail in **chapter 3.**

6.2.3 Data Collected

10 data sets are presented in this chapter. Data were collected as described in **chapter 2.4.3.** **Table 6.1** details each of the samples from which these data sets were obtained.

Experiment No.	*Sample code*	*Synthetic route*	*Post-synthetic annealed?*	*Solvent*	*Surfactants*	*Size (nm)*
1	LHN 152	Durham	No	Tetracosane	C-12 aniline	4.06
2	LHN 133	Durham	No	Docosane	Oleyl amine, AR-phosphine	3.40
3	LHN 142	Durham	No	Tetracosane	Oleylamine, aniline	7.40
4	LHN 055	Durham (Microwave)	No	Octyl ether	Oleylamine	15.90
5	LHN129a	Durham	No	Nonadecane	Oleic acid	N / A
6	LHN 129b	Durham	Yes – to 230 ℃	Nonadecane	Oleic acid	N / A
7	LHN 129c	Durham	Yes – to 430 ℃	Nonadecane	Oleic acid	N / A
8	LHN129d	Durham	Yes – to 630 ℃	Nonadecane	Oleic acid	N / A
9	LHN138	Durham	No	Nonadecane	Oleic Acid	N / A
10	Sea 001	Literature	Yes	Octyl ether	Oleylamine/Oleic acid	31.53

Table 6.1 A table detailing the samples studied using EXAFS including particle size, synthetic method and synthetic condition information.

6.3 Data analysis

6.3.1 Introduction

In order to fulfil the aims of the EXAFS experiments and to ultimately understand the data collected, a full analysis of the data was required. This incorporated three sections, the summation of data, the subtraction of background signal and finally the fitting of a calculated model to the data.

6.3.2 Preparation of data for modelling

Three sets of data were collected for each sample at each energy edge. These data were then summed using Excalib (**chapter 2**). An example of a summed data set (three individual runs) is shown in **figure 6.1**.

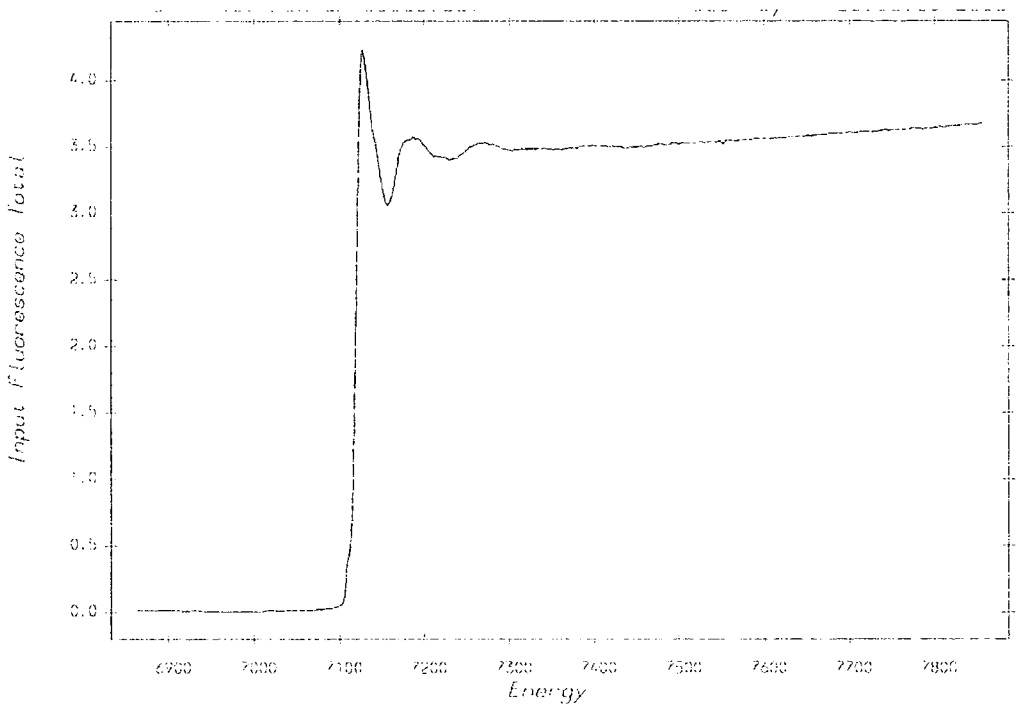

Figure 6.2 A graphical representation of the raw data obtained from a summation of three data sets obtained from EXAFS experiments with sample Sea 001 at the iron edge.

After the data sets collected relating to any given sample are summed the background component to the EXAFS spectrum is subtracted. This is performed using a program called Exspline (**chapter 2**).

6.3.3 EXAFS Data Modelling Using Excurv98

6.3.3.1 General Information

In order to build a model for EXAFS data obtained from FePt nanoparticle samples details of the expected local environment and the nearest neighbours to the centrally excited atom are required. **Figures 6.2** and **6.3** show one unit cell of an FePt nanoparticle in the fcc and fct phase respectively.

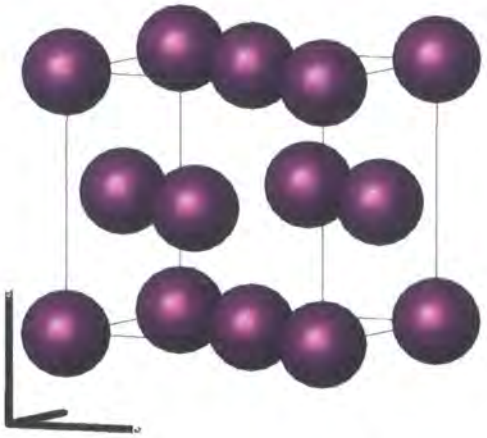

Figure 6.3 A diagram representing the face-centred cubic disordered structure of FePt nanoparticles. The purple atoms signify that each site may contain an Fe or Pt atom

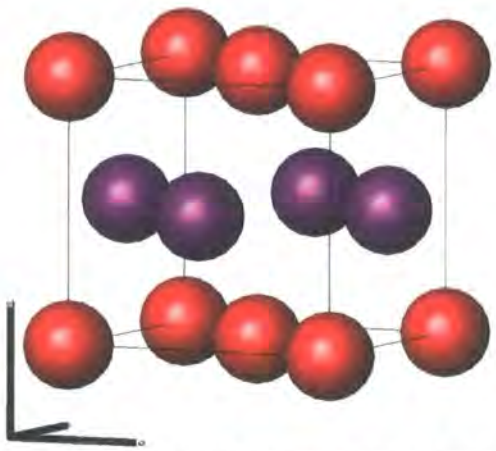

Figure 6.4 A diagram representing the face-centred tetragonal ordered structure of FePt nanoparticles. The red atoms are Fe and the purple atoms Pt

In EXAFS one centrally located atom is excited by the radiation. If this is taken as the origin atom in each figure (bottom left) then all the other atoms are considered its neighbours. It is assumed that no more than the first four nearest neighbour shells will exhibit interference in the EXAFS spectrum. If a shell contributes less than 10 % of the total EXAFS amplitude then it will be hard to fit; less than 5 % and it almost certainly can't be fitted meaningfully. **Table 6.2** provides details about the number of nearest neighbours and the ratio of iron to platinum atoms in each shell for each structure type. The distance of each shell from the central atom is also provided, assuming that the *a* cell parameter is equal to the *c* cell parameter – a = c = 3.85 Å – for both fcc and fct structures.

Shell no.	1	2	3	4
Neighbours	12	6	24	12
FCC (Fe+Pt)	6(Fe) +6(Pt)	3+3	12+12	6+6
FCT (Fe+Pt)	4(Fe) +8(Pt)	6+0	8+16	12+0
Distance (Å)	2.72	3.85	4.71	5.44

Table 6.2 Information relating to the local environment of a centrally located atom in an FePt nanoparticle for fcc and fct structures.

Figure 6.4 describes the unit cell in terms of distance of nearest neighbours from the centrally located atom in order to explain how the values arrived at in **table 6.2** were obtained. The distances quoted in **table 6.2** are not strictly correct if the sample is in the fct phase since *a* does not equal *c*. They are absolutely correct only for a pseudocubic $a = c$ tetragonal material with a= 3.85 Å. However, as *a* and *c* are similar, for data fitting it was assumed that $a = c$. In addition to the distances in **table 6.2** it is important to note there will be other interactions present rather than just Fe-Pt ones. For example there could be Fe-O, Pt-O, Fe-N or Pt-N distances depending on the purity of the sample used and the surfactant or oxide present on the surface of the sample. In order to understand the data, two models were proposed for use in the EXAFS refinements. These models are described in **section 6.3.3.2** and **6.3.3.3**.

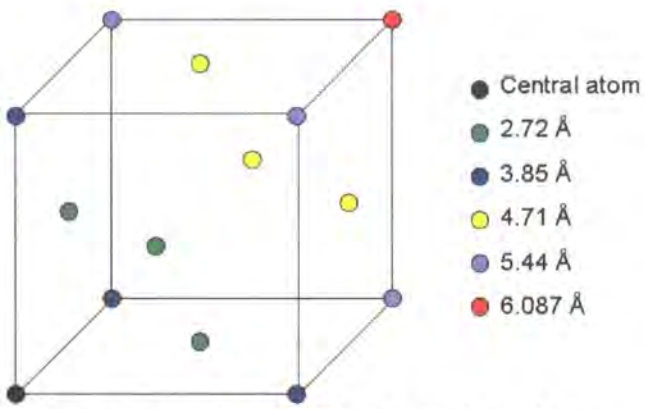

Figure 6.5 A diagram detailing the distance of each neighbour in a unit cell of FePt.

6.3.3.2 Mixed site (QA/QB model)

Each of the models presented in **sections 6.3.3.2** and **6.3.3.3** contain the same information, only it is presented in a different way. However, the reason for producing two different models is that in the first 'QA/QB' model the Pt-Pt and Pt-Fe distances are restrained to be the same when in reality they are not necessarily so. The second model allows this constraint to be removed, but otherwise incorporates the same information.

An EXAFS model will always have the same structure. The first shell will detail information relating to the central atom. The central atom is that which is excited. In the case of FePt when

EXAFS are measured at the Fe K edge this would be an Fe atom; when measured at the Pt L3 edge this would be Pt. Other shells are added to the model. Each describes one layer of neighbouring atoms, i.e all the neighbours at distance 2.72 Å will be one shell, then those at distance 3.85 Å will be another shell and so on. A shell in the EXAFS model will contain information related to the number of atoms, the distance of those atoms from the central atom, the type of atom, the Debye-Waller factor and, if it's a mixed site, the predicted occupancy of each component.

In this model the central atom can be Fe or Pt depending on the edge at which the data set being modelled was obtained. This is shell zero. Four other shells are described for the four nearest neighbours. Each of these shells can contain a mix of iron and platinum. The ratio of iron to platinum in shell one has a certain known ratio (for a fully ordered fct phase FePt nanoparticle). This ratio can be incorporated into the model by firstly defining an atom type named QA and then describing the ratio by defining the quantity perca1 in atom type QA. QA is an arbitrary name for a defined mixed Fe/Pt site composed of a certain Fe:Pt ratio. Perca1 is the percentage of atom a in site QA. Shell two has a different iron to platinum ratio. This can be modelled by defining atom type QB and describing the ratio using the quantity perca2 (percentage of atom a in QB). Shells 3 and 4 should be the same as shells 1 and 2 respectively and are described as such. The atom type is described as QA and QB in these shells also. In order to retain the ratio of iron to platinum in shells 1 and 3 the same, and also in shells 2 and 4, rules are set up governing the iron to platinum ratio. In shells 1 and 3 the ratio of iron to platinum is 0.34:0.66; in shells 2 and 4 it is 1.00:0 (in ideal fully ordered material, i.e. pure fct).

Table 6.3 provides information relating to the shells and all relevant information about each shell input to the model (when applied to Pt edge data). Nine parameters were refined. These were the four distances and their associated Debye-Waller factors and EF.

Shell	Number of atoms	Type of atom	Distance (Å)
0	1	Pt	0.0
1	12	QA	2.72
2	6	QB	3.85
3	24	QA	4.71
4	12	QB	5.44

Table 6.3 The shells and all information input to the FePt model relating to those shells.

6.3.3.3 Iron/Platinum model

The main difference between this and the mixed site model described in **6.3.3.3** is that each shell in this model describes an Fe or Pt atom type – there are no mixed sites.

The centrally excited atom can be iron or platinum depending on the data being modelled. For this description it is assumed Pt is the central atom. This is shell zero. Eight other shells are described. Shells one to four detail platinum atom type neighbours; shells five to eight detail iron atom type neighbours. Shells one and five, two and six, three and seven and four and eight share the same distance in relation to the central atom. For this reason multiple rules must be set up to ensure these distances are constrained to be equal to one another. For example, one rule must state that the distance of shell one is always equal to that of shell five. These two parameters will be refined within the model as one parameter. This also means that the number of atoms in shells one and five must be refined together as they are at the same distance. Therefore, if the number of atoms in shell one is described as a, a rule is set up such that the number of atoms in shell five is equal to 12 – a. The Debye-Waller factors in each shell pairing must also be the same.

Table 6.4 summarises this information relating to the shells and all relevant information about each shell input to the model.

Shell	Number of atoms	Type of atom	Distance (Å)
0	1	Pt	0.00
1	a	Pt	2.72
2	b	Pt	3.85
3	c	Pt	4.71
4	d	Pt	5.44
5	12-a	Fe	2.72
6	6-b	Fe	3.85
7	24-c	Fe	4.71
8	12-d	Fe	5.44

Table 6.4 General details for any FePt nanoparticle covering shells and all other relevant information.

The data in **table 6.4** are for any FePt nanoparticle. The dataset modelled in **6.3.3.4** will be done assuming it is an fct material. This allows the removal of shells 6 and 8 from any refinement model (these shells in an fct material would contain no atoms). In these shells b = 6 and d = 12. Nine parameters are refined. These are the temperature factors for shells 1-4, the distances for shells 1-4 and EF. In this model perca1 is fixed at 0.34 and perca2 at 1.00. This means site QA has a Pt:Fe ratio of 0.34:0.66 and QB 1.00:0.00, in accordance with **table 6.2**.

6.3.3.4 Which model is better?

In order to proceed one model had to be accepted over the other for use throughout all further dataset refinements. The chosen method by which to decide this was to take one data set and refine it using each proposed model. It's expected that the fit and associated R-factor would be the same for each model. If this were the case, either model could be used interchangeably.

1. QA/QB Model fit and relevant information:

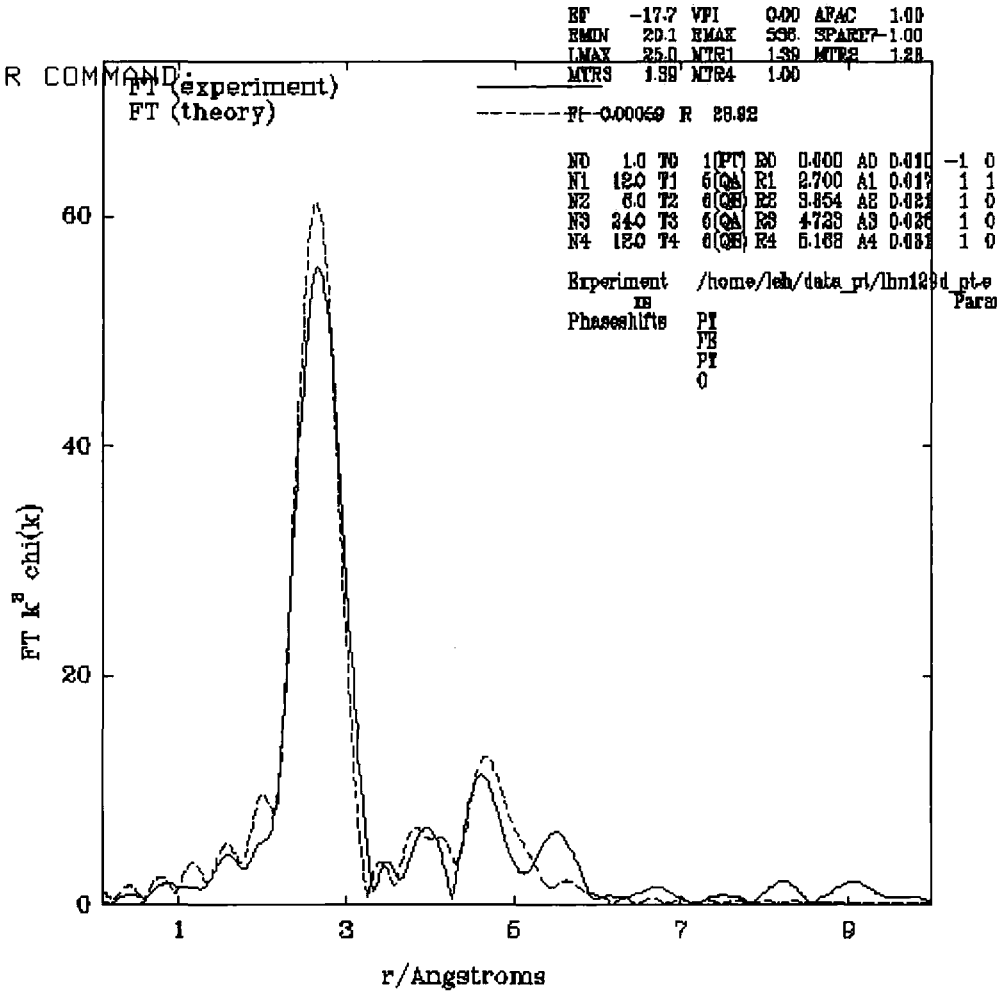

Figure 6.6 Fit of the calculated QA/QB model to the experimental data obtained from sample LHN 129d at the Pt edge (summed data set). The fit index is 28.92 %.

Refined parameters are shown in **table 6.5**.

Shell	Number of atoms	Type of atom	Distance from central atom (Å)	Pt:Fe	Debye-Waller factor
0	1	Pt	0.00	1.00:0.00	0.01
1	12	QA	2.70	0.34:0.66	0.02
2	6	QB	3.85	1.00:0.0.	0.02
3	24	QA	4.72	0.34:0.66	0.03
4	12	QB	5.16	1.00:0.00	0.03

Table 6.5 Information relating to the fit of the calculated QA/QB model to the experimental data obtained from sample LHN 129d (summed data set).

2. Pt/Fe model fit and relevant information

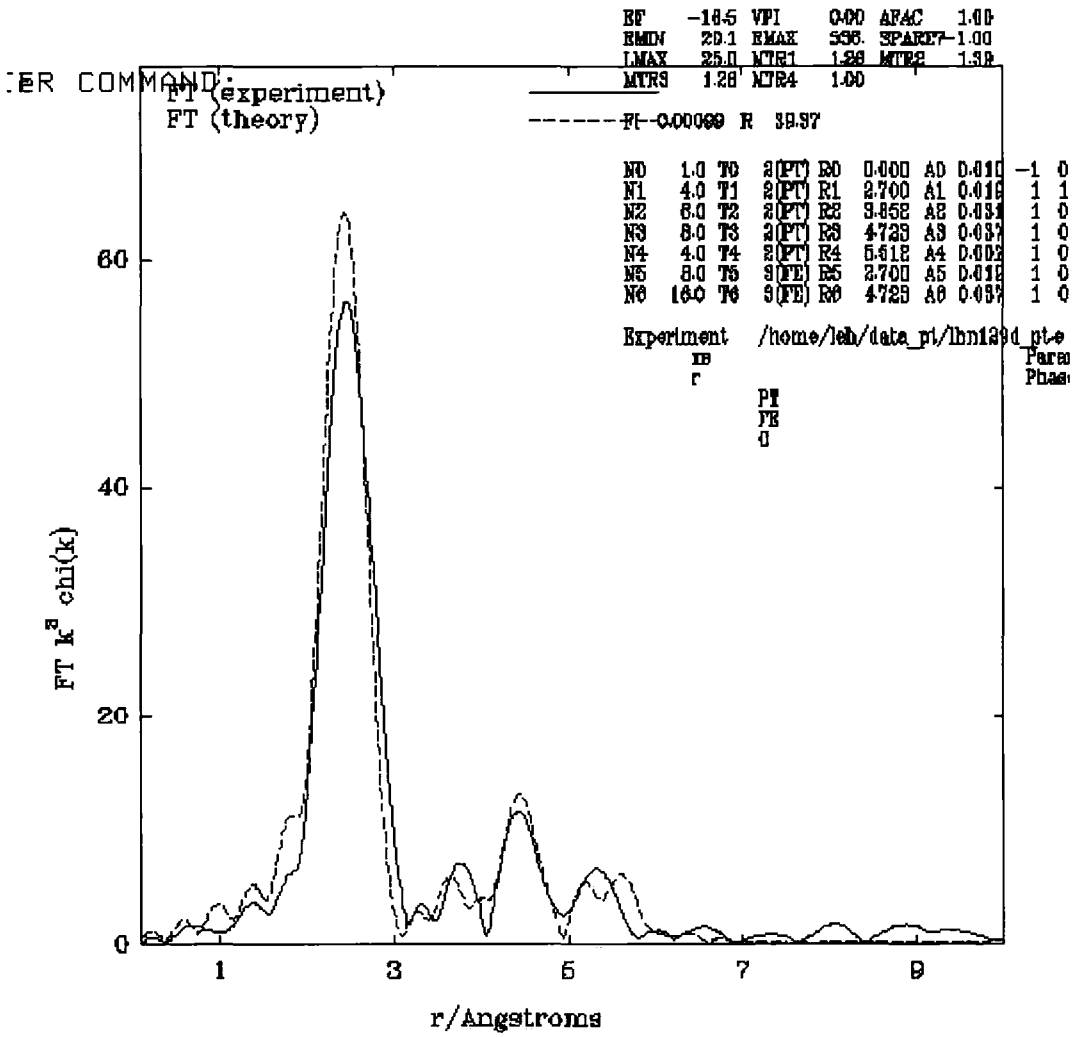

Figure 6.7 A diagram showing the fit of the calculated Fe/Pt model to the experimental data obtained from sample LHN 129d at the Pt edge (summed data set). The fit index is 39.97 %.

Refined parameters are shown in **table 6.6**.

Shell	Number of atoms	Type of atom	Distance from central atom (Å)	Debye-Waller factor
0	1	Pt	0.00	0.01
1	4	Pt	2.70	0.02
2	6	Pt	3.85	0.03
3	8	Pt	4.72	0.04
4	12	Pt	5.51	0.01
5	8	Fe	2.70	0.02
7	16	Fe	4.72	0.04

Table 6.6 A table showing the information relating to the fit of the calculated Fe / Pt model to the experimental data obtained from sample LHN 129d (summed data set).

The two models yield different R factors as well as different atomic distances and temperature factors, despite containing the same information and having the same number of degrees of freedom on refinement.

6.4 Conclusion

It is possible to model synchrotron EXAFS data and refine that model to a sensible and real minimum. Post-refinement parameters obtained on FePt nanoparticles as a result of this can be interpreted to provide information about a given sample's local structure.

However, two approaches to the creation of a model comprising the same information have been shown to yield different results, in this case at least. The most likely reason for this disparity is that Excurv98 contains a bug in the code which affects these refinements.

The QA/QB model yields the lower R-factor. For this reason this type of model will be used in further refinements. By using one approach systematically and consistently it will be possible to investigate FePt nanoparticles using EXAFS with confidence that, comparably at least, the conclusions are reliable.

6.5 Platinum edge Vs. Fe edge data

Figure 6.8 shows the EXAFS and Fourier transform of LHN129d data obtained at the Fe edge. **Figure 6.9** shows the same obtained at the Pt edge. LHN129d is an fct material by XRD. Each of the Fe and Pt edge datasets are modelled in the same way, with the adaptation that the central atom is Fe for the Fe edge and Pt for the Pt edge. Eleven parameters are refined – the shell distances and Debye-Waller factors of shells one to four, the values of perca1 and percb1 and E_F.

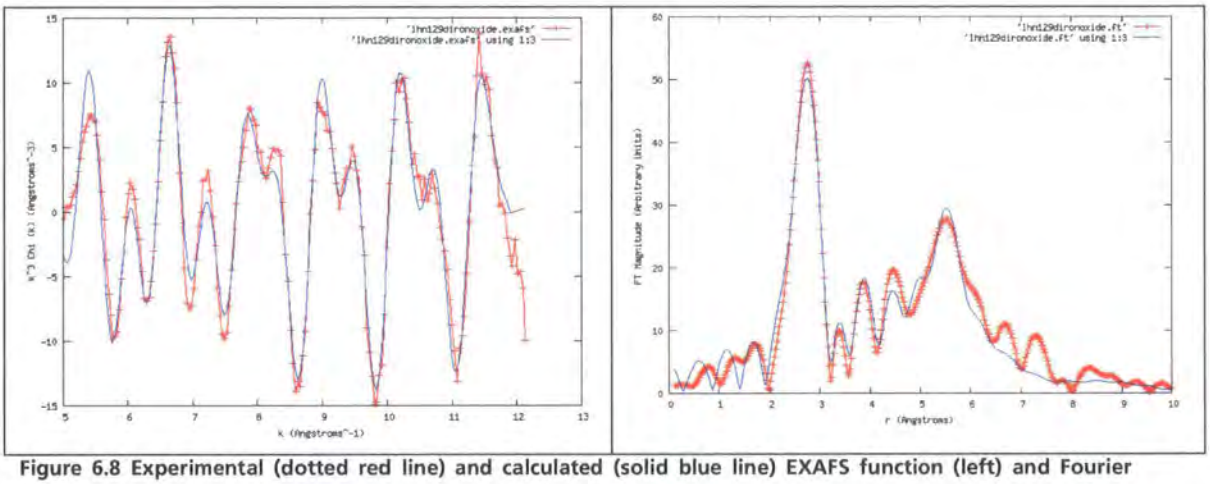

Figure 6.8 Experimental (dotted red line) and calculated (solid blue line) EXAFS function (left) and Fourier transform (right). Fe edge data, *k* range 5 -13 Å^{-1}, fit index 25.51 %.

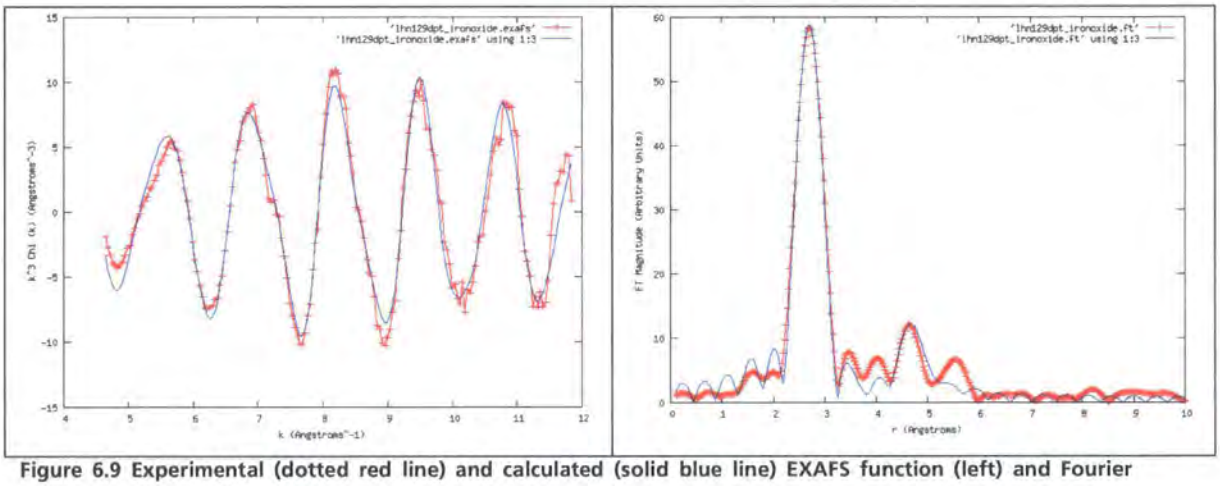

Figure 6.9 Experimental (dotted red line) and calculated (solid blue line) EXAFS function (left) and Fourier transform (right). Pt edge data, *k* range 5 -13 Å^{-1}, fit index 19.09 %.

For both refinements the same model was applied (with a different central atom). The refined parameters for each are described in **tables 6.7 and 6.8**.

Shell	Number of atoms	Type of atom	Distance from central atom (Å)	Fe:Pt composition (Fe:Pt)	Debye-Waller factor
0	1	Fe	0.00	1.00:0.00	0.01
1	12	QA	2.67	0.15:0.85	0.05
2	6	QB	3.63	0.87:0.13	0.03
3	24	QA	4.87	0.15:0.85	0.02
4	12	QB	5.55	0.87:0.13	0.02

Table 6.7 Refined parameters obtained from Fe edge data refinement

Shell	Number of atoms	Type of atom	Distance from central atom (Å)	Fe:Pt composition (Fe:Pt)	Debye-Waller factor
0	1	Pt	0.00	0.00:1.00	0.01
1	12	QA	2.70	0.42:0.58	0.02
2	6	QB	3.71	0.29:0.71	0.06
3	24	QA	4.70	0.42:0.58	0.03
4	12	QB	5.47	0.29:0.71	0.02

Table 6.8 Refined parameters obtained from Pt edge data refinement

The model's fit to the iron edge data is visually good in the main. As the distance from the central atom increases the calculated profile is less accurate. Each Debye-Waller factor is physically reasonable. Shells one and three exhibit platinum richness (more than predicted). Shells two and four indicate iron richness, close to that expected according to **table 6.2** for an fct particle.

The fit of the model to the Pt edge data is also visually good. The Debye-Waller factors are low and sensible, as is the R-factor. Shells one and three suggest an approximately equal number of platinum and iron atoms are present, where a 0.66:0.34 Fe:Pt ratio would be expected. Shells two and four are platinum rich, nearing the Fe:Pt ratio expected. The Pt edge data indicate a lesser degree of order.

Taking into consideration firstly the refined parameters relating to the first coordination shell an fct material would be expected to have Fe:Pt ratios of 0.34:0.66 and 0.66:0.34 for iron and platinum edge data respectively. The experimental data show the Fe:Pt ratio is 0.15:0.85 at the iron edge and 0.42:0.58 at the platinum edge. The iron edge data suggest the first shell is platinum rich as expected. However, the platinum edge data also indicate a platinum rich first shell, even though this surrounds a central platinum atom. The second shell yields results closer to that expected. The predicted Fe:Pt ratio is 1.00:0.00 and 0.00:1.00 for the iron and platinum edge data respectively; experimentally we observe 0.87:0.13 and 0.29:0.71.

Sample lhn129d has short range order observed by EXAFS broadly consistent with the long range order seen by XRD, i.e the data suggest some fct ordering. However, the first coordination shell is platinum rich according to both the iron and platinum edge data. The second shell is closer to that expected for an fct material. This indicates the stoichiometry is not exactly 1:1 Fe:Pt.

6.6 Durham route Vs. Literature route

It has been suggested in **chapter 5** that FePt nanoparticles prepared via the synthetic route developed in Durham have a higher degree of order than those prepared via the literature route of Sun *et al.'s*. Whilst it was not possible to determine this from the XRD data obtained, EXAFS may provide further insight due to its focus on the local structure around one central atom.

Figure 6.10 shows the EXAFS spectra obtained when measuring two samples prepared via different methods at the Pt edge. **Figure 6.11** shows the same at the Fe edge. The two samples compared are Sea001 and LHN138 (Comparable to LHN162 which was used for a similar comparison in **chapter 5**). These are both fcc phase FePt nanoparticle samples, structural details of which are given in **table 6.9**.

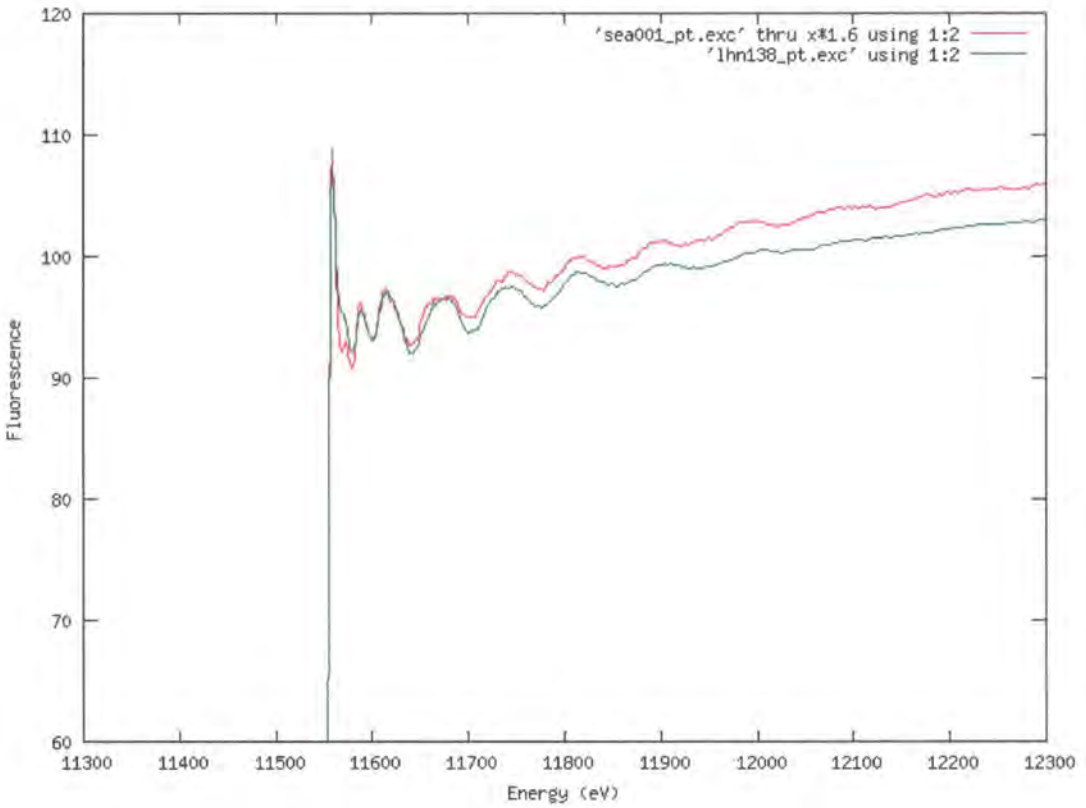

Figure 6.10 Overlay of data obtained from Pt edge measurement of Sea001 and LHN138 FePt nanoparticle samples.

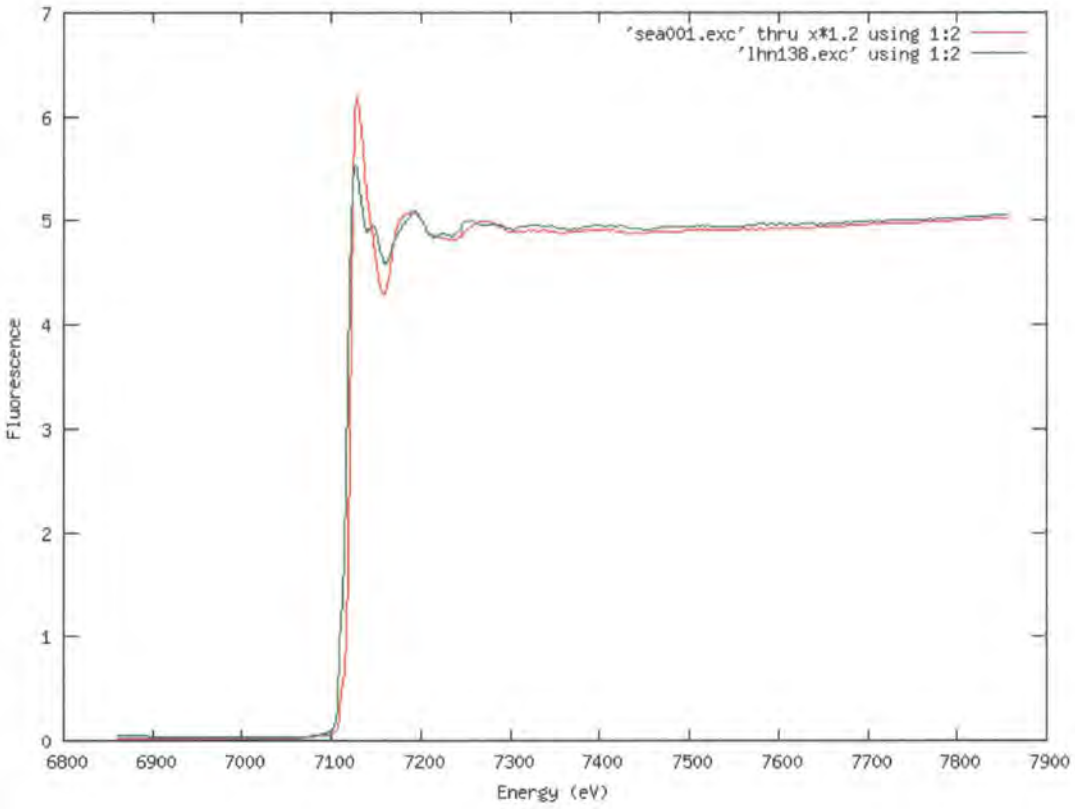

Figure 6.11 Overlay of data obtained from Fe edge measurement of Sea001 and LHN138 FePt nanoparticle samples.

Looking first at the Fe edge data it is clear that the XANES region (~ 7120 – 7170 eV) exhibits differences between the Sea001 and Lhn138 samples. There is a small shift in the initial peak, indicating that sample LHN 138 contains a higher percentage of Fe atoms in a low oxidation state than Sea001. The Sea001 sample shows greater amplitude (first peak) and fewer peaks in this region (two compared to three). This indicates the coordination of the centrally excited Fe atom in each case is different. This could suggest the presence of Fe_xO_y or Fe-surfactant coordinated at the sample surface. The Pt edge data show only minor differences between Sea001 and Lhn138 samples in the near edge region (~ 11550 – 11600 eV). The initial peaks are in the same position and the amplitude is similar suggesting a similar oxidation state. However, at the minima between the first and second peaks in the near edge region there is a different profile evident which may indicate different coordination of the Pt atom. XANES data suggest Pt (0).

Experiment No.	*Sample code*	*Synthetic route*	*Annealed*	*Solvent*	*Surfactants*	*Size (nm)*
1	*LHN 138*	*Durham*	*No*	*Octyl Ether*	*Oleyl amine*	*3.96*
2	Sea001	Sun et al.'s route	No	Octyl ether	Oleylamine/Oleic acid	2.80

Table 6.9 Structural details of two FePt samples prepared via different methods

Figures 6.12a-d show the refined EXAFS spectrum and Fourier transform of samples LHN138 and Sea001 collected at the Fe edge. **Figures 6.13a-d** show the same data collected at the Pt edge.

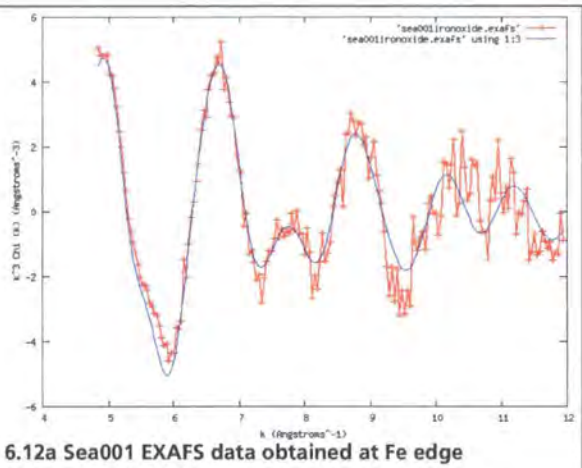

6.12a Sea001 EXAFS data obtained at Fe edge

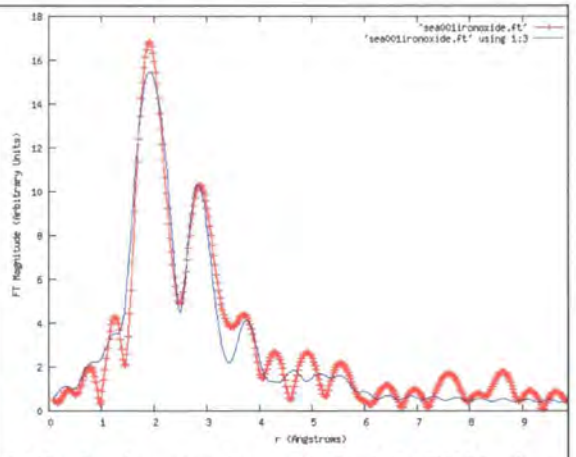

6.12b Fourier transform of Sea001 EXAFS data obtained at Fe edge, fit index of 29.47 %.

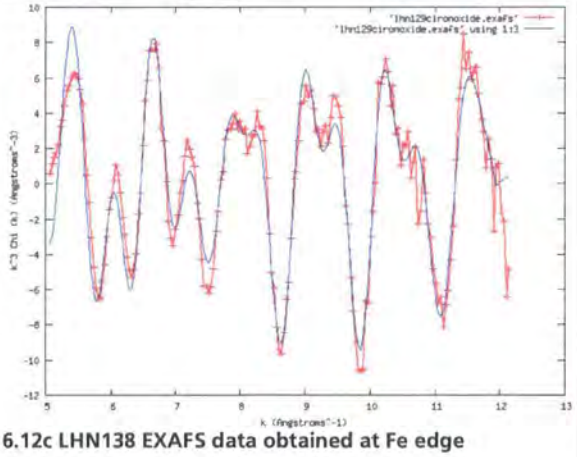

6.12c LHN138 EXAFS data obtained at Fe edge

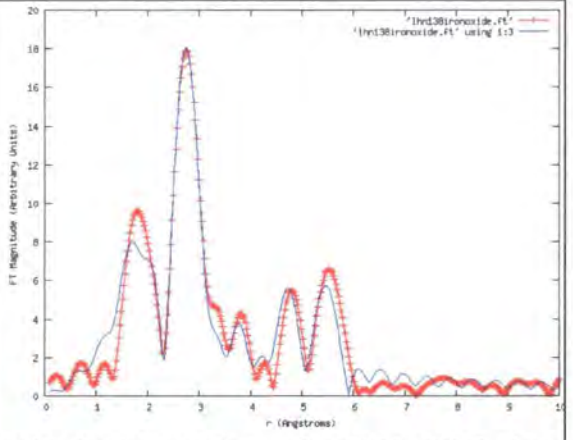

6.12d Fourier transform of LHN138 EXAFS data obtained at Fe edge, fit index of 34.91 %.

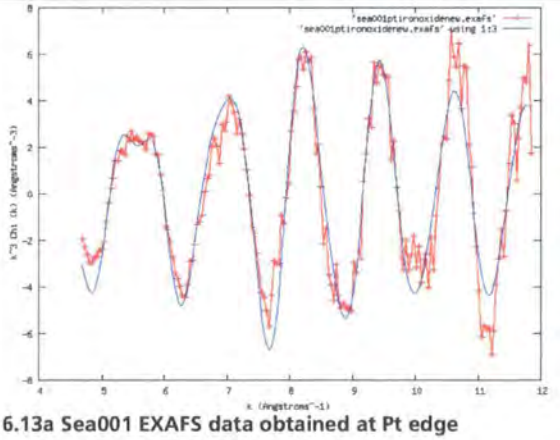

6.13a Sea001 EXAFS data obtained at Pt edge

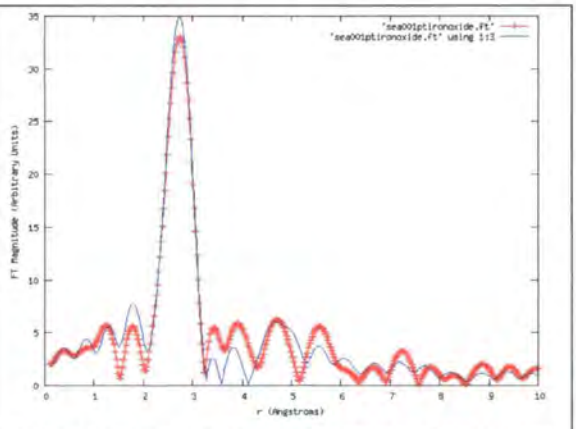

6.13b Fourier transform of Sea001 EXAFS data obtained at Pt edge, fit index of 27.94 %.

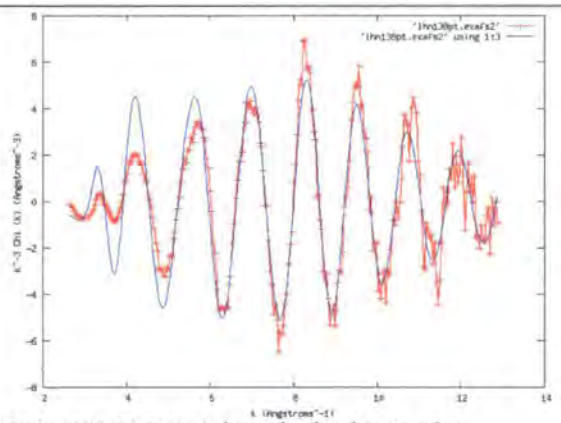

6.13c LHN138 EXAFS data obtained at Pt edge

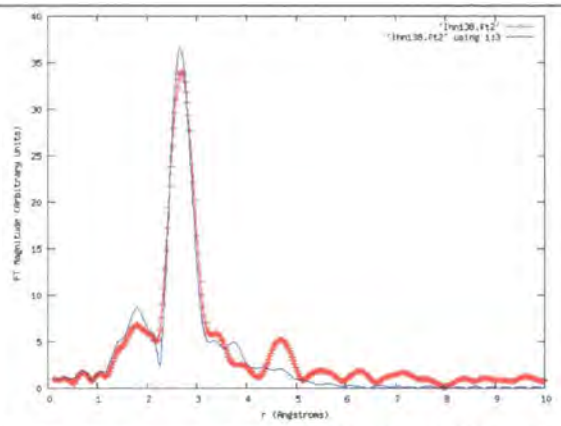

6.13d Fourier transform of LHN138 EXAFS data obtained at Pt edge, fit index of 22.30 %.

In each of **figures 6.12a to 6.13d** the dotted red line is the experimental data and the solid blue line is the calculated model fitted to the data. The *k* range was 5 – 13 $Å^{-1}$. The refined parameters of each model are shown in **tables 6.10 and 6.11**.

Shell	Number of atoms	Type of atom	Distance from central atom (Å)	Fe:Pt composition (Fe:Pt)	Debye-Waller factor
0	1	Fe	0.00		0.01
1	12	QA	2.85	0.76:0.24	0.07
2	6	QB	3.88	0.03:0.97	0.04
3	24	QA	4.50	0.76:0.24	0.09
4	12	QB	5.47	0.03:0.97	0.07
5	6	O	1.96	N/A	0.01

Table 6.10a Refinement parameters obtained from sample Sea001 at the Fe edge.

Shell	Number of atoms	Type of atom	Distance from central atom (Å)	Fe:Pt composition (Fe:Pt)	Debye-Waller factor
0	1	Pt	0.00		0.01
1	12	QA	2.74	0.07:0.93	0.02
2	6	QB	3.83	0.72:0.28	0.05
3	24	QA	4.47	0.07:0.93	0.04
4	12	QB	5.34	0.72:0.28	0.08

Table 6.10a Refinement parameters obtained from sample Sea001 at the Pt edge.

Shell	Number of atoms	Type of atom	Distance from central atom (Å)	Fe:Pt composition (Fe:Pt)	Debye-Waller factor
0	1	Fe	0.00		0.01
1	12	QA	2.71	0.71:0.29	0.06
2	6	QB	3.72	0.34:0.66	0.04
3	24	QA	4.90	0.71:0.29	0.04
4	12	QB	5.32	0.34:0.66	0.03
5	6	O	1.90	N/A	0.04

Table 6.10c Refinement parameters obtained from sample LHN 138 collected at the Fe edge.

Shell	Number of atoms	Type of atom	Distance from central atom (Å)	Fe:Pt composition (Fe:Pt)	Debye-Waller factor
0	1	Pt	0.00		0.01
1	12	QA	2.70	0.75:0.25	0.02
2	6	QB	3.67	0.00:1.00	0.05
3	24	QA	4.71	0.75:0.25	0.04
4	12	QB	5.90	0.00:1.00	0.07

Table 6.10d Refinement parameters obtained from sample LHN 138 collected at the Pt edge.

Comparing the EXAFS data for sample Sea001 collected at both edges, it appears the material is Pt rich. Site QB shows very high Pt content. For both sites a 0.50:0.50 ratio of Fe:Pt would be expected as the material is in the fcc phase. The iron edge data show that each of sample Sea001 and LHN138 exhibit a large peak at ~2 Å. Modelling of the data suggests this peak is due to Fe-O distances. This peak is larger for Sea001. This indicates there are more Fe-O environments in this sample compared to LHN138. Looking at the platinum data for either sample reveals no peak at this distance. These observations are consistent with Sea001 having a platinum core – Fe_xO_y shell morphology. This is corroborated by the Sea001 platinum edge data which show the central platinum is surrounded nearly entirely by platinum. LHN138 platinum edge data show the central atom is surrounded by more iron and the actual Fe:Pt ratio is not what is expected for an fcc material but it is approaching fct values giving some evidence of short range order. These observations are all entirely consistent with the XANES data discussed previously.

6.7 Progression from fcc to fct

Sample LHN129 was prepared via the synthetic route developed in Durham. The synthetic conditions were nonadecane (solvent), oleic acid (surfactant), with refluxing at 334 °C. The particle size was found to be 1.71 nm by XRD and the material was fcc as-synthesised.

Figure 6.14 shows the EXAFS spectra obtained for sample LHN129 as-synthesised and after annealing to each of 230, 430 and 630 °C. **Figure 6.15** is a zoomed in version of the same plot.

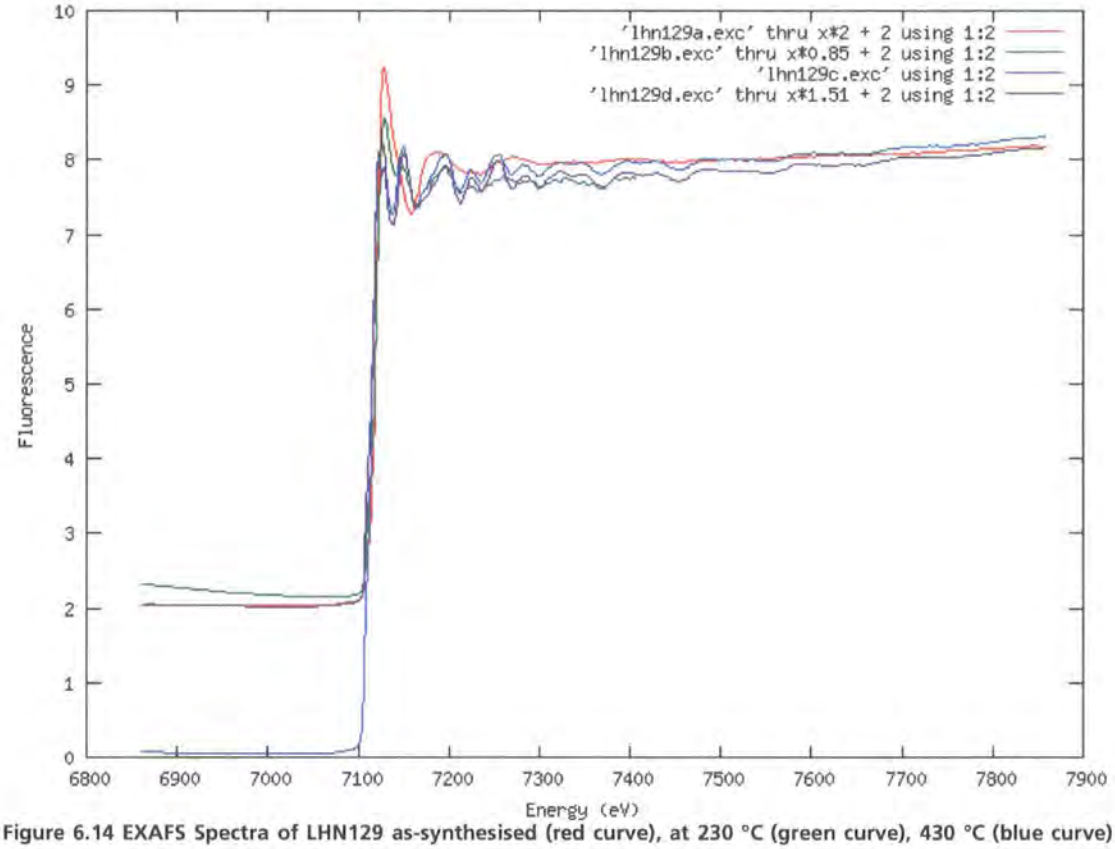

Figure 6.14 EXAFS Spectra of LHN129 as-synthesised (red curve), at 230 °C (green curve), 430 °C (blue curve) and 630 °C (purple curve) collected at Fe edge. Raw data have been scaled so data at high energy are comparable.

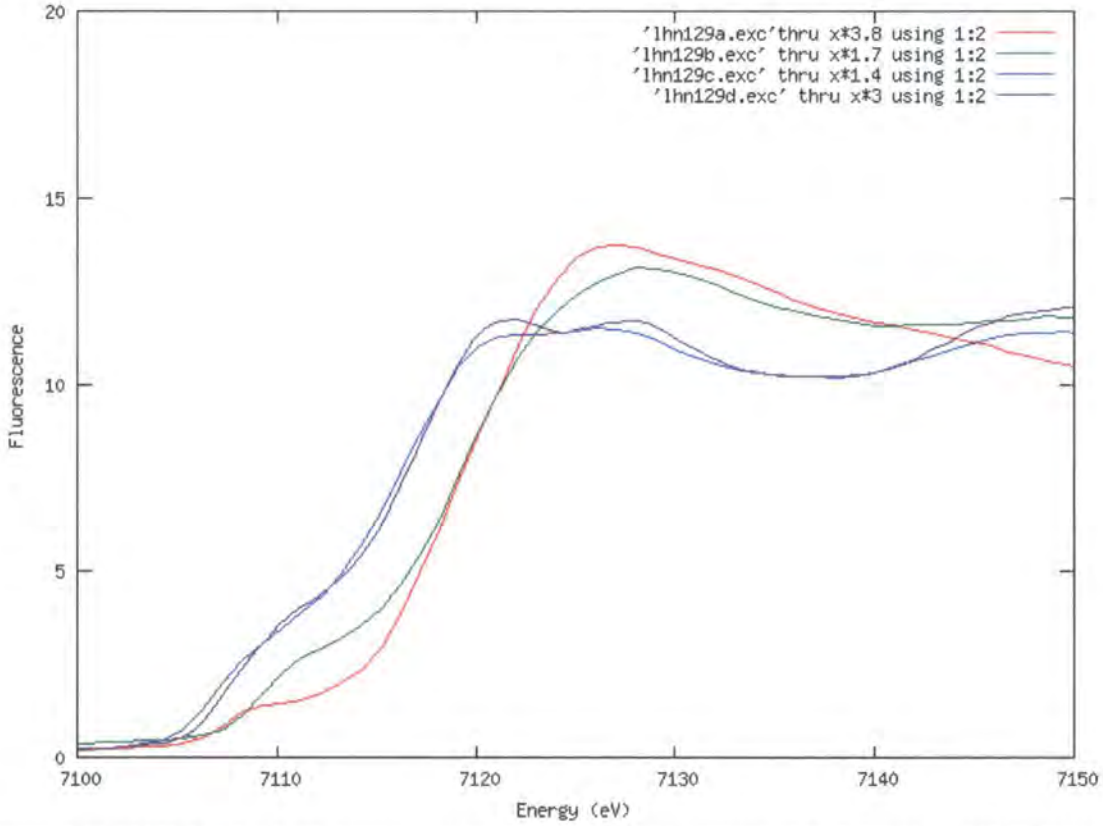

Figure 6.15 EXAFS Spectra (with narrower y range) of LHN129 as-synthesised (red curve), at 230 °C (green curve), 430 °C (blue curve) and 630 °C (purple curve).

Figures 6.16a to h show the refined EXAFS function and Fourier transform for LHN129 as-synthesised and at 230, 430 and 630 °C collected at the Fe edge. **Figures 6.17a-h** show the same for data collected at the Pt edge.

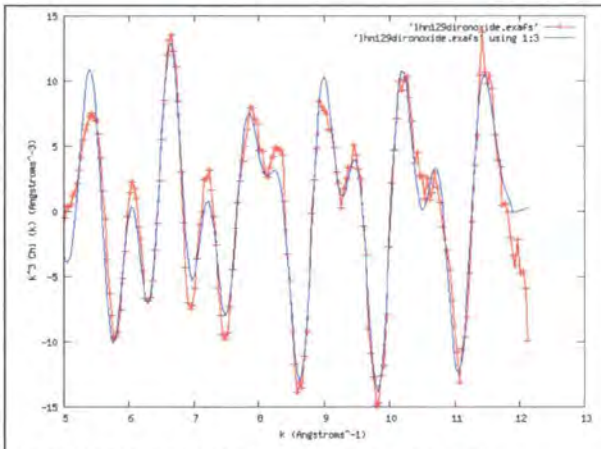

6.16a LHN129a EXAFS data obtained at Fe edge

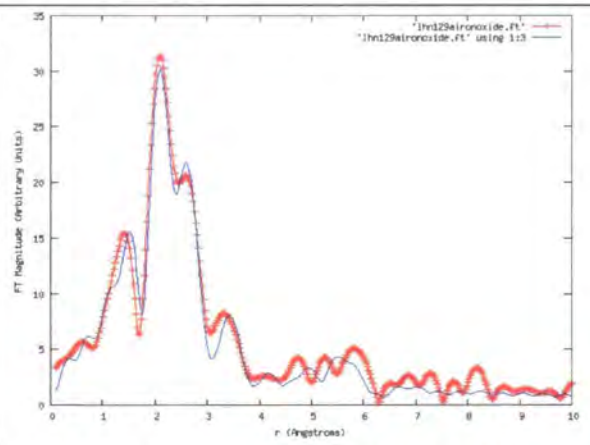

6.16b Fourier transform of LHN129a EXAFS data obtained at Fe edge, fit index of 24.87 %.

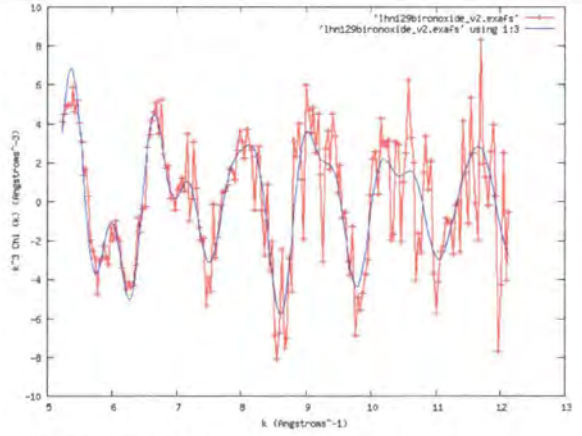

6.16c LHN129b EXAFS data obtained at Fe edge

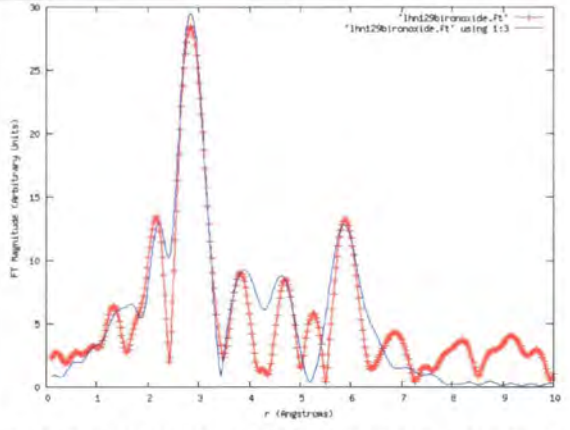

6.16d Fourier transform of LHN129b EXAFS data obtained at Fe edge, fit index of 50.12 %.

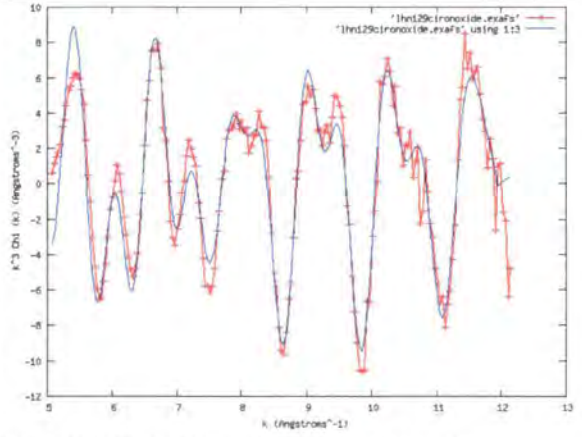

6.16e LHN129c EXAFS data obtained at Fe edge

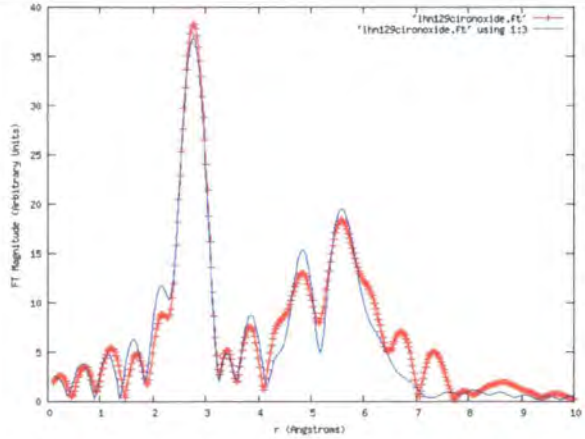

6.16f Fourier transform of LHN129c EXAFS data obtained at Fe edge, fit index of 27.69 %.

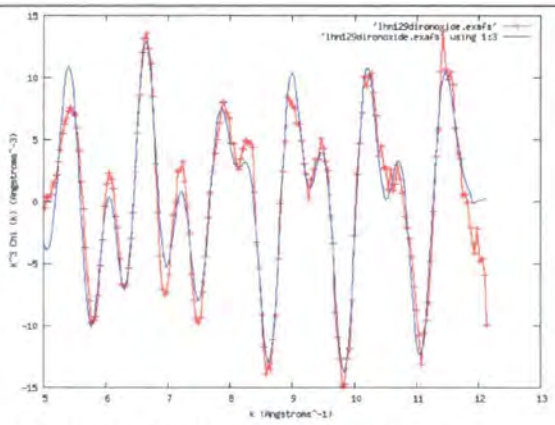

6.16g LHN129d EXAFS data obtained at Fe edge

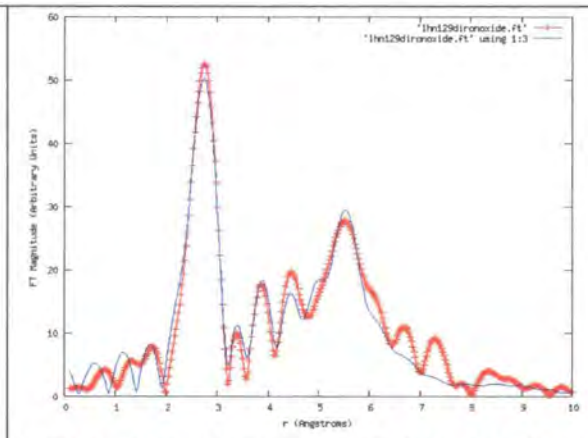

6.16h Fourier transform of LHN129d EXAFS data obtained at Fe edge, fit index of 25.51 %.

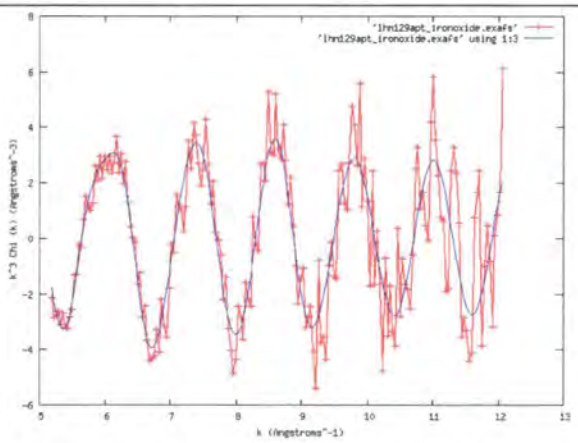

6.17a LHN129a EXAFS data obtained at Pt edge

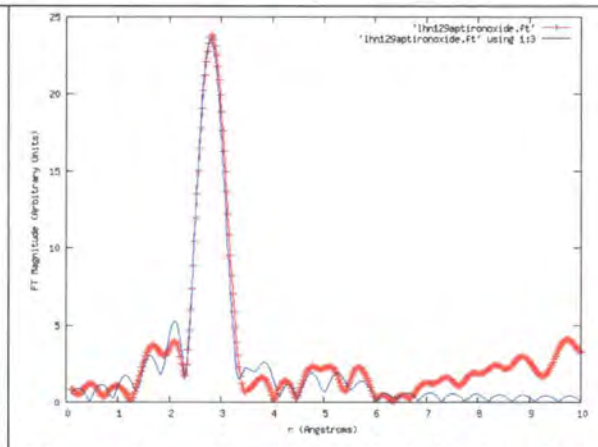

6.17b Fourier transform of LHN129a EXAFS data obtained at Pt edge, fit index of 43.08 %.

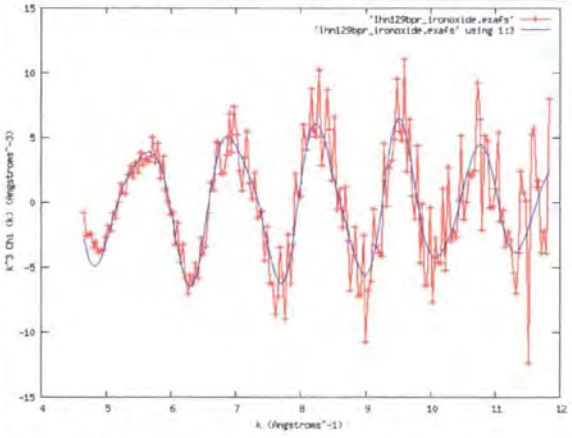

6.17c LHN129b EXAFS data obtained at Pt edge

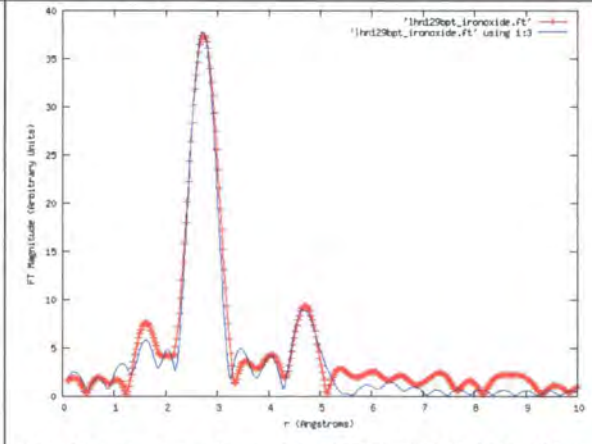

6.17d Fourier transform of LHN129b EXAFS data obtained at Pt edge, fit index of 52.26 %.

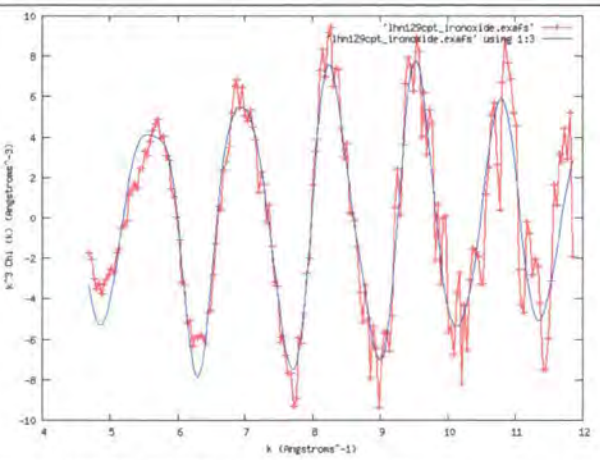

6.17e LHN129c EXAFS data obtained at Pt edge

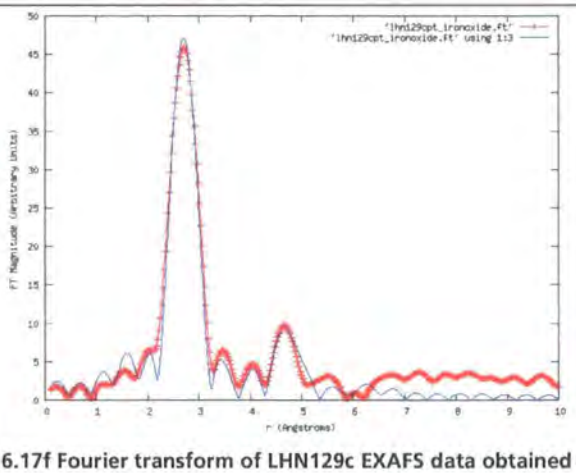

6.17f Fourier transform of LHN129c EXAFS data obtained at Pt edge, fit index of 33.62 %.

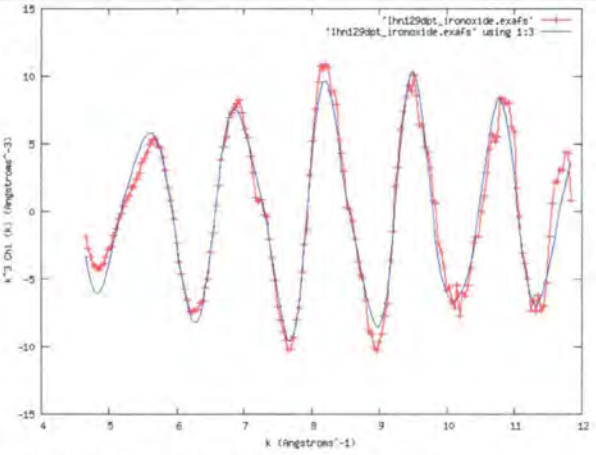

6.17g LHN129d EXAFS data obtained at Pt edge

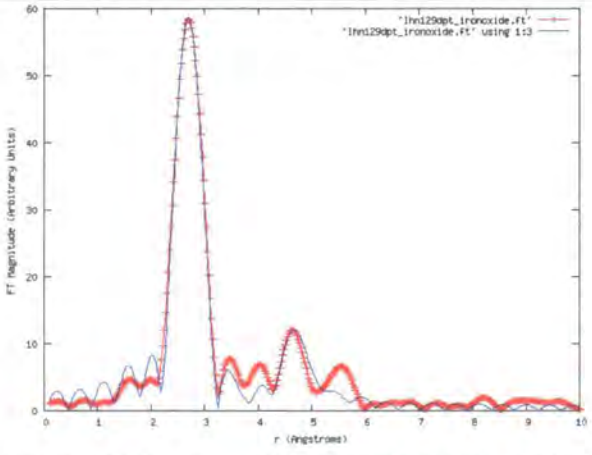

6.17h Fourier transform of LHN129d EXAFS data obtained at Pt edge, fit index of 19.09 %.

The k range was 5 – 13 $Å^{-1}$. In each instance the dotted red line is the experimental data and the solid blue line the fit of the model to the data. The refined parameters obtained at the Fe and Pt edge from each refinement can be seen in **tables 6.11a to d** and **tables 6.12a-d** respectively.

Shell	Number of atoms	Type of atom	Distance from central atom (Å)	Fe:Pt composition (Fe:Pt)	Debye-Waller factor
0	1	Fe	0.00	1.00:0.00	0.01
1	12	QA	2.51	0.74:0.26	0.04
2	6	QB	3.68	0.26:0.74	0.04
3	24	QA	4.97	0.74:0.26	0.05
4	12	QB	5.32	0.26:0.74	0.08
5	6	O	2.24	N/A	0.01

Table 6.11a Fe edge refined parameters obtained from sample LHN129 as-synthesised

Shell	Number of atoms	Type of atom	Distance from central atom (Å)	Fe:Pt composition (Fe:Pt)	Debye-Waller factor
0	1	Fe	0.00	1.00:0.00	0.01
1	12	QA	2.86	0.29:0.71	0.03
2	6	QB	3.85	0.49:0.51	0.02
3	24	QA	4.75	0.29:0.71	0.04
4	12	QB	5.82	0.49:0.51	0.03
5	6	O	2.24	N/A	0.03

Table 6.11b Fe edge refined parameters obtained from sample LHN129 after annealing to-230 °C

Shell	Number of atoms	Type of atom	Distance from central atom (Å)	Fe:Pt composition (Fe:Pt)	Debye-Waller factor
0	1	Fe	0.00	1.00:0.00	0.01
1	12	QA	2.73	0.27:0.73	0.02
2	6	QB	3.62	0.67:0.33	0.04
3	24	QA	4.84	0.27:0.73	0.03
4	12	QB	5.56	0.67:0.33	0.03
5	6	O	1.91	N/A	0.05

Table 6.11c Fe edge refined parameters obtained from sample LHN129 after annealing to 430 °C

Shell	Number of atoms	Type of atom	Distance from central atom (Å)	Fe:Pt composition (Fe:Pt)	Debye-Waller factor
0	1	Fe	0.00	1.00:0.00	0.01
1	12	QA	2.67	0.15:0.85	0.02
2	6	QB	3.63	0.87:0.13	0.04
3	24	QA	4.87	0.15:0.85	0.02
4	12	QB	5.54	0.87:0.13	0.03

Table 6.11d Fe edge refined parameters obtained from sample LHN129 after annealing to 630 °C

Shell	Number of atoms	Type of atom	Distance from central atom (Å)	Fe:Pt composition (Fe:Pt)	Debye-Waller factor
0	1	Pt	0.00	0.00:1.00	0.01
1	12	QA	2.61	0.50:0.50	0.08
2	6	QB	3.73	0.70:0.30	0.04
3	24	QA	4.42	0.50:0.50	0.07
4	12	QB	5.61	0.70:0.30	0.07

Table 6.12a Pt edge refined parameters obtained from sample LHN129 as-synthesised

Shell	Number of atoms	Type of atom	Distance from central atom (Å)	Fe:Pt composition (Fe:Pt)	Debye-Waller factor
0	1	Pt	0.00	0.00:1.00	0.01
1	12	QA	2.70	0.29:0.71	0.02
2	6	QB	3.69	0.70:0.30	0.04
3	24	QA	4.71	0.29:0.71	0.03
4	12	QB	5.83	0.70:0.30	0.09

Table 6.12b Pt edge refined parameters obtained from sample LHN129 after annealing to-230 °C

Shell	Number of atoms	Type of atom	Distance from central atom (Å)	Fe:Pt composition (Fe:Pt)	Debye-Waller factor
0	1	Pt	0.00	0.00:1.00	0.01
1	12	QA	2.69	0.34:0.66	0.02
2	6	QB	3.69	0.44:0.56	0.05
3	24	QA	4.71	0.34:0.66	0.03
4	12	QB	5.91	0.44:0.56	0.06

Table 6.12c Pt edge refined parameters obtained from sample LHN129 after annealing to 430 °C

Shell	Number of atoms	Type of atom	Distance from central atom (Å)	Fe:Pt composition (Fe:Pt)	Debye-Waller factor
0	1	Pt	0.00	0.00:1.00	0.01
1	12	QA	2.70	0.42:0.58	0.02
2	6	QB	3.70	0.29:0.71	0.05
3	24	QA	4.72	0.42:0.58	0.03
4	12	QB	5.47	0.29:0.71	0.06

Table 6.12d Pt edge refined parameters obtained from sample LHN129 after annealing to 630 °C

The near-edge data collected at the Fe edge show a distinct difference between the samples as-synthesised/annealed at 230 °C and those annealed at 430/630 °C. This is largely in the amplitude of the peaks (indicating a coordination difference) but also in the shift of the peaks. This indicates a difference in oxidation state of the Fe or Pt atom. The shift between peaks on annealing is minimal at the Pt edge; larger at the Fe edge. This may be because the as-synthesised samples contain some iron oxide impurities which upon annealing are reduced. If Fe_2O_3 or Fe_3O_4 are present in the samples at all this means there may be Fe^{3+} or a mixture of Fe^{2+}/Fe^{3+} present. The XANES spectra show that as-synthesised the iron edge is ~7126 eV and after annealing to 630 °C it is ~ 7122 eV. Literature values[6] of Fe metal and Fe_2O_3 are 7111.2 eV and 7131.0 eV. The energy edge of an Fe^{2+} material is typically lower. This suggests that Fe^{2+} or Fe^{3+} impurities are present in sample lhn129 as-synthesised. The impurity is reduced upon annealing as the edge energy decreases.

When refining models to fit the observed data shells related to Fe-O distances were required to give the best fit. This is shown in **tables 6.11a-d**. As the material was annealed this shell was removed in order to obtain the best fit of the model to the observed EXAFS profile. Aside from the model and its fit to the data it is clear visually in the iron edge data that peaks present at ~2 Å in the as-synthesised material are not present (or exhibiting only a very small amplitude) in the annealed material. The oxide impurities when annealed are reduced to iron metal. This seems to happen totally. In **section 6.6** it was shown that Sea001 had a large number of Fe-O environments and lots of platinum directly around the central atom. This is consistent with a core-shell morphology. This is not the case here. As-synthesised the Fe:Pt ratio is 0.50:0.50 according to the platinum edge data. This suggests the material exists as an FePt nanoparticle surrounded with surfactant (which gives rise to the Fe-O distances). Otherwise it may be that

there is a slightly platinum rich core and slightly iron rich shell. The data do not support a platinum core and iron oxide shell.

The Fe edge data show that on annealing the material exhibits site occupancies nearing that expected for an fct phase FePt nanoparticle. In particular the QB occupancy moves from being Pt rich as-synthesised to Fe rich after annealing which is what one would expect when the material orders.

The Pt edge data show there is Fe richness in site QB in the as-synthesised material (site QA fully disordered), and upon annealing the sites become more platinum rich, with site QB in particular exhibiting a composition near that expected of an fct material.
Effectively the electron density for sites as observed in the Fe edge data starts low for as-synthesised material and gets higher upon annealing. The electron density for sites as observed in the Pt edge data is lower after annealing to 630 °C than that of the as-synthesised material. This is consistent with a core-shell morphology, as-synthesised.

6.8 FCT samples prepared via different synthetic routes

The synthetic route to FePt nanoparticles developed in Durham has been shown as advantageous compared to Sun *et al.'s* route **in chapter 5**. This was because it was a simpler process and yielded material which ordered at a lower temperature than samples prepared using Sun *et al.'s* method. It is possible that the reason why the ordering begins at a lower temperature is because of a higher degree of order as-synthesised. By modelling the EXAFS data of FePt samples, each prepared by a different synthetic method, it may be possible to determine if one method yields samples ordered to a degree comparable to that of a fully annealed sample prepared via a different route.

Sea001a is the sample prepared via the method developed by Sun *et al.*. After synthesis it was annealed to 878 K and then an EXAFS spectrum was recorded on the annealed material. This and lhn129d (prepared via the Durham route then annealed) were the only samples prepared this way which were measured using EXAFS techniques. There were four fct phase FePt nanoparticle samples as-synthesised from which EXAFS spectra were recorded that were prepared using the Durham synthetic route. These six samples (total) are described in **table 6.13**. Samples detailed in experiment number 1-4 were fct as-synthesised according to XRD. The Pt edge EXAFS data corroborate this.

Experiment No.	*Sample code*	*Synthetic route*	*As-synthesised fct?*	*Annealed to fct phase?*	*Solvent*	*Surfactants*	*Size (nm)*
1	LHN 152	Durham	Yes	No	Tetracosane	C-12 aniline	4.06
2	LHN 133	Durham	Yes	No	Docosane	Oleyl amine, AR-phosphine	3.40
3	LHN 142	Durham	Yes	No	Tetracosane	Oleylamine, aniline	7.40
4	LHN 055	Durham (Microwave)	Yes	No	Octyl ether	Oleylamine	15.90
5	LHN129d	Durham	No	Yes	Nonadecane	Oleic acid	
6	Sea 001	Literature	No	Yes	Octyl ether	Oleylamine/Oleic acid	31.53

Table 6.13 Key details of each fct phase FePt nanoparticle from which EXAFS spectra were obtained

Given a perfect fcc disordered FePt nanoparticle or perfectly ordered fct FePt nanoparticle the structure would be as detailed in **table 6.2**.

Table 6.14 notes the refined site occupancies obtained by modelling the Pt edge spectra of each of the samples described in **table 6.13**.

Experiment no.	*Sample code*	*Fit Index*	**QA**		**QB**	
			Fe	Pt	Fe	Pt
Ideal	N/A	N/A	0.66	0.34	0.00	1.00
1	LHN 152	25.65	0.79	0.21	0.21	0.79
2	LHN 133	37.41	0.82	0.18	0.12	0.88
3	LHN 142	15.21	0.73	0.27	0.31	0.69
4	LHN 055	18.95	0.82	0.18	0.22	0.78
5	LHN 129d	19.09	0.42	0.58	0.29	0.71
6	Sea 001	27.94	0.95	0.05	0.28	0.72

Table 6.14 Site occupancies and fit index of certain Pt edge data related to FePt samples prepared vis different methods.

From **table 6.14** it is clear to see that all Durham samples exhibit fct order as evidenced by the occupancies of both site QA and QB. Sea001 does not show order according to the QA occupancy though the QB occupancy is closer to that expected.

Comparing the occupancies of samples 1-4 with those of LHN 129d (experiment number 5) shows that fct as-synthesised samples have a degree of order comparable to those annealed to the fct phase. Utilising microwave energy instead of thermal energy when synthesising the materials (experiment number 4) provides no advantage in terms of degree of order according to

the EXAFS data. It is very evident from the data that the method utilised to obtain fct FePt nanoparticles directly is very successful as the degree of ordering in such samples is wholly comparable, or superior, to that of annealed samples.

6.9 Conclusions

It has been shown that EXAFS data can be obtained on samples prepared via two different routes – a known literature method and one developed in Durham using a synchrotron radiation source. The data obtained have then been modelled such that structural information can be extracted. One specific model type – a mixed site shell model – has been utilised such that consistent and comparable results can be obtained allowing conclusions to be drawn.

Data collected at both the iron and platinum edges provide useful information. They both provide an indication of the order and structure of the nanoparticle sample under investigation. However they do not correlate with each other totally. The model's parameters when refined to fit each data set are different in terms of shell distance and site occupancy. Equally both fits are visually different. Iron edge data provide information about any iron oxide impurities.

Comparison of EXAFS obtained on samples prepared via two different routes show that those prepared via the Durham route inherently are more ordered according to the site occupancies. Equally, by looking at the near edge region of the measured spectra samples prepared via Sun *et al's.* route it is suggested that more iron oxide impurities are present. There are more iron oxide environments present in the sample prepared via the literature route. Combining the XANES/EXAFS observations sample Sea001 has a platinum core/iron oxide shell morphology. Lhn138 does not exhibit this. There are Fe-O distances present in the EXAFS but these can be attributed either to a surfactant coating of the nanoparticle or are present to a lesser extent as the site occupancies are such that the material is close to predicted in terms of occupancy (rather than being platinum rich).

By observing the structural changes of a sample when annealed via EXAFS data modelling the ordering can be seen by the changes in site occupancies from similar to that expected for an fcc material to that expected for a fully ordered fct material. Equally, by observing changes it can be seen that any oxide impurities or Fe-surfactant interactions present as-synthesised are reduced to iron as the annealing temperature increases.

EXAFS can determine whether a sample shown to be as-synthesised fct material by XRD does exhibit order. The two data sets correlate consistently. Its also true that as-synthesised material exhibits order comparable to fcc material annealed to the fct phase at high temperatures – only the particle size is smaller in that case as no agglomeration has occurred. There is no advantage

in using microwave energy over thermal energy in terms of degree of order of the resultant material. Equally, as-synthesised fct material is ordered at least to the degree of annealed samples, but typically more so.

6.10 References

1. J. Lynch, *Oil & Gas Science and Technology-Revue De L Institut Francais Du Petrole*, 2002, **57**, 281-305.

2. J. D. Grunwaldt, M. Caravati, S. Hannemann and A. Baiker, *Physical Chemistry Chemical Physics*, 2004, **6**, 3037-3047.

3. B. J. Hwang, L. S. Sarma, J. M. Chen, C. H. Chen, S. C. Shih, G. R. Wang, D. G. Liu, J. F. Lee and M. T. Tang, *Journal of the American Chemical Society*, 2005, **127**, 11140-11145.

4. M. Chen, J. P. Liu and S. H. Sun, *Journal of the American Chemical Society*, 2004, **126**, 8394-8395.

5. S. H. Sun, C. B. Murray, D. Weller, L. Folks and A. Moser, *Science*, 2000, **287**, 1989-1992.

6. G. A. Waychunas, M. J. Apted and G. E. Brown, *Physics and Chemistry of Materials*, 1983, **10**, 1-9.

Chapter 7 - Magnetic Studies of Iron platinum Nanoparticles

7.1 Introduction

This chapter describes a variety of magnetic studies designed to investigate the structure and properties of FePt nanoparticles. The first part of the chapter describes the experiments typically performed on FePt samples and details what information can be obtained from such experiments. The second part of this chapter describes the methodology and equipment developed to study materials at temperatures above room temperature and describes these studies. These results are compared to XRD results from **chapter 5**.

7.2 Zero field cooled/field cooled experiments and hysteresis loops

7.2.1 Introduction

FePt nanoparticles in the fcc phase are typically superparamagnetic. If a ferromagnetic particle is small enough there will be no energy benefit for it to form a multi-particle ferromagnetic domain. The magnetisation of each individual particle may be constrained such that it lies parallel to, or perpendicular to, a specific direction. The energy of these particles is partly defined by the term $K\sin^2\theta$, where θ is the angle between this specific direction and the particle's magnetisation, whilst K is the magnetocrystalline anisotropy of the material, effectively the energy cost per atom of an energy change in magnetic moment. This term is minimized when $\theta = 0$ or Π. The energy required to flip the magnetisation from $\theta = 0$ to $\theta = \Pi$ or vice-versa is proportional to KV, where V is the volume of a particle. Therefore, the energy required to flip the magnetisation of a particle of any given material will decrease as the particle shrinks. At a certain point the thermal energy (k_bT) becomes large enough to cause the magnetisation to flip. This is the superparamagnetic limit. This is so called because when $k_bT >> KV$ many ferromagnetic particles will behave as paramagnets, where each magnetic moment arises from multiple particles and these moments are contained within a ferromagnetic particle.

When the superparamagnetic limit is reached individual grains are more likely to undergo a change in the orientation of their associated magnetic moment. This means that as a magnetic storage medium fcc phase FePt nanoparticles are virtually useless – any data stored will be lost after random spins of the individual particle moments. FePt nanoparticles in the fct phase are

typically ferromagnetic. This means they are permanent magnets which are capable of storing magnetic data over prolonged periods of time at ambient temperature.

In order to characterise as-synthesised FePt nanoparticles, and those which have been annealed, it is important to understand the magnetic properties. This has been done by performing two main types of experiment; zero field cooled/field cooled experiments and a magnetisation versus field loops (to observe if any hysteresis is present).

7.2.2 Zero field cooled/field cooled experiments

7.2.2.1 Introduction

Zero-field cooled (ZFC) and field cooled (FC) experiments are useful for determining whether a material displays superparamagnetic or ferromagnetic properties. These are measured by cooling a sample to a low temperature in the absence of an applied field. Once stabilised, a magnetic field is applied and the magnetic moment measured as a function of increasing temperature. This is termed the zero-field cooled measurement (where zero-field indicates a residual field of <1 Oe). The measurement is repeated in the same way except that the sample is cooled in the presence of the measurement magnetic field. Field-cooled data are then collected on warming.

By taking a sample of a material and performing these experiments it is possible to qualitatively say if a sample is superparamagnetic, if there are multiple phases present and if the particle size range is small or big.

7.2.2.2 Experimental

Typically a small (~10 mg) sample of material is weighed out on aluminium foil. This is then transferred into the larger half of one gelatine, compressed and then closed by reconnection of the two halves. A G-varnish/alcohol mixture is applied to the inside of a transparent straw, at its centre. The capsule is then pushed down the centre of the straw in order to rest at the mid-point centre and is left to dry overnight (the capsule sticks to the inside of the straw via the G-varnish/alcohol mixture). The next day the capsule is secure enough to hold the straw vertically. It is then attached to the sample rod of the Quantum Design MPMS Squid Magnetometer. This sample rod is lowered according to protocol into the sample chamber and an experimental programme is set-up. This is set so that the temperature goes from ~ 300 K to 2 K in the absence of a magnetic field. A field is then applied (100 Oersteds) and the temperature is increased with a measurement of the magnetization at set intervals (every 1 K up to 20 K and thereafter every 10 K). After this is complete the temperature is decreased to 2 K once more, in the presence of the applied magnetic field, and the measurement process repeated.

7.2.2.3 Results

Figure 7.1 provides an example of the data obtained by recording zero-field cooled and field cooled measurements on a superparamagnetic sample. The point at which the ZFC and FC curves diverge (~20 K) is termed the blocking temperature, and is indicative of superparamagnetism.

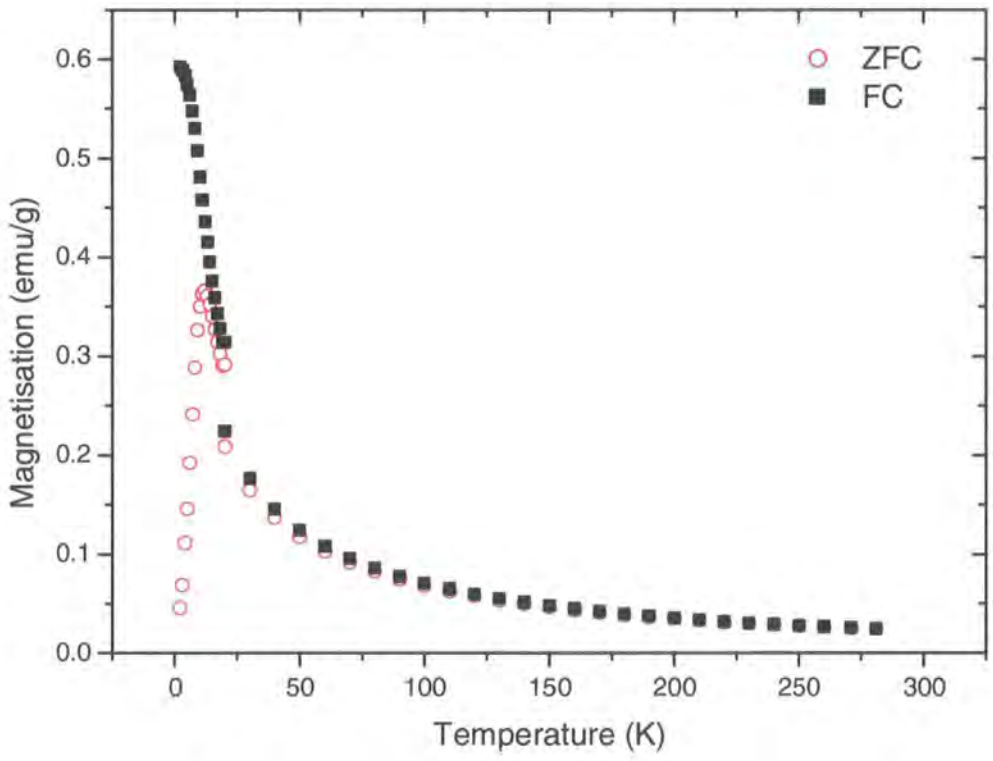

Figure 7.1 ZFC and FC curves measured for sample LHN155 (10 mg sample size) and a superparamagnetic material

The two curves lie on top of each other until the blocking temperature is reached, suggesting a very small particle size range and high purity of the material. It is also possible to use the data in **figure 7.1** to obtain a rough value of the effective anisotropy K_U as well as an indication of the particle size.

7.2.3 Hysteresis Measurements

By measuring the magnetisation of a material as a function of the applied field the presence or absence of magnetic hysteresis can be detected. Hysteresis loops are composed of magnetisation measurements from zero to high field, down to low negative field and then back to high field once more (a loop). As the magnetisation is increased until saturation is reached, reduction or removal of that applied field results in a reduction of the magnetisation to a level termed the remnant magnetisation. This indicates the material is a permanent magnet as any switch of the

direction of the magnetic moment of that material requires an applied field equal to or greater than the coercive field. The remnant magnetisation is the magnetisation in the absence of a magnetic field.

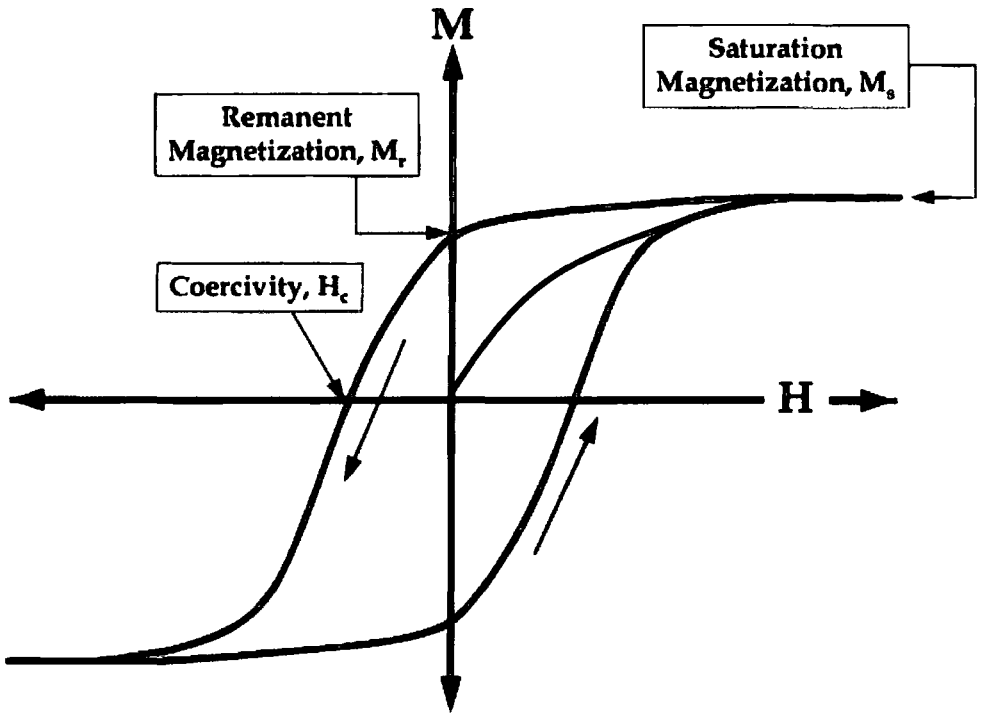

Figure 7.2 A diagram describing the saturisation magnetisation, remnant magnetisation and coercivity in relation to a hysteresis loop measurement.

7.3 Iron Platinum Nanoparticles Prepared via the Durham Route

7.3.1 Introduction

As has been shown in previous chapters we have been able to synthesise FePt nanoparticles via the Durham route which as-synthesised exist in the fcc or fct phase. Equally we have annealed fcc phase particles such that they convert to the fct phase. This section details the magnetic characterisation of FePt nanoparticles prepared using the Durham route.

7.3.2 FePt samples

Each sample prepared and studied in this thesis is detailed in **table 7.1** in terms of the sample code and the characterisation data obtained.

Sample number	Sample code	Phase	Synthetic route	Sample size by XRD (nm)	D8 run	Zero-field cooled (ZFC)	Field cooled (FC)	Hysteresis loops	High temperature measurements
1	LHN 073	FCT	Durham	2.21	D8_02588	Yes	Yes	Yes	Yes
2	LHN 59	FCT	Durham	1.65		Yes	Yes	Yes	
3	LHN 097	FCC	Sun et al.	1.95					Yes
13	LHN 155	FCC	Durham/Microwave	2.69	D8_02892	Yes	Yes	Yes	
14	LHN 155	FCC	Durham/Microwave	2.69	D8_02930	Yes	Yes	Yes	
17	LHN 162	FCC	Durham	4.20	D8_02987	Yes	Yes	Yes	Yes

Table 7.1 Description of the samples discussed in this chapter and the magnetic measurements obtained for each.

7.3.3 FCC Phase FePt nanoparticles

Figure 7.3 shows ZFC and FC magnetisation curves of sample LHN 155 (2.69 nm by XRD, 10 mg sample size), and as-synthesised fcc phase FePt nanoparticle sample. **Figure 7.4** shows hysteresis loops recorded from the same material at 10 K and 290 K.

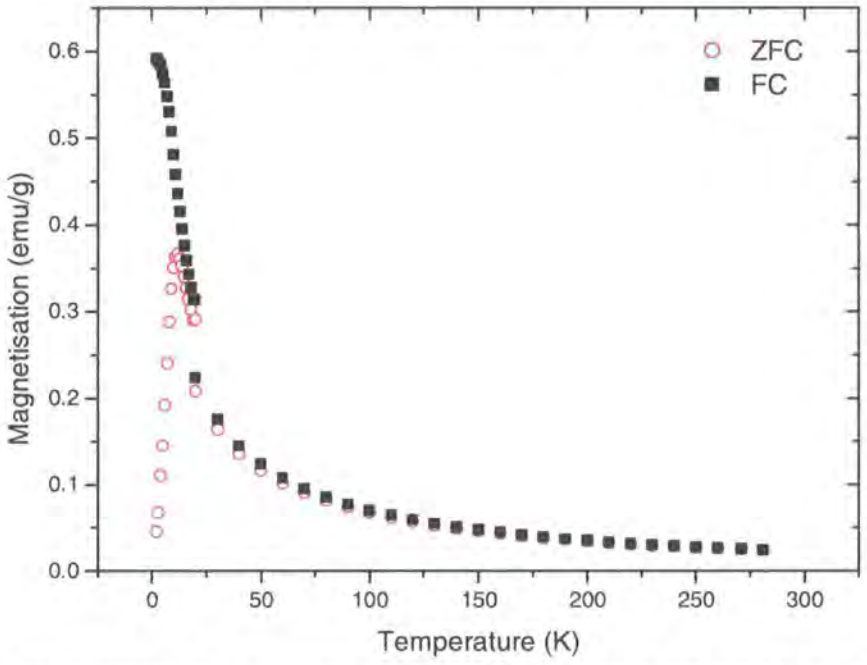

Figure 7.3 ZFC and FC magnetisation curves as a function of temperature from 5 to 290 K in an applied field of 100 Oe.

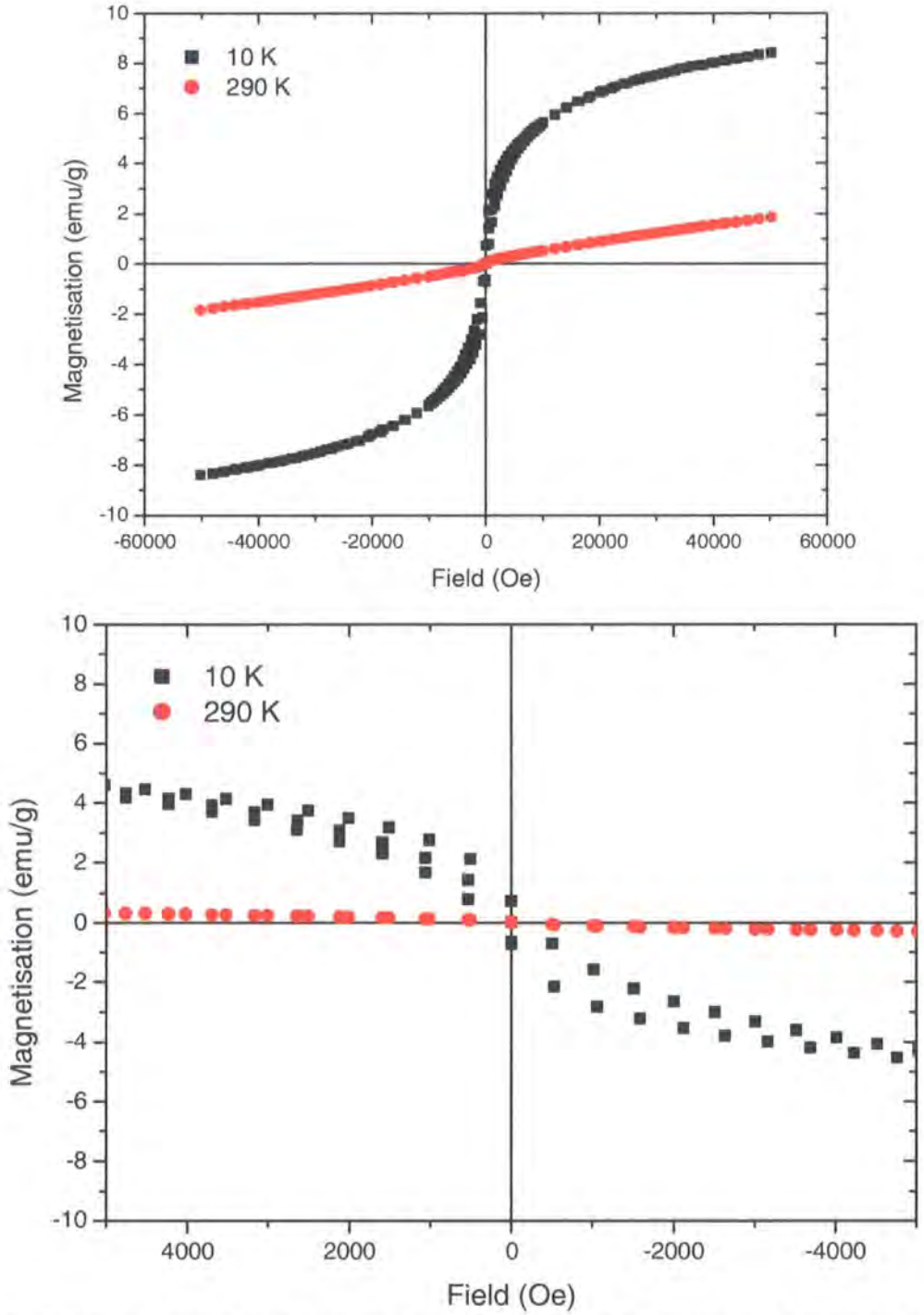

Figure 7.4a Magnetic hysteresis loops measured at 10 K and 290 K of an as-prepared FePt nanoparticle sample (LHN 155); Figure 7.4b is a zoomed image of the same data.

In **figure 7.3** a peak is present in the ZFC data at ~ 17 K. This corresponds to the blocking temperature of the material, the presence of which is characteristic of a superparamagnetic material. This blocking temperature is well defined, with a sharp rise as the temperature increases from 2 K, followed by an equally sharp drop on continued warming. This indicates the particle size range is small. **Figure 7.4** corroborates the assertion that the material is superparamagnetic. At 290 K there is evidence of a very small coercivity which is larger at 10 K. Equally the shape of

the curve at 290 K is very nearly linear, which would have indicated a paramagnetic material, but at 10 K it has the characteristic shape of a ferromagnetic material.

7.3.4 Annealed FCT phase FePt nanoparticles

A large number of the samples studied in this thesis were fcc FePt as-synthesised. In order to obtain the magnetically interesting fct phase post-synthetic annealing is necessary. **Figure 7.5** shows ZFC and FC curves measured for sample LHN 073 after annealing.

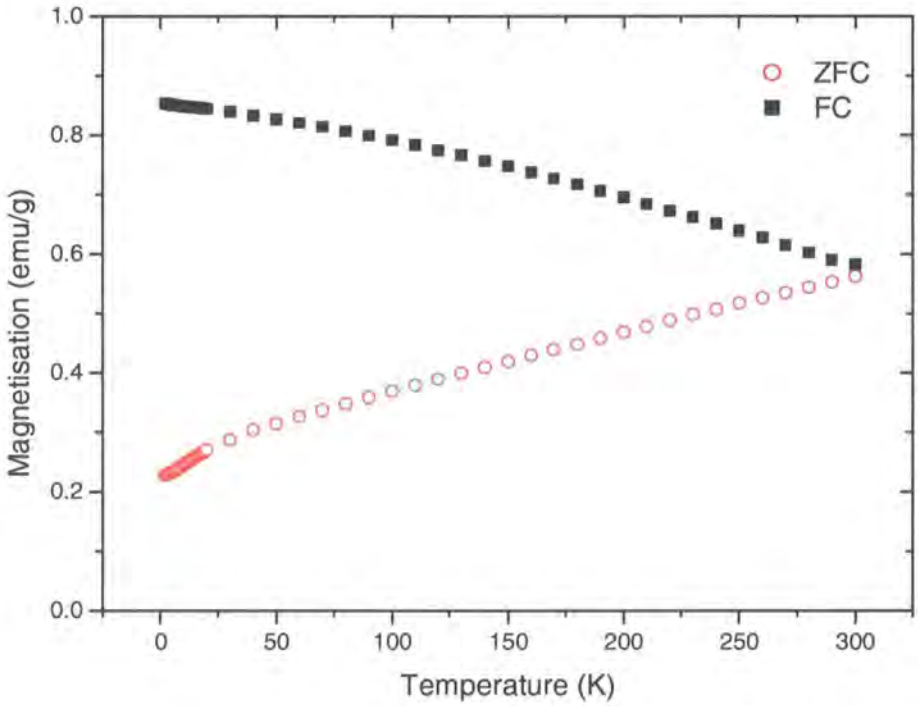

Figure 7.5 ZFC and FC magnetisation curves as a function of temperature from 5 to 290 K at a field of 100 Oe

It is clear from **figure 7.5** that the material measured does not show the superparamagnetic behaviour of that in **figure 7.3**. There is no blocking temperature immediately visible. The fact the curves do not converge on warming is indicative of a wide particle size range as well as multiple phases being present (considered due to the lack of a well-defined blocking temperature). The probability that there are multiple phases, or components, is corroborated by the different gradient of the ZFC curve at low temperature to that at high temperature (the section between ~ 5 and 25 K). This means a superparamagnetic phase may be present, but if so, its magnetisation is dominated by the other phase(s) present.

Figure 7.6 shows a hysteresis loop recorded at 290 K measuring sample LHN 073. There is a coercivity of ~ 6 kOe, a remnant magnetisation of ~ 18 emu/g and a magnetisation saturation of ~ 40 kOe. As these values are non-zero, the material can be said to be ferromagnetic

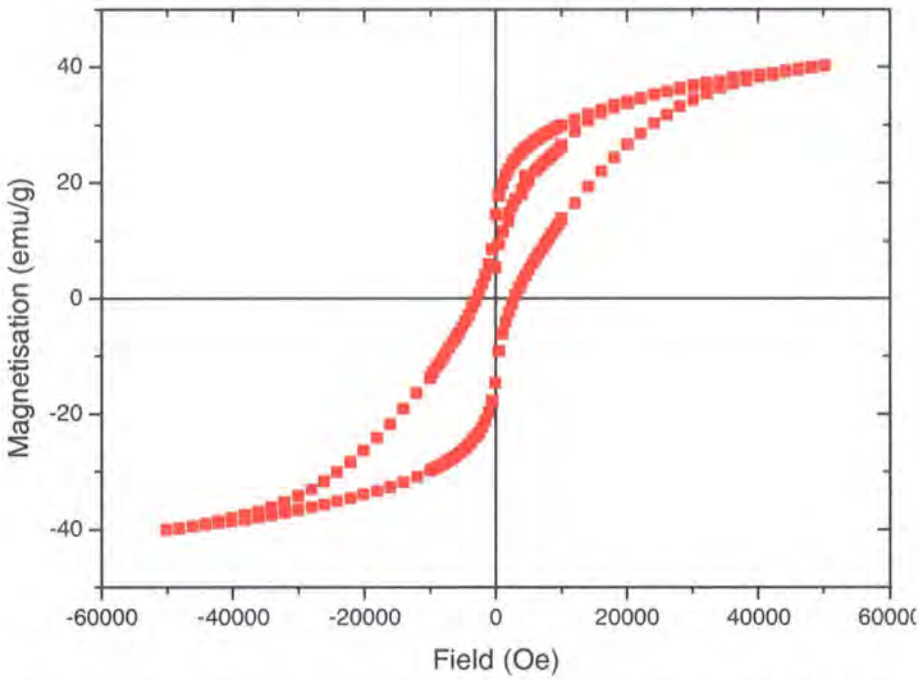

Figure 7.6 Magnetic hysteresis loop measured at 290 K of post-synthetic annealed fct FePt nanoparticles synthesised via the Durham route.

The shape of the hysteresis loop presented in **figure 7.6** is unusual in that about the origin the data seem narrower than would be expected (a classic 'S-curve'). This is probably due to the sample moving within the sample holder. Samples which were fully restricted in terms of movement would yield much 'better' shaped hysteresis loops.

7.3.5 FCT Phase FePt nanoparticles

Figure 7.7 shows the magnetisation of sample LHN 059 as a function of increasing temperature after cooling in a small residual field of < 1 Oe and in a 100 Oe field – zero field cooled and field cooled curves. The sample is a directly synthesised fct phase FePt nanoparticle.

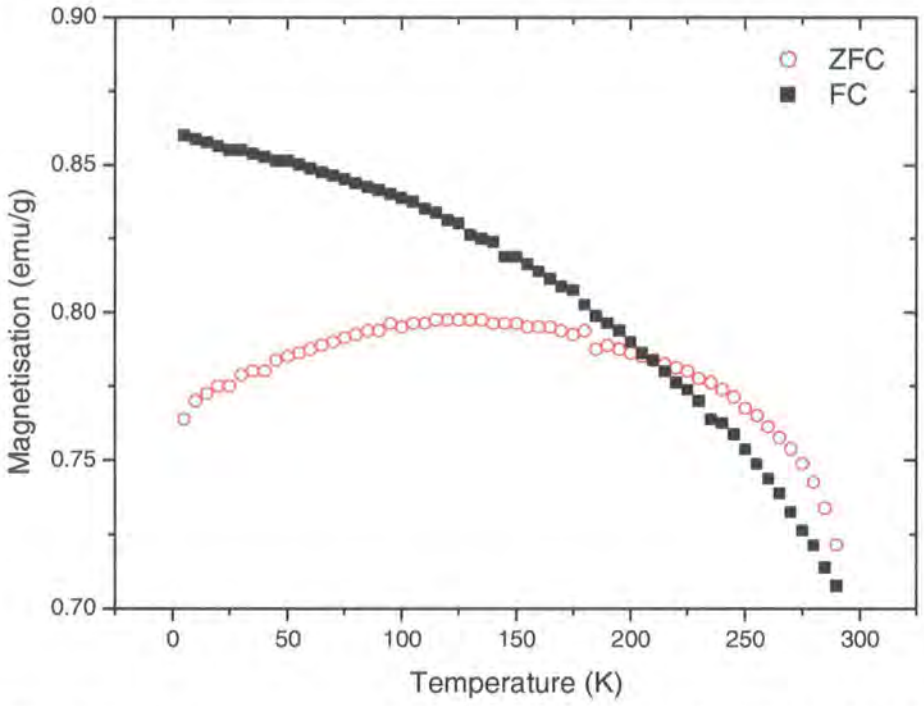

Figure 7.7 ZFC and FC magnetisation curves as a function of temperature from 5 to 290 K at a field of 100 Oe

Figure 7.7 can be interpreted in a similar fashion to that of **figure 7.5**.

Figure 7.8 shows the magnetisation versus field loops measured at 10 and 290 K for sample LHN 059.

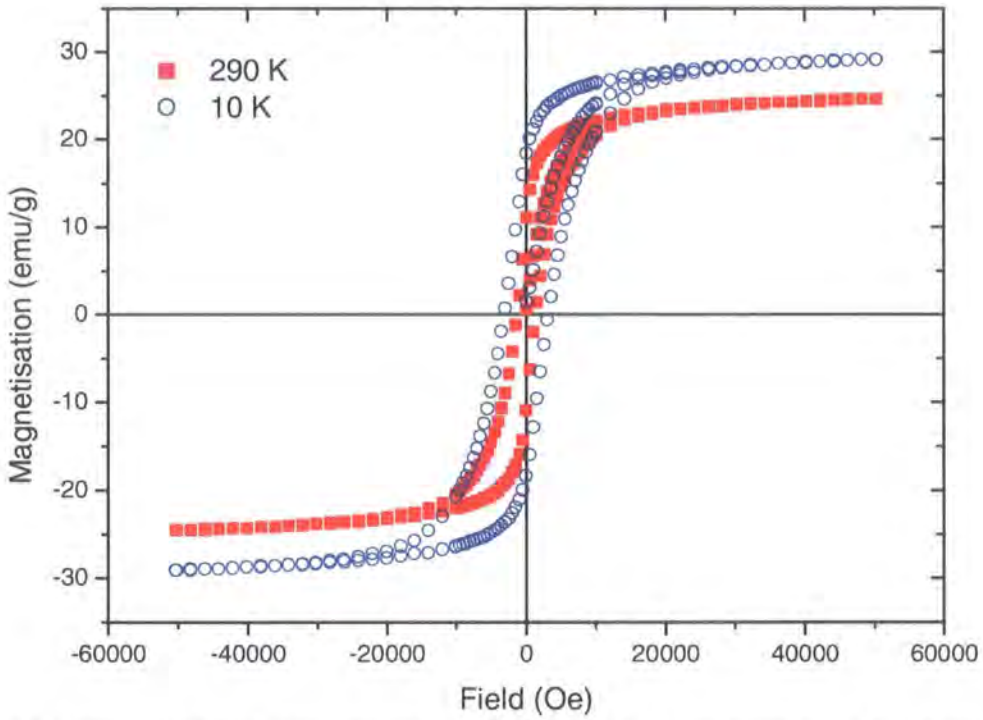

Figure 7.8 Magnetic hysteresis loops measured at 10 and 290 K of as-prepared fct FePt nanoparticles synthesised via utilisation of the Durham route.

Both hysteresis loops are remarkably well-defined. The coercivity at 290 K is ~ 3 kOe and at 10 K is ~ 6 kOe. The remnant magnetisation at 290 K is ~ 16 emu/g and at 10 K is ~ 20 emu/g. The magnetisation saturation point is ~ 28 kOe at 290 K and ~ 35 kOe at 10 K. The presence of coercivity and a remnant magnetisation indicates the material is ferromagnetic, or the dominant magnetic signal is of the ferromagnetic component.

7.3.6 Conclusion

FCC and FCT phase FePt nanoparticles have been prepared using the Durham synthetic method and this has been shown by magnetic measurements. Equally, it has been shown that fcc phase material can be successfully annealed to give fct phase material.

The magnetic measurements used within this section have yielded useful data such as the coercivity of a given sample, the saturation magnetisation and the remnant magnetisation. This has allowed description of a sample as ferromagnetic or superparamagnetic.

7.4 Variable Temperature Magnetic Studies

7.4.1 Introduction

In **chapter 5** of this thesis the transition between the fcc and fct phase of FePt nanoparticles upon annealing has been studied in detail using variable temperature X-ray diffraction methods. From this much understanding has been obtained regarding the transition in terms of structural changes to the unit cell and positional changes of atoms. The information has also provided a greater understanding of the temperature at which the transition happens for a given sample.

However, X-ray diffraction only provides some information about FePt nanoparticles. VT magnetic studies yield information on the magnetic properties of the particle upon heating which increases the understanding of the FePt nanoparticles.

7.4.2 Proof of Principle Experiment

A prototype sample holder for use at high temperature was developed, and an experiment designed to obtain magnetic measurements at high temperature. This then was tested in a 'proof of principle' experiment in order to validate both the methodology and equipment.

Using the oven attachment on the SQUID magnetometer it is possible to record measurements in the temperature range from 300 to 800 K. In order to test the system the experimental design allowed for measurements similar to those of ZFC/FC experiments and hysteresis loops. Magnetisation was measured as a function of temperature and function of applied field at set temperatures. Two fcc phase samples of FePt prepared via the Durham and Sun *et al.'s* methods were used in these experiments. The materials were as-synthesised in the fcc phase and the full set of measurements is described in **table 7.2**. The samples were chosen based upon their being the best examples of FePt nanoparticles prepared by the various routes available.

Sample	Phase	Synthetic route	Particle size by XRD (nm)	Temperature sweep	Hysteresis loop (0 - 5 T) (K)	Hysteresis loop (0 - 5 T) (K)	Hysteresis loop (0 - 5 T) (K)
LHN 073	FCC	Durham	2.21	300-750	300	475	600
LHN 097	FCC	Sun et al.	1.95	300-750	300	475	600

Table 7.2 A description of the measurements performed in a proof of principle experiment on the validity of variable temperature SQUID magnetometer measurements.

The aim for these experiments was to compare FePt nanoparticle samples prepared via the Durham and Sun *et al.'s* routes in terms of magnetic measurements upon annealing.

7.4.3 Experimental

SQUID Magnetometer Oven Attachment

Through use of an optional attachment, measurements (of the magnetisation) at temperatures up to 800 K can be made. The oven is an insulated heater assembly which is placed directly in the magnetometer sample space. It is as long as the sample space so as to maximise its use of available space and leaves a sample space with a 3.2 mm diameter when installed. The oven employs a vacuum sleeve which is capable of isolating the temperatures within the oven from those surrounding it. This means the surrounding space's temperature is still controlled by the magnetometer rather than the oven.

To perform high temperature experiments the oven attachment must be first installed into the SQUID magnetometer. After checking the electric connections of the oven to ensure they function correctly the transport head of the magnetometer is removed and the oven installed – the sample area is lowered into the main SQUID sample area and the transport head is placed on top of the oven attachment.

High Temperature Sample Holder

Standard sample holders are not suitable for high temperature experiments as they are composed of gelatin capsules and plastic straws. As such a quartz holder was developed that gave minimal background signal, minimal sample movement, was open to the atmosphere and had the ability to withstand temperatures up to 800 K. **Figure 7.9a** is a schematic showing the final design of the sample holder, whilst **figure 7.9b** is a photograph of an actual sample holder.

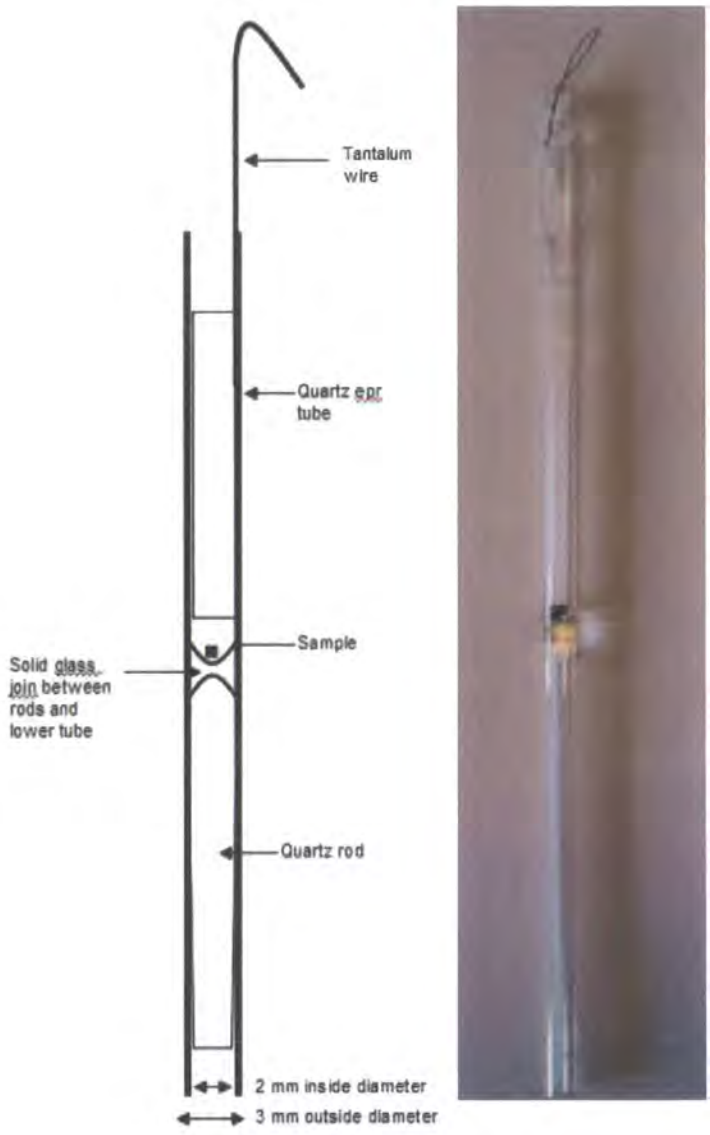

Figure 7.9a and 7.9b A schematic and a photograph of the high temperature sample holder for use in SQUID measurements between 300 and 800 K.

To make the sample holder high purity quartz was used. 2.97 mm outside diameter/1.99 mm inside diameter electron paramagnetic resonance tubes (159 mm in length) and 1.5 mm rods were obtained from Wilmad-LabGlass (0.0021 - 0.0055 % impurity; made from SiX_4). The tube is taken and the bottom is cut away to make it a hollow tube open at both ends. A glass rod is then attached to the inside of the tube just below the centre of the tube. This join is solid as any bubbles could lead to explosions when heated during experiments. The sample is then placed in the tube from the top, so that it rests on the shelf created by the rod/tube join. The second rod is then placed in the top of the tube and attached towards the top of the tube along with a metal wire. The sample is open to the atmosphere along one side of the tube to ensure that upon heating a pressure build-up leading to an explosion does not occur and to allow evacuation of the sample holder area upon loading without disturbing the actual sample material within the holder.

The reason two identical rods are placed either side of the sample is to keep the holder as symmetrical as possible so that any background signals will be minimised when the sample holder is moved through the measurement coils. Tantalum (melting point = 3290 K) wire is resistant to high temperatures, and is tied onto the quartz rods so it can be fixed onto the sample rod.

All sample holders were manufactured by Malcolm Richardson of Durham University.

General experiments are performed in the same way as for standard experiments. However, the metal rod to which the sample holder is attached is within a plastic outer covering. This outer covering had to be shortened for the sample to be installed securely (this was due to the extra length at the top of the magnetometer due to the oven).

7.4.4 Results

In figures 7.10 and 7.11 the data obtained when performing a magnetisation versus temperature measurement on each of sample LHN 073 and LHN 097 are shown.

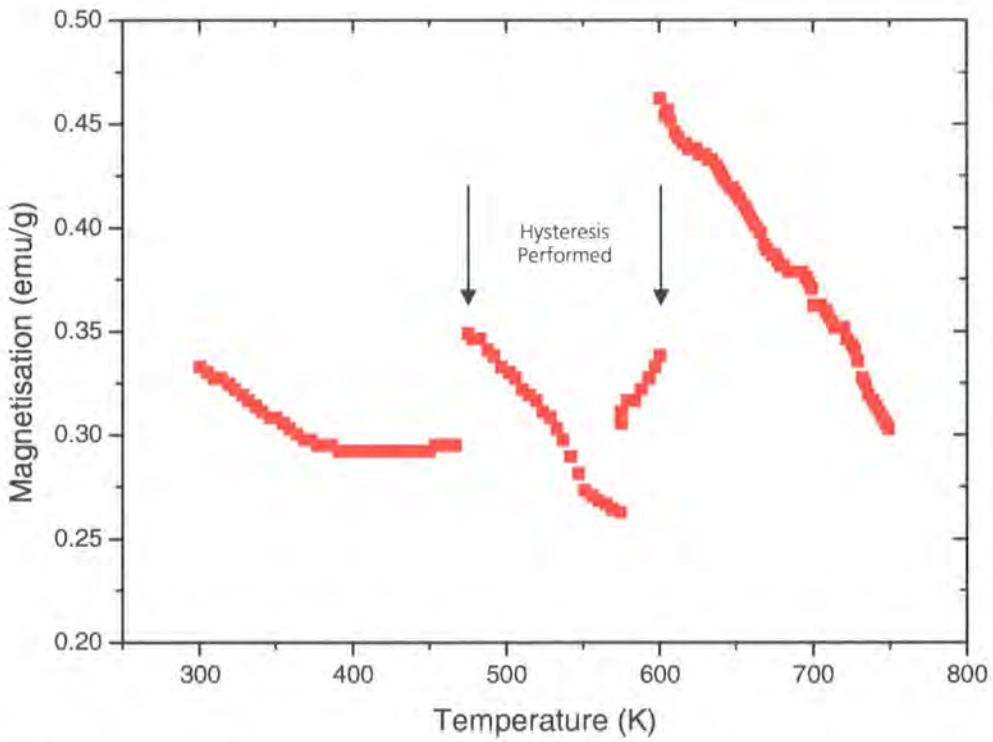

Figure 7.10 A graph showing the magnetisation of sample LHN073 on warming

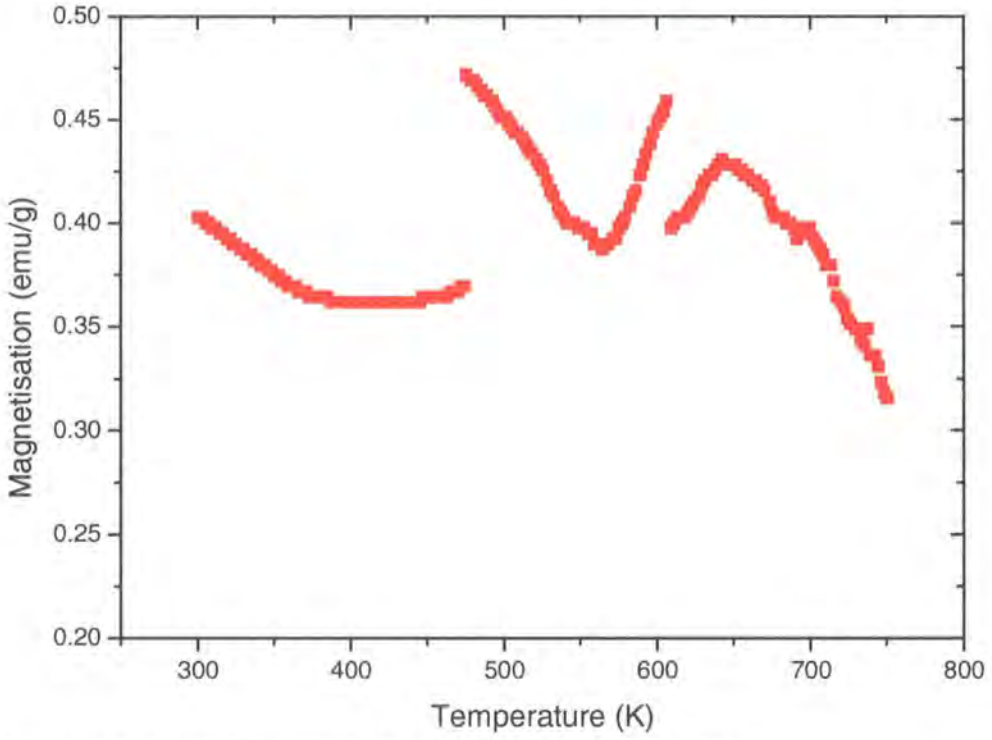

Figure 7.11 A graph showing the magnetisation of sample LHN097 on warming

Both figures show discrete sections of data separated from one another. The reason for this is that during the temperature sweep the experiment was paused in order to record hysteresis measurements at 300, 475 and 600 K. The data show, however, that measurements of magnetisation as a function of temperature are possible on warming. It should be noted that magnetisation decreases with temperature as expected whilst the shape of the curve would be similar to that of **figure 7.25** without the hysteresis discontinuities.

To measure hysteresis loops a magnetic field is applied. If this is done before a temperature sweep, there may be memory effects which lead to different magnetic moments measured due to the magnetic history of the sample. However, if the temperature sweep is measured first, the material will have undergone a phase transition to the fct phase (assuming it was fcc to begin with). In this experiment, memory effects may be the reason why in both **figures 7.10** and **7.11** at around 300, 475 and 600 K there is a large jump in magnetisation which then slowly decreases on warming (the opposite to what would be expected for an FePt nanoparticle annealing).

Figures 7.12 to **7.16** show the hysteresis loops measured during this experiment. Each figure shows only data collected in a positive field. This was all that was measured.

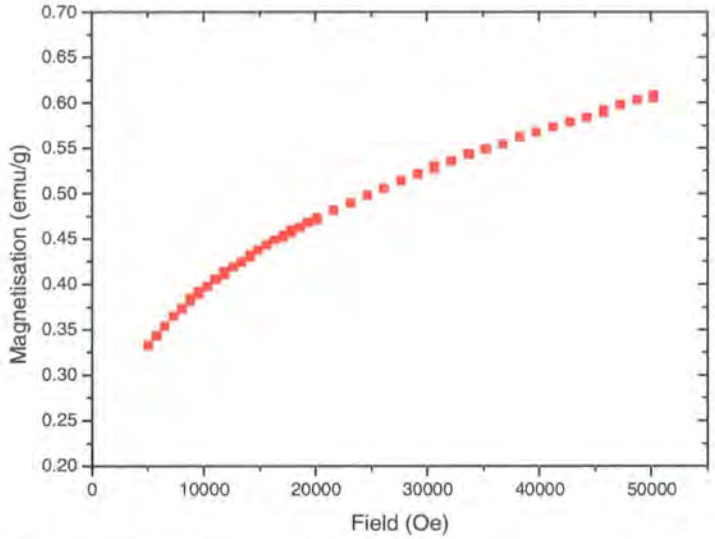

Figure 7.12 Magnetisation versus field for sample LHN073 at 300 K

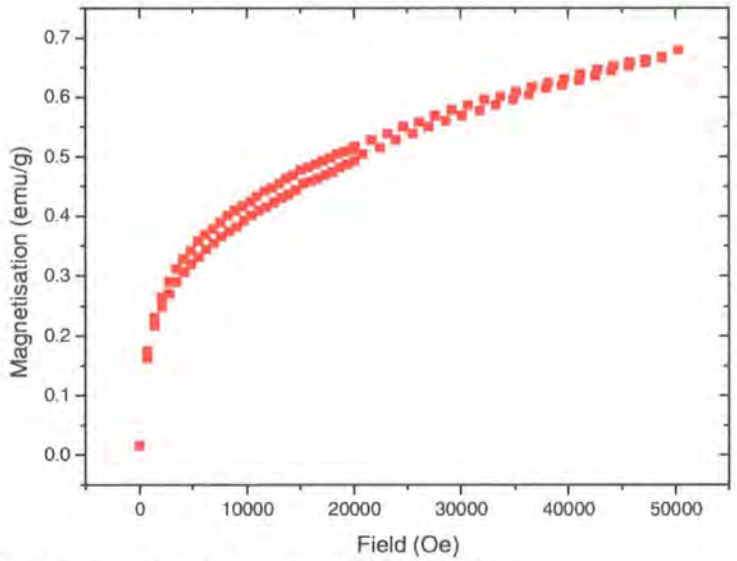

Figure 7.13 Magnetisation versus field for sample LHN073 at 475 K

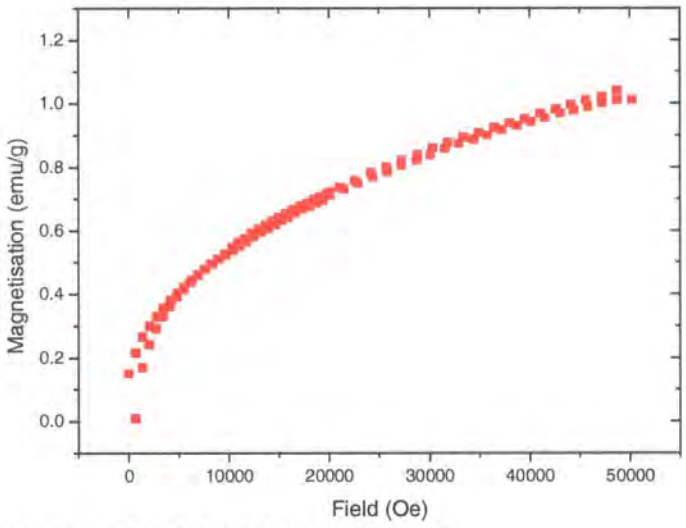

Figure 7.14 Magnetisation versus field for sample LHN073 at 600 K

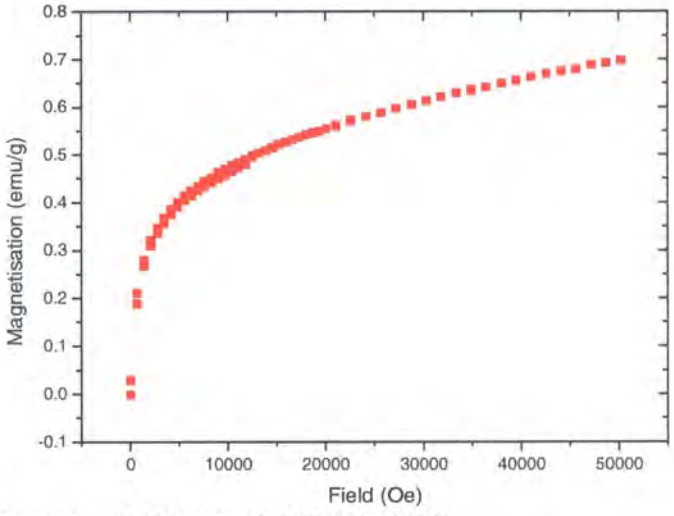

Figure 7.15 Magnetisation versus field for sample LHN097 at 300 K

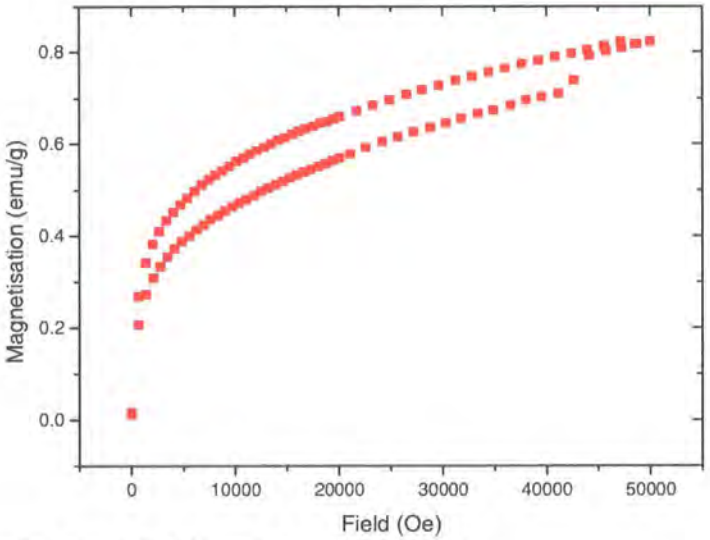

Figure 7.16 Magnetisation versus field for sample LHN097 at 475 K

Each of **figures 7.12 – 7.16** show that it is possible to measure magnetisation as a function of field at temperatures higher than room temperature using the oven attachment. It is also clear to see that as the temperature increases changes in the data obtained were occurring – magnetisation at 5 T is greater at higher temperatures, indicating the material has annealed partially and is registered by the magnetometer, as well as being able to see any hysteresis itself that exists in the material. The best and most consistent experimental protocol for obtaining VT magnetic data would be to heat to a certain temperature, record an m Vs. H loop at that temperature followed by an M vs. H loop at 300 K. After this the temperature of the sample can be increased and the measurement profile repeated.

7.4.5 Conclusions

To summarise, these 'proof of principle' measurements show that high temperature magnetic measurements can be recorded using the equipment provided by Quantum Design and the sample holder developed in Durham. The data obtained are consistent with those expected if the material were annealed *ex-situ*. A series of more systematic high temperature experiments were therefore performed. The samples for these experiments were prepared by me with the help of Malcolm Richardson, the glassblower at Durham University. The experiments themselves were run by Arnaud Serres. The data were obtained from Arnaud Serres and also manipulated by him, with some adaptation and variation performed by myself for this thesis. These are therefore only described in summary in **section 7.4.3.**

7.4.6 Variable Temperature Magnetic Studies of FePt Nanoparticles

This section discusses the study performed on a sample of LHN 162, an as-synthesised FePt nanoparticle material, studied in **chapter 5**.

The sample was prepared and loaded into the magnetometer as described in **section 7.4.2.2**.

The sample was heated to a set temperature in the absence of an applied magnetic field. At this point an M Vs. h loop was recorded from +5 T to -5 T. The temperature was then reduced to 300 K and a second M Vs. H loop recorded from +5 T to -5 T. The process was repeated until data were recorded at multiple desired temperatures. Data were recorded for temperatures 50 K apart between 400 and 500 K; 25 k apart between 500 K and 775 K. 26 measurements were made in total.

Figure 7.17 shows the hysteresis loops recorded between 400 and 775 K. **Figure 7.18** shows the hysteresis loops recorded at 300 K in between the higher temperature measurements.

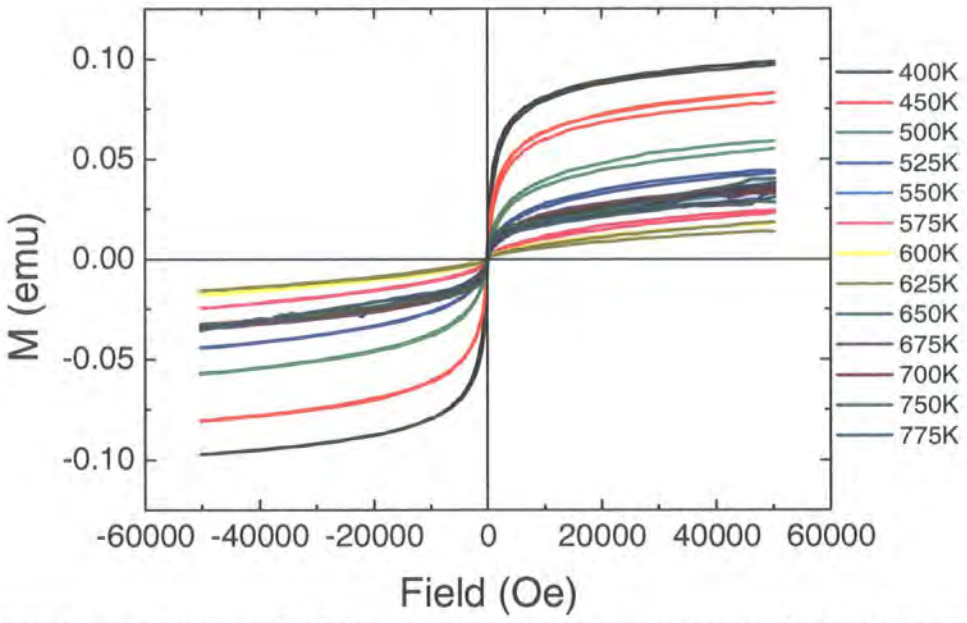

Figure 7.17 Magnetisation Vs. applied field loops measured at set temperatures ranging from 400 to 775 K.

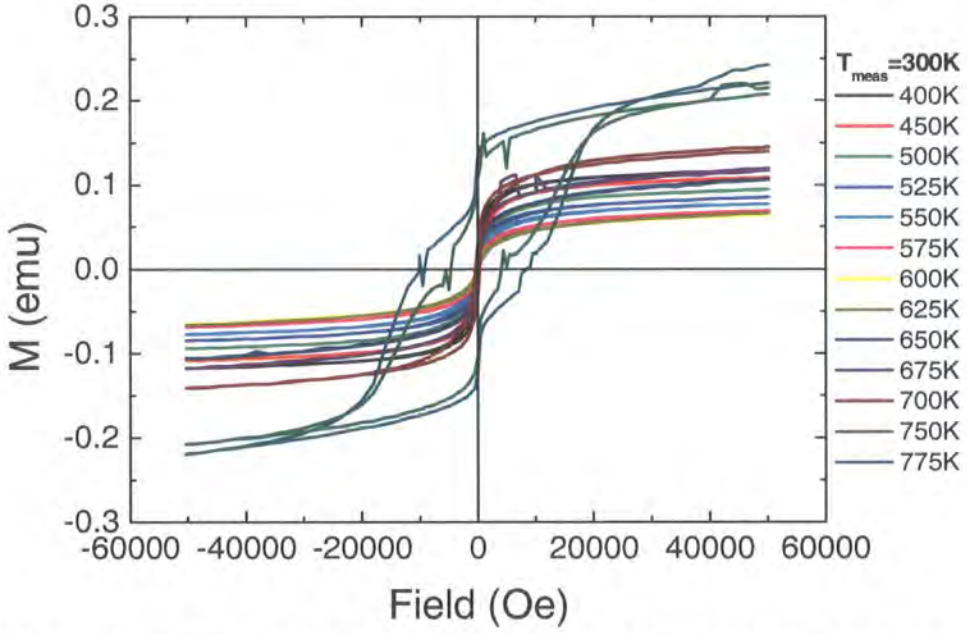

Figure 7.18 Magnetisation Vs. applied field loops measured at 300 K after the sample had been heated to temperatures ranging from 400 to 775 K.

It can be seen from both figures that after the sample had been heated to 400 K, a temperature at which the material would be expected to be in the fcc phase, the sample is superparamagnetic as the measurement is not linear about the origin, nor is any hysteresis present (which indicates no ferromagnetic or fct material is present). As the set temperature is increased, and particularly when 700 K is breached, it is clear that the material becomes ferromagnetic, from **figure 7.18**, as a coercivity, magnetisation saturation and remanence magnetisation can be seen.

Figure 7.19 shows the hysteresis loop measured at the set temperature of 400 K, i.e. before the suspected ordering temperature. **Figure 7.20** is an enlarged section of the hysteresis loop, showing the difference in magnetisation at the beginning and end of the experiment. In this case the magnetisation has decreased during the experiment.

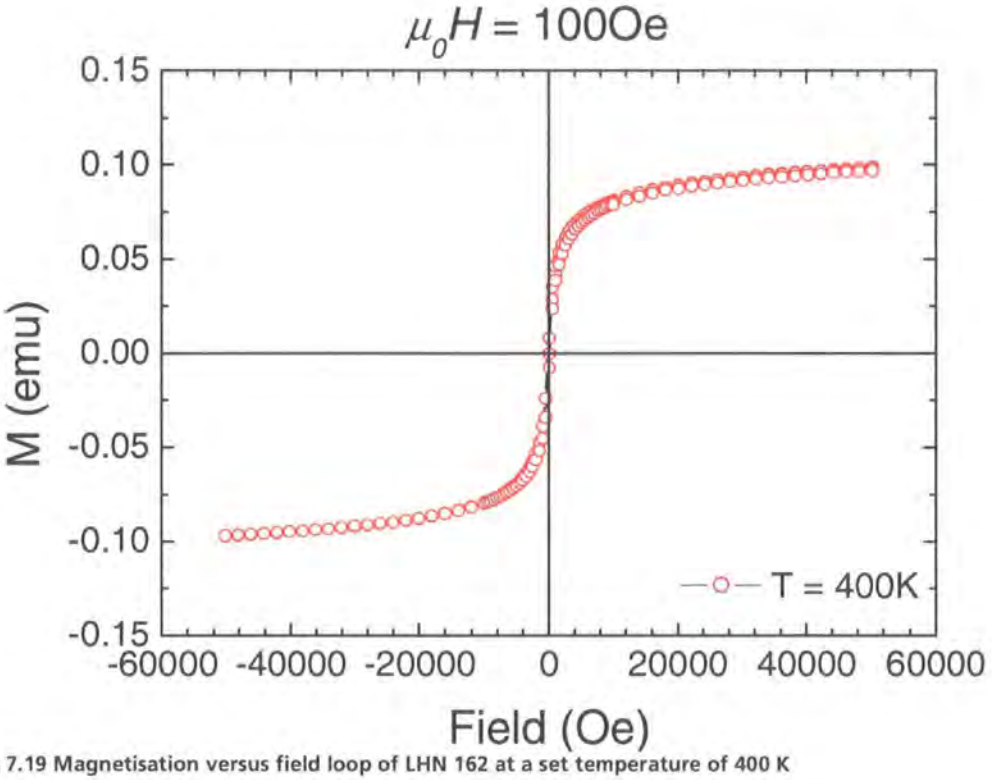

Figure 7.19 Magnetisation versus field loop of LHN 162 at a set temperature of 400 K

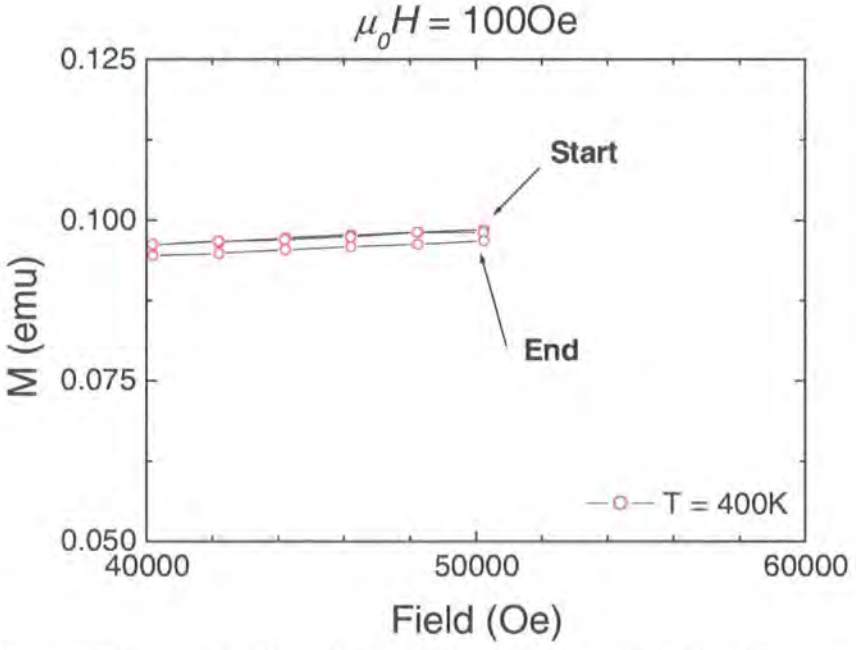

Figure 7.20 Magnetisation versus field loop of LHN 162 at a set temperature of 400 K between 4 and 5 Tesla

Figure 7.21 shows data from the same experiment but obtained at 700 K, a temperature after the suspected ordering temperature. **Figure 7.22** shows an enlarged area of **figure 7.21**

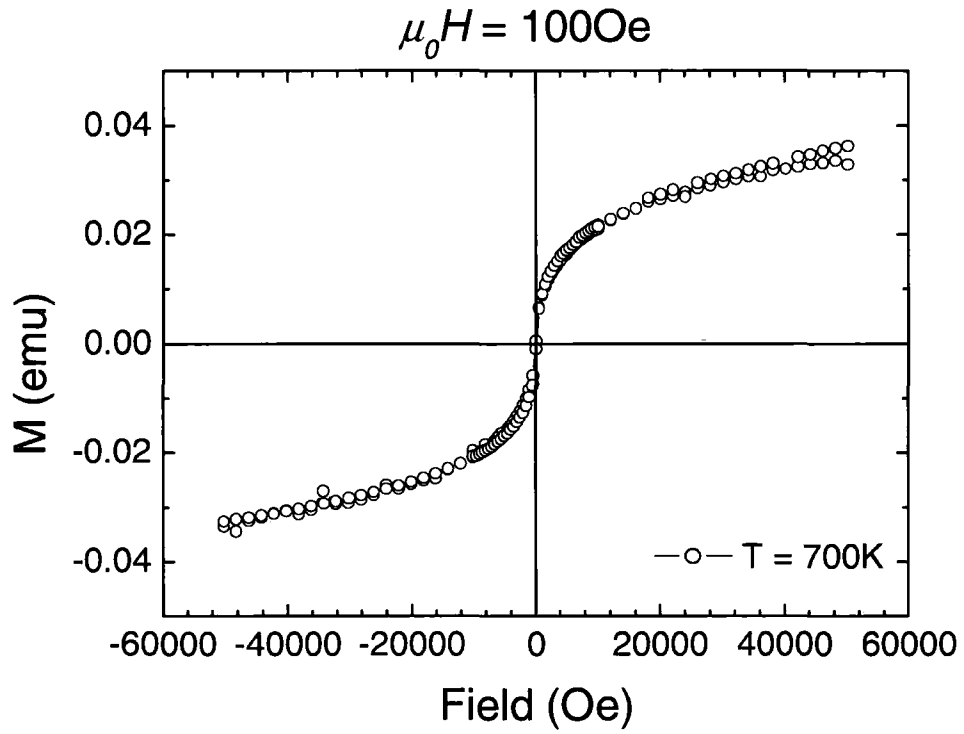

Figure 7.21 Magnetisation versus field loop of LHN 162 at a set temperature of 700 K

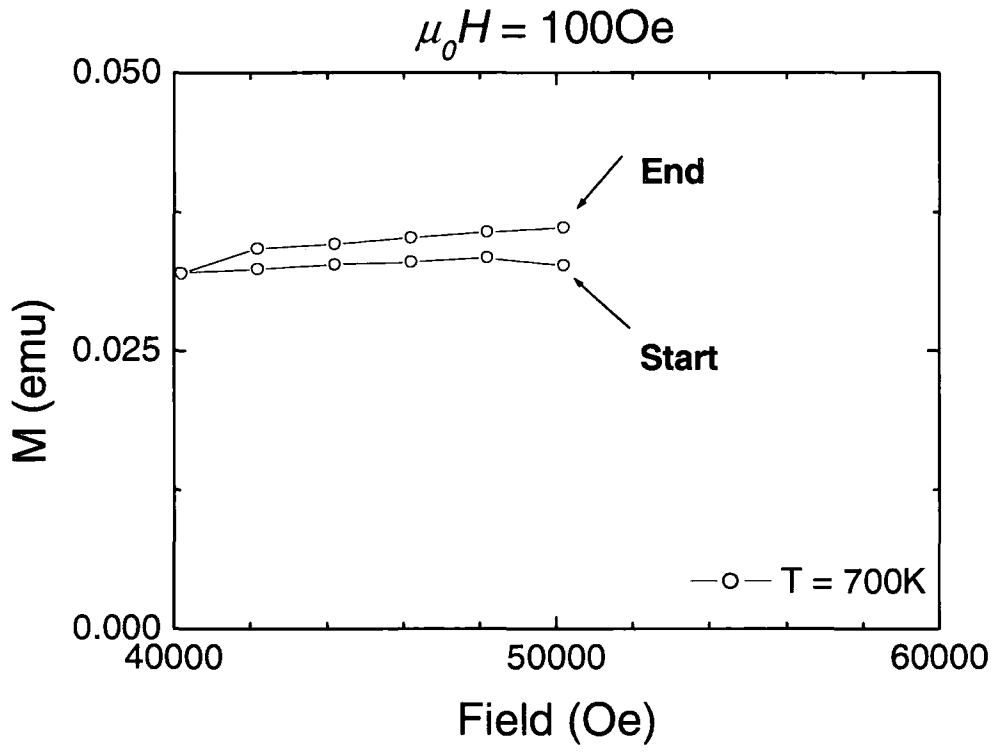

Figure 7.22 Magnetisation versus field loop of LHN 162 at a set temperature of 700 K between 4 and 5 Tesla

No hysteresis is observed when T = 700 K even though on cooling to 300 K it does. This is due to the fact that the set temperature is greater than the Curie temperature. This leads to the material losing its ferromagnetic properties.

After the material has undergone the ordering process, the magnetisation measured after a hysteresis loop is measured is greater than that before the hysteresis loop is measured. The magnetisation has increased as a result of the hysteresis loop measurement. The start of a hysteresis loop is defined as the first increase from 0 T to 5 T. The end is defined as the final increase from 0 T to 5 T.

Figure 7.23 shows the magnetisation at the start and end of the hysteresis loop measurement (i.e at +5 Tesla) as a function of temperature when measured at the set temperature of 400 K to 775 K.

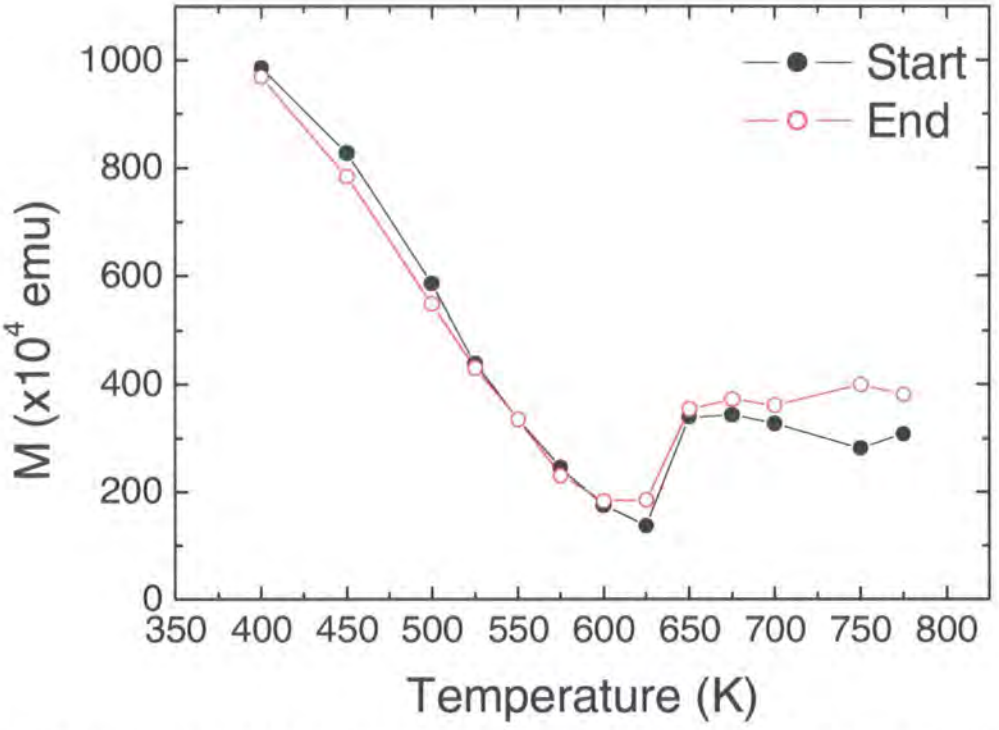

Figure 7.23 Magnetisation at 5 T as a function of temperature at the beginning and end of hysteresis loop measurement.

The difference observed between the magnetisation measured at the start and end of the hysteresis loop measurement from ~ 600 K onwards is due to the onset and continuation of FePt ordering from the fcc to fct phase. As the material has been warmed it becomes more ordered and becomes ferromagnetic as opposed to superparamagnetic. The onset of ordering is ~ 575 K as this is the point at which the magnetisation at the start of the hysteresis loop measurement becomes less than that at the end. On the application of a magnetic field the extra degree of ordering means a greater percentage of the material's magnetisation is able to align with the

magnetic field and the cumulative effect of this is to yield a greater magnetisation. These data indicate that the onset of ordering of FePt (sample LHN 162) is ~ 575 K. VTXRD studies in **chapter 5** suggested the onset of ordering for the same sample was ~629 K.

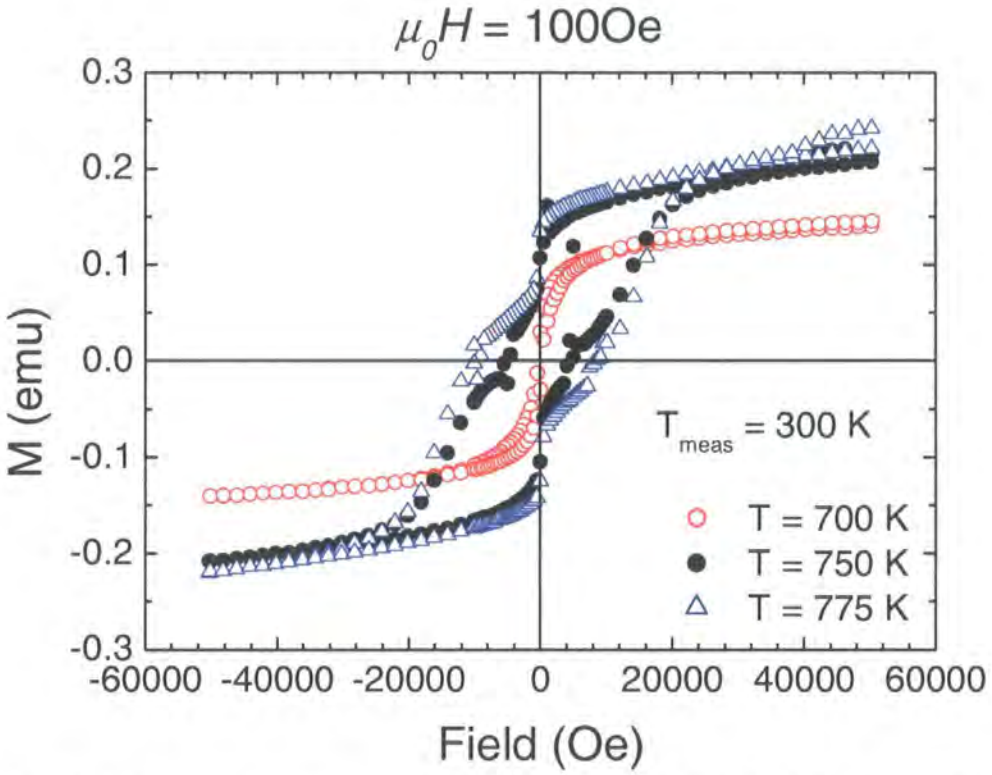

Figure 7.24 A graph showing the magnetisation versus field loops measured at 300 K after heating a sample of FePt (LHN 162) to 700, 750 and 775 K

Figure 7.24 shows that at room temperature after warming, the coercivity, remanence magnetisation and saturation magnetisation are all greater at 750 K than 700 K and greater still at 775 K. There is a significant increase in all three values between 700 and 750 K. This indicates that the material is still ordering until at least 775 K, the highest temperature which the sample was heated to. The coercivity at 775 K is ~ 18 kOe. At 700 K it is ~ 0.6 kOe.

Coercivity as a function of temperature should show that as the temperature increases, and the ordering increases, the coercivity becomes larger. This can be seen in **figure 7.25**.

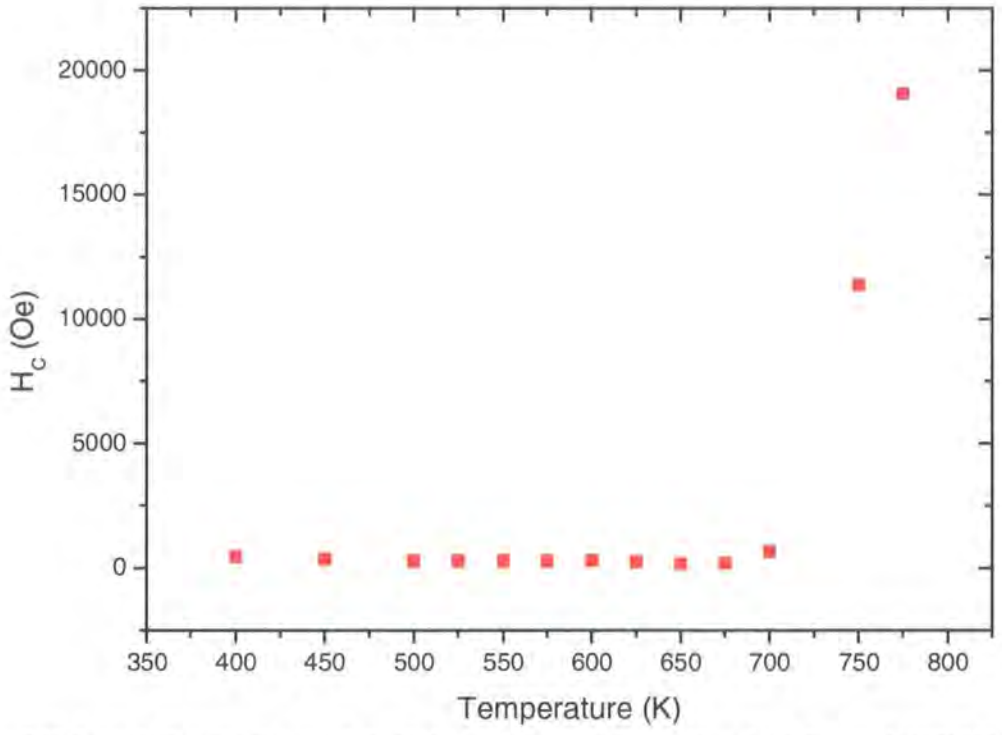

Figure 7.25 A graph showing the coercivity (Oe) as a function of temperature for FePt sample LHN 162 at 300 K after annealing to set temperatures ranging between 400 and 775 K.

7.5 Conclusion

It has been shown in this chapter that zero-field and field cooled measurements are useful for characterisation of fcc phase FePt nanoparticles in that they provide confirmation of the superparamagnetic behaviour of such material (and therefore confirmation that the material is in the fcc phase), an idea of the range of particle sizes present and also an indication of the purity of the sample being studied. They allow the measurement of magnetisation of a given FePt nanoparticle sample and enable obtainment of values for the samples which allow determination of their properties and how these can be exploited.

Magnetic characterisation of FePt nanoparticles prepared via the synthetic route developed in Durham has shown that fcc nanoparticles have been prepared; that fct nanoparticles have been directly synthesised and that fcc nanoparticles have been successfully annealed via post-synthetic heat treatment to the fct phase. This corroborates X-ray diffraction data.

In order to study the magnetic structure of FePt nanoparticles at high temperatures, and more specifically the *in-situ* study of the order-disorder transition from fcc to fct phase material, a methodology has been developed in Durham and shown to work. This has then been utilised to obtain data on the order-disorder transition of FePt nanoparticles prepared via the Durham synthetic method. These data have provided more evidence about the order-disorder process,

mainly regarding the temperature at which it occurs for a given sample, and in the case of the sample studied, correlating well with that seen from VTXRD studies in **chapter 5**.

Summary

The initial aims of this project were to develop a novel and advantageous route to FePt nanoparticles in the first instance. Once this was achieved the next steps were to characterise fully and understand the structure of the nanoparticles and ultimately to obtain the nanoparticles in the magnetically interesting fct phase whereby they could be deposited onto a chosen substrate in a monodisperse fashion – the nanoparticles needed to be consistently small (< 10 nm) and conform to the same shape so they were able to self-assemble into a hexagonal array when deposited.

This thesis describes the work done to achieve these aims and shows the success of the work. Chapter 3 shows the development work required to determine a novel route to FePt nanoparticles. It states that the route is successful, as corroborated by the characterisation data and also that the route is advantageous in multiple ways – it is a 'one-pot' synthesis therefore requiring less work to effect; it uses fewer volatile materials than previously exisiting routes and yields nanoparticles of an approximate 1:1 ratio of iron to platinum which can be annealed to the fct phase at lower temperatures than material as-synthesised via different routes.

In order to fully understand the structural transition of the FePt nanoparticles from the fcc to fct phase a suitable methodology was developed and qualified as described in chapter 4. This methodology was applied to derive Rietveld refined parameters obtained from X-ray diffraction data in chapter 5. This provided enough evidence to indicate that material prepared via the route developed in Durham and described in this thesis transitions to the fct phase at a temperature ~ 100 K below that prepared via literature routes. The data also provide other indications that material prepared via the Durham route yields samples with a greater degree of order than other synthetic methods. This all shows the benefits of the Durham route over those detailed in the literature. This was further corroborated by EXAFS experiments as detailed in chapter 6.

Finally, chapter 7 details magnetic measurements of the FePt nanoparticle samples and confirms that samples have been prepared that as-synthesised are superparamagnetic and when annealed transition to the fct phase – without significant sintering, meaning the nanoparticles are similar in size and shape allowing them to be deposited and therefore form a hexagonal array (as discussed in chapter 3).

In terms of the aims of the project they were all met and in some cases exceeded – for example not only was a synthetic route yielding superior nanoparticles developed, it was a simpler, quicker and safer route.

Appendix One

A1.1 TOPAS Academic Input File for Iron Platinum

```
'-----------------------------------------------
'input file for fitting d8 data
'-----------------------------------------------
#define phase_fept_fct 'use phase FePt_fct
'#define phase_fept_fcc 'use phase FePt_fcc
'#define phase_pt 'use phase Pt
'#define phase_fe2o3 'use phase Fe2O3
'#define phase_fe3o4 'use phase Fe3O4
'#define phase_sio2 'use phase sio2

'-----------------------------------------------
'general refinement stuff
'-----------------------------------------------
randomize_on_errors
continue_after_convergence
auto_sparse_CG
r_exp 12.719 r_exp_dash 67.831 r_wp 12.651 r_wp_dash 67.470 r_p 9.867 r_p_dash 66.686
weighted_Durbin_Watson 2.051 gof 0.995
iters 1000

'-----------------------------------------------
'next section to control whether running tb (graphical) or tc (input file mode)
'information macro used to read temperature in from command line when using tc or supply
from this
'file when running tb
'-----------------------------------------------

#define TB 'comment this line in or out if you're using TB (graphical) or TC (command line)

#ifdef TB
  macro filename {d8_xxxxx}
  macro rangeuse { 1}
  macro information {prm !te 700 prm !time 0}
#endif
information
```

```
'------------------------------------------------
'information about file, diffractometer, background, wavelength, etc
'------------------------------------------------

RAW(filename)
range rangeuse
Monochromator_Fix_Biso(!mono,27.26,!fixb, 0)

start_X 10
finish_X 120.0
Specimen_Displacement(height, -0.52491)
bkg @ 61.1640356 -40.4660327 18.3126149 -10.8339495 2.6060083 -0.927607738
0.191331458 1.63678502 -3.42612244 2.64711829 -1.51928851 0.348669887
lam
 ymin_on_ymax  0.001
 la  1 lo  1.540596 lh  0.5

'------------------------------------------------
'structural information for FePt Crangle J, Shaw J A a=3.905 c 3.735
'------------------------------------------------
#ifdef phase_fept_fct
        str

                'r_bragg  3.65985739
                scale @ 0.0000849686
                phase_name FePt_fct
                MVW( 501.850, 58.6106,percentphase_fept_fct 100.000)

                space_group "P4/mmm"
                Tetragonal(lpa_fept_fct  3.92405 min 3.8; max 4.2;,lpc_fept_fct 3.80634 min
3.6; max = lpa_fept_fct;)
                prm !c_over_a = lpc_fept_fct / lpa_fept_fct ; : 0.97000
'------------------------------------------------
'peak shape from refinement d8_0328_ideal_01.inp Y2O3 in htk1200 1 deg slits
'------------------------------------------------
                PV_Peak_Type(!pk11,    0.05895,!pk12,    0.00010,!pk13,    0.05351,!pk14,
0.29371,!pk15, 0.10909,!pk16, 0.11322)
                Crystallite_Size(crysize_fept_fct, 4.11469 min 2; max 1000;)
```

```
prm order 0.50000 min 0 max 0.5

site Fe1 x 0 y 0 z 0     occ Fe =1-order;:0.5000 occ Pt =order;:0.5000 beq bvalue_fept_fct 3.6358
min -5; max 5;
site Fe2 x 0.5 y 0.5 z 0 occ Fe =1-order;:0.5000 occ Pt =order;:0.5000 beq bvalue_fept_fct
3.6358 min -5; max 5;
site Pt1 x 0 y 0.5 z 0.5 occ Pt =1-order;:0.5000 occ Fe =order;:0.5000 beq bvalue_fept_fct
3.6358 min -5; max 5;
#endif

'------------------------------------------------
'structural information for fcc FePt i.e. same as Pt with 50% disorder on two sites - guess a
should be around 3.85
'------------------------------------------------
#ifdef phase_fept_fcc
        str
                r_bragg  1.46957431
                scale @ 0.0000732371
                phase_name FePt_fcc
                MVW( 501.850, 57.9554,percentphase_fept_fcc 100.000)

                space_group "Fm3m"
                Cubic(lpa_fept_fcc  3.86989 min 3.6; max 4.2;)
'------------------------------------------------
'peak shape from refinement d8_0328_ideal_01.inp Y2O3 in htk1200 1 deg slits
'------------------------------------------------
                PV_Peak_Type(!pk11,    0.05895,!pk12,    0.00010,!pk13,    0.05351,!pk14,
0.29371,!pk15, 0.10909,!pk16, 0.11322)
                Crystallite_Size(crysize_fept_fcc, 6.62524 min 2; max 1000;)

site Pt1 x 0 y 0 z 0 occ Pt 0.5 occ Fe 0.5 beq bvalue_fept_fcc 5.0000 min -5; max 5;
#endif

'------------------------------------------------
'structural information for Pt
' AUT  Kahler H
' REF  PHRVA 18 (1921) P. 210-217
' JRNL Physical Review (1,1893-132,1963/141,1966-188,1969)
' CELL A=4.028 B=4.028 C=4.028 `=90.0  a=90.0  g=90.0
'------------------------------------------------
```

```
#ifdef phase_pt
        str
                r_bragg  2.10928512
                scale @ 0.0000998434
                phase_name Platinum
                MVW( 780.312, 59.6631,percentphase_pt 7.763)

                space_group "Fm3m"
                Cubic(lpa_pt  3.90753 min 3.8 max 4.2)
'-------------------------------------------------
'peak shape from refinement d8_0328_ideal_01.inp Y2O3 in htk1200 1 deg slits
'-------------------------------------------------
                PV_Peak_Type(!pk11,    0.05895,!pk12,    0.00010,!pk13,    0.05351,!pk14,
0.29371,!pk15, 0.10909,!pk16, 0.11322)
                Crystallite_Size(crysize_pt, 5.86966 min 2; max 1000;)

site Pt1 x 0 y 0 z 0 occ Pt 1 beq bvalue_pt -0.4081 min -5; max 5;

#endif

'-------------------------------------------------
'structural information for Fe2O3
'AUT  Shirane G, Pickart S J, Nathans R, Ishikawa Y
'REF  JPCSA 10 (1959) P. 35-43
'JRNL Journal of Physics and Chemistry of Solids
'-------------------------------------------------
#ifdef phase_fe2o3
        str
                space_group R-3cr
                scale @ 0.0000851871
                phase_name Fe2O3
                MVW( 319.383, 107.9059,percentphase_fe2o3 31.801)
'-------------------------------------------------
'peak shape from refinement d8_0328_ideal_01.inp Y2O3 in htk1200 1 deg slits
'-------------------------------------------------
                PV_Peak_Type(!pk11,    0.05895,!pk12,    0.00010,!pk13,    0.05351,!pk14,
0.29371,!pk15, 0.10909,!pk16, 0.11322)
                Crystallite_Size(crysize_fe2o3, 2.65369 min 2; max 1000;)

                a lpa_fe2o3 5.50000  min 5.4 max 5.5
```

```
                b lpa_fe2o3 5.50000  min 5.4 max 5.5
                c lpa_fe2o3 5.50000  min 5.4 max 5.5
                al lpal_fe2o3 56.41978  min 52 max 57
                be lpal_fe2o3 56.41978  min 52 max 57
                ga lpal_fe2o3 56.41978  min 52 max 57

site Fe1 x 0.355 y 0.355 z 0.355 occ Fe 1 beq bvalue_fe2o3 1.7132 min -5; max 5;
site O1  x 0.55 y -0.05 z 0.25 occ O 1 beq bvalue_fe2o3 1.7132 min -5; max 5;

#endif

'--------------------------------------------------
'structural information for Fe3O4
'AUT  Wechsler B A, Lindsley D H, Prewitt C T
' REF  AMMIA 69 (1984) P. 754-770
' JRNL American Mineralogist
' CELL A=8.3958(2) B=8.3958(2) C=8.3958(2) `=90.0 a=90.0 g=90.0
'     V=591.8 Z=8 D=5.18
' SGR  F d 3 m (227)
'--------------------------------------------------
#ifdef phase_fe3o4
        str
                space_group Fd-3m:2
                scale @ 0.0000002634
                phase_name Fe3O4
                MVW( 1852.301, 589.3726,percentphase_fe3o4 0.435)
'--------------------------------------------------
'peak shape from refinement d8_0328_ideal_01.inp Y2O3 in htk1200 1 deg slits
'--------------------------------------------------
                PV_Peak_Type(!pk11,    0.05895,!pk12,    0.00010,!pk13,    0.05351,!pk14,
0.29371,!pk15, 0.10909,!pk16, 0.11322)
                Crystallite_Size(!crysize_fe3o4, 200.41206 min 2; max 1000;)

                a lpa_fe3o4 8.38423 min 8.3 max 8.5
                b lpa_fe3o4 8.38423 min 8.3 max 8.5
                c lpa_fe3o4 8.38423 min 8.3 max 8.5
                al 90
                be 90
                ga 90
```

```
site Fe1 x 0.125 y 0.125 z 0.125 occ Fe 1 beq bvalue_fe3o4 -4.9323 min -5; max 5;
site Fe2 x 0.5 y 0.5 z 0.5 occ Fe 1 beq bvalue_fe3o4 -4.9323 min -5; max 5;
site O1  x 0.2547 y 0.2547 z 0.2547 occ O 1 beq bvalue_fe3o4 -4.9323 min -5; max 5;
#endif

'-------------------------------------------------
' AUT  Wright A F, Lehmann M S
' REF  JSSCB 36 (1981) P. 371-380
' JRNL Journal of Solid State Chemistry
' CELL A=4.9134 B=4.9134 C=5.4052 `=90.0 a=90.0 g=120.0
'-------------------------------------------------



#ifdef phase_sio2
        str
                space_group P3221s
                scale @ 0.0000000161
                phase_name sio2
                MVW( 180.252, 112.2270,percentphase_sio2 0.000)
'-------------------------------------------------
'peak shape from refinement d8_0328_ideal_01.inp Y2O3 in htk1200 1 deg slits
'-------------------------------------------------
                PV_Peak_Type(!pk11,    0.05895,!pk12,    0.00010,!pk13,    0.05351,!pk14,
0.29371,!pk15, 0.10909,!pk16, 0.11322)
                Crystallite_Size(crysize_sio2, 750.49993 min 2; max 1000;)

                a lpa_sio2 4.92547 min 4.8 max 5
                b lpa_sio2 4.92547 min 4.8 max 5
                c lpc_sio2 5.34159 min 5.3 max 5.5
                al 90
                be 90
                ga 120

site Si1 x 0.4701 y 0.000 z 0.000 occ Si 1 beq bvalue_sio2 5.0000 min -5; max 5;
site O1 x 0.4136 y 0.2676 z 0.1191 occ O 1 beq bvalue_si02 5.0000 min -5; max 5;
#endif
```

```
'append_bond_lengths

'do_errors


'-------------------------------------------------
'set up the output file stuff here
'first put out just percentages for each phase
'follow this with more general stuff
'-------------------------------------------------
out "seed.res" append

'Out_String ("\tThis is the output file:\n")

Out(rangeuse, " Range: %11.5f")
Out(te, " Temp: %11.5f")

#ifdef phase_fept_fct
        Out(percentphase_fept_fct, " %11.5f")
#endif

#ifdef phase_fept_fcc
        Out(percentphase_fept_fcc, " %11.5f")
#endif

#ifdef phase_pt
        Out(percentphase_pt, " %11.5f")
#endif

#ifdef phase_fe2o3
        Out(percentphase_fe2o3, " %11.5f")
#endif

#ifdef phase_fe3o4
        Out(percentphase_fe3o4, " %11.5f")
#endif

#ifdef phase_sio2
        Out(percentphase_sio2, " %11.5f")
#endif
```

```
#ifdef phase_fept_fct
        Out(lpa_fept_fct, " phase_pt_a_c_crysize_bvalue: %11.5f")
        Out(lpc_fept_fct, " %11.5f")
        Out(lpc_fept_fct / lpa_fept_fct, " %11.5f")
        Out(crysize_fept_fct, " %11.5f")
        Out(bvalue_fept_fct, " %11.5f")
        Out(Get (r_wp), " %11.5f")
        Out(order, " %11.5f")
        Out(height, " %11.5f")
        Out(time, " %11.5f")

#endif

#ifdef phase_fept_fcc
        Out(lpa_fept_fcc, " phase_pt_a_crysize_bvalue: %11.5f")
        Out(crysize_fept_fcc, " %11.5f")
        Out(bvalue_fept_fcc, " %11.5f")
#endif

#ifdef phase_pt
        Out(lpa_pt, " phase_pt_a_crysize_bvalue: %11.5f")
        Out(crysize_pt, " %11.5f")
        Out(bvalue_pt, " %11.5f")
#endif

#ifdef phase_fe2o3
        Out(lpa_fe2o3, " phase_fe2o3_a_alpha_crysize_bvalue: %11.5f")
        Out(lpal_fe2o3, " %11.5f")
        Out(crysize_fe2o3, " %11.5f")
        Out(bvalue_fe2o3, " %11.5f")
#endif

#ifdef phase_fe3o4
        Out(lpa_fe3o4, " phase_fe3o4_a_crysize_bvalue: %11.5f")
        Out(crysize_fe3o4, " %11.5f")
        Out(bvalue_fe3o4, " %11.5f")
#endif
```

```
#ifdef phase_sio2
        Out(lpa_sio2, " phase_sio2_a_c_crysize_bvalue: %11.5f")
        Out(lpc_sio2, " %11.5f")
        Out(crysize_sio2, " %11.5f")
        Out(bvalue_sio2, " %11.5f")
#endif

Out(rangeuse,                    "                    Range:                    %11.5f"\n)
```

Appendix Two

A1.2 TOPAS Academic Input File for Iron Platinum

```
!this file contains everything to start excurv98
!assume that you're using a model with qa and qb for Fe/Pt sites
!

!read in datafile
r e
/home/leh/data_pt/lhn129d_pt.exs
1
32
Pt L3
0
1

!read shells etc from start.par file
r parameters
lhn129d_pt.par

!do potential/phase calculations...assume Fe neighbours everything
!( best to use light atom for neighbour)
!
set constant V
cal pot
c
Fe
-1
Fe
Fe

cal ph
n
4.825

!set up defaults for multiple scatter, kmin and k^3 weighting
c plmax 12
set ms on
```

```
c kmin 5
c kmax 12
s w 4
gs t x

!define sites
site qa
fe 0.5
pt 0.5
=
site qb
fe 0.66
pt 0.34
=

!set up rules - this one gives you a single Fe/Pt variable on two sites
rule perca2
1-percb2

rule perca1
1-percb1

!show pattern
list
site
p f

!do a refinment
ref are
12;perca1;13;perca2
c
1000
exit
n
fi
p f
```